Universität Bremen

Exploring the effects of amyloid beta (Aβ) and Tau aggregation on neuronal activity and proteotoxicity in *C. elegans*

Dissertation zur Erlangung des akademischen Grades des
Doctor rerum naturalium (Dr. rer. nat.)

eingereicht im Fachbereich 02 Biologie/Chemie
der Universität Bremen

vorgelegt von
Franziska Hirsch

Dezember 2024

Reviewer I: Prof. Dr. Janine Kirstein

Reviewer II: Prof. Dr. Olivia Masseck

Date of colloquium: 30.01.2025

TABLE OF CONTENTS

SUMMARY

Protein misfolding and aggregation in the human brain are key cellular hallmarks of neurodegenerative diseases, including Alzheimer's disease (AD). At the cellular level, AD is characterised by the formation of extracellular amyloid beta (Aβ) plaques and neurofibrillary tangles (NFTs) of hyperphosphorylated Tau protein, leading to the neuronal degeneration and cognitive decline. Evidence suggests that amyloid formation and structural abnormalities in patients' brain begin up to 20 years before clinical symptoms appear. My research aimed to correlate the aggregation and off-folding pathway of $A\beta_{1-42}$ and mutant Tau with the onset of neuronal decline using *C. elegans* as a model system. First, I developed and characterised a novel *C. elegans* Tau model pan-neuronally expressing human Tau with the patient-derived mutations P301L and V337M ($Tau^{P301L,V337M}$). I showed that $Tau^{P301L,V337M}$ aggregates with the progression of aging and exhibits multiple disease-related phenotypes. To study neuronal activity related to $Tau^{P301L,V337M}$ and $A\beta_{1-42}$ in *C. elegans*, I used a pan-neuronal GCaMP6m *C. elegans* strain. I observed that the decline of neuronal activity precedes the onset of both $Tau^{P301L,V337M}$ and $A\beta_{1-42}$ aggregation, with muscular $A\beta_{1-42}$ expression exhibiting similarly strong detrimental effect on neuronal activity as $A\beta_{1-42}$ expression in neurons.

The protein homeostasis (proteostasis) network aims to prevent the toxicity of aberrant proteins through the interplay of molecular chaperones and protein degradation systems. While intracellular chaperones assist in protein folding, refolding of misfolded proteins, preventing aggregation and disaggregating amyloids, little is known about mechanisms contributing to a functional proteome in the extracellular space. Therefore, I investigated the role of the two novel, potential extracellular modifiers (ECMs) - LYS-3 and CLEC-1 - on the aggregation and toxicity of $A\beta_{1-42}$ using *C. elegans* as a model system. Knockout of *lys-3* and *clec-1* decreased $A\beta_{1-42}$ aggregation in young adult animals, improved development and lifespan and reduced $A\beta_{1-42}$ spreading to distal tissues. Surprisingly, these findings suggest that LYS-3 and CLEC-1 contribute to $A\beta_{1-42}$ aggregation and toxicity by promoting amyloid spreading. Further studies are necessary to fully unravel the nature and mechanisms of LYS-3 and CLEC-1 functionality.

ZUSAMMENFASSUNG

Die Fehlfaltung und Aggregation von Proteinen im Gehirn sind zelluläre Kennzeichen neurodegenerativer Erkrankungen wie der Alzheimer-Krankheit. Diese ist charakterisiert durch die Ablagerung von extrazellulären Amyloid beta (Aβ)-Plaques und intrazellulärer Neurofibrillen aus hyper-phosphoryliertem Tau-Protein, welche zum Abbau neuronaler Strukturen und zur Verschlechterung kognitiver Leistungsfähigkeit führen. Studien zeigen jedoch, dass sich diese strukturelle Veränderung des Gehirns bereits bis zu 20 Jahre vor dem eigentlichen Symptombeginn entwickeln. Meine Studien hatten zum Ziel, mittels des Modelorganismus *C. elegans* einen Zusammenhang zwischen der Aggregation von $A\beta_{1-42}$ und mutierten Tau-Protein und der Abnahme neuronaler Aktivität zu finden. Zunächst generierte und charakterisierte ich ein neues *C. elegans* Tau Model, das eine mutierte Variante des Tau-Proteins mit den patienten-assoziierten Mutationen P301L und V337M ($Tau^{P301L,V337M}$) pan-neuronal exprimiert. Dabei konnte ich zeigen, dass die Aggregation von $Tau^{P301L,V337M}$ im Verlauf des Alterns zunimmt und phänotypische Merkmale des Krankheitsbildes aufweist. Um die neuronale Aktivität in Korrelation mit $Tau^{P301L,V337M}$ und $A\beta_{1-42}$ Aggregation in *C. elegans* zu messen, nutze ich einen pan-neuronalen GCaMP6m *C. elegans* Stamm. Ich beobachtete, dass die Abnahme der neuronalen Aktivität dem Einsetzen der $Tau^{P301L,V337M}$ und $A\beta_{1-42}$ Aggregation vorausgeht. Erstaunlicherweise verursachte auch die muskuläre $A\beta_{1-42}$ Expression eine ebenso starke Abnahme der neuronalen Aktivität wie die neuronale Expression.

Das Protein Homöostase (Proteostase) Netzwerk zielt darauf ab, die Toxizität fehlgefalteter Proteine durch das Zusammenspiel von molekularen Chaperonen mit Proteinabbausystemen zu regulieren. Während intrazelluläre Chaperone an der Faltung, Rückfaltung und Disaggregation fehlgefalteter Proteine beteiligt sind, ist wenig über die Mechanismen bekannt, die im extrazellulären Raum ein funktionelles Proteom unterstützen. Deshalb untersuchte ich die Wirkung zweier potenzieller extrazelluläre Modifikatoren (ECM) - LYS-3 und CLEC-1 - auf die Aggregation und Toxizität von $A\beta_{1-42}$ in *C. elegans.* Der genetische Knockout von *lys-3* und *clec-1* reduzierte die $A\beta_{1-42}$ Aggregation, vor allem in jungen Tieren, verbesserte die

Lebensspanne und Entwicklung sowie verringerte die Ausbreitung von $A\beta_{1-42}$ auf andere Gewebe. Überraschenderweise deuten diese Ergebnisse darauf hin, dass LYS-3 und CLEC-1 die Aggregation und Toxizität von $A\beta_{1-42}$ durch die Ausbreitung amyloider Fragmente fördern. Weitere Studien müssen allerdings zeigen, welche Prozesse der Funktion von LYS-3 und CLEC-1 als extrazelluläre Modifikatoren zugrunde liegen.

AUTHORSHIP DISCLAIMER

The presented work was conducted from 2021 to 2024 under the supervision of Prof. Dr. Janine Kirstein in her research group at the University of Bremen.

Parts of the data presented were obtained in collaboration with colleagues or collaborators from other research groups. Their contributions are acknowledged in the respective result sections.

Mira Sleiman and Dr. Annette Peter performed the cloning, transformation, UV integration, and backcrossing of the nGCaMP6m strain prior to the start of my PhD. Mira Sleiman also contributed to the UV integration of the Tau^{WT} plasmid. Yvonne Woitzat performed Western blots to detect Tau^{WT} and $Tau^{P301L,V337M}$ from nematode lysates in Jena.

The GCaMP6m fluorescence intensity measurements for the $A\beta_{1-42}$ and Tau and nmScarlet and mmScarlet control strains were performed in close collaboration with Dr. Nino Läubli from the lab of Gabriele Kaminski Schierle lab at the University of Cambridge.

Parts of the text may resemble or replicate the original text of the manuscript entitled "Impairment of neuronal activity occurs at the early stages of the aggregation cascade of $A\beta_{1-42}$ and mutant Tau", which is currently in preparation.

Furthermore, I would like to acknowledge the contribution of the Master's students Anuhsree Kelkar and Gurleen Kaur Kalsi and of the Bachelor's student Tom Daniel. Anushree and Gurleen performed lifespan and fecundity assays of $nTau^{WT}$, $nTau^{P301L,V337M}$, nmScarlet, and N2 wild-type strains under my supervision. Tom crossed the *lys-3(*tm2505) mutant (strain FX02505) with the $nA\beta_{1-42}$ strain and performed lifespan and developmental assays of $nA\beta_{1-42,}$ $nA\beta_{1-42}$ *lys-3*(tm2505), *lys-3*(tm2505), and nmScarlet *lys-3*(tm2505) strains under my supervision.

1 INTRODUCTION

Proteinopathies are diseases in which proteins lose their native conformation and form abnormal structures. Since the native conformation of a protein is essential for its biological function, proteins in their non-native state can lose their function and are more prone to aggregate. One class of proteinopathies is neurodegenerative diseases, which are characterised by a progressive loss of neuronal structures and are often associated with protein misfolding and aggregation in the brain. Neurodegenerative diseases such as Alzheimer's disease (AD), Parkinson's disease (PD), Huntington's disease (HD), Tauopathies, and amyotrophic lateral sclerosis (ALS) represent an economic burden to society and the healthcare system because there are few therapeutic options.

1.1 Alzheimer's disease

Alzheimer's disease is a progressive neurodegenerative disorder and the most common form of dementia, affecting 57 million people worldwide (Nichols et al., 2022). The number of cases is predicted to triple by 2050, when 153 million people will be diagnosed with this devastating disease. In 1907, the German psychiatrist Alois Alzheimer first identified the neuropathological features of the disease in the post-mortem brain of his patient Auguste Deter. He observed severe brain atrophy and, more importantly, identified the two main pathological changes in the brain (Alzheimer, 1907). These changes are now known as the accumulation of extracellular amyloid beta (Aβ) plaques and intracellular neurofibrillary tangles (NFTs) of hyperphosphorylated Tau protein (Glenner & Wong, 1984; Kosik et al., 1986). Aβ deposition and accumulation of pathological Tau are used as biomarkers for the diagnosis of AD. These can be detected in patients' brains by positron emission tomography (PET) and in cerebrospinal fluid (CSF) (Klyucherev et al., 2022; Mahaman et al., 2022).

The etiology of AD is highly complex and diverse. The precise mechanism leading to cognitive decline is still not fully understood. While Aβ and Tau play a pivotal role, a wide range of other factors contribute to the disease. These include neuroinflammation with abnormal activation of microglia, alterations in cholinergic and glutamate

signalling, oxidative stress, impairments in autophagy, and gut microbiome abnormalities (Figure 1.1). The interplay between these factors and their potential temporal sequence remains the subject of debate in current and past research (Thomas et al., 2020).

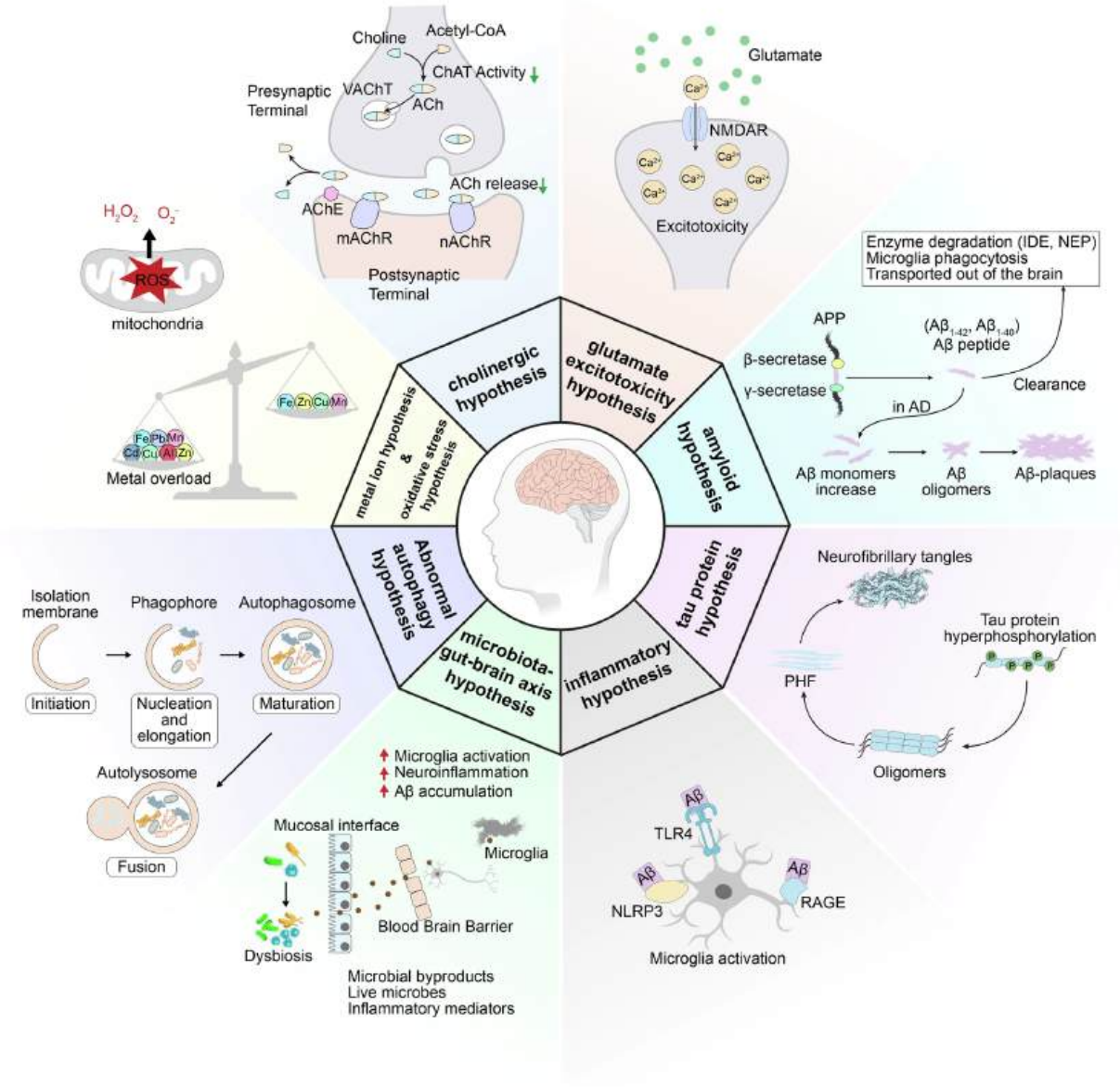

Figure 1.1: *Hypotheses leading to AD pathology.*

These include formation of Aβ plaques, Tau neurofibrillary tangles, neuroinflammation, microbiome gut abnormalities, impaired autophagy, oxidative stress, acetylcholine deficiency, and abnormal glutamate signalling. Figure from (Zhang et al., 2024).

In particular, the pathological abnormalities in patients' brains begin to form long before the first clinical symptoms appear. Studies suggest that the asymptomatic phase of AD

may precede the onset of symptoms by up to 20 years (Sperling et al., 2014). The earliest symptoms of the disease are known as mild cognitive impairment (MCI). These symptoms can be very variable and may include depression, anxiety, social withdrawal, or changes in sleep patterns. As the disease progresses, symptoms worsen and can culminate in severe memory loss, neuropsychiatric behaviour, hallucinations and delusions, and an inability to care for oneself (Knopman et al., 2021; Zhang et al., 2024).

AD can be divided into two groups, sporadic late-onset and familial early-onset AD. The latter accounts for only 1-5% of cases and is characterised by genetic mutations in distinct genes. The most common inherited autosomal dominant mutations occur in genes whose protein products are involved in the production of the Aβ peptide, such as the amyloid precursor protein (APP), presenilin 1 (PSEN1), or PS2. Symptoms of early-onset AD begin to manifest at the age of 65 and younger, while sporadic onset AD usually begins after the age of 65. Sporadic late-onset is influenced by a combination of genetic risks and environmental factors. While ageing is a major risk factor for AD, many other factors are thought to contribute to the onset of the disease. Maintaining physical health through activity, exercise, and a balanced diet is as important as mental health as we age. Social isolation, lack of mental stimulation, and emotional withdrawal are major contributors to AD (Long et al., 2023). Although the risk factors for sporadic and familial forms differ, they share similar neurological symptoms, clinical features, and treatment options. The increasing number of people with AD and the lack of effective treatments represent a growing social, economic, and health burden. Research is therefore urgently needed to elucidate the underlying mechanisms in order to find a potential cure.

1.1.1 Amyloid beta

Numerous hypotheses have been proposed to unravel the underlying mechanism leading to AD, but due to the complex and varied nature of the symptoms and clinical features, a defined cause remains elusive. One of the most extensively studied hypotheses is the amyloid cascade hypothesis, which has been proposed more than 30 years ago (Hard & Higgins, 1992). The hallmark of this hypothesis is the accumulation of plaques of the Aβ peptide, which is thought to be the causative agent

of AD, triggering a cascade of pathological events such as NFT formation, cell loss, dementia, and vascular damage. Aβ is derived from the processing of APP, a transmembrane glycoprotein. This hypothesis is further supported by mutations in genes whose protein products are involved in APP processing, such as APP itself, PSEN1, or PSEN2 in familial early-onset forms of AD. APP is expressed in many different cell types and tissues, with predominant expression in neurons/the brain. The physiological functions of APP are diverse, including neurogenesis and differentiation of neuronal cells, metal homeostasis, and synaptic functions (Müller et al., 2017). APP can be processed by two different sets of secretases in a non-amyloidogenic and an amyloidogenic pathway (Figure 1.2).

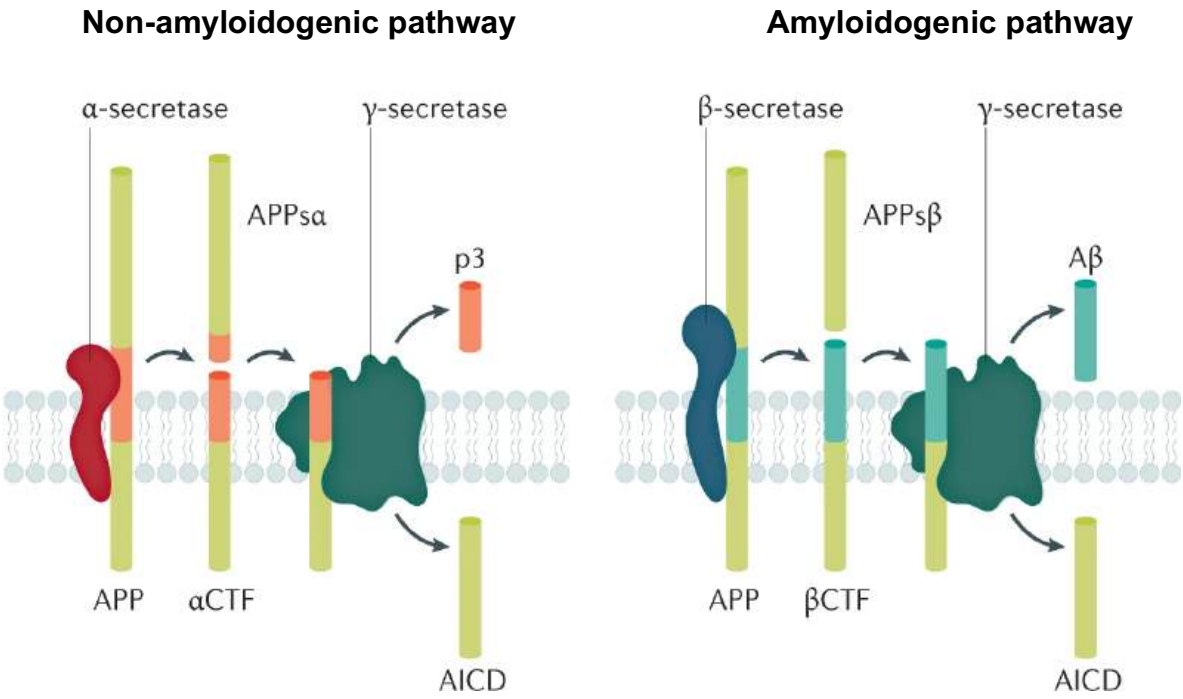

Figure 1.2: *Schematic representation of APP processing.*

APP is processed in a non-amyloidogenic pathway through α-secretase followed by γ-secretase cleavage (left graph). The α-secretase cleaves within the Aβ sequence, yielding p3 and AICD (Amyloid precursor protein intra-cellular domain). The amyloid pathway involves APP processing through sequential endoproteolytic cleavage by the β-secretase and γ-secretase, yielding Aβ and AICD. Figure adapted from (Knopman et al., 2021).

In the amyloidogenic pathway, the Aβ peptide is produced by β-secretase (e.g., BACE1), subsequent γ-secretase cleavage (e.g., presenilin 1 or 2) and secreted into

the extracellular space (Figure 1.2, right graph). The Aβ peptide has a molecular weight of approximately 4 kDa and occurs in different lengths depending on the exact γ-secretase cleavage site. The most abundant forms of Aβ peptides are $A\beta_{1-40}$ and $A\beta_{1-42}$, although other shorter Aβ species exist. $A\beta_{1-42}$ is the major species found in amyloid plaques and is therefore thought to exert greater toxicity than $A\beta_{1-40,}$ which has a lower tendency to aggregate, although it is more abundant in the CSF (Lane et al., 2018; Portelius et al., 2010). Soluble monomeric Aβ may have physiological functions, as picomolar concentrations have been found in the brain of healthy individuals. The presence of Aβ has been found to enhance synaptic plasticity, memory and learning, and has been shown to be neuroprotective during aging (Soucek et al., 2003; Puzzo et al., 2008; Morley et al., 2009; Kent et al., 2020). Alternatively, APP is processed in a non-amyloidogenic pathway by α-secretase- and γ-secretase-mediated cleavage, which does not generate Aβ (Figure 1.2, left graph).

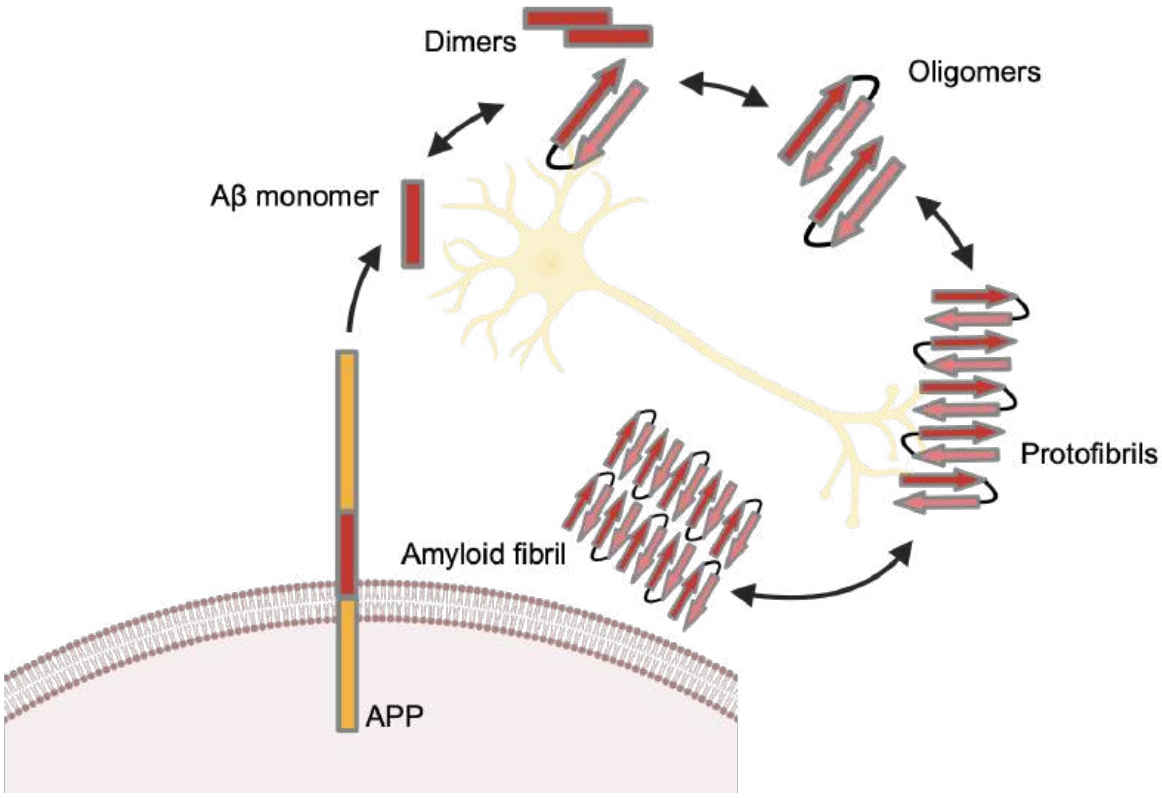

Figure 1.3: *Aβ fibrilisation from monomers, dimers, oligomers, protofibrils to insoluble amyloid fibrils.*

Aggregate species exist in a steady-state and can be rapidly and reversibly converted from one form to another. Figure created with BioRender.

Once secreted into the extracellular space, Aβ can form amyloid fibrils starting from various intermediate assemblies to ultimately insoluble amyloid plaques (Figure 1.3). An increase in Aβ monomers leads to the formation of oligomeric Aβ species. Chemically, oligomeric Aβ are defined as Aβ assemblies that cannot be pelleted from physiological fluids by high-speed centrifugation (Kulenkampff et al., 2021). Soluble Aβ oligomers can range from dimers to dodecamers, and although the structure of oligomers in the human brain has not been defined, *in vitro* studies suggest the presence of β-sheets within oligomeric assemblies (Yu et al., 2009; Hampel et al., 2021). Aβ oligomers can grow into large, soluble intermediate species with a molecular weight of around 75 kDa. These Aβ species are known as protofibrils (Johansson et al., 2006; Walsh et al., 1997). Aβ fibrils that form amyloid plaques are characterised by the typical cross-β-sheet structure of amyloid fibrils, which are insoluble and highly stable. These Aβ amyloid assemblies consist of β-sheets with β-strands perpendicular to the long axis of the fibrils and are stabilised by hydrogen bonds (Lu et al., 2013). The structure of $A\beta_{1-42}$ fibrils from human brain has been examined *in vitro* and *ex vivo* using cryo-electron microscopy (cryo-EM) (Yang et al., 2022). It was shown that two S-shaped protofibrils intertwine to give rise to two differently structured filaments, type I and II. Interestingly, type I filaments were predominantly found in the brains of sporadic AD patients, whereas type II filaments were found in individuals with familial AD.

Aβ fibrils have been shown to sequester other metastable proteins, thereby inhibiting the biological functions of these proteins (Knowles et al., 2014). In addition, large fibrils mechanically disrupt plasma membranes (Sciacca et al., 2021), complex metal ions, and increase the generation of reactive oxygen species (ROS) (Crnich et al., 2021). Most importantly, Aβ aggregates induce secondary nucleation of Aβ monomers at the fibril surface, which increases the pool of oligomers and subsequently accelerates further fibril formation (Cohen et al., 2013).

Although the amyloid cascade hypothesis is considered to be the most popular theory for the toxicity in AD, the formation of Aβ plaques as the driving factor in AD is strongly debated. The hypothesis that Aβ plaques are not the toxic species in AD is supported by studies in APP transgenic mouse models. Synaptic loss and neuronal damage were

observed in the absence of plaques (Mucke et al., 2000). In addition, Aβ plaque burden and cognitive decline are weakly correlated, and numerous clinical trials aimed to reduce amyloid burden failed (Ayton & Bush, 2021; Zhang et al., 2023). It is also considered that soluble Aβ oligomers are the primary neurotoxic Aβ species leading to neurodegeneration and cell death (Cline et al., 2018). Aβ oligomers have been shown to disrupt the integrity of cell membranes (Viles, 2023), activate inflammatory responses (White et al., 2005; Salminen et al., 2009), cause calcium homeostasis imbalance and mitochondrial dysfunction (Norambuena et al., 2018; Fani et al., 2021; Meng et al., 2024), induce oxidative stress (De Felice et al., 2007), and synapse degeneration (Wilcox et al., 2011). In addition, the solubility and small molecular size of Aβ oligomers facilitate spreading and propagation of Aβ throughout the brain (Langer et al., 2011; Stöhr et al., 2012; Jucker & Walker, 2013).

Future studies are needed to elucidate whether Aβ deposition and plaque formation are the actual primary causes driving toxicity in AD, or whether they are a consequence or secondary factor of the pathological process (Glass & Arnold, 2012; Fedele, 2023). Thus, the assembly of oligomers into mature fibrils could be a protective mechanism to reduce the toxicity of oligomers (Mannini et al., 2012).

1.1.2 Tau protein

Tau is one of many microtubule-associated proteins (MAPs) and was discovered in 1975 (Cleveland et al., 1977). At physiological conditions, Tau is located in the cytoplasm of axons, but has also been found in presynaptic and postsynaptic compartments. While it is mainly present in neurons, low levels of Tau have also been found in other cell types of the brain, such as astrocytes and oligodendrocytes (Wang & Mandelkow, 2016; Parra Bravo et al., 2024). In 1985, Tau was found to be the major protein component forming NFTs, which consist of hyperphosphorylated, filamentous Tau within the cell bodies (Kosik et al., 1986). NFTs are considered the pathological hallmark of primary Tauopathies such as frontotemporal lobar degeneration with Tau pathology (FTLD-tau) or progressive supranuclear palsy (PSP), in which Tau filaments are the primary cause of toxicity. In secondary Tauopathies such as AD, Tau inclusions form in response to other pathological processes (Sexton et al., 2022).

Pathologically, Tauopathies can also be distinguished by the specific isoform of Tau that forms the filaments. Human Tau is encoded by the *microtubule-associated protein tau (MAPT)* gene located on chromosome 16. It consists of 16 exons and alternative splicing of exons 2, 3, and 10 generates 6 unique splicing isoforms, referred to as 2N4R, 1N4R, 0N4R, 2N3R, 1N3R, and 0N3R according to the number of C- and N-terminal domains (Figure 1.4) (Brunello et al., 2020). The length of the isoforms varies, with the 2N4R isoform being the longest and the 0N4R being the shortest isoform.

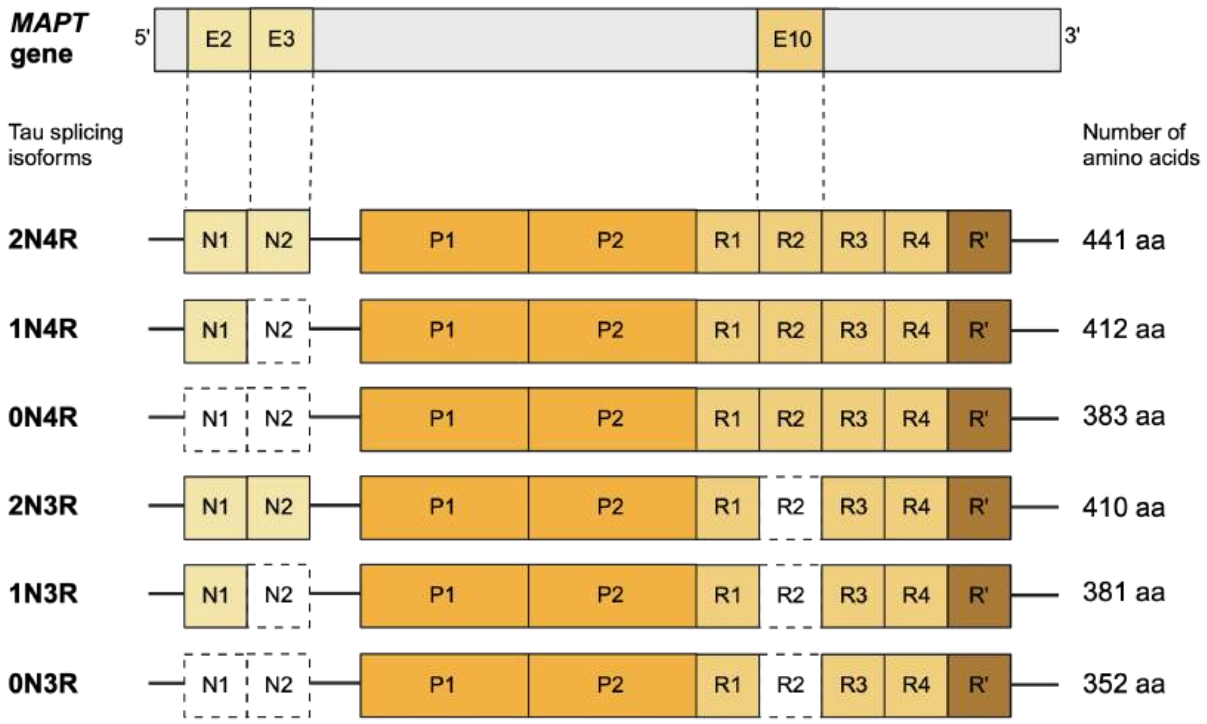

Figure 1.4: *Human MAPT gene locus encoding Tau.*

Alternative splicing of exons 2, 3, and 10 generates 6 unique Tau splicing isoforms that differ in the inclusion of the N1, N2, and R2 regions. The isoforms are named according to the presence of the N-terminal regions N1 and N2 (light yellow) and the microtubule-binding domains (MTBDs) R1-R4 (dark yellow). Figure created with BioRender.

The 3R or 4R isoforms consist of three or four microtubule-binding domains (MTBRs), respectively, and the 0N, 1N, and 2N isoforms consist of either none, only one or both N-terminal regions N1 and N2, respectively. Different Tau isoforms are differentially expressed in different cell types, developmental stages, and tissues. 3R Tau is known as fetal Tau and is only expressed during neurogenesis, whereas 4R Tau is known as adult Tau. In a healthy human brain, 3R and 4R isoforms are expressed at equal levels,

but the ratio of 3R:4R is altered in the brains of individuals with Tauopathies (Buchholz & Zempel, 2024). In AD, a mixture of 3R and 4R isoforms is expressed whose ratio changes with the progression of the pathology.

The Tau protein has four domains: the N-terminal projection domain (NTD), a proline-rich domain (PRD) in the middle part, the microtubule-binding domain (MTBD), and the C-terminal domain (CTD) (Figure 1.5) (Zeng et al., 2021). The NTD is intrinsically disordered, negatively charged at a physiological pH, and is also referred to as the projection domain because N1 and/or N2 project away from the microtubules when Tau binds to microtubules.

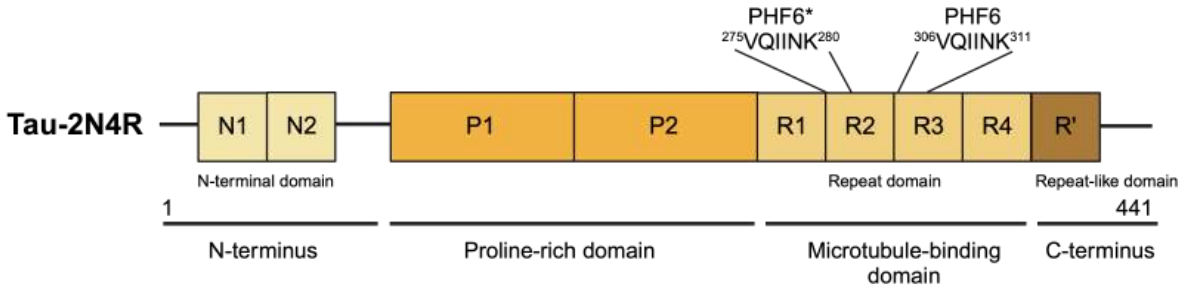

Figure 1.5: *Domain organisation of the longest Tau isoform, 2N4R.*

The 2N4R Tau isoform contains two N-terminal domains (NTD) N1 and N2, two proline-rich domains (PRD) P1 and P2, four repeat domains R1-R4 of the microtubule-binding domain (MTBD), and the repeat-like domain (R1) in the C-terminus (CTD). The two hexapeptide sequences PHF6* and PHF6 in the repeat domains R2 and R3 promote Tau aggregation. Figure created with BioRender.

The adjacent PRD consists of seven proline-X-X-proline (PXXP) motifs and is positively charged. It contains multiple phosphorylation sites and facilitates binding to signalling proteins with SRC homology 3 (SH3) domains. The MTBD contains up to 4 repeat domains R1-R4 that facilitate binding and attachment to the microtubules. Due to the additional R2 repeat domain, 4R isoforms have a higher microtubule-binding affinity than 3R isoforms and are therefore more effective in assembling microtubules. The aggregation propensity of Tau is determined by two hexapeptide sequences ^{275}VQIINK^{280} and ^{306}VQIVYK^{311} (PHF6* and PHF6) located on the R2 and R3 repeats of the MTBD, respectively. Consequently, 4R isoforms are more prone to aggregate due to the presence of the R2 domain, which contains an additional PHF6* motif. The PHF6 and PHF6* motifs adopt β-strand conformations (Von Bergen et al., 1999). Upon

aggregation, the PHF6 and PHF6* motifs of the MTBD form the fibril core by parallel packing of multiple repeats, forming β-sheets (Von Bergen et al., 1999; Andronesi et al., 2008). The remaining Tau protein fragments protrude from the amyloid core outwards to form a fuzzy coat (Dregni et al., 2019). Lastly, the CTD contains the repeat-like domain (R'), which is again intrinsically disordered, negatively charged and assists in microtubule-binding and assembly. Tau is subject to post-translational modifications (PTMs) that are major drivers of Tau behaviour and function. Tau can, for instance, get phosphorylated, ubiquitylated, acetylated, methylated and SUMOylated (Parra Bravo et al., 2024). Tau phosphorylation is the best-studied PTM with 80 identified residues, predominantly within the PRD and MTBD, that can be phosphorylated (Wegmann et al., 2021).

Monomeric, soluble Tau has a wide range of physiological functions in addition to its central role as a microtubule-stabilising protein (Parra Bravo et al., 2024). Binding of Tau via its MTBD to microtubule structures in neuronal axons serves to maintain neuronal integrity and dynamics. Tau is not only involved in microtubule stability but also in their polymerisation. In addition, Tau can inhibit motor protein binding to microtubules, thereby regulating transport mechanisms along the axons (Wang & Mandelkow, 2016; Parra Bravo et al., 2024). Tau has also been detected in the nucleus and has been implicated in genomic DNA stability, nuclear calcium homeostasis, and chromatin dynamics (Sultan et al., 2011; Violet et al., 2014). Synaptic, monomeric, soluble Tau regulates synaptic plasticity and neuronal activity by interacting with presynaptic proteins and receptors impacting vesicle and neurotransmitter dynamics (Tracy et al., 2022). In mitochondria, Tau was found to interact with proteins of the outer membrane, intermembrane space and matrix, and mutant Tau was shown to cause mitochondrial dysfunction (Tracy et al., 2022). The diverse functions of soluble Tau and its interactions with various other proteins demonstrate its importance in maintaining neuronal health and physiology.

At pathological conditions, such as in neurodegenerative diseases, an imbalance in the activity of phosphatases and kinases leads to hyperphosphorylation of Tau mainly within the MTBD (Zhang et al., 2024). These post-translational modifications lead to dissociation of Tau from the microtubules and the accumulation of hyperphosphorylated Tau monomers in the cytoplasm. Conformational changes in the

MTBD of free Tau monomers cause exposure of the PHF6 and PHF6* motifs and determine the conversion of monomeric, soluble Tau with physiological function into pathological aggregation-prone Tau (Brunello et al., 2020). The pairing of either PHF6 or PHF6* leads to Tau dimerisation, the first step in Tau oligomerisation (Figure 1.6). Tau dimers form nucleation centres to which other Tau monomers and dimers can be recruited to form elongated oligomers. These oligomers further aggregate and form the subunits of the filaments, called Tau protomers, which adopt the parallel, cross-β-sheet structure typical of amyloid aggregates (Meraz-Ríos et al., 2010). Two protomers form the mature Tau paired helical filaments (PHFs), which are the building blocks of NFTs.

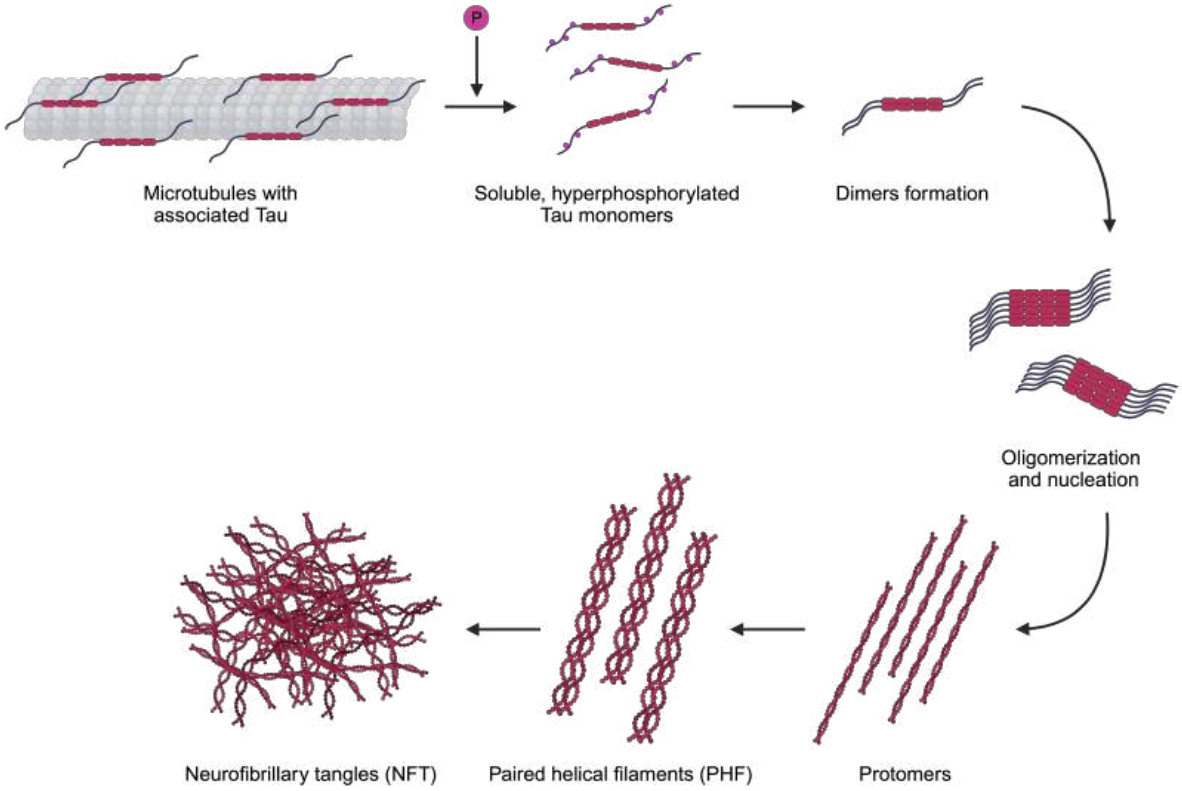

Figure 1.6: *Schematic representation of Tau aggregation.*

Hyperphosphorylation of Tau within its MTBD leads to detachment of Tau from microtubules. Freely soluble, hyperphosphorylated Tau monomers in the cytoplasm undergo conformational changes leading to dimerisation of Tau monomers through the assembly of the hexapeptide sequences PHF6 or PHF6*. Oligomerisation at nucleation centres leads to the formation of Tau protomers, paired helical filaments that form NFTs. Figure created with BioRender.

Many structures of aggregated Tau have been determined experimentally (Pizzarelli et al., 2020). Solid-state nuclear magnetic resonance (ssNMR) experiments determined the structure of Tau fibrils formed of P2R Tau containing both PRD, all four

MTBD and the C-terminus (Mammeri et al., 2023). Two- and three-dimensional NMR spectra indicated that the R2 and R3 repeat domains form a rigid β-sheet core. Surprisingly, the R2 domain was shown to form distinct temperature-dependent structures, either a β-arch at 24°C or a continuous β-strand at 12°C, which facilitate dimerisation with the R2 of another protofibril.

Tau aggregation and the generation of pathogenic Tau exert neurotoxicity at multiple levels (Wang & Mandelkow, 2016; Polanco et al., 2018). Hyperphosphorylation of Tau reduces its binding to microtubules, leading to microtubule disassembly and axonal transport deficits. Aggregation of Tau dissociated from microtubules also reduces the levels of functional, soluble Tau involved in several other functions (described above). In addition, intracellular aggregates affect vital physiological functions by steric hindrance, leading to cell death. Therefore, Tau aggregation and phosphorylation have been commonly implicated in the loss of Tau function and neurodegeneration. Although the progression and formation of NFTs in distinct brain regions correlate well with the severity of cognitive decline in patients, it is debated whether NFTs are the primary cause of neurodegeneration and synaptic loss. Neuronal loss in individuals with AD greatly exceeds the number of NFTs, and numerous AD mouse models suggest that the occurrence of neuronal loss is not correlated with NFT formation, as neurons die prematurely without forming Tau fibrils (Gómez-Isla et al., 1997; Morsch et al., 1999; Andorfer et al., 2005). Another pathological feature of pathogenic Tau, which contributes enormously to the toxicity in AD, is the ability of oligomeric Tau species to seed and propagate (Vogel et al., 2020). This phenomenon is referred to as spreading originating from prion disease and the spreading of Tau is therefore considered prion-like (Tanley & Rusiner, 2001). A prion disease such as Creutzfeldt-Jakob disease (CJD) is characterised by the misfolding of prion protein through previously misfolded prion proteins using their β-rich structure as a template. In Tauopathies such as AD, seeding-competent pathogenic Tau species, including misfolded oligomers, are released from a donor to a recipient cell by multiple mechanisms including exocytosis, synaptic vesicle release, ectosomes, exosomes and nanotube translocation (Brunello et al., 2020) (Figure 1.7). Within the recipient cell, pathogenic Tau species facilitate the formation of new Tau aggregates. In this way the aggregation and toxicity of Tau spread to multiple regions of the brain. The propagation

of Tau pathology in the brains of AD patients is staged according to the Braak staging scheme. Initial Tau pathology is usually observed first in the entorhinal cortex (Braak stages I and II), spreading to the hippocampus (Braak stages III and IV) and later to the cortex (Braak stages V and VI) (Braak & Braak, 1991).

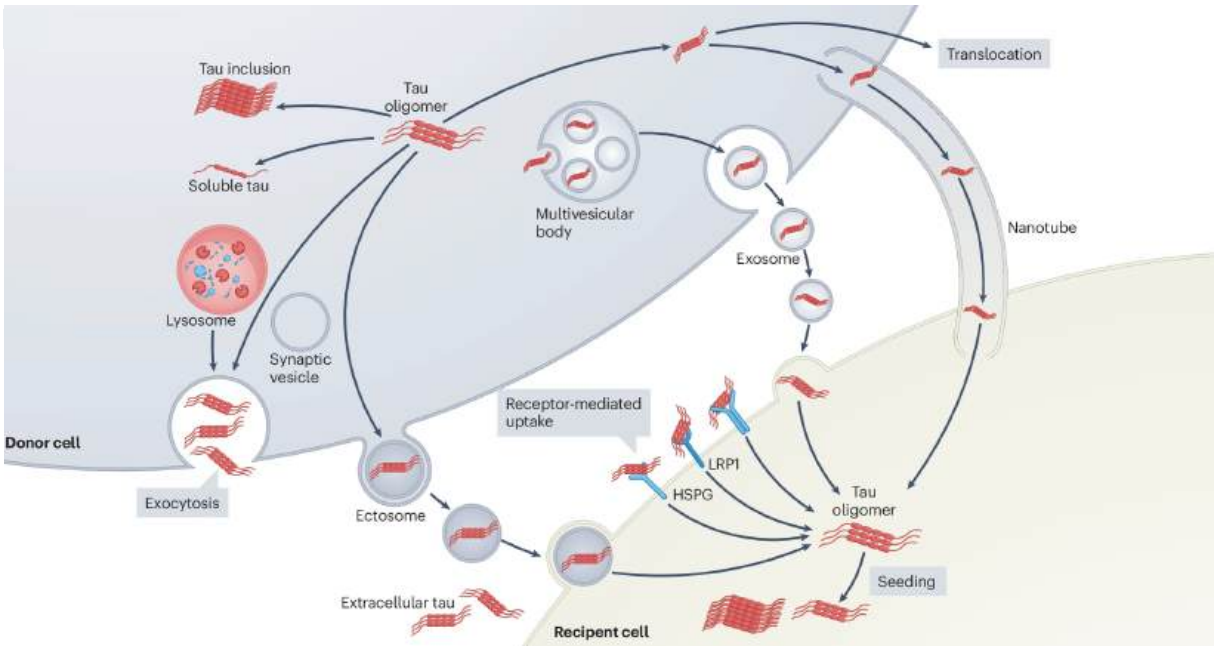

Figure 1.7: *Seeding and propagation of pathogenic Tau.*

Trans-cellular transfer of seeding-competent pathogenic Tau species, e.g., oligomers occurs via lysosomal exocytosis, ectosomes, exosomes, direct translocation or nanotubes. In the recipient cell, Tau oligomers induce template-mediated seeding of new Tau aggregates. Figure adapted from (Parra Bravo et al., 2024).

To date, approximately 115 mutations have been identified within the human *MAPT* gene that, occurring in both intronic and exonic gene regions (Alzforum.org website: Mutations MAPT). *MAPT* mutations are not associated with familial early-onset forms of AD, but are known to cause frontotemporal dementia (FTD) and several other Tauopathies characterised by Tau aggregation. The mutations are classified as pathogenic, benign, protective, or unclear and generally alter alternative splicing and the relative production of Tau isoforms. Mutations within the MTBD alter the microtubule-binding affinity and/or the propensity of Tau to aggregate. Missense mutations alter the sequence of Tau and are predominantly localised within the MTBD or in flanking regions. Tau proteins with the missense mutations, proline to leucine at residue 301 (P301L) and valine to methionine at residue 337 (V337M) have reduced affinity for microtubules and an increased tendency to aggregate (Goedert, 2005). Both

of these mutations have been commonly observed in patients with frontotemporal dementia (FTD). P301L is located within the R2 repeat domain of the MTBD and leads to a strong increase in intracellular Tau deposits in various regions of the brain. It leads to severe neuronal loss and gliosis (Dumanchin et al., 1998; Hutton et al., 1998). V337M flanks the R3 repeat domain of the MTBD at the C-terminal end. It enhances NFTs and PHFs in several regions of the neocortex, amygdala and parahippocampal gyrus (Poorkaj et al., 1998). P301L and V337M have been studied in various mouse models (Tanemura et al., 2001; SantaCruz et al., 2005; Vega et al., 2005). All transgenic mouse models expressing human Tau P301L or V337M developed behavioural and motor deficits, neurodegeneration, loss of microtubules and Tau aggregation. However, these murine Tau P301L or V337M models do not provide a temporal correlation between Tau aggregation and disease-related phenotypes. Close *in situ* monitoring of Tau aggregation as the mouse ages is not possible in living mice because analysis of Tau aggregation in the mouse brain requires the animals to be killed. Furthermore, mice as a biological model system are generally quite long-lived, with medium lifespans varying widely between genotypes, from a minimum of 291 to a maximum of 964 days (Vanhooren & Libert, 2013). To overcome these obstacles, another biological model system with shorter lifespan, such as the nematode *Caenorhabditis elegans* (*C. elegans*) might be better suited to study the aggregation of Tau P301L or V337M. To date, there are no *C. elegans* models available that express the mutant human Tau with both mutations, P301L and V337M.

1.2 The nematode *C. elegans*

Caenorhabditis elegans (*C. elegans*) is a small, free-living nematode (roundworm) found in soil that feeds on bacteria. Its suitability as a model organism in biological research - spanning fields such as molecular biology, developmental biology, neurobiology, aging and genomics - was recognised over 50 years ago in 1973 by the British biologist Sydney Brenner (Brenner, 1973). Among its many benefits, *C. elegans* boasts a simple anatomy while still being a multicellular eukaryotic organism. It possesses multiple tissues (e.g., reproductive system, intestine, body wall muscles, pharynx, and nervous system) and cell types that make it ideal for biological research (Figure 1.8) (Altun & Hall, 2012).

1.2.1 Usage of *C. elegans* as model system in biological research

C. elegans is a non-parasitic nematode that can be found worldwide. It exists in two sexes, self-fertilizing hermaphrodites with two X chromosomes (XX) and males with only one X chromosome (XO). Hermaphrodites make up over 99% of the population under normal conditions, while males occur less frequently (0.1%) and can only arise through spontaneous non-disjunction events in the hermaphrodite germ line. However, male frequency can increase to 50% through mating. Adult hermaphrodites have about 1000 somatic cells and reproduce via self-fertilisation, producing homozygous, genetically identical offspring. Males have 1031 somatic cells and a distinctive fan-shaped tail that is essential for mating with hermaphrodites. The presence of both hermaphrodites and males makes *C. elegans* ideal for genetic crossing, enabling the combination of multiple genotypes (Anderson et al., 2010).

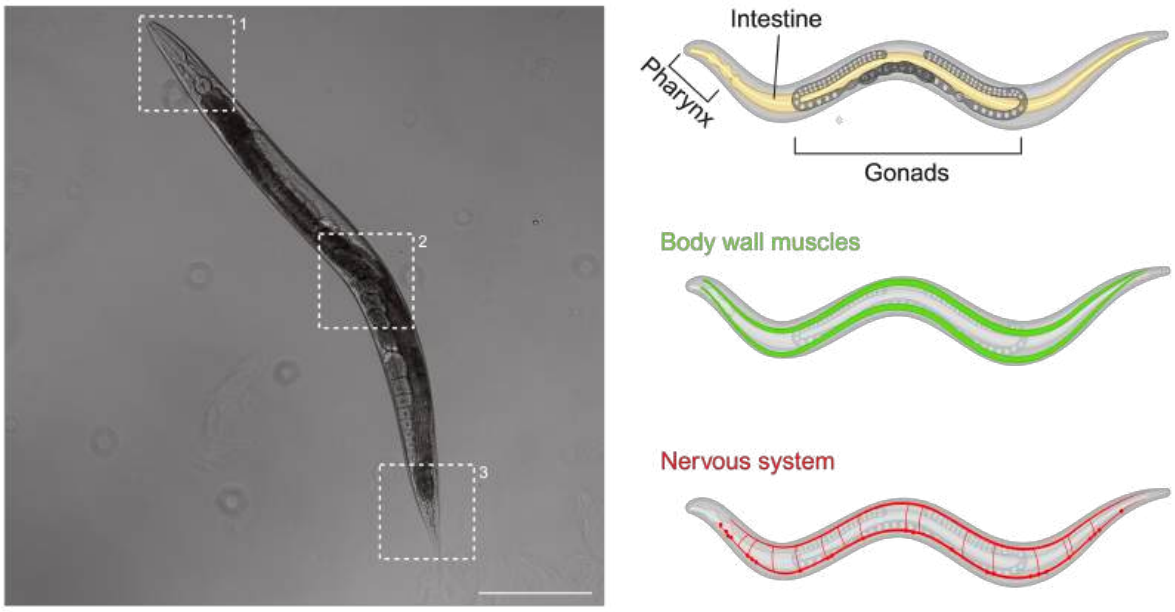

Figure 1.8: *Anatomy of an adult C. elegans.*

The basic anatomy of an adult, fertile *C. elegans* includes the pharynx, intestine, reproductive system, body wall muscles and nervous system. The left image is a representative confocal microscopy picture of an adult nematode with insets exhibiting head (1), mid-body region with embryos (2) and tail (3). Scale bar is 200 µm. On the right, a schematic represents different types of tissues including intestine, pharynx, gonads (top), body wall muscles (center) and nervous system (bottom). Figure created with BioRender.

Another advantage of using *C. elegans* as a biological model organism is its short lifecycle of about 30 days when cultured at 20°C. Aging *C. elegans* exhibit distinct

cellular and molecular changes (e.g., reduction in motility, infertility and degeneration of tissues) that are widely shared across evolution and species. This makes nematodes increasingly attractive for studying aging processes (Mack et al., 2018). *C. elegans* develops from the embryo into an egg-laying adult through four specific larval stages (L1, L2, L3 and L4) in about 3.5 days, followed by a 4-day fertility phase. One hermaphrodite produces around 300 embryos through self-fertilisation, which can increase to 1200-1400 embryos through mating (Corsi, 2015). Nematodes are easily cultured and maintained in the laboratory at low cost, either on agar plates or in liquid cultures with *E. coli* OP50 as a food source. With a transparent body and a size of about 1 mm, *C. elegans* is ideal for microscopy studies. The use of fluorescence dyes and marker proteins allows monitoring protein expression, localisation and aggregation of proteins in a living organism. The *C. elegans* genome was fully sequenced and annotated in 1998, enabling the generation of genetic tools and multiple genetically modified strains (The *C. elegans* Sequence Consortium, 1998; Hillier et al., 2005). Proteomic analysis has shown that 83% of the *C. elegans* proteome has homologous genes in humans, with only 11% of proteins being nematode-specific (Lai et al., 2000). Several signalling pathways, such as the insulin/insulin-like pathway, are conserved between humans and nematode (Dorman et al., 1995). *C. elegans* also has great potential in neuroscience and neurobiology research. It has a simple, but powerful nervous system of exactly 302 neurons and 56 glial cells. These neurons have fixed positions and, the connectome between individual neurons has been fully characterised (Cook et al., 2019).

1.2.2 *C. elegans* as a model for protein misfolding disease

C. elegans is an ideal model for studying human protein misfolding diseases that progress with aging, largely due to its short lifecycle (Mack et al., 2018). Protein misfolding and aggregation are hallmarks of neurodegenerative diseases. By expressing aggregation-prone, disease-related proteins in the neurons or muscles of *C. elegans*, these diseases can be mimicked. The modelling of neurodegenerative diseases in *C. elegans* has a rich history. The first *C. elegans* AD model, expressing the human Aβ, was created in 1995 (Link, 1995). Since then, numerous models of protein misfolding and neurodegenerative diseases have been generated. These include *C. elegans* models of AD, Parkinson's disease (PD), Huntington's disease

(HD) and amyotrophic lateral sclerosis (ALS). These models express disease-related proteins such as Aβ, Tau, α-synuclein, polyQ or Huntington-Exon1, TDP-43, SOD1 or FUS (Good & van Oosten-Hawle, 2020; Gallrein et al., 2021; Pigazzini et al., 2021).

C. elegans models of AD were generated by expressing Aβ (Alvarez et al., 2022) or Tau protein (Table 1.1). Although *C. elegans* possess an APP-related gene (*apl-1*), nematodes do not produce Aβ due to the lack of a β-secretase gene (Daigle & Li, 1993; Ewald et al., 2012). Overexpression of different Aβ variants in neurons and body wall muscles has proven toxic for cells, causing identifiable proteotoxic phenotypes, neurodegeneration and aggregation (Alvarez et al., 2022). However, some of the most widespread Aβ *C. elegans* models only express a truncated version of Aβ, $A\beta_{3-42}$ even though $A\beta_{1-42}$ has been found to be the most toxic form. Consequently, these models did not fully recapitulate Aβ pathology (McColl et al., 2009). In addition, none of the available models exhibiting a disease-related phenotype used a fluorescence marker protein to track and characterise the localisation and aggregation state of Aβ. A model expressing a genetic fusion of Aβ with green fluorescent protein (GFP) did not exhibit aggregation or foci formation in the nematodes (Ochiishi et al., 2016). To overcome these limitations, the Kirstein lab recently developed a novel approach to substoichiometrically label human $A\beta_{1-42}$ with the red fluorescent protein mScarlet for expression in the neurons and body wall muscles of *C. elegans* (Gallrein et al., 2021). Neuronal expression is facilitated by the pan-neuronal promoter *rgef-1,* while the *myo-3* promoter targets $A\beta_{1-42}$ expression to the body wall muscles (Figure 1.9). These novel AD *C. elegans* models exhibited $A\beta_{1-42}$ aggregation that increased with the progression of aging, severe proteotoxic phenotypes with impairments of lifespan, fecundity, and motility, as well as neurodegeneration and neurological defects. Both, the neuronal and muscle $A\beta_{1-42}$ strains, along with their respective control strains (neuronal mScarlet and muscle mScarlet), were used for the experiments conducted in this study and are referred to as $nA\beta_{1-42}$, $mA\beta_{1-42}$, nmScarlet, and mmScarlet.

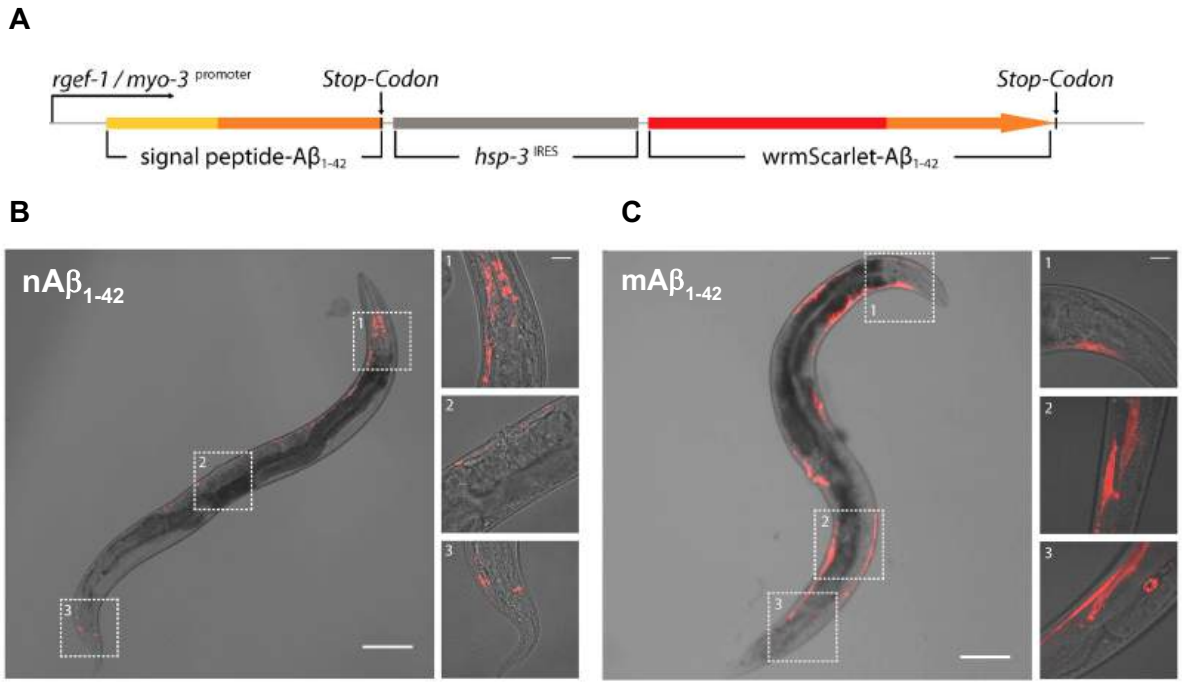

Figure 1.9: *Novel AD C. elegans strains expressing human Aβ1-42.*

A Schematic representation of the operon structure enabling substoichiometric labelling of Aβ1-42 in neurons (*rgef-1*) and body wall muscles (*myo-3*). Untagged Aβ1-42 is produced through cap-dependent translation and directed to the secretory pathway via a signal peptide. mScarlet-tagged Aβ1-42 is produced through less efficient cap-independent translation via the internal ribosome entry side (IRES). This approach ensures an excess of untagged Aβ1-42 over mScarlet-tagged Aβ1-42. Figure adapted from (Gallrein et al., 2021).

B Representative confocal microscopy image of the novel neuronal Aβ1-42 (nAβ1-42) strain. The left image is magnified 100-fold with a scale bar of 50 µm. The insets 1-3 show the close-ups of the head, mid-body and tail. Those images are magnified 630-fold with a scale bar of 20 µm. Figure adapted from (Gallrein et al., 2021).

C Representative confocal microscopy image of the novel muscle Aβ1-42 (mAβ1-42) strain. The left image is magnified 100-fold with a scale bar of 50 µm. The insets 1-3 show the close-ups of the head, mid-body and tail. Those images are magnified 630-fold with a scale bar of 20 µm. Figure adapted from (Gallrein et al., 2021).

Various attempts have been made to mimic Tau pathology in *C. elegans.* The only gene in *C. elegans* encoding a protein similar to human Tau is the protein with tau-like repeats (*ptl-1*), a member of the microtubule-associated proteins (MAPT). The genes of *ptl-1* and human Tau share about 50% sequence homology in their microtubule-binding domains and, to a lesser extent, in the N-terminal domain (Goedert et al., 1996). The PTL-1 protein is predominantly expressed in neurons and maintains

neuronal integrity, regulates mechanosensation, development, and lifespan (Gordon et al., 2008; Chew et al., 2013). Although PTL-1 binds and stabilises microtubules similarly to human Tau, it has not been shown to recapitulate Tau pathology in terms of fibrilisation and aggregate formation. As a result, overexpressing human Tau variants regulated by a pan-neuronal promoter has become the preferred method for generating *C. elegans* models of Tau pathology (Natale et al., 2020; Pir et al., 2017) (Table 1.1).

Table 1.1: *C. elegans models expressing human Tau.*

List of published *C. elegans* Tau model strains expressing various Tau variants. Some experiments were not conducted or the information is unavailable (n/a).

Publication	Tau variant	Promoter	Aggregation	Physiological Defects
Kraemer et al., 2003	1N4R^{WT} 1N4R^{P301L} 1N4R^{V337M}	*aex-3**	yes	motility defects, nerve cord degeneration
Miyasaka et al., 2005	0N4R^{WT} 0N4R^{P301L} 0N4R^{R406W}	*mec-7***	n/a	reduced touch response, abnormal neuronal structures
Brand et al., 2009	0N3R^{WT} 0N3R-HPH 0N3R-NPH	*rgef-1**	no	motility defects
Fatouros et al., 2012	1N3R^{V337M} + RD$^{\Delta K280}$	*rab-3**, *aex-3**	yes	Paralysis, axonal degeneration, presynaptic defects, synapse loss, mitochondrial transport defects

Chew et al., 2013	2N4R^{WT}	*ptl-1***	n/a	reduced lifespan, reduced touch response, abnormal neuronal strucutres
Pir et al., 2016	2N4R^{WT} 2N4R^{A152T} N't-Tau^{A152T}	*snb-1**	no	paralysis, motility defects, abnormal neuronal structures, neuronal dysfunction
Morelli et al., 2018	2N4R^{WT} 2N4R^{V363A} 2N4R^{V363I}	*aex-3**	yes	motility defects, pharyngeal dysfunction, synaptic impairments
Butler et al., 2019	1N4R^{WT} 1N4R^{A152T} 1N4R^{A152E}	*aex-3**	n/a	developmental defects, axonal transport defects
Nunez et al., 2022	2N4R^{WT}::GFP 2N4R^{P301S}::GFP 2N4R^{3PO}::GFP	*rgef-1**	yes	reduced lifespan motility defects
Han et al., 2024	1N4R^{WT}::Dendra2	*snb-1**	n/a	motility defects

**pan-neuronal promoter; **mechanosensory neuron promoter; ***ptl-1 endogenous promoter; RD$^{\Delta K280}$*: highly amyloidogenic aggregation-prone Tau fragment encompassing repeat domains only; N't-Tau: Tau encompassing N-terminal domains only; HPH: pseudo-hyperphosphorylated Tau mutant; NPF: non-phosphorylatable Tau mutant; 3PO: synthetic Tau fragment with high aggregation propensity.

The employed models express a wide variety of Tau isoforms and mutant Tau variants. The used Tau mutations are based on gene variations predominantly found in patients

with frontotemporal dementia (FTD), a highly severe and aggressive form of tauopathy characterised by progressive formation of Tau fibrils. While Tau expression in neurons causes severe pathogenic phenotypes in all reported *C. elegans* strains, it remains unclear whether these defects result from Tau aggregation. The majority of expressed Tau proteins are not fluorescently tagged. However, a fluorescence tag is indispensable for the localisation or *in situ* assessment of amyloid formation. *C. elegans* models expressing human Tau have been used to identify compounds or genes that suppress neurotoxicity. For example, the small-molecule drugs bb14 and BSc3094 have been shown to decrease Tau aggregation and motility defects (Fatouros et al., 2012). Azaperone, a dopamine D2 receptor antagonist, was identified in a drug library screen to improve motility of Tau-expressing nematodes, reduce insoluble Tau levels and neurodegeneration (McCormick et al., 2013). A genome-wide RNA interference (RNAi) screen in *C. elegans* expressing mutant Tau^{V337M} revealed 75 genes that enhanced Tau-mediated toxicity. These genes included kinases, chaperones, proteases, and phosphatases (Kraemer et al., 2006; Kraemer & Schellenberg, 2007).

1.3 Proteostasis network

Proteins are large biomolecules essential for the function of cells. Proteins differ from one another in their intrinsic amino acid sequence, which is determined by the nucleotide sequence of their genes. This amino acid sequence is initially produced through translation of the mRNA by ribosomes in the cytosol. The resulting linear polypeptide chain then folds into its specific native conformation, critical for the function of the protein. Although, the assembly of proteins into their native conformation is determined by the amino acid sequence, only a small number of proteins fold spontaneously into the correct conformation. Folding intermediates can misfold and consequently impair their cellular function. Misfolded or unfolded proteins expose their hydrophobic regions, increasing their tendency to aggregate and form insoluble deposits. Off-pathway reactions - including misfolding, unfolding and aggregation - are favoured by various factors such as mutations, stress, translation aberration, mRNA defects, molecular crowding, and aging (Hipp et al., 2019). The formation of aberrant protein conformations causes toxicity through either a loss-of-function or gain-of-toxicity (Hipp & Hartl, 2024). Loss-of-function primarily reduces the levels of the native,

functional state of the misfolded protein, while gain-of-toxicity is mediated by an increase in large insoluble protein deposits that cause toxic effects (e.g., aberrant protein interactions, membrane damage). Consequently, protein misfolding and aggregation are common features in numerous diseases and are not limited to neurodegenerative diseases.

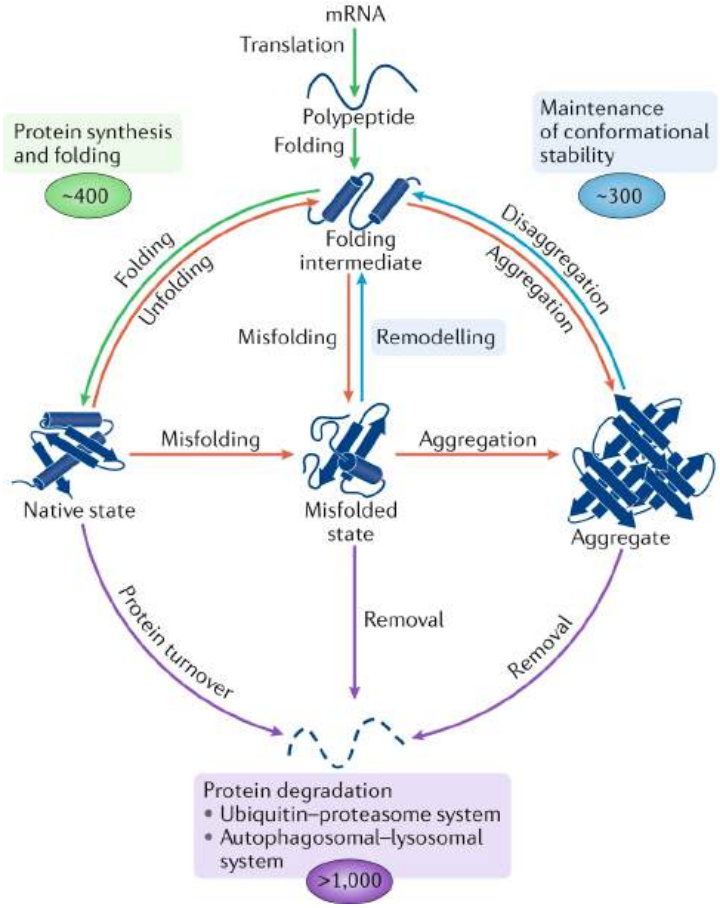

Figure 1.10: *The proteostasis network (PN).*

Proteins adopt their native state through chaperone-mediated folding (green). Off-pathway reactions such as misfolding, unfolding and aggregation (red) cause the formation of misfolded proteins and lead to the formation of protein aggregates. Chaperones are capable of disaggregating aggregates and revert them into a soluble state (blue). Cellular protein degradation systems facilitate the turnover of native proteins and remove misfolded proteins and aggregates (purple). Figure adapted from (Hipp et al., 2019).

To maintain the functionality of the proteome and prevent proteotoxicity, cells have evolved sophisticated methods to counteract protein misfolding and aggregation. These mechanisms, known as the proteostasis network (PN), comprise the interplay of molecular chaperones and components that efficiently degrade misfolded protein species (Hipp & Hartl, 2024). Molecular chaperones and co-chaperones assist in

protein folding e.g., to aid proteins in adopting their native conformation (*de novo* folding), refolding of misfolded protein species and disaggregation of aggregated proteins. In humans, more than 300 different chaperones have been identified, which are also highly conserved among different species (Brehme et al., 2014). Members of the chaperone protein family are often referred to as stress or heat-shock proteins (HSPs), as they were historically found to be upregulated during heat stress. The cellular protein degradation systems – ubiquitin-proteasome system (UPS) and autophagosomal-lysosomal system – are capable of degrading misfolded or unfolded proteins as well as larger, insoluble protein aggregates (Tai & Schuman, 2008; Aman et al., 2021).

Aging is one of the major factors contributing to the decline of the PN and is associated with the accumulation of aberrant and misfolded proteins (Labbadia & Morimoto, 2015). In turn, protein aggregates titrate PN components, further reducing its capacity to counteract unfavourable protein species. The connection between the proteostasis collapse and the increasing pool of aberrant protein species creates a feed-forward loop that accelerates with aging (Hipp & Hartl, 2024). Consequently, numerous age-related diseases are characterised by protein misfolding and aggregation. In *C. elegans,* the decline of proteostasis and the increase in protein misfolding begins early in adulthood, coinciding with the onset of fertility (Ben-Zvi et al., 2009; Labbadia & Morimoto, 2014).

1.3.1 Intracellular chaperones

A molecular chaperone is defined as a protein that interacts with, stabilises or helps another protein to acquire its native conformation without being present in the native structure. Molecular chaperones are grouped into different families based on their molecular weight: small HSP (sHSP), HSP40 or J-domain proteins (JDPs), HSP60, HSP70, HSP90 and HSP110. Stress induces the expression of most chaperones, which is transcriptionally regulated by the heat-shock response (HSR) (Vabulas et al., 2010). Genes controlled by the HSR have a conserved promoter sequence in the 5'UTR called heat shock element (HSE). When the transcription factor heat-shock factor 1 (HSF-1) binds to the HSE, it activates the transcription of *hsp* genes, leading

to the translation of HSPs. However, some chaperones, such as HSC70 (HSPA8) of the HSP70 family, are constitutively expressed within cells (Kampinga et al., 2009). Chaperones of the families of HSP60 (chaperonins), HSP70 and HSP90 are multicomponent molecular machineries that facilitate *de novo* protein folding and refolding through ATP- and cofactor-regulated binding and release cycles (Hartl et al., 2011). The HSP70 chaperone family is the most ubiquitous, comprising 13 protein members in humans and 10 in *C. elegans* (Nikolaidis & Nei, 2004; Kampinga et al., 2009;). The ATP-dependent reaction cycle of HSP70 is regulated by co-chaperones of the HSP40 family (J-domain proteins) and nucleotide exchange factors of e.g., the HSP110 family. The trimeric HSP70-HSP40-HSP110 chaperone machinery suppresses the aggregation of human amylogenic proteins such as Huntington or Aβ (Ayala Mariscal et al., 2022; Rosenzweig et al., 2019; Scior et al., 2018). HSP40 chaperones, or J-domain protein (JDPs), are a diverse family comprising 51 proteins in humans and 31 in *C. elegans* (Malinverni et al., 2023). HSP40s regulate the ATPase activity of HSP70 through their HSP70-interacting J-domain and can also directly bind to unfolded polypeptides. These polypeptides are targeted to specific HSP70 chaperones, driving HSP70 substrate specificity. HSP40 chaperones are grouped into class A, B and C according to their domain architecture (Ayala Mariscal & Kirstein, 2021). HSP110s are large chaperones of about 100 kDa, originally classified as non-canonical HSP70 members but are now recognised as a distinct class (Yakubu & Morano, 2018). Humans express four proteins of the HSP110 family, while *C. elegans* has only one (Kampinga et al., 2009; Rampelt et al., 2012). The main role of HSP110 chaperones is their function as nucleotide exchange factors for HSP70-mediated folding cycles (Rosenzweig et al., 2019). Additionally, HSP70-HSP40-HSP110 possess disaggregation activity and has been shown to disaggregate fibrils of Huntington, Tau and α-synuclein (Gao et al., 2015; Scior et al., 2018; Nachman et al., 2020).

Molecular chaperones serve two main functions: as “foldases” and “holdases”. Foldases assist *de novo* folding, refolding, and disaggregating in an ATP-dependent manner. In contrast, holdases such as sHSPs are ATP-independent chaperones that bind the exposed, hydrophobic amino acid residues of misfolded or unfolded proteins, preventing aggregation. sHSPs are small chaperones (12-45 kDa) that form homo- or

heterodimers. Humans express 10 identified sHSPs, while there are 14 sHSPs in *C. elegans* (Peter & Candido, 2002; Janowska et al., 2019).

1.3.2 Extracellular chaperones and proteostasis

Previous research in the field of proteostasis has primarily focused on the study of cytoplasmic, intracellular chaperones. However, growing evidence suggests that secreted proteins can influence protein folding and aggregation in the extracellular space (Wyatt et al., 2013; Braun, 2023; Wilson et al., 2023). Proteins in this environment face harsh conditions such as shear stress, oxidation and fluctuating pH, which can lead to protein destabilisation resulting in misfolding (Wyatt et al., 2013). Constitutively secreted extracellular chaperones (ECs) are thought to play a crucial role in maintaining the functionality of proteins and protecting cells from the consequences of protein misfolding and aggregation in extracellular fluids (Braun, 2023). Unlike their intracellular counterparts, ECs likely do not participate in active refolding and disaggregation due to low ATP availability in the extracellular space. Additionally, the concentrations of extracellular chaperones are several orders of magnitude lower than those within cells (Lyon & Milligan, 2019). Evidence suggest that ECs bind to misfolded proteins preventing protein aggregation and toxicity – similar to holdase chaperones like sHSPs (Wilson et al., 2023). EC then deliver these misfolded proteins to cell surface receptors for endocytosis. Internalisation facilitates safe disposal through intracellular protein degradation machineries (Mesgarzadeh et al., 2022). In addition to EC-mediated endocytosis of misfolded protein, other mechanisms contribute to extracellular proteostasis including extracellular proteases, the plasminogen activation system and endocytic cell surface receptors (Itakura et al., 2020; Yepes, 2021; Jongsma et al., 2023). Proteases can digest aggregates through enzymatic activity, producing protease-generated protein fragments (PGPFs) that are subsequently bound by ECs (Figure 1.11).

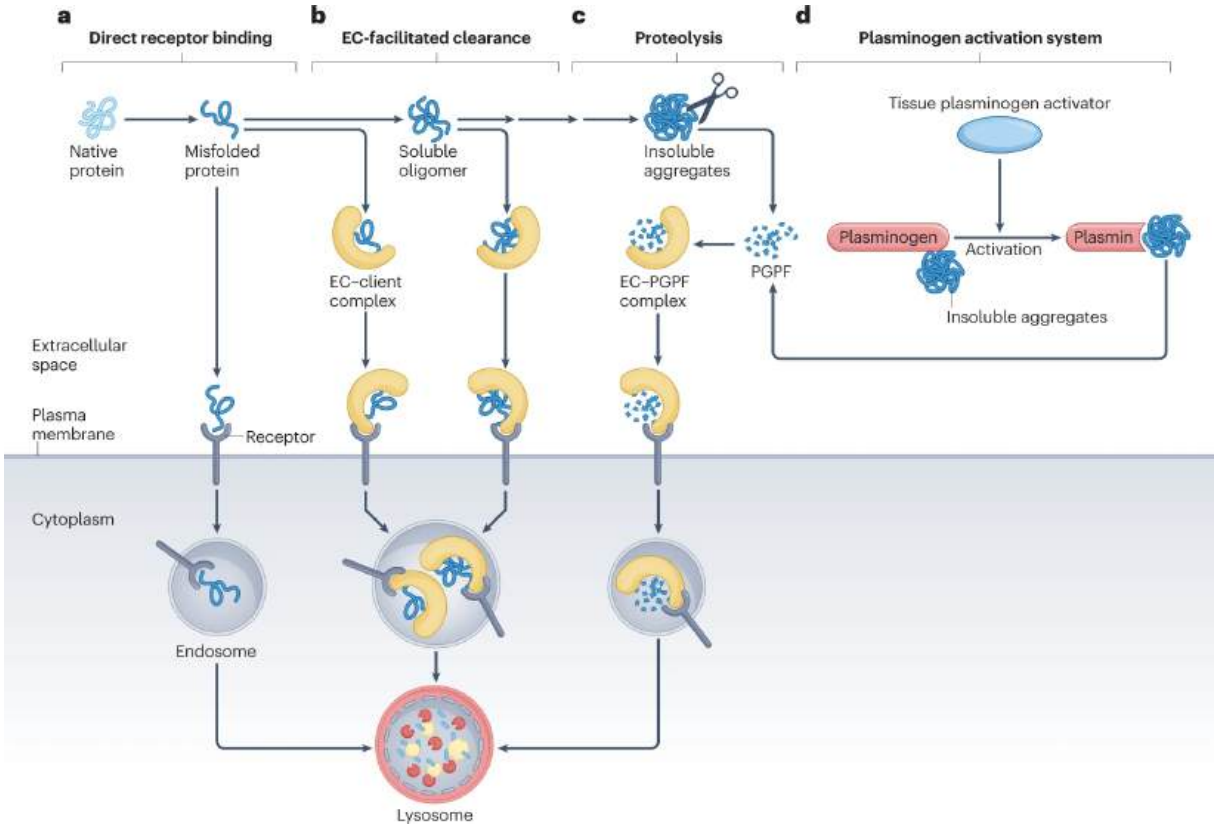

Figure 1.11: *The function of the extracellular proteostasis network.*

Misfolded proteins in the extracellular space are internalised either directly by endocytic cell surface receptors (a) or through binding to extracellular chaperones (EC) (b). Extracellular proteases digest insoluble aggregates, creating protease-generated protein fragments (PGPFs) that bind to ECs (c). The plasminogen activation system degrades aggregates, also yielding PGPFs (d). EC-client complexes are then internalised through receptor-mediated endocytosis, followed by lysosomal degradation. Figure from (Wilson et al., 2023).

The apolipoprotein Clusterin, identified in 1999, was the first EC discoverd and remains the most extensively studied EC in the context of neurodegenerative disease research (Humphreys et al., 1999). Studies have demonstrated the ability of Clusterin to delay fibrilisation of Aβ and other amyloidogenic proteins through direct binding *in vitro* (Yerbury et al., 2007; Narayan et al., 2012). However, *in vivo* studies have reported both beneficial and detrimental effects of Clusterin on protein aggregation and proteotoxicity (Yuste-Checa et al., 2022). Since 1999, around 20 human ECs with chaperone-like activity have been identified (Wilson et al., 2023). Animal models of neurodegenerative disease have demonstrated that administering EC or increasing EC expression levels can be beneficially affect protein aggregation and toxicity (Chaplot et al., 2020). However, the nature of the chaperone activity remains elusive for most ECs and requires further clarification *in vivo*. Identified human ECs are highly

diverse, multifunctional proteins with a wide range of functional domains. Consequently, mechanistic studies are needed to understand how each EC functions individually, both *in vitro* and *in vivo*.

Past research focused on the identification of novel extracellular modifiers (ECM) with potential chaperone-like function (Gallotta et al., 2020; Geraghty et al., 2021). A major challenge in studying extracellular proteostasis has been the identification of a suitable model system. In 2020, a genome-wide RNAi screen in *C. elegans* identified 57 potential ECMs for the first time in this model organism (Gallotta et al., 2020). The identified genes and their protein products showed striking functional diversity, with half of the genes having human orthologues expressed in the brain. These human orthologues encode proteins involved in the immune system, fibrinolytic system, extracellular matrix, cell migration, lipid transport and reproductive system. Future studies need to determine whether those ECMs possess chaperone-like functions that modulate human protein aggregation and toxicity in extracellular proteostasis.

2 OBJECTIVES

Protein aggregation is a pathological hallmark of neurodegenerative diseases such as Alzheimer's disease. The presence of Aβ plaques and Tau neurofibrillary tangles in the brains of AD patients is associated with cognitive decline, neuronal loss, severe dementia and various psychological symptoms. While clear therapeutic strategies remain elusive, recent treatments have shown promise in counteracting and delaying amyloid formation, potentially alleviating symptoms and postponing the onset of pathology. Thus, there is an urgent need for research to deepen our understanding of the physiological effects of amyloid formation, the correlation between aggregation and neuronal function, and the modulators that can influence the aggregation process.
This thesis is structured into three parts, each addressing different aspects of Aβ and Tau aggregation in AD using *C. elegans* as a model system. The specific research questions guiding these investigations are as follows:

1. **Objective**:
   Establishing a novel mutant Tau model to study the off-folding pathway of human Tau with the patient-derived mutations P301L and V337M in *C. elegans*. Does human mutant Tau fulfil the pathological hallmarks of a disease-associated amyloid protein in the nematode, such as aggregation and propagation to other cells and tissues and does it exert proteotoxicity?

2. **Objective:**
   How is neuronal decline correlated with Aβ and mutant Tau aggregation during aging *in vivo*? Establishing an experimental setup to analyse neuronal activity in *C. elegans* in a high-throughput manner using the encoded calcium sensor GCaMP6m.

3. **Objective:**
   Are components of extracellular proteostasis such as extracellular modifiers, capable of modifying $A\beta_{1-42}$ aggregation and proteotoxicity in an $A\beta_{1-42}$ *C. elegans* model?

3 RESULTS

3.1 Generation and characterisation of a novel *C. elegans* model expressing human Tau

Amyloid fibril formation is a hallmark, observed in the brains of patients suffering from neurodegenerative diseases such as AD. The Tau protein is one of the key proteins known to aggregate as AD progresses, ultimately forming NFTs in different brain areas (Braak et al., 2006; St-Onge et al., 2024). Despite numerous studies aiming to elucidate the molecular mechanisms of Tau aggregation and its cellular consequences, it remains poorly understood. Therefore, *in vivo* models are needed to further characterise Tau. *C. elegans* as a model system offers great potential, especially in the field of neurobiology and aging research. Thus, I investigated Tau in *C. elegans*.

3.1.1 Generation of *C. elegans* strains pan-neuronally expressing human wild-type Tau (Tau^{WT}) and mutant Tau ($Tau^{P301L,V337M}$)

To track the aggregation and propagation of Tau in a living organism such as *C. elegans*, I generated two strains: one expressing human wild-type Tau (Tau^{WT}) and another expressing a Tau variant harboring the patient-derived mutations P301L and V337M ($Tau^{P301L,V337M}$) in neurons (Figure 3.1).

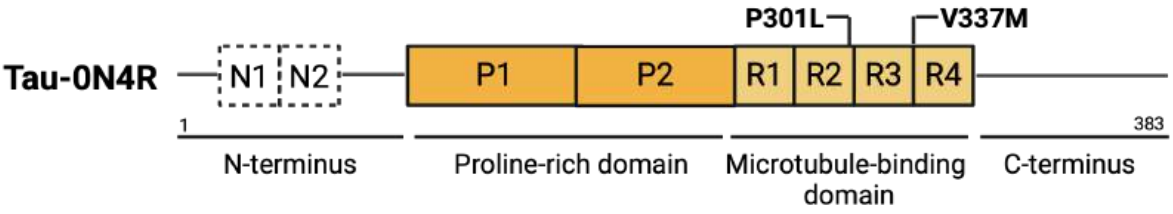

Figure 3.1: *Protein structure of Tau 0N4R.*

Protein domain structure of the human Tau protein isoform 0N4R used for overexpression. The N-terminus of Tau-0N4R lacks the two N-terminal domains N1 and N2 (dashed squares), followed by a proline-rich domain, the four repeat domains (R1-R4) of the microtubule-binding domain and the C-terminus. The positions of the two point-mutations - Proline-to-Leucine at residue 301 (P301L) and Valine-to-Methionine at residue 337 (V337M) - used to generate the mutant Tau strain are indicated. These mutations are associated with frontotemporal dementia (FTD). Figure created with BioRender.

Analogous to the amyloid beta ($A\beta_{1-42}$) *C. elegans* model developed in the Kirstein lab (Gallrein et al., 2021), I generated a bicistronic operon that is regulated by the pan-neuronal promoter *rgef-1* (Figure 3.2 A and C).

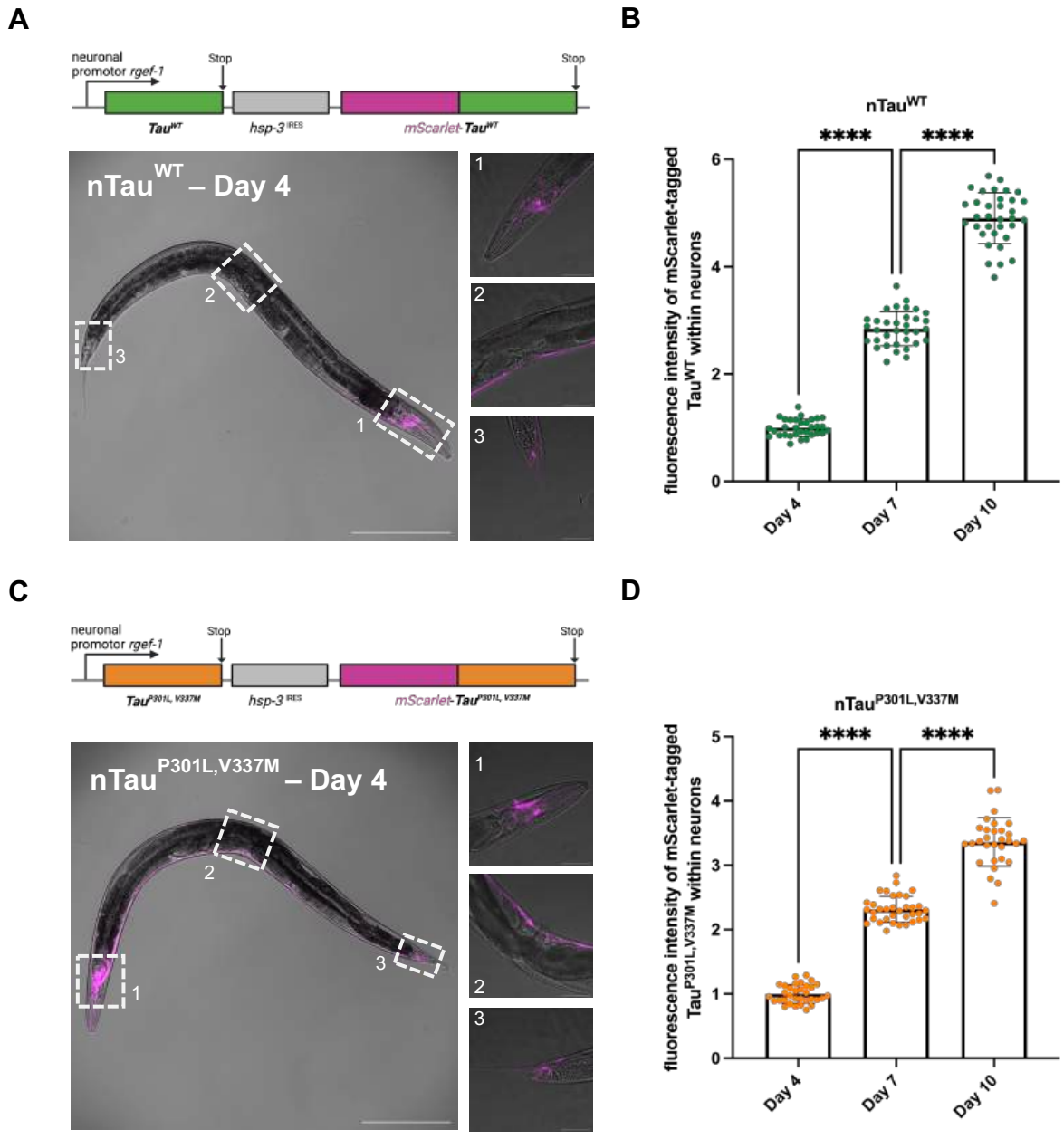

Figure 3.2: *New C. elegans models expressing wild-type Tau (Tau^{WT}) and mutant Tau ($Tau^{P301L,V337M}$).*

A Schematic representation of the neuronal Tau^{WT} ($nTau^{WT}$) expression construct and corresponding confocal fluorescent images of a young adult (day 4-old) animal. Untagged Tau^{WT} and mScarlet-tagged Tau^{WT} are pan-neuronally expressed driven by the *rgef-1* promoter. Cap-dependent translation leads to an overexpression of untagged Tau^{WT} and *hsp-3*^{IRES} cap-independent translation allows for substoichiometric expression of mScarlet-Tau^{WT}. The image on the left is magnified 100-fold

(scale bar is 200 µm). Insets 1-3 show the respective close-ups of the head-, mid-body and tail region. Close-up images on the right are 400-fold magnified (scale bars are 50 µm).

B Quantification of mScarlet-Tau^{WT} fluorescence intensity with the progression of aging of day 4-, 7- and 10-old nematodes of nTau^{WT} strain. Confocal fluorescent images of three cohorts of total 32-35 nematodes were recorded; fluorescence intensities were quantified using Fiji and normalised to day 4. Data are displayed as mean fluorescence intensity ± SD. Significance was tested by one-way ANOVA + Bonferroni post hoc test (**** = $p < 0.0001$).

C Schematic representation of the neuronal Tau^{P301L,V337M} (nTau$^{P301L,V337M)}$ construct and corresponding fluorescent confocal microscopy images of a young adult (day 4-old) animal. The presented operon structure follows the same principle of expression as described in Fig. 2A. Image on the left is 100-fold magnified (scale bar is 200 µm). Insets 1-3 show the respective close-ups of the head-, mid-body and tail region. The close-up images on the right are magnified 400-fold (scale bars are 50 µm).

D Quantification of mScarlet-Tau^{P301L,V337M} fluorescence intensity with the progression of aging of day 4-, 7- and 10-old nematodes of nTau$^{P301L,\ V337M}$ strain. Confocal fluorescent images of three cohorts of total 32-35 nematodes were recorded; fluorescence intensities were quantified using Fiji and normalised to day 4. Data are displayed as mean fluorescence intensity ± SD. Significance was tested by one-way ANOVA + Bonferroni post hoc test (**** = $p < 0.0001$).

This approach produces untagged Tau through highly efficient cap-dependent translation, while mScarlet-tagged Tau is translated less efficiently via a cap-independent internal ribosome entry site (IRES). This results in an excess of untagged Tau and substoichiometric amounts of mScarlet-tagged Tau. To date, most available *C. elegans* Tau models do not use a fluorescently labelled Tau, with one exception that is fused to GFP (Aquino Nunez et al., 2022). Consequently, these models rely on immunostaining to localise Tau. This renders the experimental procedure more technically demanding and does not allow to quantify Tau aggregation *in situ*.

I confirmed the efficient pan-neuronal expression of the mScarlet-tagged Tau^{WT} and mScarlet-tagged Tau^{P301L,V337M} by confocal imaging of the mScarlet fluorescence (Figure 3.2 A and C). Using the pan-neuronal *rgef-1* promoter, I observed expression of the mScarlet-tagged Tau variants in the head and tail neurons as well as along the ventral nerve cord (Figure 3.2 A and C, insets 1-3). Interestingly, the expression of both mScarlet-tagged Tau variants increased with the progression of aging, as analysed by quantifying mScarlet fluorescence intensities from whole-body confocal images on day 4, 7 and 10 of life (Figure 3.2 B and D). The mScarlet-tagged Tau^{WT} fluorescence intensity relative to day 4 increased to 2.9-fold (± 0.32) on day 7 and to 4.9-fold (± 0.45)

on day 10. The fluorescence intensity of mScarlet-tagged Tau^{P301L,V337M} relative to day 4 increased to 2.3-fold (± 0.2) on day 7 and to 3.36-fold (± 0.39) on day 10. This observation differs from the neuronal Aβ_{1-42} strain, which showed a decrease in mScarlet-tagged Aβ_{1-42} expression with aging of 0.8-fold (± 0.1) on day 7 relative to day 4 (Figure 8.1). Of note, the mScarlet-tagged nTau^{P301L,V337M} strain exhibited a 3.1-fold (± 0.45) higher expression than the mScarlet-tagged Tau^{WT} on day 4 (Figure 3.3).

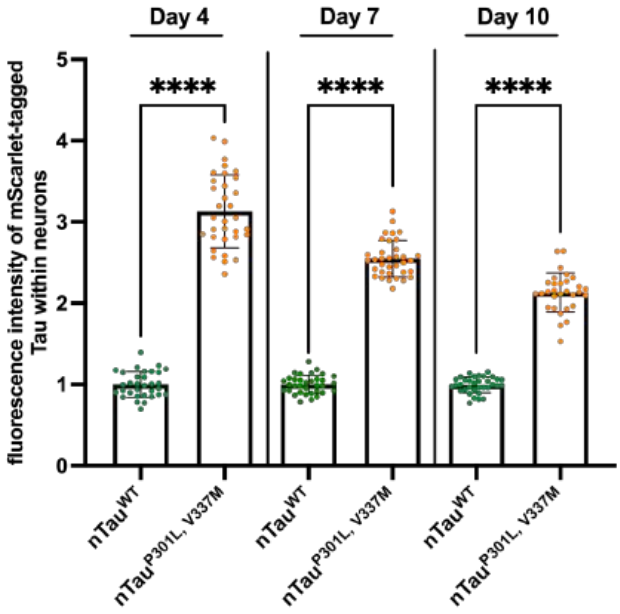

Figure 3.3: *Expression levels of mScarlet-tagged mutant Tau are elevated compared to mScarlet-tagged wild-type Tau.*

Quantification of mScarlet-Tau^{WT} and mScarlet-Tau^{P301L,V337M} fluorescence intensity of young adult (day 4-old), adult (day 7-old) and old adult (day 10-old) nematodes of the nTau^{WT} and nTau^{P301L,V337M} strain. Confocal fluorescent images of three cohorts of a total 32-35 nematodes were recorded; fluorescence intensities were quantified using Fiji and normalised to nTau^{WT}. Data are displayed as mean fluorescence intensity ± SD. Significance between nTau^{P301L,V337M} and nTau^{WT} at day 4, 7, and 10, respectively, was tested by Student's t-test with Welch's correction (**** = $p < 0.0001$).

This pattern remained consistent with aging, showing a 2.5-fold (± 0.23) excess of mScarlet-tagged Tau^{P301L,V337M} relative to mScarlet-tagged Tau^{WT} on day 7 and a 2.1-fold (± 0.24) excess on day 10.

To ensure correct expression of the untagged Tau variants as well, a Western blot (WB) was performed using protein lysates of nTau^{WT} and nTau^{P301L,V337M} animals by my colleague Yvonne Woitzat (Figure 3.4)

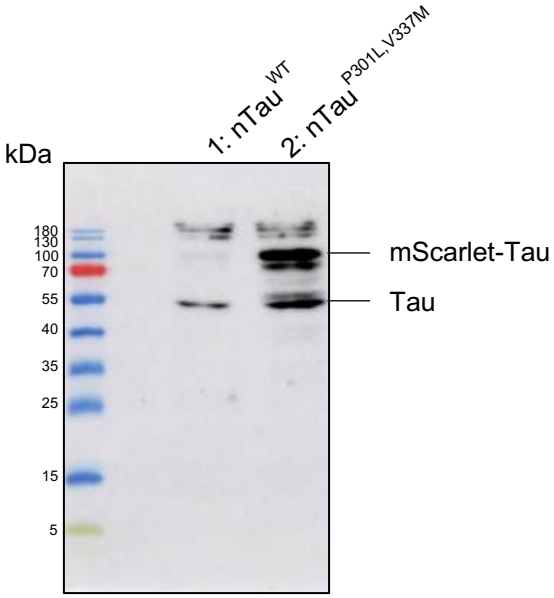

Figure 3.4: *Verification of the expression of untagged mutant and untagged wild-type Tau by Western blot.*

Detection of untagged and mScarlet-tagged Tau protein from lysates of nTau^{WT} and nTau$^{P301L,\ V337M}$ animals. Representative uncropped Western blot of protein lysates of nTau^{WT} (lane 1) and nTau^{P301L,V337M} (lane 2). Detection was performed with Mouse-anti-Tau-5 (MA5-12808, ThermoFisher) and Goat-anti-mouse-HRP. Protein bands of Tau, mScarlet-Tau and molecular weights of the protein ladder (kDa) are labelled.

Immunodetection was performed using an anti-Tau (Tau-5) antibody. In lysates from both strains, a band was detected above the 70 kDa molecular weight marker, corresponding to the mScarlet-tagged Tau variant. A second band appeared at approximately 55 kDa, corresponding to the untagged Tau variant. The intensity of the untagged and mScarlet-tagged Tau bands from the nTau^{P301L,V337M} lysate was higher than in nTau^{WT} and thus confirms the fluorescence data (Figure 3.3). Surprisingly, the signal intensity of the mScarlet-tagged Tau appeared similar to that of the untagged Tau, despite expectations of higher untagged Tau abundance. This could be attributed to differing stabilities between the tagged and untagged Tau variants, as the mScarlet-tag likely enhances the protein's stability, and the untagged Tau was less stable.

3.1.2 Mutant Tau aggregates over ageing and accumulates in coelomocytes

Fluorescence lifetime imaging microscopy (FLIM) was employed to study the aggregation of Tau in nTau^{WT} and nTau^{P301L,V337M} nematodes with the progression of

aging *in vivo*. FLIM has been shown to be a reliable and straightforward technique for quantifying protein aggregation of various amyloidogenic proteins in *C. elegans* (Kaminski Schierle et al., 2011; Laine et al., 2019; Gallrein et al., 2021; Pigazzini et al., 2021; Tittelmeier et al., 2022). It measures the fluorescence lifetime (τ) of the respective fluorescent protein. While being independent of its concentration and fluorescence intensity, fluorescence lifetime changes due to its microenvironment (Becker, 2012). As Tau aggregates and mScarlet-tagged Tau incorporates into growing fibrils, the mScarlet fluorophore gets quenched, leading to a reduction of its fluorescence lifetime. This reduction serves as a proxy for increased aggregation. Thus, FLIM on nTau^{WT} and nTau^{P301L,V337M} nematodes allows a non-invasive quantification and monitoring of Tau aggregation. Fluorescence lifetime of mScarlet-tagged Tau variants was measured in the head neurons of nTau^{WT} and nTau^{P301L,V337M} nematodes on day 4 and day 10 of life. As a control, FLIM measurements were performed in the head neurons of day 4- and day 10-old nmScarlet nematodes, which expressed only the fluorophore mScarlet in their neurons (Figure 3.5). 4-day-old nematodes were considered young adults, while 10-day-old animals were classified as old adults. Young adults usually become fertile around day 4 and exit the reproductive phase around day 8. Thus, old adult animals with the age of 10 days are infertile. The aging process begins on day 4, correlating with a decline in proteostasis capacity (Labbadia & Morimoto, 2014). Consequently, protein aggregates start to form, allowing aggregation to be monitored as aging progresses.

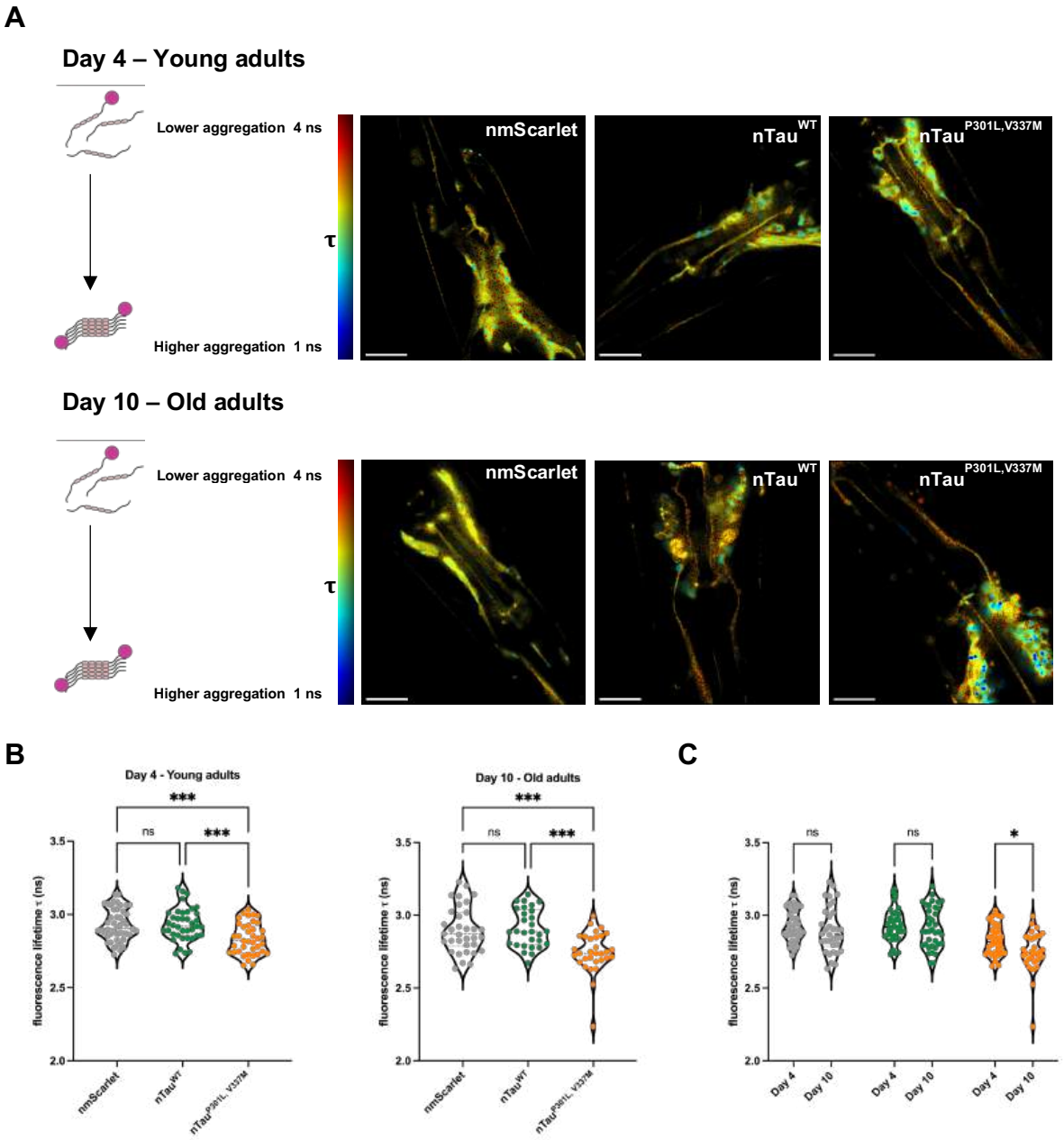

Figure 3.5: *Mutant Tau shows age-dependent aggregation.*

A Representative TCSPC-FLIM images of nmScarlet, nTau^{WT} and nTau^{P301L,V337M}. Head neurons of young adult (day 4-old) animals (upper row) and old adult (day 10-old) animals (lower row) were analysed. Images depict the pixel-wise fluorescent lifetime (**τ**) merged with the fluorescent intensity. Fluorescence lifetime is colour-coded: blue represents low fluorescent lifetimes (1 ns) showing regions with aggregated Tau and red represents high fluorescent lifetimes (4 ns) showing region with soluble Tau species that are schematically depicted on the left. Scale bars are 20 µm.

B Violin dot plot of the average fluorescent lifetime (**τ**) of young adult animals (left) and old adult animals (right) of nmScarlet, nTau^{WT} and nTau^{P301L,V337M}. Data displays average fluorescent lifetimes ± SD of nmScarlet (grey), nTau^{WT} (green) and nTau$^{P301L, V337M}$ (orange). Every dot represents the average fluorescent lifetime for the head neurons of one single nematode. Three independent cohorts of in total

31-47 nematodes were analysed. Significance was tested by one-way ANOVA + Bonferroni post hoc test for young adult animals and by Kruskal-Wallis test with Dunn's post hoc test for old animals (ns = $p > 0.05$; *** = $p \leq 0.001$).

C Violin dot plot of the average fluorescent lifetime ($\boldsymbol{\tau}$) of young adult animals (day 4-old) and old adult animals (day-10 old) of nmScarlet, nTau^{WT} and nTau^{P301L,V337M}. The graph shows the combined data sets depicted in individual graphs of (B). Data displays average fluorescent lifetimes ± SD of nmScarlet (grey), nTau^{WT} (green) and nTau^{P301L,V337M} (orange). Every dot represents the average fluorescent lifetime for the head neurons of one single nematode. Three independent cohorts of in total 31-47 animals were analysed. Significance was tested by two-way ANOVA + Bonferroni post hoc test (ns = $p > 0.05$; * = $p \leq 0.05$).

The fluorescence lifetime values of mScarlet within the neurons of the nematodes can be visualised in FLIM images using false-colouring (Figure 3.5 A). Areas with high lifetime values (τ) are depicted in red-yellow colour, reflecting soluble protein (i.e., nmScarlet, nTau^{WT}). Conversely, cyan-blue areas represent lower τ values, indicating aggregated protein (nTau^{P301L,V337M}). The mean τ value of all head neurons for each nematode was plotted in a violin graph (Figure 3.5 B and C). Purified mScarlet has an intrinsic fluorescence lifetime of 3.9 ns (Bindels et al., 2016). When expressed in the neurons of the nematodes, the τ value of mScarlet decreased to 2.93 ns in day 4-old nmScarlet animals. While nTau^{WT} exhibited τ values similar to nmScarlet on day 4, nTau^{P301L,V337M} showed lower τ values (blue foci) compared to both nmScarlet and nTau^{WT}. The τ value of nTau^{P301L,V337M} was reduced from 2.93 ns to 2.83 ns (*** = $p < 0.001$) compared to nTau^{WT}, indicating aggregation of Tau^{P301L,V337M} on day 4. As the τ value of nTau^{WT} with 2.93 was not altered compared to nmScarlet control nematodes (ns = $p \geq 0.5$), suggests that Tau^{WT} does not aggregate and remains soluble. In old adult animals on day 10 of life, nTau^{P301L,V337M} τ values were again lower compared to those of nmScarlet and nTauWT, exhibiting more blue foci. Indeed, nTau^{P301L,V337M} showed a decrease in the τ value compared to nTau^{WT} and nmScarlet from 2.75 ns to 2.9 ns (*** = $p < 0.001$) and 2.91 ns (*** = $p < 0.001$) respectively. Additionally, aggregation of Tau^{P301L,V337M} was aggravated with aging as evidenced by increased blue foci in the FLIM images and a decrease in the τ value from 2.83 ns to 2.75 ns (* = $p < 0.05$) when comparing day 4- and day 10-old nTau^{P301L,V337M} nematodes . The τ value was not significantly altered neither for nmScarlet nor for nTau^{WT} comparing day 4- to day 10-old animals, indicating that mScarlet and Tau^{WT} do not aggregate upon

aging. Thus, as expected the P301L and V337M mutations favour Tau aggregation propensity in both young and old adult animals, while Tau^{WT} and mScarlet remain soluble as the nematodes age.

Amyloidogenic proteins such as Tau are known to spread to the extracellular space, which is considered a hallmark of neurodegenerative diseases. Spreading accelerates aggregation by forming new aggregation seeds (Michel et al., 2014; Nussbaum-Krammer et al., 2015; Tittelmeier et al., 2020). To analyse spreading of $Tau^{P3011L,V337M}$ from neurons to other tissues in *C. elegans*, I quantified the amount of mScarlet-tagged $Tau^{P3011L,V337M}$ in the coelomocytes. These scavenger cells, located in the body cavity possess lysosomal activity and are capable to take up macromolecules from the extracellular space through endocytosis. To identify and localise coelomocytes, $nTau^{P301L,V337M}$ and $nTau^{WT}$ strains were crossed with a strain expressing GFP in the coelomocytes (ZIM1048, kindly provided by the Zimmer lab). Confocal microscopy was used to image coelomocytes in $nTau^{P301L,V337M}$ and $nTau^{WT}$ animals and fluorescence intensities of mScarlet-tagged $Tau^{P301L,V337M}$ and Tau^{WT} were quantified (Figure 3.6). Spreading was analysed on day 4 and day 7, while FLIM analysis was performed on day 4- and day 10-old animals. As the visualisation of coelomocytes becomes unreliable at day 10 due to high autofluorescence in the GFP channel, I decided to quantify Tau levels in day 7-old animals instead.

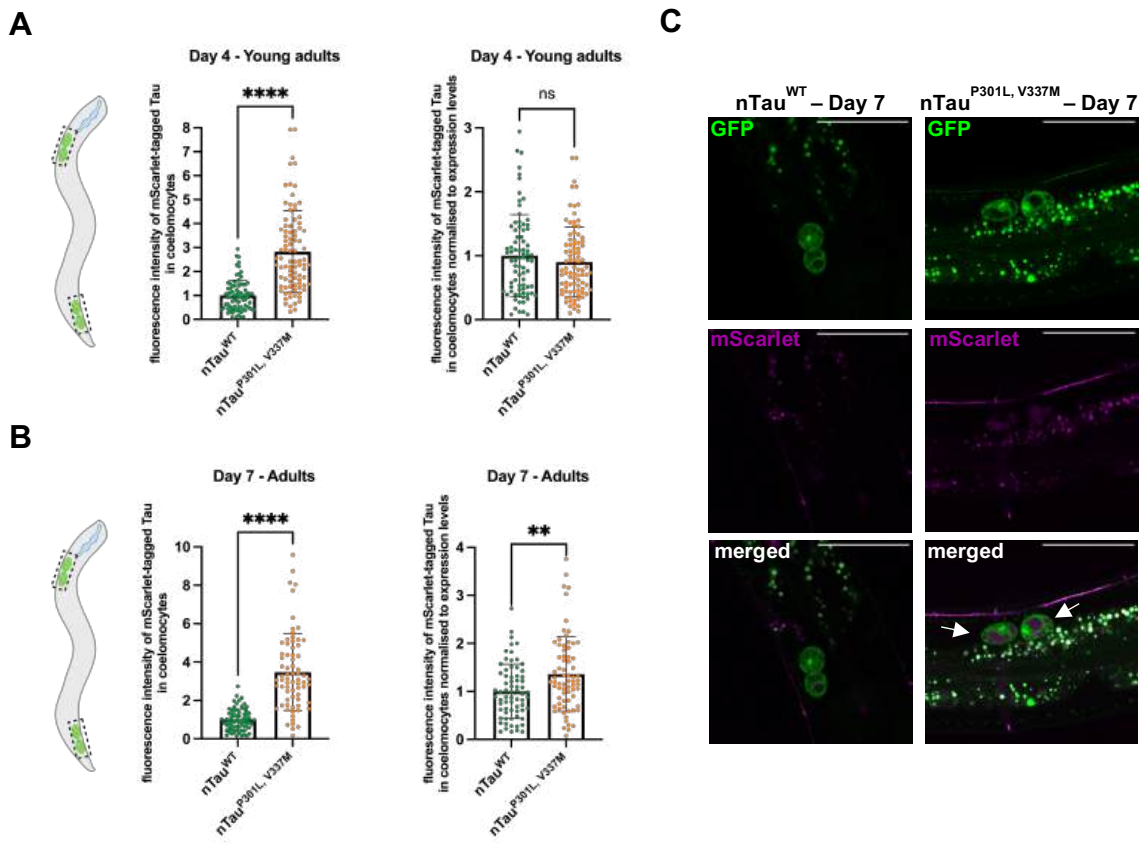

Figure 3.6: *Mutant Tau shows propagation and accumulation in coelomocytes.*

A Scatter dot plot of the average Tau levels in the coelomocytes of nTau^{WT} and nTau^{P301L,V337M} young adult animals (left graph) as well as normalised to the Tau expression levels (right graph). For identification of coelomocytes nTau^{WT} and nTau^{P301L,V337M} animals were crossed with the ZIM1048 strain expressing GFP in coelomocytes. Tau fluorescence levels were quantified in the head and the tail coelomocytes by Fiji analysis of confocal images. Every dot represents the level of Tau in head or the tail coelomocytes for nTau^{WT} (green) and nTau$^{P301L,\ V337M}$ (orange). Fluorescence intensities were normalised to day 4 of the signals of nTau^{WT}. Three cohorts of a total of 32-38 nematodes were analysed. Significance was assessed by Mann-Whitney-U test (ns = $p > 0.05$; **** = $p \leq 0.0001$).

B Scatter dot plot of the average Tau levels in the coelomocytes of nTau^{WT} and nTau^{P301L,V337M} adult animals (left graph) as well as normalised to the Tau expression levels (right graph). Tau fluorescence levels were quantified in the head and tail coelomocytes by Fiji analysis of confocal images. Every dot represents the level of Tau in head or the tail coelomocytes for nTau^{WT} (green) and nTau^{P301L,V337M} (orange). Fluorescence intensities were normalised to day 7 of the signals of nTau^{WT}. Three cohorts of in total 37-38 nematodes were analysed. Significance was assessed by Mann-Whitney-U test (** = $p \leq 0.01$; **** = $p \leq 0.0001$).

C Confocal fluorescent images of nTau^{WT} (left) and nTau^{P301L,V337M} (right) adult animals (day 7-old) crossed with the coelomocyte marker (unc-122p::gfp) strain ZIM1048. Scale bars are 50 µm. Arrows in the merged panel of Tau^{P301L,V337M} point to coelomocytes that show incorporated magenta, fluorescent material representing mScarlet-tagged Tau^{P301L,V337M}.

At both analysed ages, nTau$^{P301L, V337M}$ animals exhibited higher levels of mScarlet-tagged Tau relative to nTau^{WT} in the coelomocytes with a 2.82-fold (± 1.7) increase at day 4 (Figure 3.6 A, left graph and C) and a 3.47-fold (± 2) at day 7 (Figure 3.6 B, left graph and C). Notably, when fluorescence intensity values were normalised to the pan-neuronal expression levels for both days, I observed that levels of Tau^{P301L,V337M} relative to Tau^{WT} were increased only on day 7 (Figure 3.6 A and B, right graph). Hence, the increased spreading of Tau^{P301L,V337M} in older animals correlates with the aggregation level seen in FLIM, which was also increased with the progression of aging (Figure 3.5 C).

3.1.3 Aggregation of mutant Tau exerts systemic defects

Based on the observed aggregation and spreading of Tau^{P301L,V337M}, I wondered whether this might also impair the physiology and health of nTau^{P301L,V337M} animals. Several assays analysing the potential proteotoxicity of Tau expression were conducted on nTau^{P301L,V337M}, nTau^{WT}, and nmScarlet.

First, I performed a developmental assay to analyse the development from egg to fertile adult animal through the L1, L2, L3, and L4 larval stages (Figure 3.7). The developmental stage of the nematodes, starting from eggs, was monitored every day until fertility was reached.

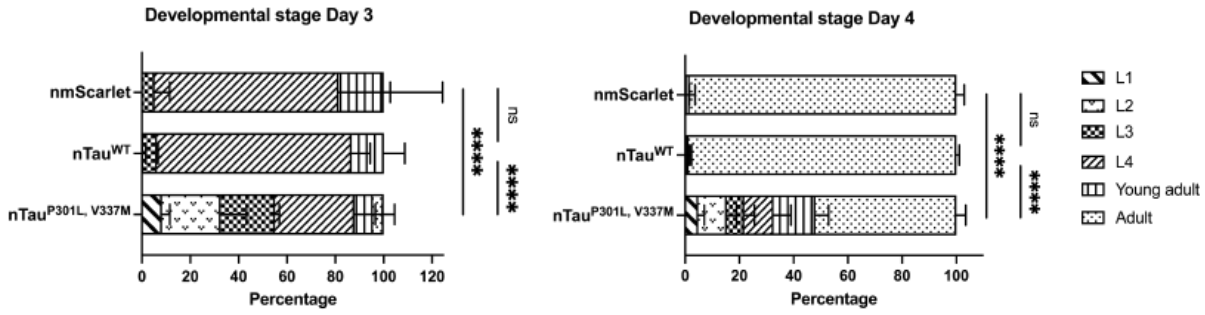

Figure 3.7: *Mutant Tau animals are developmentally delayed.*

Developmental assay of nmScarlet, nTau^{WT}, and nTau^{P301L,V337M} animals. The graph displays percentage of developmental stages of the nematodes within a population on day 3 (left) and day 4 (right) of life. Three independent cohorts of 40-60 nematodes each were analysed. Kruskal-Wallis test was employed to test significance between fractions of L4 animals (left) and adult animals (right) (ns = $p > 0.05$; **** = $p \leq 0.0001$).

Typically, a healthy nematode reaches the L4 larval stage by day 3 of life, so the percentage of L4 animals within a population indicates how well the population develops. On day 3 of life, only 33.1% of nTau^{P301L,V337M} nematodes reached L4 larval stages while 55% of analysed nematodes were still in L1, L2 and L3 larval stages. In contrast, nmScarlet and nTau^{WT} nematodes showed 76.7% and 80.4% L4 animals, with only 4.7% and 6.1% of nematodes in L1, L2 and L3 larval stages, respectively. By day 4, healthy nematodes reach adulthood, characterised by the first visible, fertilised egg inside the gonads. While 98% and 98.8% of nmScarlet and nTau^{WT} nematodes were adult on day 4, only 52.1% of analysed nTau^{P301L,V337M} animals reached adulthood and 48% were still in larval stages. These results demonstrate that aggregation of Tau^{P301L,V337M} severely delays the development in the early days of life, even before the first aggregates form.

A lifespan assay was conducted to assess whether Tau$^{P301L, V337M}$ aggregation would affect the physiology of the nematode systemically (Figure 3.8). Lifespan measures the survival in days and is therefore an important readout in the aging context.

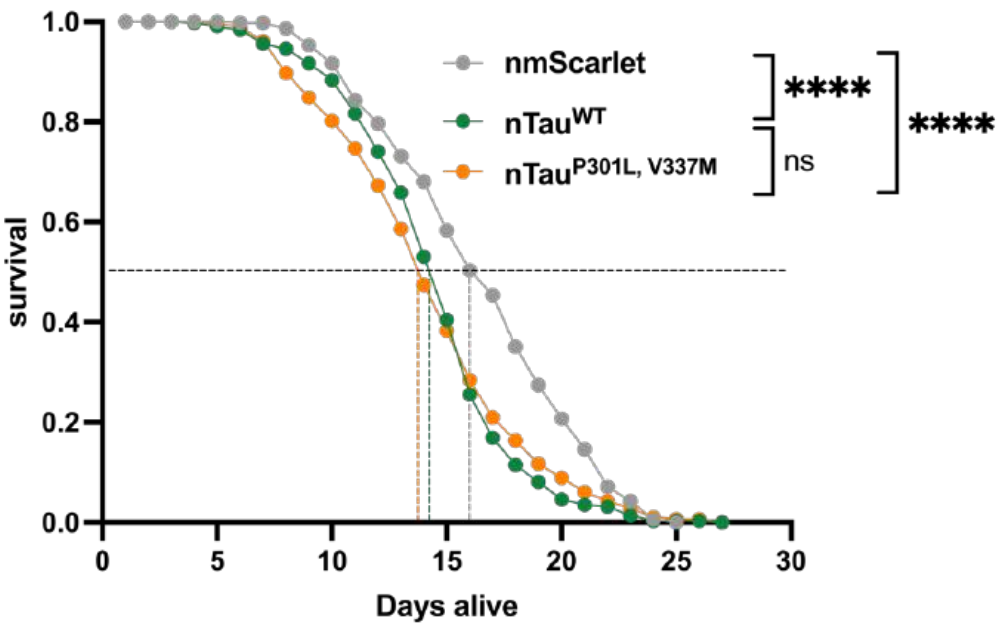

	Median (days)	Maximum (days)
nmScarlet	16.5 ± 1	23.7 ± 0.6
$nTau^{WT}$	14.4 ± 0.8	22 ± 5
$nTau^{P301L,V337M}$	14.2 ± 1.1	22 ± 3.5

Figure 3.8*: Expression of mutant Tau, but also wild-type Tau, reduces lifespan of nematodes.*

Assessment of the lifespan of nmScarlet, $nTau^{WT}$ and $nTau^{P301L,V337M}$ animals. The graph shows the cumulative survival probability (survival) versus age (days alive) of nmScarlet (grey), $nTau^{WT}$ (green) and $nTau^{P301L,V337M}$ (orange). Three independent cohorts of 150-180 nematodes each were analysed, and significance was tested by Log-rank test using the Oasis2 online tool (ns = $p > 0.05$; *** = $p \leq 0.001$, **** = $p \leq 0.0001$). The average median lifespan ± SD and average maximum lifespan ± SD are shown in the table below.

The median lifespan of $nTau^{P301L,V337M}$ was reduced by 2.3 days (from 16.5 ± 1 days to 14.2 ± 1.1 days) and the maximum lifespan by 1.7 days (from 23.7 ± 0.6 days to 22 ± 5 days) compared to nmScarlet. Surprisingly, $nTau^{WT}$ nematodes also exhibited a median lifespan reduction of 2.1 days compared to nmScarlet (from 16.5 ± 1 days to 14.4 ± 0.8 days). The maximum lifespan was impaired as well, decreasing from 23.7 ± 0.6 days to 22 ± 3.5 days compared to nmScarlet. These data demonstrate that not only the aggregation of $Tau^{P301L,V337M}$ affects lifespan but also the expression of Tau^{WT}. To further characterise systemic fitness of Tau-expressing nematodes, I performed a fecundity assay to evaluate the number of viable offspring of $nTau^{P301L,V337M}$, $nTau^{WT}$

and nmScarlet nematodes (Figure 3.9 A). As hypothesised, the nTau^{P301L,V337M} exhibited a brood size reduction of 48% compared to nmScarlet nematodes, from 267 (± 53) to 139 (± 32) viable offspring per nematode (**** = p < 0.0001).

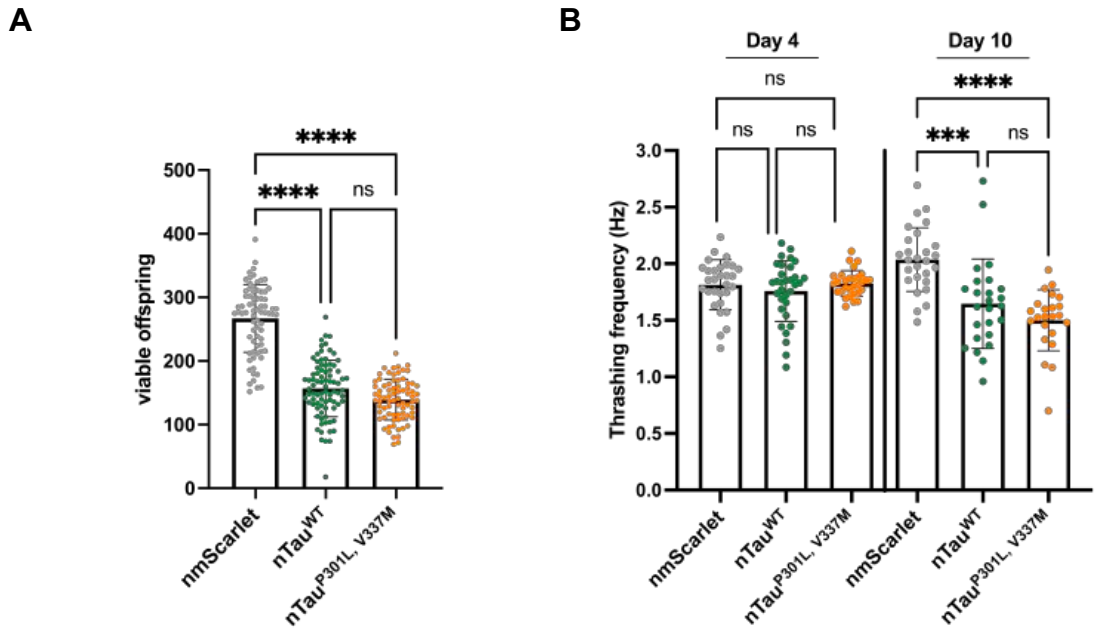

Figure 3.9: *Expression of mutant Tau, but also wild-type Tau, impairs fecundity and muscular function.*

A Fecundity analysis of nmScarlet, nTau^{WT} and nTau^{P301L,V337M} animals. The scatter dot plot displays average number of viable offspring of nmScarlet (grey), nTau^{WT} (green) and nTau^{P301L,V337M} (orange). Every dot represents the absolute number of viable offspring of a single nematode. Significance was assessed by one-way ANOVA + Bonferroni post hoc test (ns = p > 0.05; **** = p ≤ 0.0001). Three independent cohorts a total of 74-83 nematodes were tested.

B Scatter dot plot of the thrashing capability of nmScarlet (grey), nTau^{WT} (green) and nTau^{P301L,V337M} (orange) animals at day 4 (left) and day 10 (right) of life. Every dot represents the thrashing frequency of a single nematode. Three cohorts of 8-15 nematodes per strain were recorded for 20 s, and thrashing frequency was analysed from the recorded videos for each animal individually. Significance for day 4 and 10, respectively was assessed by Kruskal-Wallis test with Dunn's post hoc test (ns = p > 0.05; *** = p ≤ 0.001; **** = p ≤ 0.0001).

However, a 41% decrease in brood size compared to nmScarlet was also observed for nTau^{WT} nematodes, from 267 (± 53) to 157 (± 45) viable offspring per nematode (**** = p < 0.0001). Thus, both nTau^{P301L,V337M} and nTau^{WT} showed similar deficits in fecundity.

Lastly, I tested the nematodes' swimming ability in liquid medium by counting body thrashes, which serves as a measure of muscle activity and vitality (Figure 3.9 B). Day

4- and day 10-old nematodes of nTau^{P301L,V337M}, nTauWT, and nmScarlet were placed in M9 medium and videos were recorded using a stereomicroscope. An automated software was used to analyze the videos and calculate the thrashing frequency of each nematode. A full body thrash consists of two body bends with maximum amplitude to each side to the nematode's body. The thrashing frequency, measured in Hertz (Hz), represents the number of thrashes per second. Day 4-old nematodes of all three strains did not exhibit any deficits in thrashing ability with thrashing frequencies of 1.83 (± 0.1) Hz, 1.76 (± 0.3) Hz and 1.81 (± 0.2) Hz, respectively. However, on day 10, nTau^{P301L,V337M} nematodes exhibited a 26% reduction in thrashing frequency compared to nmScarlet, decreasing from 2.03 (± 0.3) Hz to 1.5 (± 0.3) Hz. Similarly, nTau^{WT} showed a 19% reduction compared to nmScarlet on day 10, which, from 2.03 (± 0.3) Hz to 1.65 (± 0.4) Hz, mirroring the deficit observed for nTau^{P301L,V337M}.

As Tau aggregation and fibril formation lead to neurodegeneration and a decline of neuronal function in Alzheimer's disease patients, I hypothesised that aggregation of Tau^{P301L,V337M} in *C. elegans* could also cause a loss of neuronal function. Therefore, a chemotaxis assay was employed to test the nematodes' ability to sense volatile odorants (Figure 3.10). As developmental delay in nTau^{P301L,V337M} animals was already observed on day 3 and day 4, I wondered whether chemotaxis would be also already impaired in day 4-old nematodes.

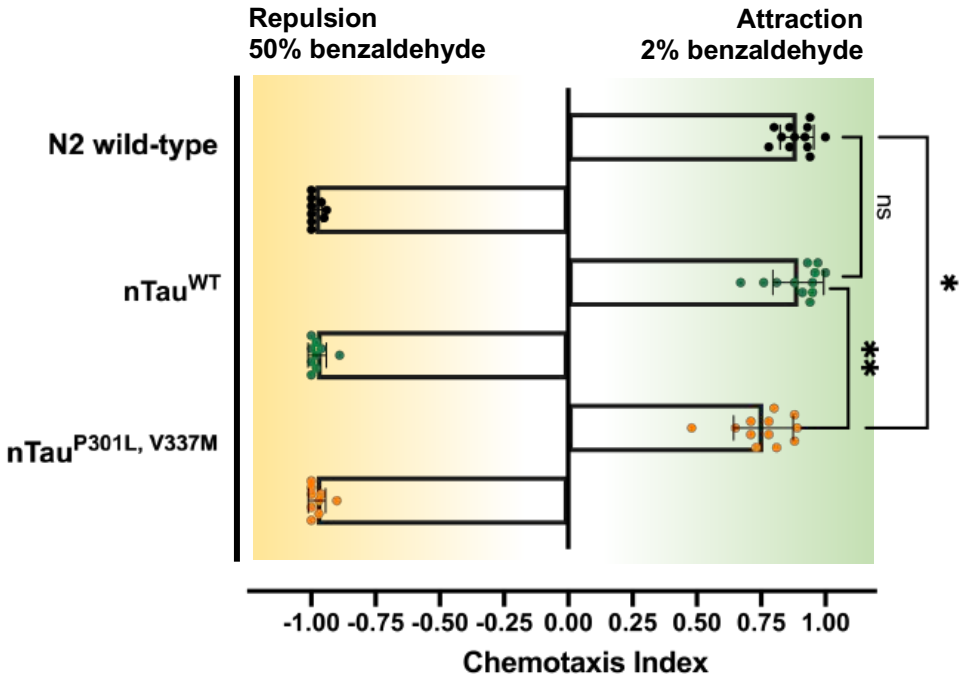

Figure 3.10: *Mutant Tau nematodes exhibit impaired chemotaxis.*

Assessment of chemotaxis towards 50% (repulsion) and 2% (attraction) benzaldehyde of nTau^{WT} and nTau^{P301L,V337M} animals. The scatter plot displays chemotaxis index of nTau^{WT} (green) and nTau^{P301L,V337M} (orange) whereas each dot represents the calculated chemotaxis index for one technical replicate. Three to four independent cohorts of each 200-300 young adult nematodes were tested, divided into three technical replicates. Significance was assessed by Kruskal-Wallis test with Dunn's post hoc test (ns = $p > 0.05$; * = $p \leq 0.05$; ** = $p \leq 0.01$).

AWC neurons, a pair of odor-sensing neurons in the lateral ganglion, sense diluted benzaldehyde (Bargmann et al., 1993). To test attraction and repulsion behaviors, diluted (2%) and concentrated (50%) benzaldehyde were used, respectively. The chemotaxis index indicates how well nematodes sense the odorant, with values close to 1 showing strong attraction and values close to minus 1 showing strong repulsion. As expected, N2 wild-type and nTau^{WT} animals showed high attraction to 2% benzaldehyde, with chemotaxis indices of 0.89 (± 0.02) and 0.9 (± 0.06). In contrast, nTau^{P301L,V337M} nematodes exhibited weaker attraction, with a significantly lower chemotaxis index of 0.76 (± 0.06) compared to N2 wild-type (* = $p < 0.05$) and nTau^{WT} (** = $p < 0.01$). All strains were equally strongly repelled by 50% benzaldehyde. These results suggest that the aggregation of Tau^{P301L,V337M}, as observed by FLIM, leads to impaired chemotaxis already at day 4.

The results of all performed physiological assays clearly demonstrate that the aggregation of $Tau^{P301L,V337M}$ exerts a strong toxic effect on the health of these nematodes. Unexpectedly, however I also observed toxicity due to expression of Tau^{WT}, which did not show aggregation in the FLIM assay (Figure 3.5). Notably, the detrimental effect of Tau^{WT} expression only manifested in assays that are evaluated on longer periods of the nematodes' life such as lifespan (day 1 to 25) and fecundity (day 4 to 8) (Figure 3.8 A and Figure 3.9 A). On the contrary, I did not observe impairments in development on day 3 and 4 and chemotaxis and motility on day 4 (Figure 3.7, Figure 3.9 B and Figure 3.10). This suggests that the toxic effect of Tau^{WT} expression is not dependent on the formation of aggregates, as it is for $Tau^{P301L,V337M}$.

To further explore the toxic effect of Tau^{WT} in the neurons of *C. elegans*, I crossed the $nTau^{WT}$ with a *ptl-1* knockout mutant (*ptl*-1(ok621); strain RB809). *ptl-1* is the endogenous Tau orthologue in *C. elegans* and an important protein mainly expressed in mechanosensory neurons that stabilises and maintains neuronal integrity (Goedert et al., 1996; Gordon et al., 2008). Mutations in the *ptl-1* gene render neurons vulnerable to neurodegeneration and shorten the lifespan of nematodes systemically (Chew et al., 2013). I performed a lifespan assay to replicate these data and observed a reduction in the median lifespan of 3.1 days in *ptl-1*(ok621) nematodes compared to N2 wild-type from 17.6 $\pm$ 1.2 days to 14.5 $\pm$ 0 days (Figure 3.11).

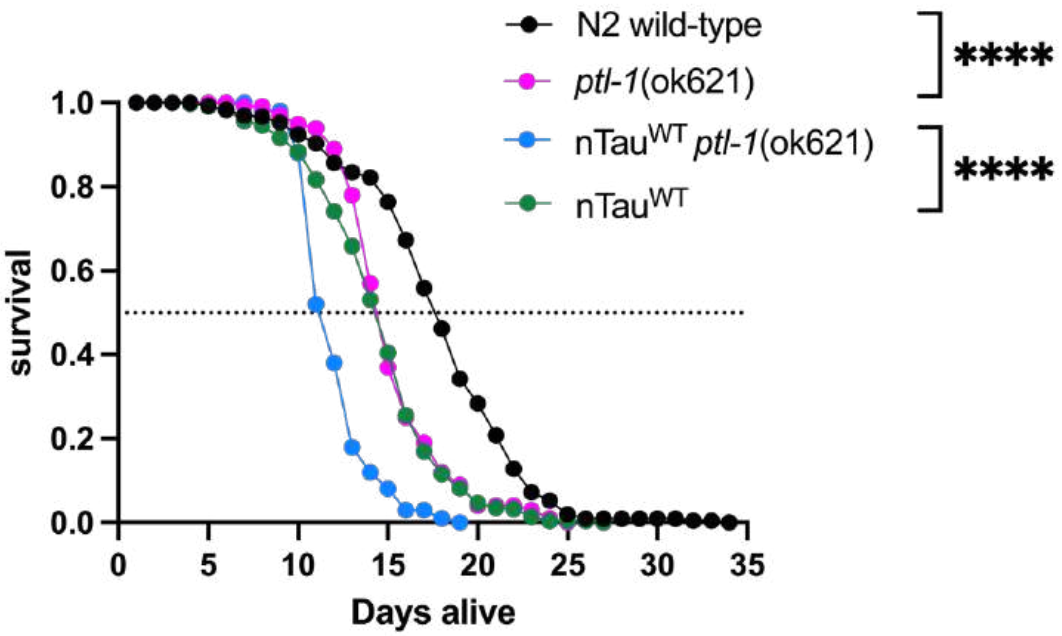

	Median (days)	Maximum (days)
N2 wild-type	17.6 ± 1.2	28.3 ± 5
ptl-1(ok621)	14.5 ± 0	24 ± 0
nTau^{WT} *ptl-1*(ok621)	11.2 ± 0	18 ± 0
nTau^{WT}	14.4 ± 0.8	22 ± 5

Figure 3.11: *Expression of wild-type Tau in ptl-1 deficient nematodes further impairs lifespan.*

Lifespan assay of *ptl-1* knockout mutant and nTau^{WT} cross. Assessment of the lifespan of N2 wild-type, *ptl-1*(ok621), nTau^{WT} *ptl-1*(ok621) and nTau^{WT} animals. Graph shows the cumulative survival probability (survival) versus age (days alive) of N2 wild-type (black), ptl-1(ok621) (magenta), nTau^{WT} *ptl-1*(ok621) (blue) and nTau^{WT} (green). Significance was tested by Log-rank test using the Oasis2 online tool (**** = $p \leq 0.0001$). Average of the mean median lifespan ± SD and average maximum lifespan ± SD are shown in the table below.

The median lifespan of crossed nTau^{WT} *ptl-1*(ok621) animals was further reduced by 3.3 days compared to nTau^{WT} from 14.4 ± 0.8 days to 11.2 ± 0 days. While previous studies showed that ectopic expression of *ptl-1* in *ptl-1*(ok621) animals rescues lifespan reduction (Chew et al., 2013), my approach failed to achieve this, and Tau^{WT} could not compensate for the loss of *ptl-1.* In fact, the loss of *ptl-1* in nTau^{WT} animals exacerbated the toxic effect of Tau^{WT} expression, which was independent of aggregation (Figure 3.5)

3.2 Analysis of neuronal activity in *C. elegans* models of AD

Neurodegenerative diseases such as AD are characterised by progressive degradation of neuronal structures and loss of neuronal function. The accumulation of Aβ plaques and Tau neurofibrillary tangles are neuropathological hallmarks and key drivers of the disease. Despite numerous studies on AD pathology in multiple model organisms, it is still unclear how Aβ and Tau aggregation lead to neuronal destruction and subsequent impairments in neuronal activity. Using the newly established *C. elegans* Tau models and well-characterised *C. elegans* Aβ models, I investigated how neuronal activity and function change with the progression of Tau and Aβ aggregation and proteotoxicity.

3.2.1 Assessment of neuronal activity by quantification of fluorescence intensity levels of a *C. elegans* model expressing the calcium indicator GCaMP6m

To analyse neuronal activity in *C. elegans*, a genetically encoded Ca^{2+} indicator was employed, the calcium-sensitive GCaMP fluorophore. GCaMP proteins typically consist of an engineered GFP fluorophore fused to the high-affinity calcium-binding protein Calmodulin and a M13 helix, making it sensitive to surrounding calcium concentrations. Upon Ca^{2+} binding, GCaMP undergoes a conformational change that causes an increase in fluorescence intensity of the GFP protein. In neurons, action potentials at the presynapse trigger Ca^{2+} influx through voltage-gated Ca^{2+} channels in the membrane. This Ca^{2+} influx can be detected by GCaMP and thus, changes in the fluorescence intensity of GCaMP serve as readout for neuronal activity.

The first GCaMP fluorophore (GCaMP1) was developed in 2001, followed by the generation of GCaMP-expressing mouse models (Nakai et al., 2001; Ji et al., 2004; Tallini et al., 2006). In subsequent years, GCaMP fluorophores have been progressively improved to enhance sensitivity, response time and signal strength. These developments culminated in the generation of a new class of high-sensitivity indicators called GCaMP6 proteins (Chen et al., 2013).

For my studies, I used a *C. elegans* strain that expresses the GCaMP6m pan-neuronally under the control of the well-established *rgef-1* promoter (nGCaMP6m) (Figure 3.12). This strain was recently developed in the Kirstein lab (unpublished data).

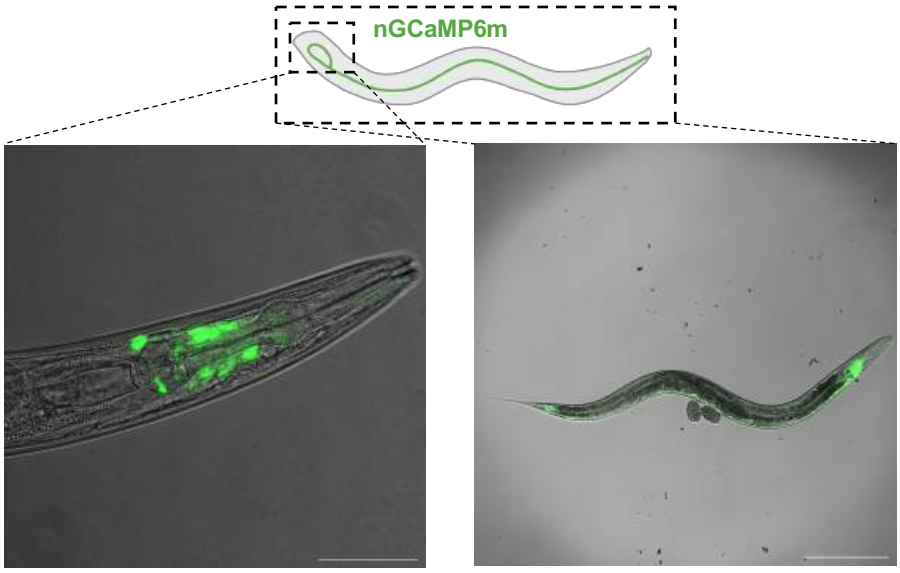

Figure 3.12: *C. elegans model with pan-neuronal overexpression of the calcium indicator GCaMP6m.*

Representative confocal fluorescent images of a young adult animal (day 4-old) of the pan-neuronal GCaMP6m strain (nGCaMP6m). The image on the right is magnified 100-fold (scale bar is 200 µm). The inset shows respective close-up of the head region. Close-up image is magnified 400-fold (scale bar is 50 µm).

Using confocal fluorescence microscopy, I confirmed the pan-neuronal expression of GCaMP6m, visible as green fluorescence, and observed a strong expression, particularly in the head neurons, of the nGCaMP6m nematodes (Fig. 3.12). *In vivo* calcium imaging of *C. elegans* is technically challenging, as the nematodes need to be safely immobilised. Pharmacological substances such as levamisole or sodium azide reliably paralyze animals; however, they also affect neuronal activity. To overcome this obstacle, I used a microfluidic device designed and fabricated in the Kaminski lab (CEB, University of Cambridge UK). This microfluidic device physically restrains the nematodes and restricts body movements while preserving animal physiology during fluorescence intensity measurements (Figure 3.13). Each microfluidic device consists of up to 12 microchannels, and nematodes are allowed to enter the channels through a fabricated inlet via gravity flow. A constriction smaller in diameter than the actual channels, prevents nematodes from escaping at the other end (Figure 3.13 A). Within the channels, nematodes are trapped along their body sides but can still move their heads and tails.

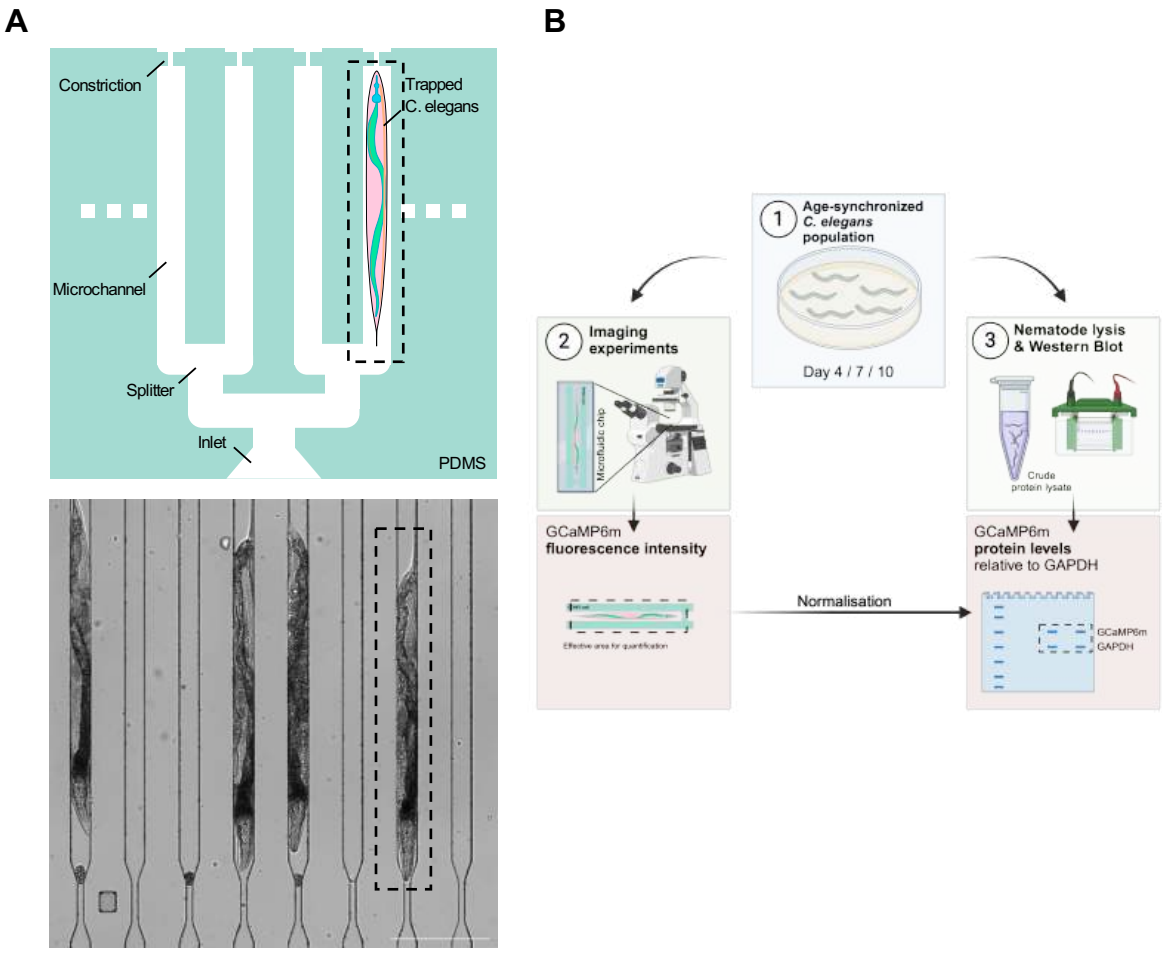

Figure 3.13: *Quantification of GCaMP6m fluorescence intensity levels of living animals in a microfluidic device.*

A Schematic representation of the design of the Polydimethylsiloxane (PDMS) microfluidic device used for the imaging of living *C. elegans* (top image, figure created and kindly provided by Dr. Nino Läubli). Animals enter the device at the inlet by gravity and are drawn into the channels by applying gentle negative pressure. The constriction prevents animals from escaping at the opposing side. Inside the channels, the animals are mechanically trapped along their bodies and *C. elegans* are straightened. The device allows for the simultaneous imaging of multiple animals. The image depicted at the bottom is 100-fold magnified with scale bar of 200 µm.

B Workflow for the quantification of GCaMP6m fluorescence intensity in living *C. elegans* as a readout for the assessment of neuronal activity. Generation of age-synchronised cohorts of young adults (day 4-old) and older animals (day 7- and day 10-old) (1). Imaging experiments are performed using PDMS microfluidic devices to record GCaMP6m fluorescence intensities from alive animals. In the subsequent analysis step, GCaMP6m fluorescence intensities are quantified from single snapshot images. Age-synchronised nematodes are lysed to obtain the crude protein fraction (2). Lysates are analysed by Western blotting. GCaMP6m protein levels are quantified relative to GAPDH and are used to normalize GCaMP6m fluorescence intensities. Figure created with BioRender.

In collaboration with the Kaminski lab, I designed an easy workflow to allow non-invasive quantification of GCaMP6m intensities in GCaMP6m-expressing nematodes as a readout for neuronal activity (Figure 3.13 B). Fluorescence measurements were conducted on young adult (day 4), adult (day 7) and old adult (day 10) animals to reflect the progression of aging. Aged nematode populations were generated through synchronisation (1) and then either subjected to imaging experiments (2) or processed for nematode lysis and Western blot (3). To record GCaMP6m fluorescence intensities, nematodes were placed into the microfluidic devices and then imaged using a widefield fluorescence microscope. From the recorded images, the fluorescence intensity of the GCaMP sensor was quantified. In parallel, nematodes were lysed, and GCaMP protein levels were determined using an anti-GFP antibody. Finally, GCaMP6m protein levels were normalised to GAPDH and were used to normalise the fluorescence intensity of GCaMP6m. This normalisation step accounts for variations in GCaMP6m expression levels at different ages and between different strains.

3.2.2 Proof-of-concept – impairment of neuronal activity in *unc-13* mutant nematodes and upon treatment with Nemadipine A

To establish and test the functionality of the GCaMP6m reporter in the neurons of *C. elegans*, I analysed the GCaMP6m fluorescence intensity in *unc-13* mutant animals (*unc-13*(n3813); strain MT8004) (Figure 3.14). UNC-13 is a synaptic protein that is part of the presynaptic machinery responsible for synaptic vesicles exocytosis and transmitter release (Calahorro and Izquierdo, 2018). In *C. elegans,* mutations in the *unc-13* gene impair synaptic vesicle fusion (Richmond et al., 1999). Therefore, I hypothesised that *unc-13* mutations should should result in a reduced Ca^{2+} influx, resulting in decreased GCaMP6m fluorescence intensity.

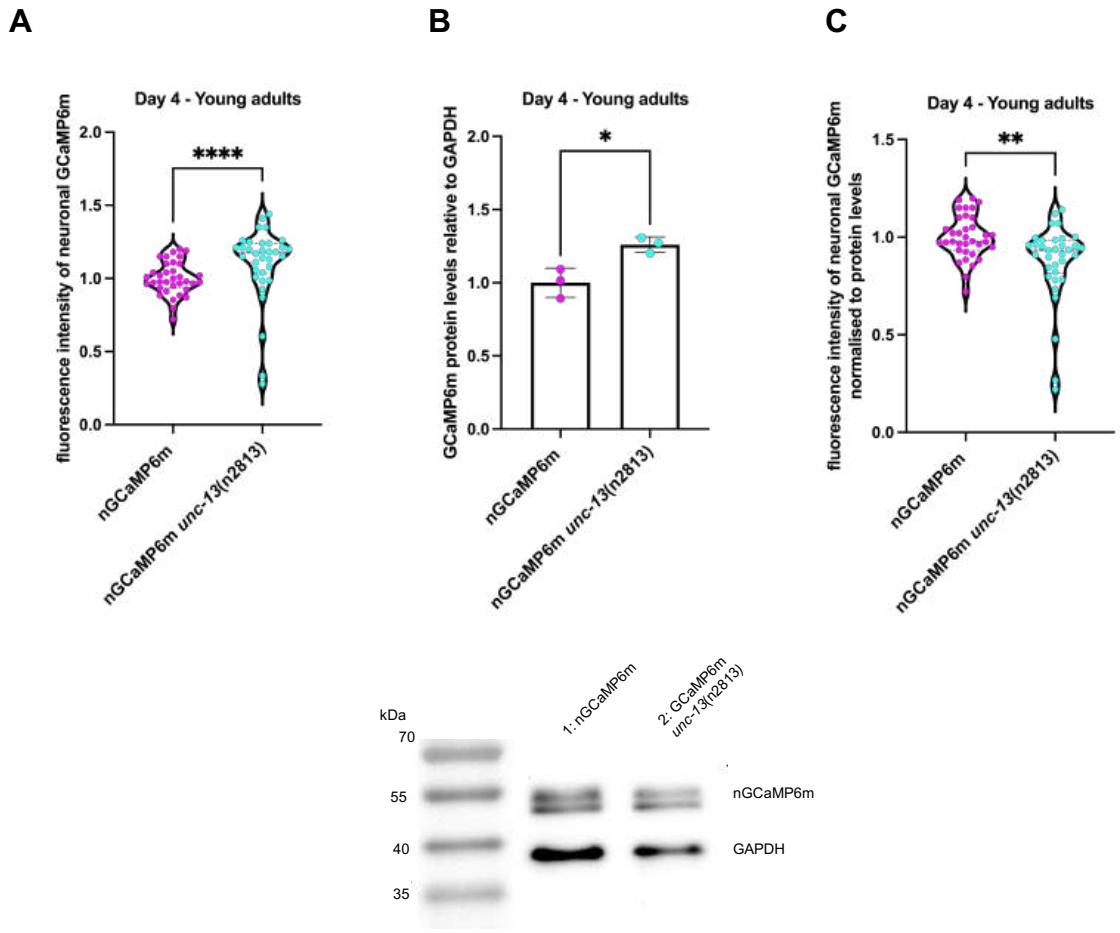

Figure 3.14: *unc-13 mutant nematodes exhibit decreased neuronal function.*

A Violin dot plot of the average GCaMP6m fluorescence of young adult animals (day 4-old) of the neuronal GCaMP6m strain (nGCaMP6m) and the nGCaMP6m *unc-13*(n2813) mutant strain. The mutant unc-13(n2813) (strain MT8004) was crossed with the nGCaMP6 strain and GCaMP6m intensities were measured in animals using microfluidic devices with a widefield fluorescence microscope as outlined in Figure 3.13. GCaMP6m intensities were quantified using Fiji. Every dot represents the neuronal GCaMP6m fluorescence intensity of a single animal of nGCaMP6m (magenta) and nGCaMP6m *unc-13*(n2813) (turquoise). n = 3 and N = 35 animals. Mann-Whitney-U test was performed to assess significance (****= $p \leq 0.0001$).

B Quantification of GCaMP6m protein levels by Western blot from crude protein lysates of young adult (day 4-old) nGCaMP6m (magenta) and nGCaMP6m *unc-13*(n2813) (turquoise) animals. The scatter dot plot shows quantification of GCaMP6m protein levels relative to GAPDH from 3 independent cohorts. Unpaired Student's t-test with Welch's correction was performed to assess significance (* = $p \leq 0.05$). Image below is a representative Western blot using mouse anti-GFP(B34) antibodies to detect GCaMP6m.

C Violin dot plot of the average GCaMP6m fluorescence intensity normalised to the GCaMP6m protein level of young adult animals (day 4-old) of the neuronal GCaMP6m strain (nGCaMP6m) and the

nGCaMP6m *unc-13*(n2813) mutant strain. GCaMP6m intensities as depicted in figure 3.14 A were multiplied with the ratio between nGCaMP6m protein levels of the nGCaMP6m strain and nGCaMP6m *unc-13*(n2813) mutant strain. Every dot represents the neuronal GCaMP6m fluorescence intensity normalised to GCaMP6m protein levels of a single animal of nGCaMP6m (magenta) and *nGCaMP unc-13*(n2813) (turquoise). n = 3 and N = 35 animals. Mann-Whitney-U test was performed to assess significance (**= $p \leq 0.001$).

First, I quantified the neuronal GCaMP6m fluorescence intensity in nGCaMP6m and nGCaMP6m *unc-13*(n2813) animals on day 4 (Figure 3.14 A). The fluorescence intensity in nGCaMP6m *unc-13*(n2813) was 1.1-fold (± 0.3) higher compared to nGCaMP6m animals. Next, GCaMP6m protein levels relative to GAPDH were quantified, which were 1.26-fold (± 0.05) higher in nGCaMP6m *unc-13*(n2813) than in nGCaMP6m animals (Figure 3.14 B). The GCaMP6m fluorescence intensity was then normalised to the GCaMP6m protein levels. As expected, nGCaMP6m *unc-13*(n2813) exhibited a 0.13-fold (± 0.2) decrease in normalised GCaMP6m fluorescence intensity compared to nGCaMP6m animals (Figure 3.14 C).

As an additional control, I treated nGCaMP6m animals with Nemadipine A, a calcium channel inhibitor that acts as an antagonist for the EGL-19 L-type calcium channel in *C. elegans* (Kwok et al., 2006) (Figure 3.15). Previous studies have shown that Nemadipine A treatment reduces GCaMP intensity and calcium signalling (Larsch et al., 2013; Zullo et al., 2019).

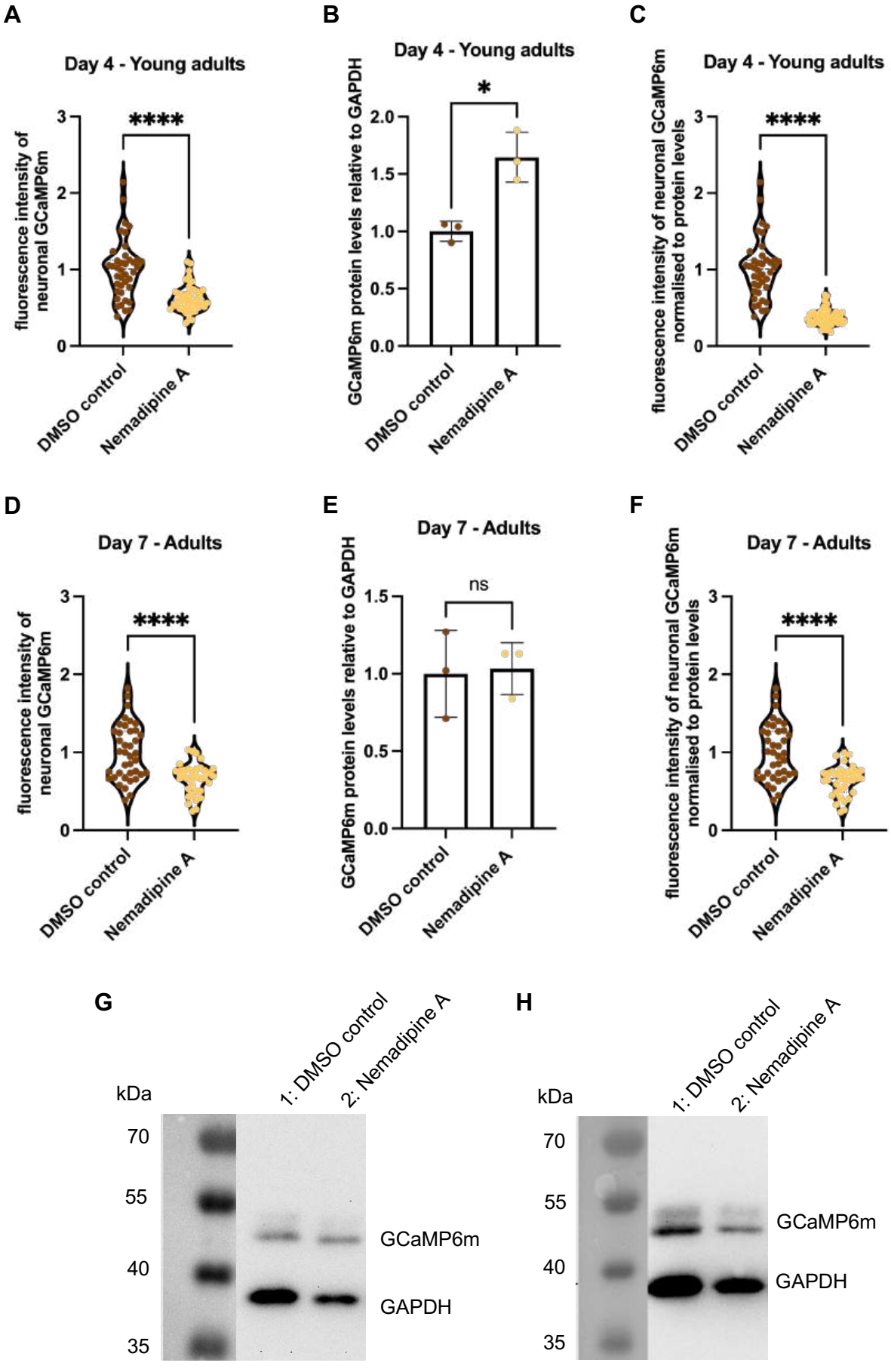
A
Day 4 - Young adults
fluorescence intensity of neuronal GCaMP6m
****
DMSO control
Nemadipine A
B
Day 4 - Young adults
GCaMP6m protein levels relative to GAPDH
*
DMSO control
Nemadipine A
C
Day 4 - Young adults
fluorescence intensity of neuronal GCaMP6m normalised to protein levels
****
DMSO control
Nemadipine A
D
Day 7 - Adults
fluorescence intensity of neuronal GCaMP6m
****
DMSO control
Nemadipine A
E
Day 7 - Adults
GCaMP6m protein levels relative to GAPDH
ns
DMSO control
Nemadipine A
F
Day 7 - Adults
fluorescence intensity of neuronal GCaMP6m normalised to protein levels
****
DMSO control
Nemadipine A
G
kDa
1: DMSO control
2: Nemadipine A
70
55
40
35
GCaMP6m
GAPDH
H
kDa
1: DMSO control
2: Nemadipine A
70
55
40
35
GCaMP6m
GAPDH

Figure 3.15: *The L-type calcium channel inhibitor Nemadipine A inhibits neuronal function.*

A Scatter dot plot of the average GCaMP6m fluorescence intensity of young adult animals (day 4-old) treated with Nemadipine A or with DMSO solvent control. GCaMP6m intensities were measured in alive animals immobilised with polystyrene beads with a confocal fluorescence microscope and intensities were quantified using Fiji. Every dot represents the neuronal GCaMP6m fluorescence intensity of a single animal treated with DMSO control (brown) and Nemadipine A (yellow). n = 3 and N = 40-46 animals. Significance was assessed by Mann-Whitney-U test (**** = $p \leq 0.0001$).

B Quantification of GCaMP6m protein levels by Western blot from total protein lysates of young adult animals (day 4-old) treated with DMSO solvent control or Nemadipine A. The scatter dot plot shows quantification of GCaMP6m protein levels relative to GAPDH from three independent cohorts. Significance was assessed by unpaired Student's t-test with Welch's correction (* = $p < 0.05$). Representative Western blot is shown in G using mouse anti-GFP(B34) antibodies to detect GCaMP6m.

C Scatter dot plot of the average GCaMP6m fluorescence intensity normalised to the GCaMP6m protein level of young adult animals (day 4-old) treated with Nemadipine A or with DMSO solvent control. GCaMP6m intensities were measured in alive animals immobilised with polystyrene beads with a confocal fluorescence microscope and intensities were quantified using Fiji. GCaMP6m intensities as depicted in figure 3.15 A were multiplied with the ratio between nGCaMP6m protein levels of the DMSO treated animals and Nemadipine A-treated animals. Every dot represents the neuronal GCaMP6m fluorescence intensity normalised to GCaMP6m protein levels of a single animal treated with DMSO control (brown) and Nemadipine A (yellow). n = 3 and N = 40-46 animals. Significance was assessed by Mann-Whitney-U test (**** = $p \leq 0.0001$).

D Scatter dot plot of the average GCaMP6m fluorescence intensity of adult animals (day 7-old) treated with Nemadipine A or with DMSO solvent control. GCaMP6m intensities were measured in alive animals immobilised with polystyrene beads with a confocal fluorescence microscope and intensities were quantified using Fiji. Every dot represents the neuronal GCaMP6m fluorescence intensity of a single animal treated with DMSO control (brown) and Nemadipine A (yellow). n = 3 and N = 35-39 animals. Significance was assessed by unpaired Student's t-test with Welch's correction (**** = $p \leq 0.0001$).

E Quantification of GCaMP6m protein levels by Western blot from total protein lysates of adult animals (day 7-old) treated with DMSO solvent control or Nemadipine A. The scatter dot plot shows quantification of GCaMP6m protein levels relative to GAPDH from three independent cohorts. Significance was assessed by unpaired Student's t-test with Welch's correction (ns = $p > 0.05$). Representative Western blot is shown in H using mouse anti-GFP(B34) antibodies to detect GCaMP6m.

F Scatter dot plot of the average GCaMP6m fluorescence intensity normalised to the GCaMP6m protein level of adult animals (day 7-old) treated with Nemadipine A or with DMSO solvent control. GCaMP6m intensities were measured in alive animals immobilised with polystyrene beads with a confocal fluorescence microscope and intensities were quantified using Fiji. GCaMP6m intensities as

depicted in figure 3.15 D were multiplied with the ratio between nGCaMP6m protein levels of the DMSO treated animals and Nemadipine A treated animals. Every dot represents the neuronal GCaMP6m fluorescence intensity normalised to GCaMP6m protein levels of a single animal treated with DMSO control (brown) and Nemadipine A (yellow). n = 3 and N = 35-39 animals. Significance was assessed by unpaired Student's t-test with Welch's correction (**** = $p \leq 0.0001$).

G Representative Western blot for quantification of GCaMP6m protein levels of young adults (day 4-old) treated with DMSO solvent control or Nemadipine A.

F Representative Western blot for quantification of GCaMP6m protein levels of adults (day 7-old) treated with DMSO solvent control or Nemadipine A.

Nemadipine A was dissolved in DMSO and added to NGM agar plates. Control nematodes were grown in the presence of DMSO only, which served as a solvent control. nGCaMP6m fluorescence intensity of Nemadipine A-treated animals was 0.37-fold (± 0.2) decreased compared to nematodes treated with DMSO on day 4 (Figure 3.15 A). GCaMP6m protein levels relative to GAPDH between Nemadipine A and DMSO-treated animals were 1.65-fold (± 0.2) increased in the Nemadipine A-treated nematodes (Figure 3.15 B). Consequently, once nGCaMP6m fluorescence intensity was normalised to the GCaMP6m protein levels, Nemadipine A treatment caused a 0.62-fold (± 0.1) reduction of nGCaMP6m fluorescence intensities compared to the DMSO treatment (Figure 3.15 C). The same analysis was performed with Nemadipine A or DMSO treated animals at 7 days of age. Nematodes were exposed to Nemadipine A or DMSO-containing NGM agar plates while being transferred to fresh plates daily. The nGCaMP6m fluorescence intensity in Nemadipine A-treated nematodes was 0.34-fold (± 0.2) reduced compared to the DMSO-treated animals (Figure 3.15 D). As the nGCaMP6m protein level relative to GAPDH was not significantly altered between both treatments, the normalised nGCaMP6m fluorescence intensity of Nemadipine A-treated was 0.36-fold (± 0.2) lower than DMSO-treated nematodes (Figure 3.15 E and F).

In summary, both methods - genetic modulation of an important synaptic protein and treatment with the calcium channel inhibitor Nemadipine A - reduced the nGCaMP6m fluorescence intensity in nematodes of different ages. Thus, I conclude that the established experimental setup can reliably report on neuronal activity using nGCaMP6m fluorescence intensity as a readout.

3.2.3 Decline of neuronal activity precedes the accumulation of $A\beta_{1-42}$ aggregates

The assessment of neuronal activity in Aβ-expressing nematodes was performed by crossing the nGCaMP6m strain with neuronal $A\beta_{1-42}$ ($nA\beta_{1-42}$) or control nematodes expressing only the fluorescent protein mScarlet in the neurons (nmScarlet) (Figure 3.16). $nA\beta_{1-42}$ animals exhibited an age-dependent progression of aggregation along with severe proteotoxic effects at the physiological level (Gallrein et al., 2021). In young adult animals at day 4 of life, $A\beta_{1-42}$ aggregates were detectable only in the IL2 neurons. However, in older adults at day 7 of life, nematodes showed enhanced and severe $A\beta_{1-42}$ aggregation affecting the entire nervous system. Consequently, I aimed to correlate aggregation propensity with neuronal activity.

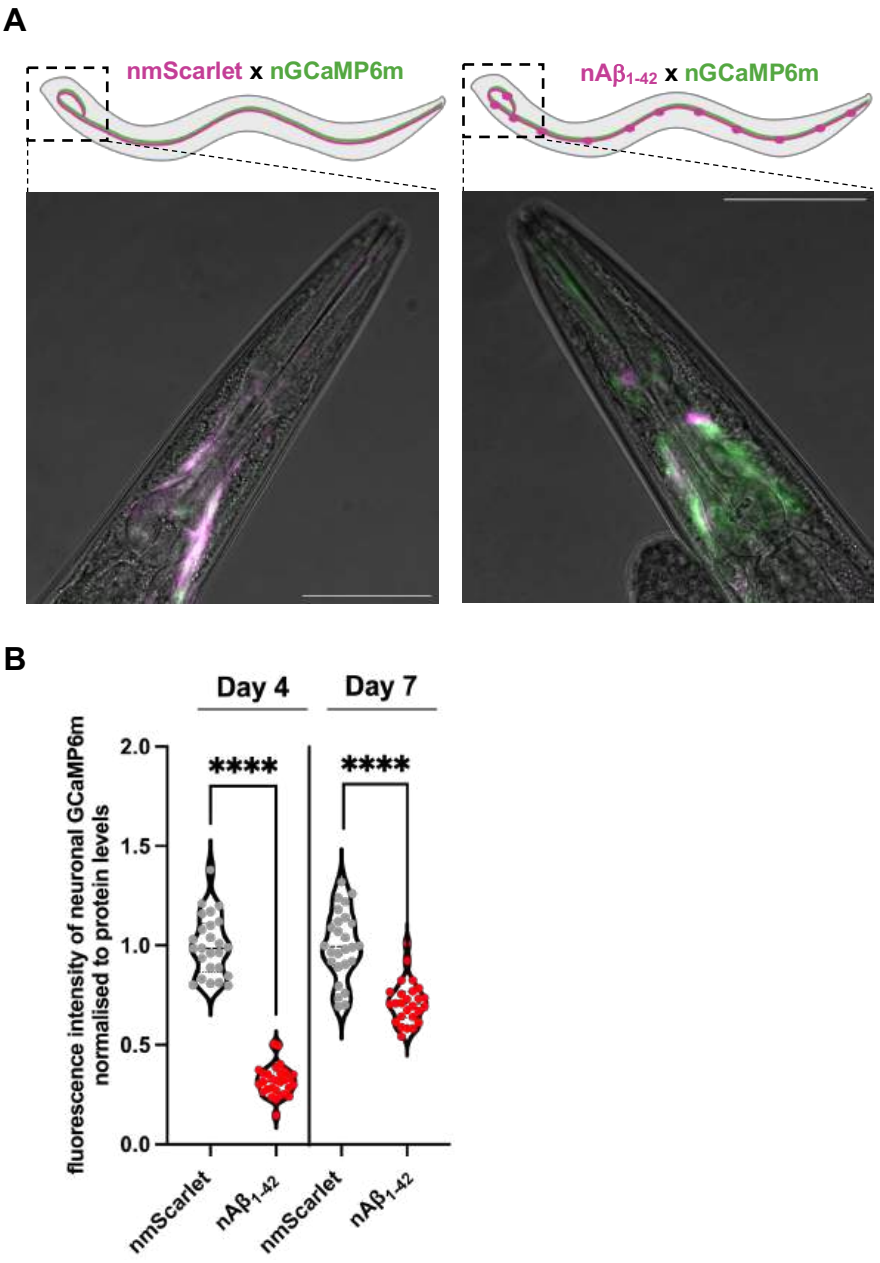

Figure 3.16: *Decrease in neuronal activity precedes the accumulation of neuronal Aβ_{1-42} aggregates.*

A Representative confocal fluorescent images of a young adult animal (day 4-old) of the nmScarlet × nGCaMP6m cross on the left and of the cross nAβ_{1-42} × nGCaMP6m on the right. Shown are close-up images of the head region. Images are magnified 400-fold and scale bars are 50 µm.

B Violin dot plot of the average GCaMP6m fluorescence intensity normalised to the GCaMP6m protein level of young adult animals (day 4-old) and adult animals (day 7-old) of the control strain expressing neuronal mScarlet (nmScarlet) and nAβ_{1-42}. GCaMP6m intensities as depicted in Figure 8.2 A were multiplied with the ratio between nGCaMP6m protein levels of the nmScarlet × nGCaMP6m cross and nAβ_{1-42} × nGCaMP6m cross for day 4 and 7 respectively. GCaMP6m protein quantification and a corresponding Western blot are shown in Figure 8.3 A. Every dot represents the neuronal

GCaMP6m fluorescence intensity normalised to GCaMP6m protein levels of a single animal of nmScarlet (grey) and nAβ_{1-42} (red). n = 3 and N = 25-29 animals. Significance was assessed between nmScarlet day 4 and nAβ_{1-42} day 4 and nmScarlet day 7 and nA$_{1-42}$ day 7, respectively, by unpaired Student's t-test with Welch's correction (**** = $p \leq 0.0001$).

The successfully generated crosses between the nGCaMP6m and either the nAβ_{1-42} or nmScarlet strain (nmScarlet × nGCaMP6m and nAβ_{1-42} × nGCaMP6m) were confirmed by confocal microscopy. This was done through the detection of dual fluorescence - mScarlet (magenta) and GCaMP6m (green) - in the head neurons of the nematodes (Figure 3.16 A). I then measured neuronal activity following the workflow depicted above at two time points: day 4 of life (young adults) and day 7 (adults) (Figure 3.16 B; Figure 8.2 A and Figure 8.3 A). Notably, by day 4, nAβ_{1-42} nematodes showed a 0.68-fold (± 0.08) reduction in nGCaMP6m fluorescence intensity normalised to protein levels compared to nmScarlet control animals. As expected, on day 7, the nGCaMP6m fluorescence intensity normalised to protein levels of nAβ_{1-42} was reduced 0.29-fold (± 0.11) compared to nmScarlet. Counterintuitively, in the nAβ_{1-42} nematodes, the nGCaMP6m fluorescence intensity was lower on day 4 compared to day 7. This surprising result is likely due to a survivorship bias: nematodes mostly affected by Aβ_{1-42} aggregation die prematurely. With the median lifespan of nAβ_{1-42} being only about 9 days, prematurely dead animals are absent from the analysis on day 7, which therefore reports only on the fittest animals surviving until day 7.

I next asked whether GCaMP6m fluorescence intensity in neurons could also be affected when the Aβ_{1-42} peptide is expressed in a distal tissue. To investigate this, I used a strain that expresses the Aβ_{1-42} peptide in the body wall muscles (mAβ_{1-42}) (Gallrein et al., 2021). Similar to the nAβ_{1-42} strain, nematodes expressing Aβ_{1-42} in the body wall muscles exhibited an age-dependent aggregation of Aβ_{1-42} in the muscles, though less severe than in nAβ_{1-42} nematodes. Aβ_{1-42} aggregation in body wall muscle also has strong proteotoxic effects, impacting the organisms' fitness and motility. The nGCaMP6m strain was then crossed with mAβ_{1-42} or the control nematodes that express only the mScarlet fluorophore in the body wall muscles (mmScarlet).

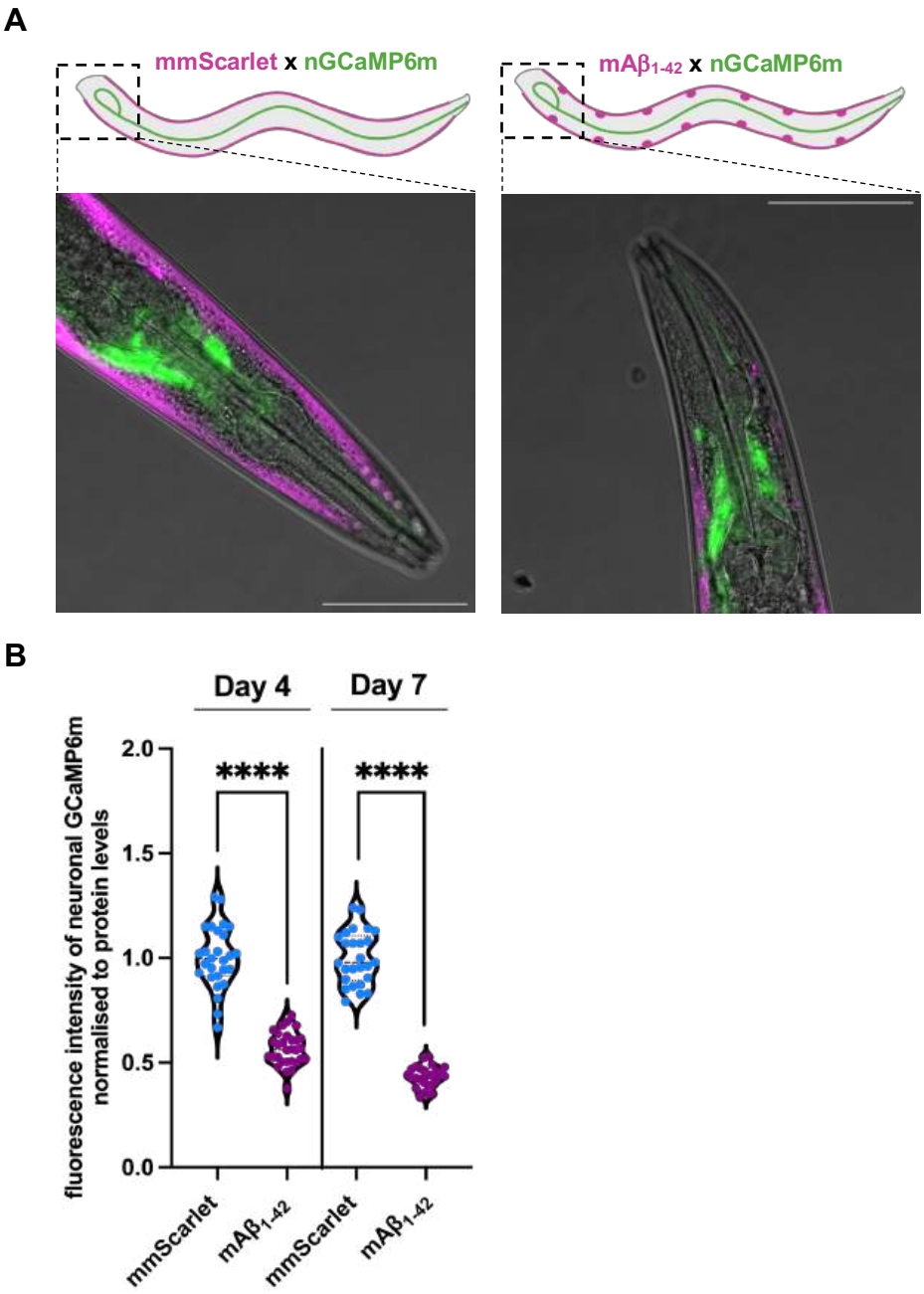

Figure 3.17*: Decrease in neuronal activity precedes the accumulation of Aβ_{1-42} aggregates in the muscles.*

A Representative confocal fluorescent images of a young adult animal (day 4-old) of the mmScarlet × nGCaMP6m cross on the left and of the mAβ_{1-42} × nGCaMP6m cross on the right. The mAβ_{1-42} strain as well as the respective mmScarlet control strain were crossed with the nGCaMP6 strain. Shown are close-up images of the head region. Images are magnified 400-fold and scale bars are 50 µm.

B Violin dot plot of the average GCaMP6m fluorescence intensity normalised to the GCaMP6m protein level of young adult animals (day 4-old) and adult animals (day 7-old) of the control strain

expressing muscle mScarlet (mmScarlet) and mAβ_{1-42}. GCaMP6m intensities were measured in alive animals using microfluidic devices with a widefield fluorescence microscope. GCaMP6m intensities as depicted in Figure 8.2 B were multiplied with the ratio between nGCaMP6m protein levels of the mmScarlet × nGCaMP6m cross and mAβ_{1-42} × nGCaMP6m cross for day 4 and 7 respectively. GCaMP6m protein quantification and a corresponding Western blot are shown in Figure 8.3 B. Every dot represents the neuronal GCaMP6m fluorescence intensity normalised to GCaMP6m protein levels of a single animal of mmScarlet (turquoise) and mAβ_{1-42} (purple). n = 3-4 and N = 26-30 animals. Significance was assessed between mmScarlet day 4 and mAβ_{1-42} day 4 and mmScarlet day 7 and mAβ_{1-42} day 7, respectively, by unpaired Student's t-test with Welch's correction (**** = $p \leq 0.0001$).

Detection of the dual fluorescence of mScarlet (magenta) and GCaMP6m (green) using confocal microscopy confirmed the successful generation of the mmScarlet × nGCaMP6m and mAβ_{1-42} × nGCaMP6m crosses (Figure 3.17 A). Quantification of nGCaMP6m fluorescence intensity in day 4- and day 7-old nematodes was carried out as described above (Figure 3.17 B, Figure 8.2 B and Figure 8.3 B). Surprisingly, even in young adult animals at day 4, GCaMP6m fluorescence intensity normalised to protein levels in neurons was 0.43-fold (± 0.08) lower in nematodes of the mAβ_{1-42} strain compared to the mmScarlet control (Figure 3.17 B). Furthermore, in older animals at day 7 of life, I observed a 0.57-fold (± 0.05) reduction in nGCaMP6m fluorescence intensity normalised to protein levels in mAβ_{1-42} compared to mmScarlet nematodes. Notably, on closer observation, not only did Aβ_{1-42} peptide expression in neurons reduce neuronal GCaMP6m fluorescence intensity, but Aβ_{1-42} expression in body wall muscles also showed a similarly strong detrimental effect on neuronal GCaMP6m fluorescence intensity in younger and older animals (Figure 3.18).

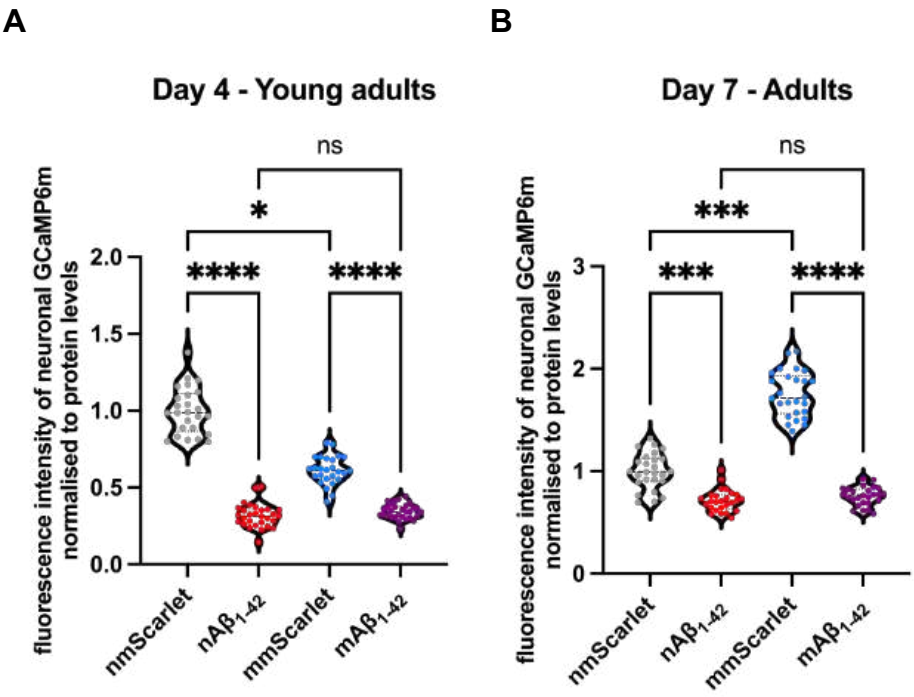

Figure 3.18: *Accumulation of Aβ_{1-42} aggregates in neuronal as well as muscle tissue follows the decline of neuronal function.*

A Violin dot plot of the average GCaMP6m fluorescence intensity normalised to the GCaMP6m protein level of young adult animals (day 4-old) of the nmScarlet, nAβ_{1-42}, mmScarlet and mAβ_{1-42} strain. GCaMP6m intensities were measured in alive animals using microfluidic devices with a widefield fluorescence microscope and were multiplied with the ratio between nGCaMP6m protein levels of the nmScarlet × nGCaMP6m cross and nAβ_{1-42} × nGCaMP6m, mmScarlet × nGCaMP6m, mAβ_{1-42} × nGCaMP6m, respectively, to allow comparison between tissues. Every dot represents the neuronal GCaMP6m fluorescence intensity normalised to GCaMP6m protein levels of a single animal of nmScarlet (grey), and nAβ_{1-42} (red), mmScarlet (turquoise) and mAβ_{1-42} (purple). n = 3-4 and N = 25-30 animals. Significance was assessed by Kruskal-Wallis test with Dunn's's post hoc test (**** = p ≤ 0.0001).

B Violin dot plot of the average GCaMP6m fluorescence intensity normalised to the GCaMP6m protein level of adult animals (day 7-old) of the nmScarlet, nAβ_{1-42}, mmScarlet and mAβ_{1-42} strain. GCaMP6m intensities were measured in alive animals using microfluidic devices with a widefield fluorescence microscope and were multiplied with the ratio between nGCaMP6m protein levels of the nmScarlet × nGCaMP6m cross and nAβ_{1-42} × nGCaMP6m, mmScarlet × nGCaMP6m, mAβ_{1-42} × nGCaMP6m, respectively, to allow comparison between tissues. Every dot represents the neuronal GCaMP6m fluorescence intensity normalised to GCaMP6m protein levels of a single animal of nmScarlet (grey), and nAβ_{1-42} (red), mmScarlet (turquoise) and mAβ_{1-42} (purple). n = 3 and N = 26 animals. Significance was assessed by Kruskal-Wallis test with Dunn's's post hoc test (**** = p ≤ 0.0001).

Thus, these data clearly demonstrate that neuronal activity is reduced early in $A\beta_{1-42}$-expressing nematodes and occurs before severe $A\beta_{1-42}$ aggregation has been reported (Gallrein et al., 2021). Furthermore, neuronal activity is equally affected by $A\beta_{1-42}$ expression in neurons and in distal tissues such as the body wall muscles.

3.2.4 Aggregation of mutant Tau occurs after loss of neuronal function

After observing loss of neuronal activity preceding $A\beta_{1-42}$ aggregation, I aimed to correlate also the aggregation of mutant $Tau^{P301L,V337M}$, with neuronal activity in the newly generated *C. elegans* Tau models (see 3.1). To achieve this, I crossed the nGCaMP6m strain with both the $nTau^{P301L,V337M}$ and $nTau^{WT}$ strain ($nTau^{P301L,V337M}$ × nGCaMP6m and $nTau^{WT}$ × nGCaMP6m). The previously generated nmScarlet × nGCaMP6m strain served as a control.

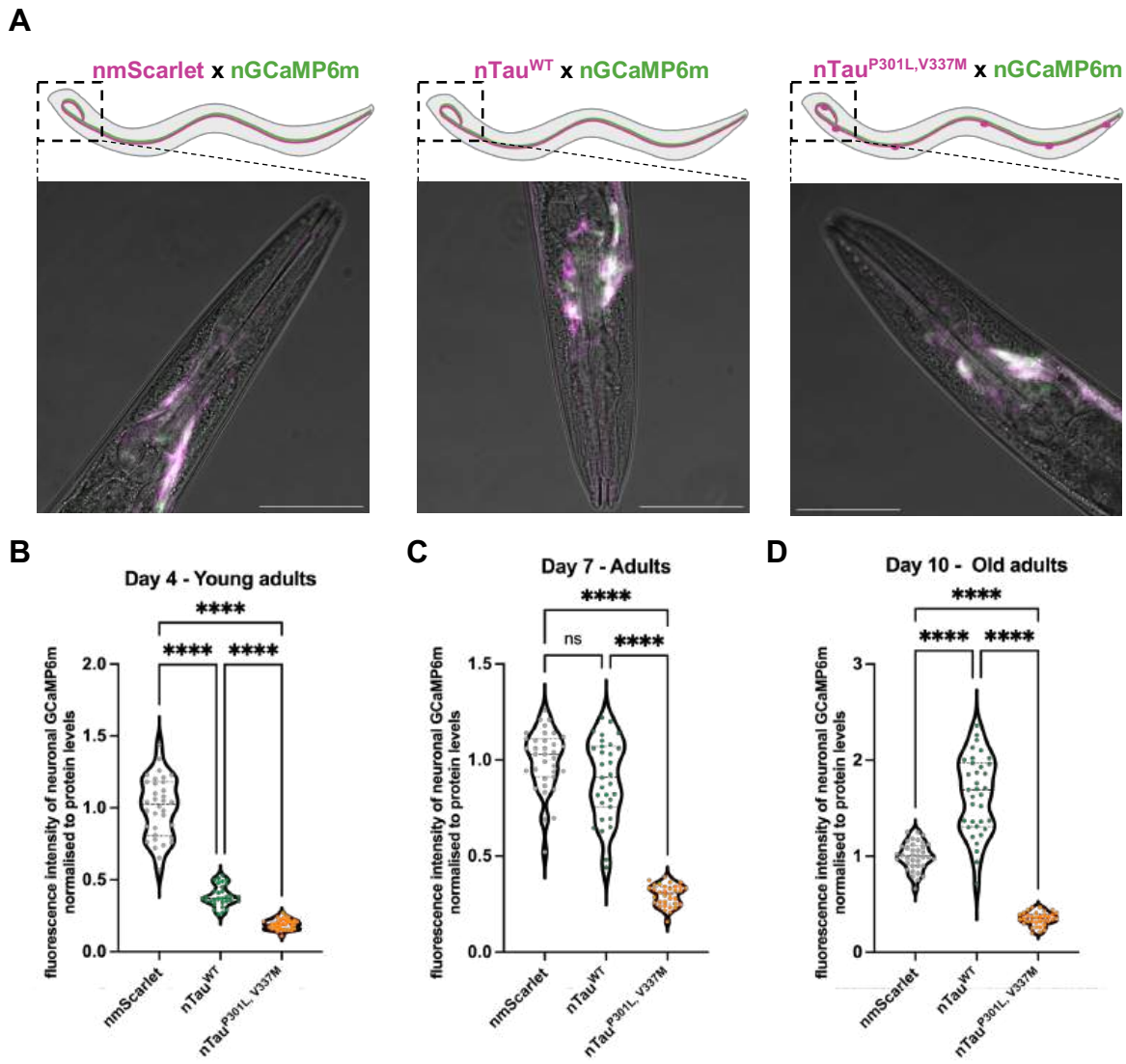

Figure 3.19: *Loss of neuronal function precedes Tau aggregation.*

A Representative confocal fluorescent images of a young adult animal (day 4-old) of the nmScarlet × nGCaMP6m, nTau^{WT} × nGCaMP6m, and nTau^{P301L,V337M} × nGCaMP6m cross from left to right. The Tau-expressing strains as well as the nmScarlet control strain were crossed with the nGCaMP6 strain. Shown are close-up images of the head region. Images are magnified 400-fold and scale bars are 50 µm.

B Violin dot plot of the average GCaMP6m fluorescence intensity normalised to the GCaMP6m protein level of young adult animals (day 4-old) of the control strain nmScarlet, nTau^{WT} and nTau^{P301L,V337M}. GCaMP6m intensities were measured in alive animals using microfluidic devices with a widefield fluorescence microscope. GCaMP6m intensities as depicted in Figure 8.2 C were multiplied with the ratio between nGCaMP6m protein levels of the nmScarlet × nGCaMP6m cross and nTau^{WT} × nGCaMP6m cross, nTau^{P301L,V337M} × nGCaMP6m respectively. GCaMP6m protein quantification and a corresponding Western blot are shown in Figure 8.4 A Every dot represents the neuronal GCaMP6m fluorescence intensity normalised to GCaMP6m protein levels of a single animal of nmScarlet (grey)

and nTau^{WT} (green) and nTau^{P301L,V337M} (orange). n = 5 and N = 31-34 animals. Significance was assessed by one-way ANOVA + Bonferroni post hoc test (**** = p ≤ 0.0001).

C Violin dot plot of the average GCaMP6m fluorescence intensity normalised to the GCaMP6m protein level of adult animals (day 7-old) of the control strain nmScarlet, nTau^{WT} and nTau^{P301L,V337M}. GCaMP6m intensities were measured in alive animals using microfluidic devices with a widefield fluorescence microscope. GCaMP6m intensities as depicted in Figure 8.2 D were multiplied with the ratio between nGCaMP6m protein levels of the nmScarlet × nGCaMP6m cross and nTau^{WT} × nGCaMP6m cross, nTau^{P301L,V337M} × nGCaMP6m respectively. GCaMP6m protein quantification and a corresponding Western blot are shown in Figure 8.4 B. Every dot represents the neuronal GCaMP6m fluorescence intensity normalised to GCaMP6m protein levels of a single animal of nmScarlet (grey) and nTau^{WT} (green) and nTau^{P301L,V337M} (orange). n = 4-5 and N = 31-35 animals. Significance was assessed by Kruskal-Wallis test with Dunn's post hoc test (ns = p > 0.05; **** = p ≤ 0.0001).

D Violin dot plot of the average GCaMP6m fluorescence intensity normalised to the GCaMP6m protein level of old adult animals (day 10-old) of the control strain nmScarlet, nTau^{WT} and nTau^{P301L,V337M}. GCaMP6m intensities were measured in alive animals using microfluidic devices with a widefield fluorescence microscope. GCaMP6m intensities as depicted in Figure 8.2 E were multiplied with the ratio between nGCaMP6m protein levels of the nmScarlet × nGCaMP6m cross and nTau^{WT} × nGCaMP6m cross, nTau^{P301L,V337M} × nGCaMP6m respectively. GCaMP6m protein quantification and a corresponding Western blot are shown in Figure 8.4 C. Every dot represents the neuronal GCaMP6m fluorescence intensity normalised to GCaMP6m protein levels of a single animal of nmScarlet (grey) and nTau^{WT} (green) and nTau^{P301L,V337M} (orange). n = 4-5 and N = 34-37 animals. Significance was assessed by one-way ANOVA + Bonferroni post hoc test (**** = p ≤ 0.0001).

Confocal images revealed the simultaneous presence of magenta mScarlet and green nGCMaP6m fluorescence in the head neurons of the generated crosses (Figure 3.19 A). Subsequently, nGCaMP6m fluorescence intensity normalised to protein levels was quantified analogous to the Aβ_{1-42} analyses (Figure 3.19 B-D, Figure 8.2 C-E and Figure 8.4). Tau^{P301L,V337M} animals exhibited a significant reduction in nGCaMP6m fluorescence intensity normalised to protein levels of 0.81-fold (± 0.04) at a young age (day 4) compared to nmScarlet controls (Figure 3.19 A). This reduction persisted throughout aging, with a 0.7-fold (± 0.06) decrease in adult animals (day 7) (Figure 3.19 B) and a 0.65-fold (± 0.07) decrease in old adult animals (day 10) (Figure 3.19 C). These data demonstrate that expression of the aggregation-prone Tau^{P301L,V337M} leads to a severe reduction in neuronal activity even in young animals, mirroring the effects observed for Aβ_{1-42} expression. Surprisingly, nTau^{WT} animals also exhibited altered nGCaMP6m fluorescence intensity levels normalised to protein levels compared to

nmScarlet controls that however varied with aging. Young nTau^{WT} animals (day 4) showed a 0.61-fold (± 0.07) decrease in nGCaMP6m fluorescence intensity normalised to protein levels (Figure 3.19 A), while adult animals (day 7) exhibited a non-significant 0.1-fold (± 0.21) reduction (Figure 3.19 B). In contrast, old adult nTau^{WT} nematodes (day 10) exhibited a 1.64-fold (± 0.04) increase in nGCaMP6m fluorescence intensity normalised to protein levels compared to nmScarlet controls (Figure 3.19 C). These findings, in conjunction with the previously observed defects in the physiological assays (Figure 3.8 and Figure 3.9), further support the hypothesis that ectopic expression of Tau^{WT} in the nervous system of *C. elegans* exerts toxic effects on the nematodes' physiology including impairment of neuronal activity.

.

3.3 Alteration of Aβ1-42 aggregation and toxicity by extracellular modifiers

The formation of amyloid structures and protein aggregation is a neuropathological hallmark of many neurodegenerative diseases. Preventing aggregation or resolubilizing amyloidogenic protein aggregates, such as the Aβ1-42 peptide involved in Alzheimer's disease, offers a promising approach to modulate amyloid formation, ultimately identifying new therapeutic targets. For instance, a human trimeric chaperone complex of HSC70-APG2-DNAJB1 has been shown to suppress Aβ1-42 aggregate formation *in vitro* (S. M. Ayala Mariscal et al., 2022), while the chaperone HSP-110 could modulate it in a *C. elegans* Aβ1-42 model (Montresor et al., 2024). However, most chaperones are expressed intracellularly, whereas Aβ1-42 aggregation presumably starts in the extracellular space after the Aβ1-42 peptide is secreted from the neurons. Consequently, a better understanding of extracellular proteostasis regulation is highly needed, but suitable *in vivo* models for comprehensive studies are missing. A recent study identified 57 regulators of extracellular protein aggregation in *C. elegans* (Gallotta et al., 2020). This led me to the question of whether these identified extracellular modifiers (ECMs) could potentially alter Aβ1-42 aggregation. To explore this, I investigated the role of two specific ECMs, LYS-3 and CLEC-1, on Aβ1-42 aggregation and toxicity in *C. elegans*.

3.3.1 Characterisation of *lys-3* and *clec-1* mutant *C. elegans* strains

The extracellular proteins LYS-3 and CLEC-1 were identified as potential ECMs as RNA-interference (RNAi) mediated knockdown initially increases the number of visible foci of the extracellular, aggregation-prone protein LBP-2 in a *C. elegans* reporter strain. These RNAi-based observations were confirmed using two *C. elegans* mutant strains with mutated versions of lys-3 and clec-1, respectively. Due to the strong effect these mutants exerted on LBP-2 aggregation, I used those two strains for my studies on Aβ1-42 (Figure 3.20).

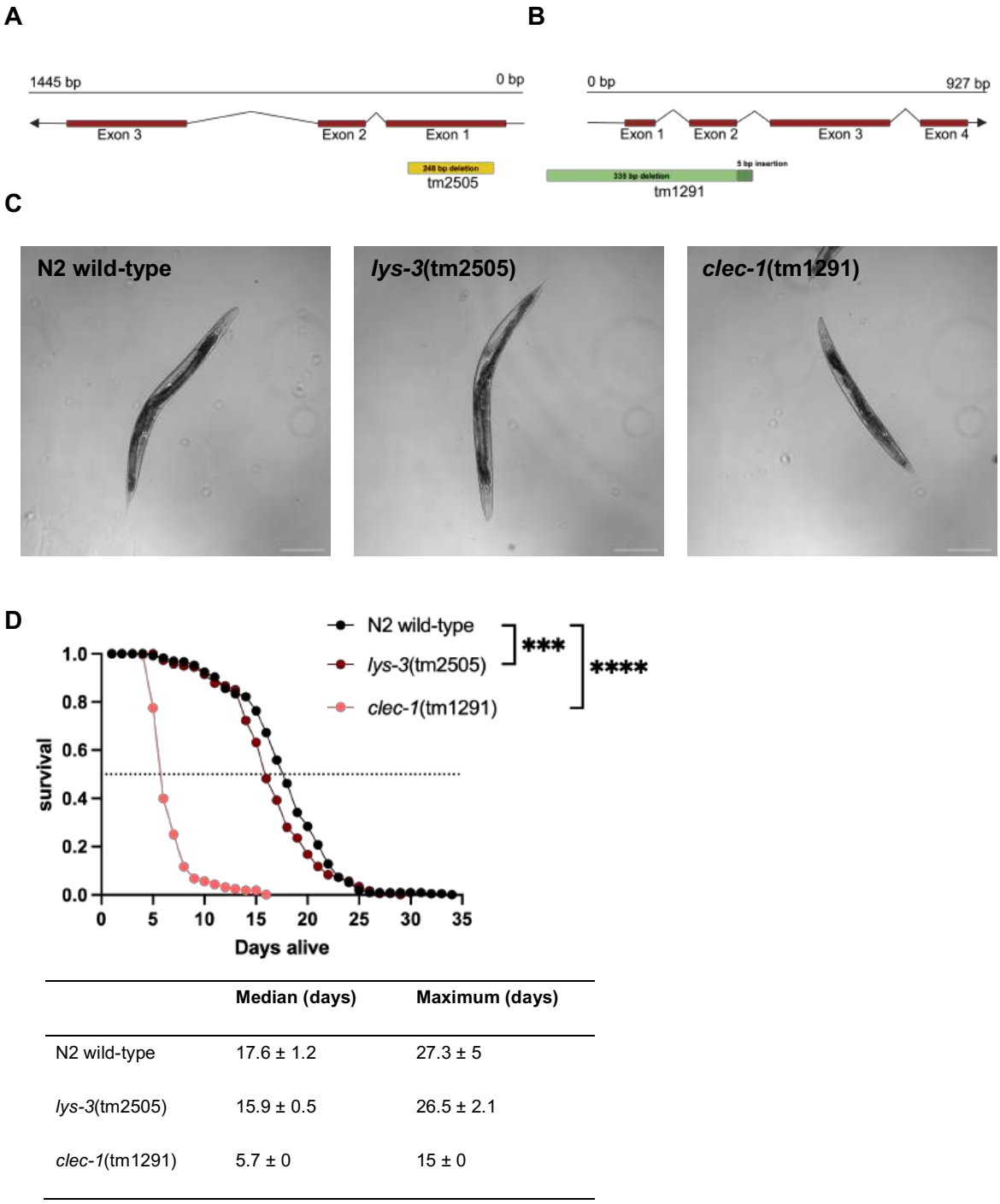

	Median (days)	Maximum (days)
N2 wild-type	17.6 ± 1.2	27.3 ± 5
lys-3(tm2505)	15.9 ± 0.5	26.5 ± 2.1
clec-1(tm1291)	5.7 ± 0	15 ± 0

Figure 3.20: *C. elegans deletion mutants lys-3(tm2505) and clec-1(tm1291).*

A Scheme of the *lys-3* gene locus. The *lys-3* gene locus (sequence Y22F5A.6) consists of 3 exons (burgundy) spanning over 1445 base pairs located on the antisense strand of chromosome V. The deletion mutant strain FX2505 (variation tm2505) lacks 248 base pairs of exon 1.

B Scheme of the *clec-1* gene locus. The *clec-1* gene locus (sequence F25B4.9) consists of 4 exons (burgundy) spanning over 927 base pairs located on the sense strand of chromosome V. The

deletion-insertion mutant strain FX1291 (variation tm1291) lacks 335 base pairs and contains an insertion of 5 additional base pairs.

C Representative confocal images of a young adult animal (4 days old) of the N2 wild-type, *lys-3*(tm2505) and *clec-1*(tm1291) strains. Images are magnified 100-fold (scale bar is 200 µm).

D Lifespan assay of N2 wild-type, *lys-3*(tm2505) and *clec-1*(tm1291) animals. Graph shows the cumulative survival probability (survival) versus age (days alive) of N2 wild-type (black), *lys-3*(tm2505) (burgundy) and *clec-1*(tm1291) (salmon). Two to three independent cohorts of 120-180 nematodes each were analysed, and significance was tested by Log-rank test using the Oasis2 online tool (**** = $p \leq 0.0001$). Average of the mean median lifespan ± SD and average maximum lifespan ± SD are shown in the table below.

The *lys-3* mutant strain (*lys-3*(tm2505); strain FX02505) has a 248 bp deletion within exon 1 of the lys-3 gene, causing a DNA frameshift that leads to a shortened amino acid sequence of the LYS-3 protein (Figure 3.20 A).The clec-1 mutant (clec-1(tm1291), strain FX01291) carries a 335 bp deletion and a 5 bp insertion within the 3'UTR, exon 1, intron 1, exon 2, and partially intron 2 of the clec-1 gene (Figure 3.20 B). This mutation causes a visible Dumpy (Dpy) phenotype, characterised by a disproportional reduction in body size, thicker middle body, and shorter length (Cho et al., 2021). Using confocal microscopy, I confirmed the Dpy phenotype of clec-1(tm1291) mutants and observed that lys-3(tm2505) nematodes showed no visibly altered phenotype compared to nematodes of the N2 wild-type strain (Figure 3.20 C). To further assess the physiology of lys-3(tm2505) and clec-1(tm1291) mutants, I performed a lifespan assay to test the organismal fitness of the nematodes (Figure 3.20 D). The median lifespan of lys-3(tm2505) nematodes was reduced by 1.6 days compared to N2 wild-type animals, from 17.6 days (± 1.2) to 15.9 days (± 0.5), while the maximum lifespan was only slightly altered from 27.3 days (± 5) to 26.5 days (± 2.1). The mutation in *clec-1*(tm1291) nematodes caused a drastic reduction of the median lifespan of about 11.9 days, from 17.6 days (± 1.2) to 5.7 days (± 0.00), and also of the maximum lifespan of about 12.3 days, from 27.3 days (± 5) to 15 days (± 0.00) compared to N2 wild-type. These data demonstrate that the mutations in the *lys-3* and *clec-1* genes are detrimental to organismal fitness and reduce the lifespan of the nematodes, with *clec-1*(tm1291) causing a particularly severe effect.

3.3.2 Generation of neuronal Aβ$_{1-42}$ and mScarlet control strains with *lys-3* and *clec-1* mutant background

To better understand the role of LYS-3 and CLEC-1 as potential ECMs on Aβ$_{1-42}$ aggregation and proteotoxicity *in vivo*, I used the Aβ$_{1-42}$ *C. elegans* model previously established in the Kirstein lab. This strain expresses untagged Aβ$_{1-42}$ under the pan-neuronal promoter *rgef-1*, which is secreted through fusion to a signal peptide sequence, along with a substoichiometric amount of Aβ$_{1-42}$ tagged with the mScarlet fluorophore. This strain allows Aβ$_{1-42}$ to be visualised by fluorescence microscopy *in situ*, enabling tracking and quantification of aggregation. The neuronal Aβ$_{1-42}$ model (nAβ$_{1-42}$) mimics Alzheimer's disease pathology, exhibiting severe Aβ$_{1-42}$ aggregation that leads to impaired organismal fitness, neurodegeneration and propagation to distal tissues. Furthermore, the same model has already been used to study the modulation of Aβ$_{1-42}$ aggregation by various modifiers (Pras et al., 2021; Gallrein et al., 2023; Schiavi et al., 2023; Montresor et al., 2024).

I crossed the nAβ$_{1-42}$ strain with both the *lys-3* and *clec-1* mutant strains, obtaining nAβ$_{1-42}$ *lys-3*(tm2505) and nAβ$_{1-42}$ *clec-1*(tm1291) strains (Figure 3.21). As a control, I used the nmScarlet strain, which expresses only the mScarlet fluorophore in the neurons, and produced the nmScarlet *lys-3*(tm2505) and nmScarlet *clec-1*(tm1291) crosses. To confirm the presence and homozygosity of the deletion within the *lys-3* and *clec-1* gene in the generated crosses, I performed a genotyping PCR. This technique amplifies a specific gene region using primers that bind upstream and downstream of the deleted region. The resulting amplicons of different sizes allow to distinguish between strains homozygous for *lys-3*(tm2505) and those homozygous for the wild-type version of the respective genes.

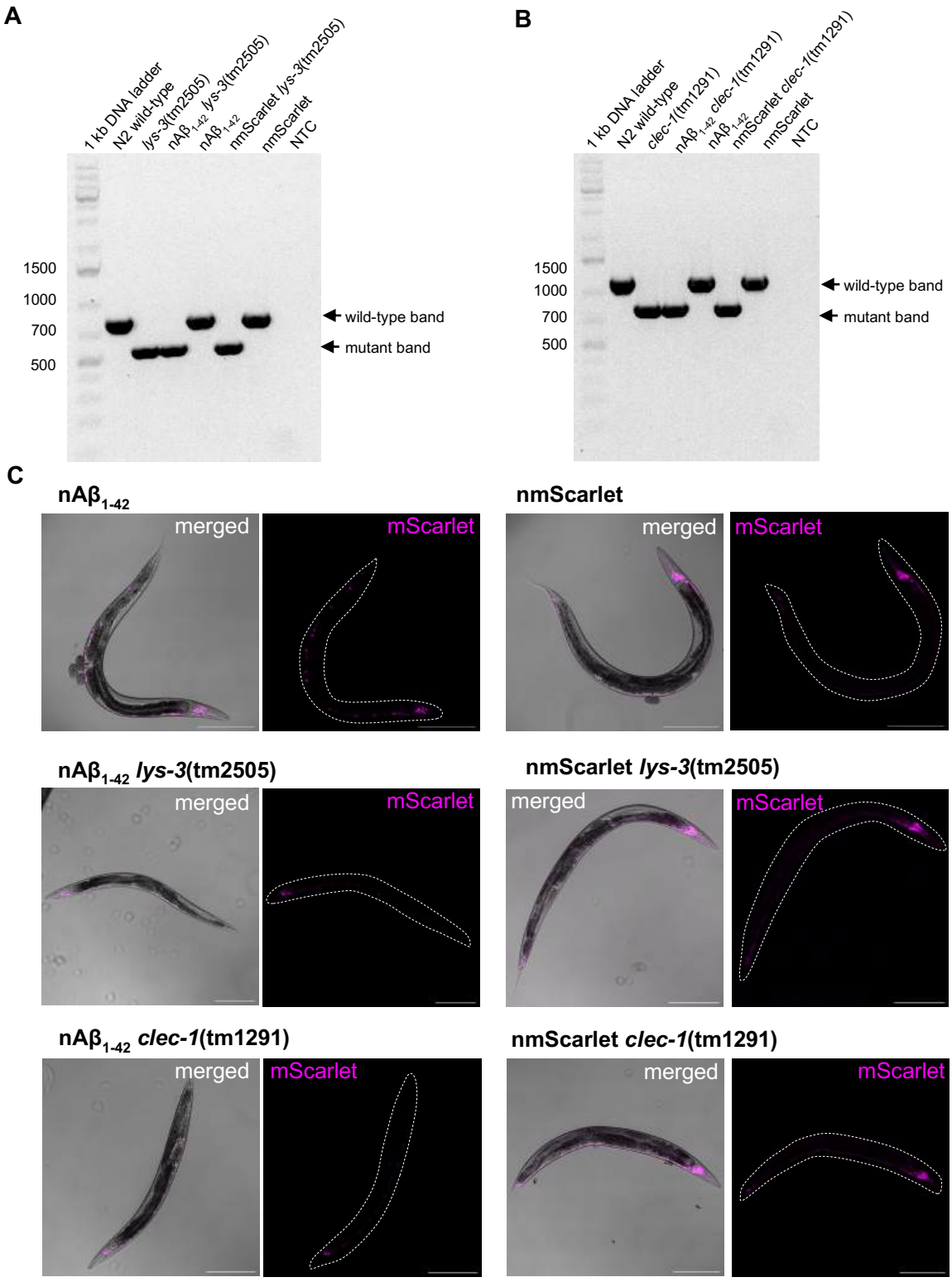
A
1 kb DNA ladder
N2 wild-type
lys-3(tm2505)
nAβ1-42 lys-3(tm2505)
nAβ1-42
nmScarlet lys-3(tm2505)
nmScarlet
NTC
1500
1000
700
500
wild-type band
mutant band
B
1 kb DNA ladder
N2 wild-type
clec-1(tm1291)
nAβ1-42 clec-1(tm1291)
nAβ1-42
nmScarlet clec-1(tm1291)
nmScarlet
NTC
1500
1000
700
500
wild-type band
mutant band
C
nAβ1-42
merged
mScarlet
nmScarlet
merged
mScarlet
nAβ1-42 lys-3(tm2505)
merged
mScarlet
nmScarlet lys-3(tm2505)
merged
mScarlet
nAβ1-42 clec-1(tm1291)
merged
mScarlet
nmScarlet clec-1(tm1291)
merged
mScarlet

D

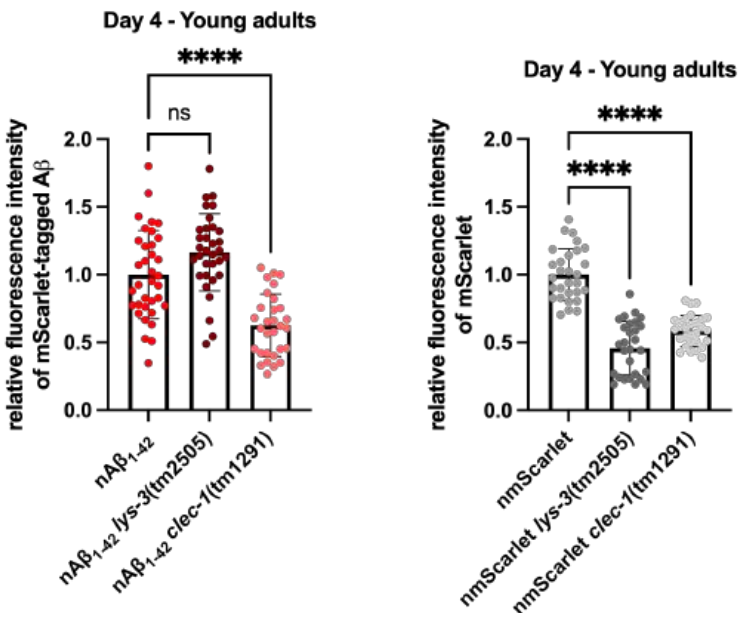

Figure 3.21*: Generation of nAβ_{1-42} and nmScarlet strains with lys-3 and clec-1 deletion.*

A Agarose gel electrophoresis of genotyping the *lys-3* gene locus in nematodes of N2 wild-type, *lys-3*(tm2505), nAβ$_{1-42}$ *lys-3*(tm2505), nAβ$_{1-42}$, nmScarlet lys-3(tm2505) and nmScarlet. The PCR amplifies an 817 bp DNA fragment for the *lys-3* WT nematodes (i.e., N2 wild-type, nAβ$_{1-42}$, and nmScarlet) while a PCR of the genomic DNA of nematodes with a *lys-3* deletion (*lys-3*(tm2505), nAβ$_{1-42}$ *lys-3*(tm2505) and nmScarlet *lys-3*(tm2505)) generates a DNA fragment of 569 bp. A notemplate control (NTC) was used to check for contamination or non-specific amplification.

B Agarose gel electrophoresis of genotyping the *clec-1* gene locus in nematodes of N2 wild-type, *clec-1*(tm1291), nAβ$_{1-42}$ *clec-1*(tm1291), nAβ$_{1-42}$, nmScarlet *clec-1*(tm1291) and nmScarlet. The PCR amplifies a 1201 bp DNA fragment of the genomic DNA of *clec-1* WT nematodes (i.e., N2 wild-type, nAβ$_{1-42}$, and nmScarlet) while a PCR of genomic DNA of nematodes with a *clec-1* deletion (*clec-1*(tm1291), nAβ$_{1-42}$ *clec-1*(tm1291) and nmScarlet *clec-1*(tm1291)) amplifies a DNA fragment of 871 bp. A no-template control (NTC) was used to check for contamination or non-specific amplification.

C Representative confocal fluorescent images of a young adult animal (4 days old) of the parental strains, neuronal Aβ$_{1-42}$ (nAβ$_{1-42}$) and neuronal mScarlet (nmScarlet) (first row) and the crosses nAβ$_{1-42}$ *lys-3*(tm2505), nmScarlet *lys-3*(tm2505) (second row), nAβ$_{1-42}$ *clec-1*(tm1291) and nmScarlet *clec-1*(tm1291) (third row). The images are 100-fold magnified (scale bar is 200 µm). The white dashed line shows the outline of the nematodes and images are depicted as merge and mScarlet fluorescence (magenta) only.

D Quantification of mScarlet-Aβ$_{1-42}$/mScarlet fluorescence intensity in young adult (4 days old) nematodes of nAβ$_{1-42}$, nAβ$_{1-42}$ *lys-3*(tm2505) and nAβ$_{1-42}$ *clec-1*(tm1291) (left graph) and nmScarlet, nmScarlet *lys-3*(tm2505) and nmScarlet *clec-1*(tm1291) (right graph). Confocal fluorescent images of two to three cohorts, totaling 28-35 nematodes, were recorded, and fluorescence intensities were

quantified by Fiji and normalised to nAβ_{1-42} / nmScarlet. Data are displayed as mean fluorescence intensity ± SD. Significance was tested by one-way ANOVA + Bonferroni post hoc test (ns = $p > 0.05$; **** = $p < 0.0001$).

The validation of the correct genotype of the crosses nAβ_{1-42} *lys-3*(tm2505), nmScarlet *lys-3*(tm2505), nAβ_{1-42} *clec-1*(tm1291) and nmScarlet *clec-1*(tm1291) was confirmed by genotyping (Figure 3.21 A and B). Confocal microscopy confirmed the fluorescence of mScarlet-tagged Aβ_{1-42} and mScarlet alone (magenta) in the neurons of the nematodes (Figure 3.21 C). Whole-body images revealed the distinct expression pattern of Aβ_{1-42}, particularly visible through strong fluorescence in the IL2 neurons and the nerve ring in the head region. In contrast, mScarlet showed a more ubiquitous expression throughout the whole head region. nAβ_{1-42} *clec-1*(tm1291) and nmScarlet *clec-1*(tm1291) nematodes exhibited the previously observed Dpy phenotype caused by the mutation in *clec-1*. I quantified the fluorescence intensity of mScarlet-tagged Aβ_{1-42} and mScarlet in the newly generated crosses relative to the parental strains nAβ_{1-42} and nmScarlet in young adult animals (day 4) using the confocal images (Figure 3.21 D). The fluorescence intensity of mScarlet-tagged Aβ_{1-42} remained unchanged in nAβ_{1-42} *lys-3*(tm2505) compared to nAβ_{1-42}. However, nAβ_{1-42} *clec-1*(tm1291) animals exhibited a 0.37-fold (± 0.23) reduction in fluorescence intensity of mScarlet-tagged Aβ_{1-42} compared to nAβ_{1-42}. In contrast, the mScarlet fluorescence intensity was 0.54-fold (± 0.2) and 0.41-fold (± 0.11) decreased in nmScarlet *lys-3*(tm2505) and nmScarlet *clec-1*(tm1291), respectively, compared to nmScarlet nematodes. These data highlight that crossing nAβ_{1-42} and nmScarlet nematodes with mutant strains likely causes changes in the expression levels of mScarlet-tagged Aβ_{1-42} and mScarlet.

3.3.3 Knockout of *lys-3* and *clec-1* ameliorates Aβ_{1-42} aggregation and reduces Aβ_{1-42} in coelomocytes

To study the effect of *lys-3* and *clec-1* knockout on Aβ_{1-42} aggregation during aging, I used fluorescence lifetime imaging microscopy. The measured fluorescence lifetime (τ) of mScarlet serves as a proxy for the Aβ_{1-42} aggregation propensity (3.1.2). A decrease in the τ value indicates increased Aβ_{1-42} aggregation, while a higher τ value suggests less aggregation. FLIM measurements were performed on the head neurons

of young adult and adult animals at days 4 and 7. The strains examined were nAβ_{1-42}, nAβ_{1-42} *lys-3*(tm2505) and nAβ_{1-42} *clec-1*(tm1291), along with their respective controls nmScarlet, nmScarlet *lys-3*(tm2505) and nmScarlet *clec-1*(tm1291) (Figure 3.22 and Figure 3.23). I hypothesised that mutations in *lys-3* or *clec-1* would negatively affect Aβ_{1-42} aggregation. Since mutations in *lys-3* or *clec-1* increased foci formation of the *C. elegans* endogenous protein LBP-2 (Gallotta et al., 2020), I hypothesised they might also accelerate Aβ_{1-42} aggregation.

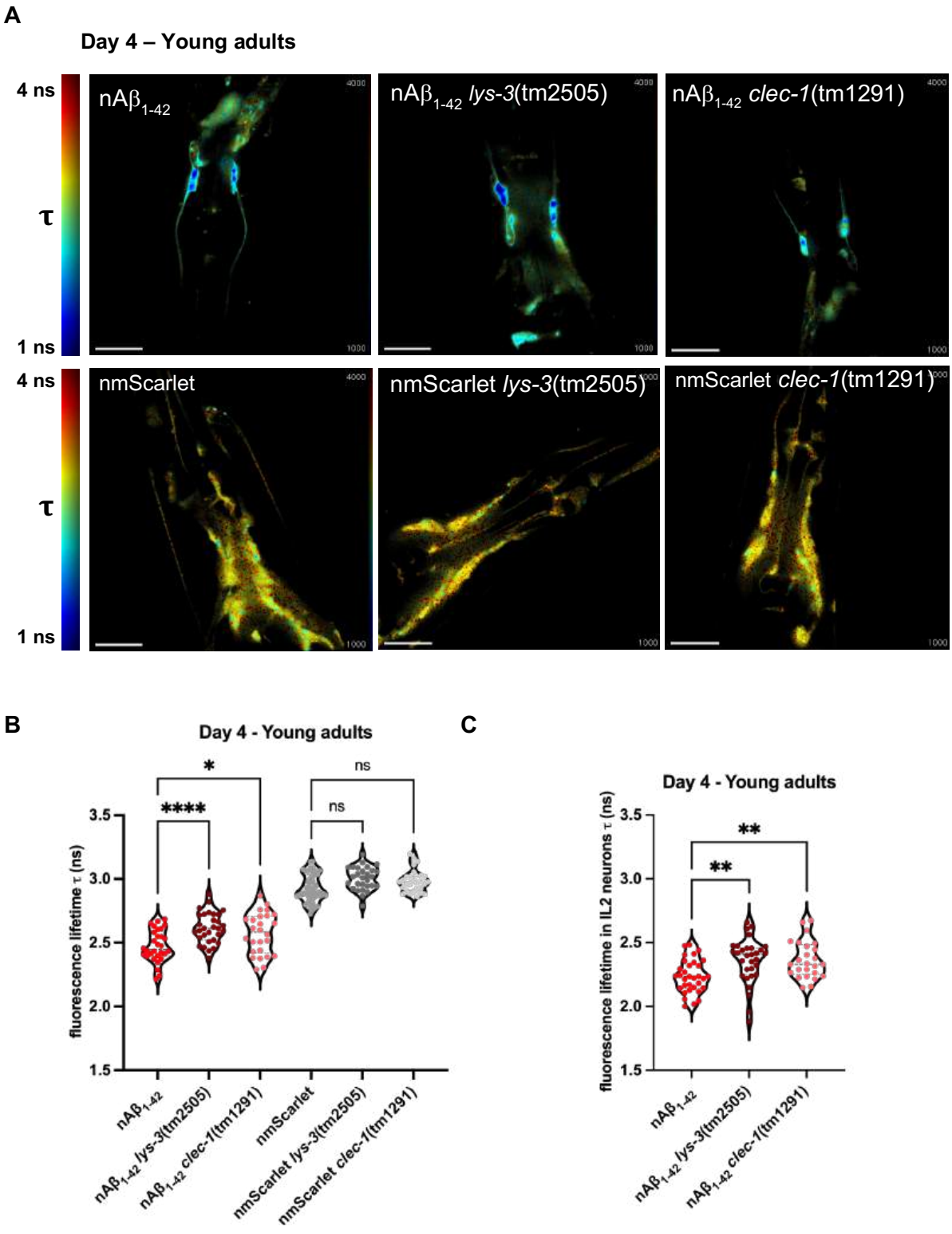

Figure 3.22: *lys-3 and clec-1 knockout ameliorates Aβ_{1-42} aggregation in young adult animals.*

A Representative TCSPC-FLIM images of nAβ_{1-42}, nAβ_{1-42} *lys-3*(tm2505), nAβ_{1-42} *clec-1*(tm1291) (upper row) and nmScarlet, nmScarlet *lys-3*(tm2505), nmScarlet *clec-1*(tm1291) (lower row). Head neurons of young adult (day 4-old) animals were analysed. Images depict the pixel-wise fluorescent lifetime (**τ**) merged with the fluorescent intensity. Fluorescence lifetime is colour-coded: blue represents

low fluorescent lifetimes (1 ns) showing regions with aggregated Aβ_{1-42} and red represents high fluorescent lifetimes (4 ns) showing region with soluble Aβ_{1-42} species. Scale bars are 20 µm.

B Violin dot plot of the average fluorescent lifetime (τ) of young adult animals (day 4-old) of nAβ_{1-42}, nAβ_{1-42} *lys-3*(tm2505), nAβ_{1-42} *clec-1*(tm1291), nmScarlet, nmScarlet *lys-3*(tm2505) and nmScarlet *clec-1*(tm1291). Data displays average fluorescent lifetimes ± SD of nAβ_{1-42} (red), nAβ_{1-42} *lys-3(*tm2505) (burgundy), nAβ_{1-42} *clec-1*(tm1291) (salmon), nmScarlet (grey), nmScarlet *lys-3*(tm2505) (dark grey) and nmScarlet *clec-1*(tm1291) (light grey). Every dot represents the average fluorescent lifetime for the head neurons of one single nematode. Two to three independent cohorts of in total 26-47 animals were analysed. Significance was tested by one-way ANOVA + Bonferroni post hoc test (ns = $p > 0.05$; * = $p \leq 0.05$; **** = $p < 0.0001$).

C Violin dot plot of the average fluorescent lifetime (τ) of young adult animals (day 4-old) of nAβ_{1-42}, nAβ_{1-42} *lys-3*(tm2505), nAβ_{1-42} *clec-1*(tm1291) in the IL2 neurons, Data displays average fluorescent lifetimes ± SD of nAβ_{1-42} (red), nAβ_{1-42} *lys-3*(tm2505) (burgundy) and nAβ_{1-42} *clec-1*(tm1291) (salmon). Every dot represents the average fluorescent lifetime in the IL2 neurons of one single nematode. Three independent cohorts of in total 25-33 animals were analysed. Significance was tested by one-way ANOVA + Bonferroni post hoc test (** = $p < 0.01$).

In the depicted FLIM images, fluorescence lifetime values in specific areas of the head region are visualised using a false-colour code (Figure 3.22 A and Figure 3.23 A). Blue-cyan colours indicate areas with lower τ values and more aggregates, while red-yellow colours indicate for areas with lower aggregation load and higher τ values. The mean τ value in nanoseconds (ns) for whole head region of each nematode is plotted to compare different strains (Figure 3.22 B and Figure 3.23 B). As previously reported, the τ values of nAβ_{1-42} are reduced compared to nmScarlet on both day 4 from 2.93 ns (± 0.12) to 2.47 ns (± 0.13) (**** = $p < 0.0001$) and day 7 from 2.85 ns (± 0.13) to 2.36 ns (± 0.16) (**** = $p < 0.0001$). This reduction in fluorescence lifetime is evident in the FLIM images, shown by an increase in blue foci. Furthermore, Aβ_{1-42} aggregation increases with aging, as indicated by a decrease in the τ values of nAβ_{1-42} nematodes from 2.47 ns (± 0.13) to 2.36 ns (± 0.16) between day 4 and day 7 (** = $p < 0.01$). nAβ_{1-42} *lys-3*(tm2505) and nAβ_{1-42} *clec-1*(tm1291) nematodes exhibited an increase of fluorescence lifetime values from 2.47 ns (± 0.13) to 2.62 ns (± 0.12) (**** = $p < 0.0001$) and from 2.47 ns (± 0.13) to 2.56 ns (± 0.16) (* = $p \leq 0.05$), respectively, on day 4. The increases of fluorescence lifetime suggest reduced Aβ_{1-42} aggregation in both mutant strains. As expected, the τ values of nmScarlet *lys-3*(tm2505) and nmScarlet *clec-*

1(tm1291) remained unchanged compared to nmScarlet nematodes (Figure 3.22 B). IL2 neurons are a subset of head neurons where the first Aβ_{1-42} aggregates form (Gallrein et al., 2021). I wondered if *lys-3* or *clec-1* knockout would affect the onset of aggregation specifically in these neurons in young adult animals. To analyse τ values in the IL2 neurons only, the whole head measurements dataset was segmented for IL2 neurons (Figure 3.22 C). The difference between nAβ_{1-42} *lys-3*(tm2505) and nAβ_{1-42} nematodes persisted, with τ values increasing from 2.23 ns ($\pm$ 0.13) to 2.36 ns ($\pm$ 0.18) on day 4 (** = $p < 0.01$). nAβ_{1-42} *clec-1*(tm1291) exhibited an increase in the τ values from 2.23 ns ($\pm$ 0.13) to 2.37 ns ($\pm$ 0.15) compared to nAβ_{1-42} (** = $p < 0.01$), showing higher statistical significance than observed in the whole head neurons. These results suggest that mutations in *lys-3* or *clec-1* decrease Aβ_{1-42} aggregation specifically in the IL2 neurons, with *clec-1* showing a particularly strong ameliorative effect.

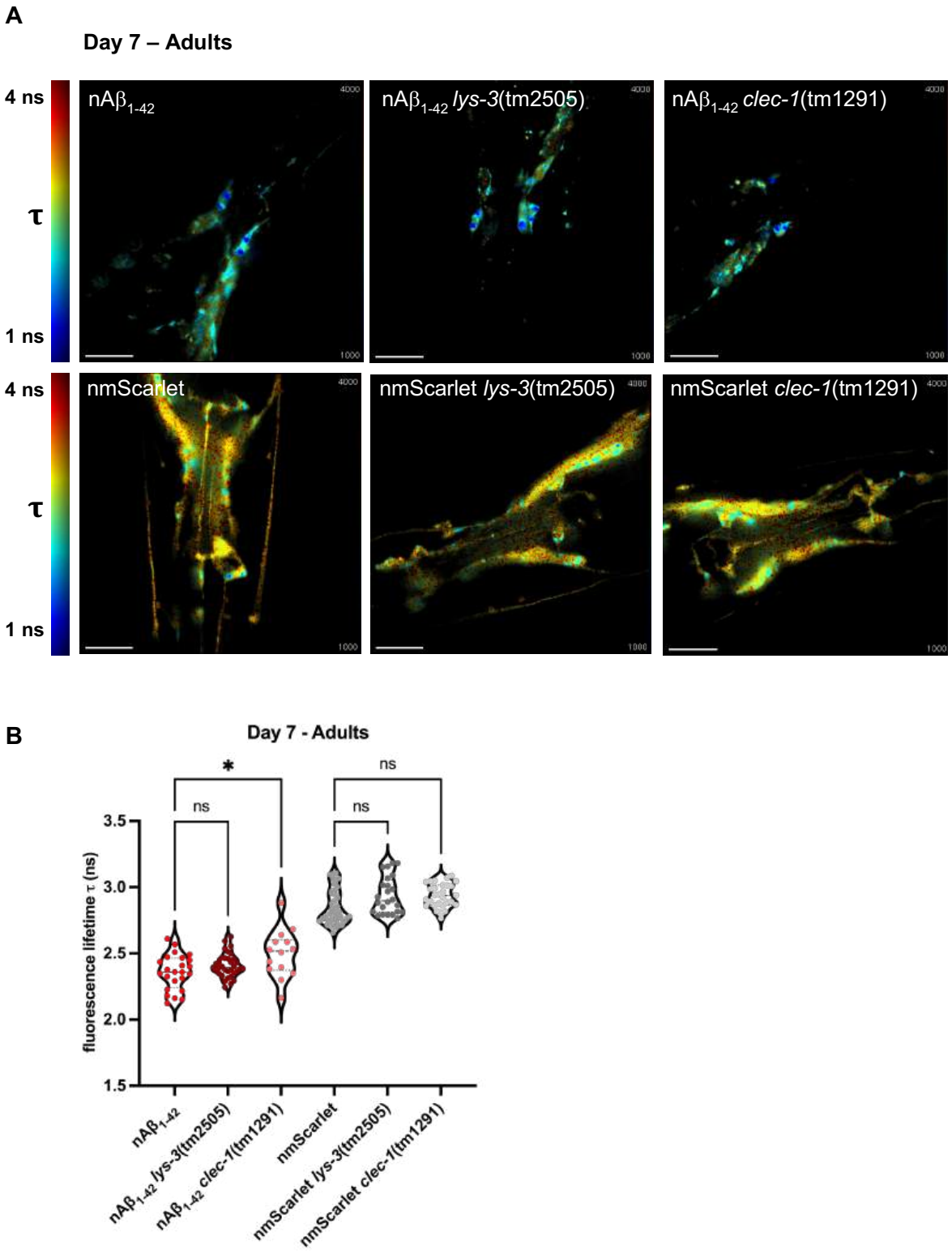

Figure 3.23: *Aβ1-42 aggregation is not altered in older animals upon lys-3 knockout.*

A Representative TCSPC-FLIM images of nAβ1-42, nAβ1-42 *lys-3*(tm2505), nAβ1-42 *clec-1*(tm1291) (upper row) and nmScarlet, nmScarlet *lys-3*(tm2505), nmScarlet *clec-1*(tm1291) (lower row). Head neurons of adult (day 7-old) animals were analysed. Images depict the pixel-wise fluorescent lifetime (τ) merged with the fluorescent intensity. Fluorescence lifetime is colour-coded: blue represents low

fluorescent lifetimes (1 ns) showing regions with aggregated Aβ_{1-42} and red represents high fluorescent lifetimes (4 ns) showing region with soluble Aβ_{1-42} species. Scale bars are 20 µm.

B Violin dot plot of the average fluorescent lifetime (**τ**) of adult animals (day 7-old) of nAβ_{1-42}, nAβ_{1-42} *lys-3*(tm2505), nAβ_{1-42} *clec-1*(tm1291), nmScarlet, nmScarlet *lys-3*(tm2505) and nmScarlet *clec-1*(tm1291). Data display average fluorescent lifetimes ± SD of nAβ_{1-42} (red), nAβ_{1-42} *lys-3*(tm2505) (burgundy), nAβ_{1-42} *clec-1*(tm1291) (salmon), nmScarlet (grey), nmScarlet *lys-3*(tm2505) (dark grey) and nmScarlet *clec-1*(tm1291) (light grey). Every dot represents the average fluorescent lifetime for the head neurons of one single nematode. Two to three independent cohorts of a total of 14-42 animals were analysed. Significance was tested by one-way ANOVA + Bonferroni post hoc test (ns = $p > 0.05$; * = $p \leq 0.05$).

Interestingly, in older animals on day 7, the *lys-3* mutation did not cause a significant alteration in the fluorescence lifetime value in nAβ_{1-42} animals (Figure 3.23). Consistent with this, both nmScarlet *lys-3*(tm2505) and nmScarlet *clec-1*(tm1291) nematodes exhibited no change in the τ values compared to nmScarlet. However, a moderate increase in fluorescence lifetime from 2.36 ns (± 0.16) to 2.5 ns (± 0.18) was observed in day 7-old nematodes of nAβ1-42 clec-1(tm1291) compared to nAβ1-42 nematodes (* = $p \leq 0.05$). I hypothesised that this result might be due to a survivorship bias. With a median lifespan of 5.7 days observed in clec-1(tm1291) animals (Figure 3.20 D), more than half of the population would have died by day 7 when the FLIM analysis was performed. Consequently, the nematodes that survived until day 7 were likely the healthiest ones with the lowest Aβ_{1-42} aggregation load, leading to the apparent increase in fluorescence lifetime in nAβ_{1-42} *clec-1*(tm1291) nematodes on day 7.

In conclusion, these data show that a knockout of *lys-3* and *clec-1* causes a decrease in Aβ_{1-42} aggregation in young adult animals at day 4, which is also apparent in the IL2 neurons - most vulnerable to Aβ_{1-42} aggregation. However, this ameliorative effect was not observed in older animals at day 7, where no difference in Aβ_{1-42} aggregation was detected. Contrary to my initial hypothesis and previous data, the knockout of *lys-3* or *clec-1* surprisingly ameliorated Aβ_{1-42} aggregation. This beneficial effect was only visible in young animals, not in older ones. This suggests that either LYS-3 *and* CLEC-1 are only active at a young age or when the Aβ_{1-42} aggregation load is still relatively low.

Additionally, I tested the effect of two other potential ECMs that have been identified in *C. elegans*: TAG-196 and DOD-21 (Figure 8.5). Analogously to CLEC-1 and LYS-3, I also used *tag-196* and *dod-21* mutant strains that I crossed with the nAβ_{1-42} strain (Figure 8.5 A and B). However, no significant difference in fluorescence lifetime was observed in either of these crosses at day 4 or at day 7 (Figure 8.5 C and D). Consequently, I focused subsequent analyses on CLEC-1 and LYS-3, as they showed the most promising results in the FLIM measurements.

After investigating Aβ_{1-42} aggregation within neurons, I aimed to study Aβ_{1-42} in the extracellular space and explore whether the knockout of *lys-3* or *clec-1* affects Aβ_{1-42} propagation and spreading. Aβ_{1-42} can be detected both within and outside of neurons and accumulates in coelomocytes in the body cavity. Coelomocytes are scavenger cells with lysosomal function that take up macromolecules. To investigate whether LYS-3 or CLEC-1 affect Aβ_{1-42} secretion, I quantified the amount of Aβ_{1-42} in the coelomocytes of nAβ_{1-42} *lys-3*(tm2505) and nAβ_{1-42} *clec-1*(tm1291) animals relative to nAβ_{1-42}. Visualisation of coelomocytes was achieved using a strain that expresses a GFP fluorophore specifically in coelomocytes (ZIM1048 strain from the Zimmer lab). This strain was crossed with nAβ_{1-42}, nAβ_{1-42} *lys-3*(tm2505) and nAβ_{1-42} *clec-1*(tm1291) nematodes, respectively, and confocal images were then taken to quantify the fluorescence of mScarlet-tagged Aβ_{1-42} inside the coelomocytes (Figure 3.24). I analysed Aβ_{1-42} levels in coelomocytes only in young adult animals at day 4, as the FLIM measurements showed an effect on Aβ_{1-42} aggregation by *lys-3* and *clec-1* knockout only at a young age.

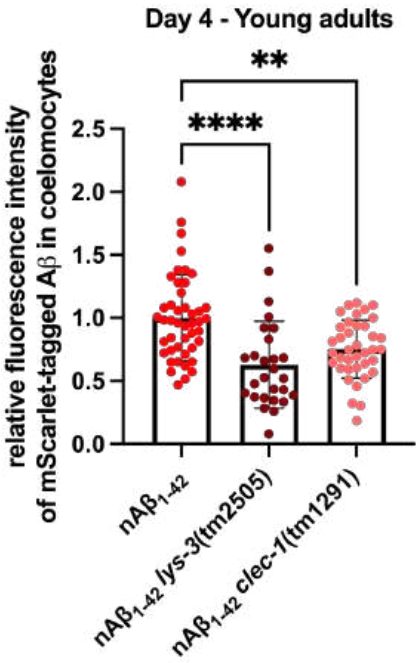

Figure 3.24: *lys-3 and clec-1 knockout reduce levels of Aβ_{1-42} in coelomocytes.*

Scatter dot plot of the average Aβ_{1-42} levels in the coelomocytes of nAβ_{1-42}, nAβ_{1-42} *lys-3*(tm2505) and nAβ_{1-42} *clec-1*(tm1291) young adult animals. For identification of coelomocytes nAβ_{1-42}, nAβ_{1-42} *lys-3*(tm2505) and nAβ_{1-42} *clec-1*(tm1291) were crossed with ZIM1048 strain expressing GFP in coelomocytes. Aβ_{1-42} fluorescence levels were quantified in the head coelomocytes by Fiji analysis of confocal images. Every dot represents the level of Aβ_{1-42} in head coelomocytes for nAβ_{1-42} (red), nAβ_{1-42} *lys-3*(tm2505) (burgundy), nAβ_{1-42} *clec-1*(tm1291) (salmon). Fluorescence intensities were normalised to the signals of nAβ_{1-42}. Three cohorts of in total 17-25 nematodes were analysed. Significance was assessed by Kruskal-Wallis test (** = $p \leq 0.01$; **** = $p \leq 0.0001$).

In both nAβ_{1-42} *lys-3*(tm2505) and nAβ_{1-42} *clec-1*(tm1291) nematodes, the fluorescence intensity of mScarlet-tagged Aβ_{1-42} in the coelomocytes was found to be decreased compared to nAβ_{1-42}. *lys-3* knockout caused a 0.28-fold reduction of Aβ_{1-42} in coelomocytes and *clec-1* knockout reduced Aβ_{1-42} levels in coelomocytes by 0.25-fold relative to nAβ_{1-42}. Thus, both *lys-3* and *clec-1* knockout seem to affect either the propagation of Aβ_{1-42} from the neurons to the extracellular space or the transport and uptake of secreted Aβ_{1-42} from the body cavity to the coelomocytes.

3.3.4 *lys-3* knockout alleviates physiological defects of Aβ_{1-42} nematodes

Based on the previous Aβ_{1-42} FLIM measurements, I wondered whether the observed effects impacted the nematodes' physiology. The knockout of *lys-3* and *clec-1* reduced

Aβ$_{1-42}$ aggregation, which in turn could potentially improve the nematodes' organismal fitness. To systemically assess the physiology of the nematodes, I conducted two experiments: a lifespan assay and a developmental assay (Figure 3.25). A lifespan assay monitors the survival of nematodes from day 1 until death. A developmental assay assesses the percentage of developmental stages within a population from day 1 to day 4. The lifespan was performed on nAβ$_{1-42}$, nAβ$_{1-42}$ *lys-3*(tm2505) and nAβ$_{1-42}$ *clec-1*(tm1291) nematodes, along with their respective controls. The developmental assay was performed on nAβ$_{1-42,}$ nAβ$_{1-42}$ *lys-3*(tm2505) and control strains.

A

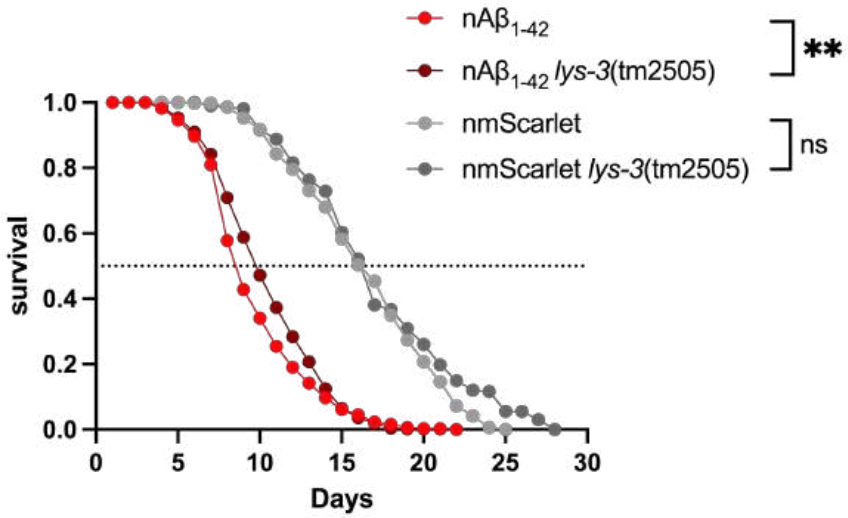

	Median (days)	Maximum (days)
nAβ$_{1-42}$	8.9 ± 0.5	18.3 ± 2.5
nAβ$_{1-42}$ *lys-3*(tm2505)	10 ± 0.3	18.3 ± 1.7
nmScarlet	16.5 ± 1	23.7 ± 0.6
nmScarlet *lys3*(tm2505)	16.1 ± 0.1	27 ± 0

B

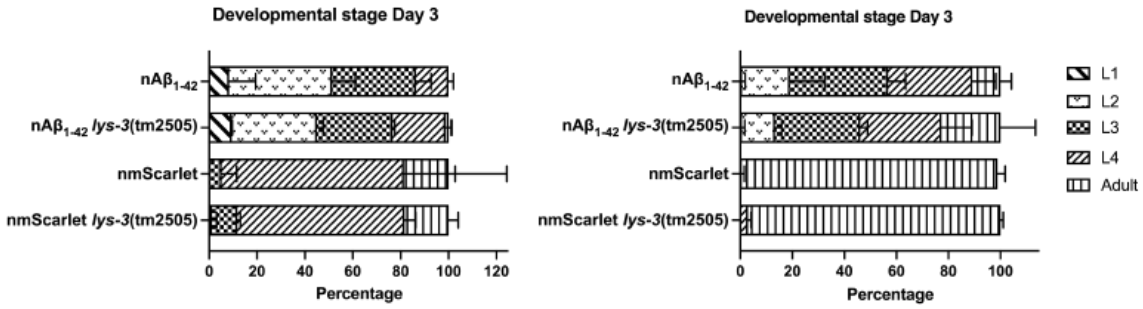

C

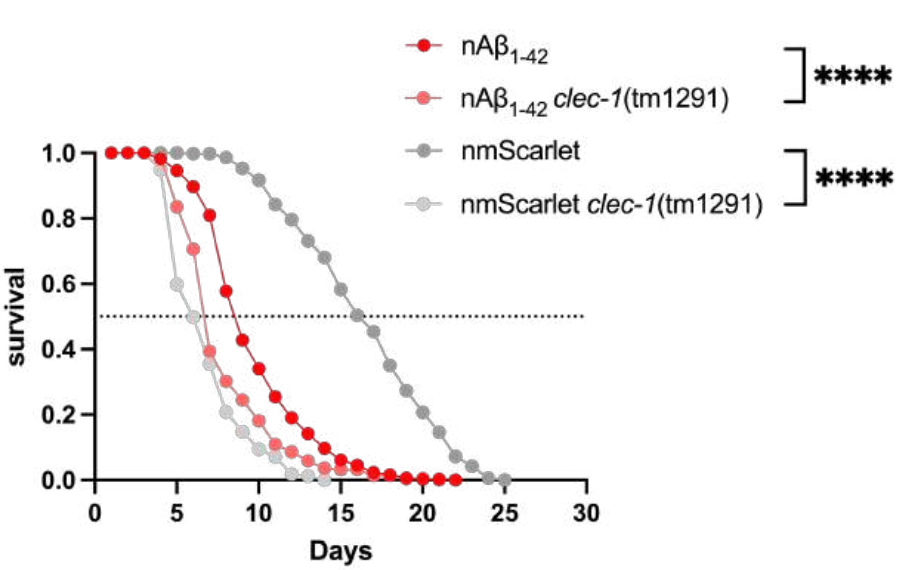

	Median (days)	Maximum (days)
nAβ1-42	8.9 ± 0.5	18.3 ± 2.5
nAβ1-42 *clec-1*(tm1291)	6.7 ± 0	19 ± 1.4
nmScarlet	16.5 ± 1	23.7 ± 0.6
nmScarlet *clec-1*(tm1291)	6.5 ± 0.6	13 ± 0

Figure 3.25*: lys-3 knockout improves organismal fitness of Aβ1-42 nematodes*

A Assessment of the lifespan of nAβ1-42, nAβ1-42 *lys-3*(tm2505), nmScarlet and nmScarlet *lys-3*(tm2505) animals. The graph shows the cumulative survival probability (survival) versus age (days alive) of nAβ1-42 (red), nAβ1-42 *lys-3*(tm2505) (burgundy), nmScarlet (grey) and nmScarlet *lys-3*(tm2505) (dark grey). Two to three independent cohorts of 120-180 nematodes each were analysed, and significance was tested by weighted Log-rank test (Fleming-Harrington Test) using the Oasis2 online tool (ns = $p > 0.05$; ** = $p \leq 0.01$). Average of the mean median lifespan ± SD and average maximum lifespan ± SD are shown in the table below.

B Developmental assay of nAβ1-42, nAβ1-42 *lys-3*(tm2505), nmScarlet and nmScarlet *lys-3*(tm2505) animals. The graph displays percentage of developmental stages of the nematodes within a population

at day 3 (left) and day 4 (right) of life. Three independent cohorts of 40-60 nematodes each were analysed.

C Assessment of the lifespan of nAβ_{1-42}, nAβ_{1-42} *clec-1*(tm1291), nmScarlet and nmScarlet *clec-1*(tm1291) animals. The graph shows the cumulative survival probability (survival) versus age (days alive) of nAβ_{1-42} (red), nAβ_{1-42} *clec-1*(tm1291) (salmon), nmScarlet (grey) and nmScarlet *clec-1*(tm1291) (light grey). Two to three independent cohorts of 120-180 nematodes each were analysed, and significance was tested by Log-rank test using Oasis2 online tool (**** = $p \leq 0.0001$). Average of the mean median lifespan ± SD and average maximum lifespan ± SD are shown in the table below.

lys-3 knockout increased the median lifespan of nAβ_{1-42} nematodes by about 1.1 days from 8.9 days (± 0.5) to 10 days (± 0.3), while the maximum lifespan remained unchanged (Figure 3.25 A). As expected, the median lifespan of nmScarlet *lys-3*(tm2505) nematodes (16.1 days (± 0.1) did not differ significantly from nmScarlet (16.5 days (± 1)). The developmental assay revealed an improvement of nAβ_{1-42} *lys-3*(tm2505) compared to nAβ_{1-42} nematodes (Figure 3.25 B). I analysed the developmental stages of individual nematodes within a population at two points. At day 3, nematodes of healthy strains such as nmScarlet or nmScarlet *lys-3*(tm2505) are mostly in the L4 larval stages or older. Both nmScarlet or nmScarlet *lys-3*(tm2505) exhibited approximately 70% L4 stage nematodes and 18% adult animals. In contrast, nAβ_{1-42} nematodes showed only about 14% L4 larvae and no adult animals. However, *lys-3* knockout in nAβ_{1-42} *lys-3*(tm2505) nematodes increased the percentage of L4 animals by 1.5-fold, from approximately 14% to 22%. At day 4, nematodes typically become adults, entering the fertile phase and laying eggs. nmScarlet and nmScarlet *lys-3*(tm2505) nematodes exhibited approximately 98% and 97% of adult animals, respectively, while only 11% of nAβ_{1-42}. animals reached adulthood. In contrast, a *lys-3* knockout more than doubled the number of adult animals from 11% to 23% compared to nAβ_{1-42}. Hence, knockout of *lys-3* ameliorates the systemic fitness defects of nAβ_{1-42} nematodes likely as a consequence of reduced Aβ_{1-42} aggregation.

Furthermore, I analysed the lifespan of nAβ_{1-42} *clec-1*(tm1291) and control nematodes to assess whether *clec-1* knockout causes a similar ameliorative effect on nAβ_{1-42} nematodes as *lys-3* knockout. However, the median lifespan of nAβ_{1-42} *clec-1*(tm1291) nematodes was further reduced by 2.2 days, from 8.9 days (± 0.5) to 6.7 days (± 0.0) (Figure 3.25 C). Additionally, nmScarlet *clec-1*(tm1291) nematodes exhibited a severe

reduction in median lifespan by 10 days, from 16.5 days (± 0.1) to 6.5 days (± 0.6), compared to nmScarlet. These severe impairments in the nematodes' lifespan, however, are due to the nature of the *clec-1* knockout itself rather than clec-1 affecting $A\beta_{1-42}$. clec-1(tm1291) mutant animals exhibited a median lifespan of 5.7 days (Figure 3.20 D). Therefore, in this assay, $nA\beta_{1-42}$ clec-1(tm1291) nematodes are not suitable for analysing the effect of clec-1 knockout on Aβ1-42-induced proteotoxicity.

4 DISCUSSION

4.1 Novel *C. elegans* model to study aggregation and proteotoxic effects of Tau^{P301L,V337M}

In this study, I generated and characterised two novel *C. elegans* Tau strains. One strain expresses Tau wild-type and the other a mutant variant of Tau bearing two patient-derived point mutations P301L and V337M (Tau^{P301L,V337M}) pan-neuronally (Dumanchin et al., 1998; Hutton et al., 1998; Poorkaj et al., 1998). Both mutations were shown to accelerate the aggregation of Tau into filaments, so I hypothesised that I would observe Tau^{P301L,V337M} aggregation in *C. elegans* (Goedert, 2005).

The pathology of human mutant Tau has been mimicked in *C. elegans* in several models (Kraemer et al., 2003; Fatouros et al., 2012; Morelli et al., 2018; Aquino Nunez et al., 2022). However, correlating aggregation of Tau with aging along with physiological impairments has not been possible in these models. To study Tau aggregation, previously published *C. elegans* Tau models relied on serial extraction. Based on solubility, Tau proteins were separated into soluble, detergent soluble or detergent insoluble fractions to characterise potential Tau aggregates. This method has however some limitations: i) it does not allow to analyse Tau aggregation in a living organism and ii) it involves nematode lysis. Extracting amyloidogenic proteins from *C. elegans* is also technically challenging. Tau can easily aggregate during the extraction process itself and thereby creating artefacts. To overcome these obstacles, I used a substoichiometric labelling approach to enable simultaneous aggregation and visualisation of Tau in the living animal. Tau is fluorescently labelled in a substoichiometric manner. This approach allows simultaneous visualisation of Tau expression by fluorescence microscopy and its aggregation in the living animal. The substoichiometric labelling approach has been already successfully employed in *C. elegans* to study another amyloidogenic protein, Aβ_{1-42} (Gallrein et al., 2021). It has been observed that earlier models aiming to fuse the Aβ peptide to GFP only formed oligomers *in vitro* and did not exhibit aggregation *in vivo* (Ochiishi et al., 2016). My generated model overcomes these obstacles by allowing *in situ* and *in vivo* monitoring of Tau^{P301L,V337M} aggregation using the cutting-edge technique FLIM. Through FLIM, I was able to detect Tau^{P301L,V337M} aggregation with the progression of aging.

The aggregation of Tau^{P301L,V337M} in the novel *C. elegans* model elicits multiple disease-related phenotypes observed in behavioural assays. These ranged from defects in overall organismal fitness, with reduced lifespan and fecundity to impaired motility and deficits in neuronal function as reflected by compromised chemotaxis. My observations align with previous *C. elegans* Tau models that reported defects in lifespan, fecundity and motility as well (Fatouros et al., 2012; Kraemer et al., 2003; Miyasaka et al., 2005; Morelli et al., 2018; Pir et al., 2016). What still remains to be elucidated is whether Tau^{P301L,V337M} causes structural degeneration of neurons or abnormalities in neuronal morphologies. Indeed, accumulation of insoluble, mutant Tau (Tau^{P301L} or Tau^{V337M}) and an insoluble aggregation-prone Tau variant (Tau$^{F3\Delta K280}$) was observed along with degenerated axons and axonal discontinuities (gaps) in previous *C. elegans* Tau models (Kraemer et al., 2003; Fatouros et al., 2012). Abnormal branching of axons occurred in mutant Tau-expressing nematodes (Tau^{P301L} or Tau^{R406W}) (Miyasaka et al., 2005). However, previous models did not report on neurodegeneration with the progression of aging and its correlation with the aggregation-propensity of Tau. My generated model could fills this gap as it allows to measure neurodegeneration in parallel to an analysis of Tau^{P301L,V337M} aggregation by FLIM and thus allows to establish a temporal sequence of pathogenesis.

Tau is known to propagate to other tissues, which is a common feature of Tau pathology in AD (Fares & Greenwald, 2001; Jucker & Walker, 2013). I demonstrated that Tau^{P301L,V337M} propagates from its tissue of expression (neurons) to other tissues through a yet unknown mechanism. Tau^{P301L,V337M} was found in the body cavity of the animals and in phagocytic vacuoles of the coelomocytes. The exact Tau^{P301L,V337M} species (i.e., monomers, oligomers, aggregates) secreted from the neurons and that accumulate in the coelomocytes have not yet been identified. However, I speculate that these species are small oligomers, as they have been shown to efficiently exit neurons via secretory pathways (Brunello et al., 2020; Amro et al., 2021). The uptake of Tau^{P301L,V337M} by the coelomocytes could be a potential clearance mechanism for Tau. Indeed, it has been observed that coelomocytes are capable of degrading endocytosed proteins like GFP (Fares & Greenwald, 2001). I observed higher amounts of Tau^{P301L,V337M} in coelomocytes compared to the non-aggregating Tau^{WT}. This suggests that the aggregation of Tau^{P301L,V337M} might enhance intracellular aggregation by propagation transcellularly in a prion-like manner.

The disease-related behavioural impairments correlated with the onset of aggregation in the nTau^{P301L,V337M} strain indicating that the observed physiological deficits are a consequence of Tau^{P301L,V337M} aggregation. In nTau^{WT} nematodes, I did not observe protein aggregation but I could still note an impairment in lifespan, fecundity and motility in aged animals. These detrimental effects of Tau^{WT} were only observed in assays that are based on longer periods of the nematodes' life and on older animals. Therefore, the phenotypes in nTau^{WT} animals are independent of aggregation but might result from pan-neuronal ectopic expression of Tau^{WT}. Similar effects were also shown in previous Tau *C. elegans* models, where the expression of wild-type Tau exerted detrimental effects on lifespan, motility and neurodegeneration (Chew et al., 2013; Pir et al., 2016). Notably, Pir and co-authors demonstrated that overexpression of wild-type Tau in neurons causes toxic effects that manifest at an older age. Additionally, these pathologic phenotypes were dose-dependent, with nematodes showing lower Tau^{WT} expression being less affected.

ptl-1, the only *C. elegans* Tau orthologue, is a microtubule-stabilizing protein responsible for neuronal integrity. Its loss is associated with reduced lifespan (Chew et al., 2013; Yogev et al., 2016). Hence, a potential interaction between Tau^{WT} and the endogenous *C. elegans* Tau PTL-1 could be responsible for the toxicity of Tau^{WT} expression. As PTL-1 and human Tau have a sequence homology of around 50% in their microtubule-binding domains (Goedert et al., 1996), I hypothesised that Tau^{WT} could compensate for the loss of PTL-1. However, my attempt to rescue the lifespan deficits of *ptl-1* mutants by expressing human Tau^{WT} showed the opposite and even worsened the phenotype. I conclude that human Tau^{WT} is insufficient to compensate for the loss of PTL-1 with regards to the whole organismal fitness and negatively affects it when present alongside endogenous PTL-1. It remains to be shown whether pan-neuronally expressed Tau^{WT} could rescue neuron-specific deficits, such as touch sensitivity observed in *ptl-1* mutants. Furthermore, the gene dosage of *ptl-1* is crucial, as both *ptl-1* knockout and overexpression caused detrimental effects (Chew et al., 2013). Hence, the expression levels of pan-neuronal human Tau^{WT} could be too high and should be adjusted to the endogenous expression levels of PTL-1.

In conclusion, I have generated two novel pan-neuronal Tau expressing strains. The nTau^{WT} strain exhibited as expected no aggregation; however, it exerted impairments

of lifespan, fecundity and motility in older animals due to a yet unknow, aggregation-independent mechanism. Therefore, nTau^{WT} should not be used as a control alongside nTau^{P301L,V337M} and data of nTau^{WT} should be interpreted carefully. Instead, I suggest the nmScarlet strain as a more suitable control for nTau^{P301L,V337M}, as it shows no deficits in behaviour. The nTau^{P301L,V337M} shows instead severe Tau aggregation and pronounced physiological defects. This model serves as a promising tool that could be used to investigate the role of potential chaperones and other proteins in modulating Tau aggregation and proteotoxicity. Indeed, numerous proteins have been shown to influence Tau aggregation (Nachman et al., 2020; Irwin et al., 2021; Saha et al., 2023).

4.2 Decline in neuronal activity precedes aggregation of Aβ_{1-42} and Tau^{P301L,V337M}

This work demonstrated that the loss of neuronal activity precedes the aggregation of Aβ_{1-42} and Tau^{P301L,V337M} in *C. elegans* models. To measure neuronal activity and correlate it to aggregation, I quantified the fluorescence intensity levels of the pan-neuronally expressed calcium reporter GCaMP6m in nematodes exhibiting Aβ_{1-42} and Tau^{P301L,V337M} aggregation. Since GCaMP measurements are typically challenging due to the nematodes' motility, I used specially designed microfluidic chambers that restrict movement and enable high-throughput GCaMP imaging. Thus far, the usage of microfluidic tools in *C. elegans* research is not novel to the field (Midkiff & San-Miguel, 2019; San-Miguel & Lu, 2013; Levine & Lee, 2020). However, unfortunately, most of the available approaches rely on specialised equipment, reducing accessibility and preventing manual operation in the lab (Hulme et al., 2007; Mondal et al., 2016). In contrast, the microfluidic system used in these studies is superior due to its simple application and ease of use. It allows imaging of up to 16 nematodes in parallel and permits the release of the animals post-imaging, enabling investigations throughout their lifespan.

GCaMP calcium imaging in *C. elegans* is usually performed with temporal resolution. This means nematodes are imaged for extended periods and changes in fluorescence intensity - usually as referred to ΔF – are analysed over time (Larsch et al., 2013; Schrödel et al., 2013). However, this approach requires the use of specific bioinformatic pipelines, complicating the analysis part. My established method

eliminates this drawback. Quantification of the neuronal GCaMP6m fluorescence intensity is performed from a single confocal image using the publicly available imaging software Fiji (Schindelin et al., 2012), rather than a complex bioinformatic pipeline. This allows to assess neuronal activity from a single snapshot, proving a simpler and more straightforward approach than employing complex bioinformatic tools.

However, since the GCaMP6m reporter is expressed pan-neuronally, I could only assess neuronal activity at a systemic level. To further explore neuronal decline upon $A\beta_{1-42}$ and $Tau^{P301L,V337M}$ aggregation, expressing the GCaMP6m reporter in single neurons or specific neuronal circuits might be promising. Neuronal activity in selected neurons might differ from the systemic analysis, as specific neurons could be more or less affected by their aggregation load. For example, the IL2 neurons in *C. elegans* were shown to be the most vulnerable to $A\beta_{1-42}$, suggesting these neurons might be less active than others upon $A\beta_{1-42}$ expression. Another approach would be to express the GCaMP6m reporter in cholinergic neurons regulated by a specific promoter such as *unc-17*. This would allow to assess neuronal activity only in neurons using acetylcholine as a neurotransmitter. Cholinergic neurons predominantly degenerate within the nucleus basalis of Meynert in the basal forebrain of AD patients (Whitehouse et al., 1981). This brain region is crucial for memory formation and preservation.

I observed that neuronal activity declines already in young adult animals, early in the progression of AD pathology. These observations were reflected not only by GCaMP6m fluorescence intensity measurements but also strengthened by chemotactic defects in both $nA\beta_{1-42}$ and $nTau^{P301L,V337M}$ strains in young adult nematodes (Gallrein et al., 2021; this study).These results were surprising, as various previous studies in mice and humans established that neuronal hyperactivity occurs in the early, pre-symptomatic stages of AD pathology (Stargardt et al., 2015; Targa Dias Anastacio et al., 2022). Aberrant neuronal hyperexcitability was reported in the cortex and hippocampus of murine AD models, which are genetically modified to express AD-related mutations, most commonly in the *APP* or *PSEN1* gene (Busche et al., 2003; Palop et al., 2007; Šišková et al., 2014; Lerdkrai et al., 2018). The introduction of these manipulated genes is usually associated with increased levels of the Aβ peptide, plaque formation of Aβ and/or Tau, and memory and cognitive deficits.

Hyperexcitability of neurons is linked to Aβ oligomers. It was shown that local application of soluble Aβ dimers through direct injection into the mices' brain induced neuronal hyperactivity before the formation of Aβ plaques in an AD mouse model (Busche et al., 2012). Mechanistically, Aβ-dependent hyperactivity is associated with abnormal glutamate release and reuptake, dysfunction of ion channels and impaired inhibitory GABAergic interneuron function (Busche & Konnerth, 2016; Palop & Mucke, 2016) ultimately disrupting the excitatory-inhibitory balance between distinct areas of the brain (Giorgio et al., 2024). In a mouse model expressing human Tau^{P301L}, hyperexcitability of neurons was observed even before the formation of NFTs (Crimins et al., 2012). On the other hand, hypoactivity – a decrease in neuronal function as observed in my studies – is typically observed later during AD progression in AD mouse models and was shown to coincide with memory loss and the onset of physiological symptoms (Fu et al., 2017; Hatch et al., 2017). Moreover, reduction of neuronal function manifested when amyloid fibrils and aggregates were already formed. Hence, I believe that the *C. elegans* models used in my studies might not represent all aspects of AD onset and progression. Due to the simplicity of the *C. elegans* nervous system, factors that contribute to neuronal hyperexcitability in humans and higher animal models might be missing in *C. elegans*. However, I could clearly connect the onset of $Aβ_{1-42}$ and $nTau^{P301L,V337M}$ aggregation with neuronal decline by measuring the fluorescence intensities of the GCaMP6m calcium reporter. It needs to be clarified whether the neuronal activity in $Aβ_{1-42}$ and $nTau^{P301L,V337M}$ -expressing animals younger than those analysed is altered and whether hyperexcitability could perhaps be observed during larval development.

Surprisingly, the expression of $Aβ_{1-42}$ in muscle tissue exhibited the same detrimental effect on neuronal activity as $Aβ_{1-42}$ expression in neurons. This raises the question: How can proteotoxic stress originating from the muscle tissue affect neuronal activity? $mAβ_{1-42}$ nematodes showed severe aggregation with $Aβ_{1-42}$ spreading from muscles to distal tissues such as the hypodermis, along with physiological impairments (Gallrein et al., 2021). Given that $Aβ_{1-42}$ can evade its tissue of expression and severely rupture plasma membranes, $Aβ_{1-42}$ could propagate from muscle to neuronal cells. The invading $Aβ_{1-42}$ species then likely exert a toxic effect on neuronal activity. Additionally, spreading of $Aβ_{1-42}$ from muscle tissue to neurons and the subsequent reduction of

neuronal activity could occur through neuromuscular junctions, which provide a direct contact between sensory neurons and muscle tissue. Another possible explanation is the involvement of transcellular signalling pathways that transmit muscle tissue proteotoxicity to neurons without $A\beta_{1-42}$ being actually present in the neurons (van Oosten-Hawle et al., 2013; Miles et al., 2023; van Oosten-Hawle, 2023). In *C. elegans*, a myosin temperature-sensitive mutation in muscle cells induced expression of the chaperone HSP90 not only in muscle cells but also in peripheral tissue such as the intestine, regulated by the FoxA transcription factor PHA-4. The resulting increased HSP90 levels throughout the whole animal have been shown to be beneficial for muscular myosin folding. This raises the questions of whether $A\beta_{1-42}$ induced proteotoxic stress in muscles affects neurons, leading to reduced neuronal activity. However, signalling from muscles to neurons in *C. elegans* has not been reported yet. In *Drosophila,* an insulin-dependent signalling pathway through FOXO/4E-BP regulation in muscle tissue delays accumulation of protein aggregations in fly brains. These findings support a potential signalling cascade regulating cell-nonautonomous proteostasis mechanisms between muscle tissue and neurons in *Drosophila*.

Notably, I also observed reduced neuronal activity in the Tau^{WT}-expressing strain that however varied with aging. $nTau^{WT}$ nematodes did not exhibit aggregation or Tau propagation, but showed impairments in lifespan, fecundity and motility. These neuronal activity data further support that ectopic Tau^{WT} expression in the nervous system of *C. elegans* causes toxicity and alters the animals' physiology independent of aggregation.

4.3 LYS-3 and CLEC-1 modulate $A\beta_{1-42}$ aggregation and propagation

My data showed that the extracellular modifiers (ECMs) LYS-3 and CLEC-1 modulate $A\beta_{1-42}$ aggregation in a *C. elegans* model. The progression of neurodegenerative disorders is linked to the accumulation of aberrant proteins, with extracellular Aβ aggregation being a pathological hallmark of Alzheimer's disease. While the exact mechanism leading to AD onset remains unknown, studies suggest that Aβ aggregation contributes to proteotoxicity. Thus, preventing or delaying Aβ aggregation could be a potential therapeutic approach (Hampel et al., 2021).

For decades, research has focused on understanding the intracellular proteostasis network, which includes the interplay between chaperones, co-chaperones and protein degradation systems like autophagy and the ubiquitin-proteasome system (UPS). Intracellular chaperones play a crucial role in the proteostasis network by inhibiting and reversing aberrant protein associations and refolding misfolded protein. As such, they are of special interest as therapeutic targets in neurodegenerative disease (Sharma et al., 2024). However, our understanding of the mechanism and chaperones that maintain proteostasis in the extracellular space remains limited (Satapathy & Wilson, 2022; Braun, 2023). While extracellular proteostasis had never been addressed in *C. elegans* before, a recent publication of potential extracellular modifiers advanced the possibilities of exploring the process in a simple, yet powerful animal model (Gallotta et al., 2020). My studies aimed to use this opportunity by analysing the effect of two promising ECMs, LYS-3 and CLEC-1, in an Aβ_{1-42} *C. elegans* model. I manipulated the abundance of these ECMs by genetic knockout in the Aβ_{1-42}-expressing nematodes using two distinct loss-off-function mutants, which were previously employed by Gallotta et al., 2020. My data indicate that *lys-3* or *clec-1* knockout ameliorates Aβ_{1-42} aggregation in whole head- and IL2 neurons of *C. elegans*. These findings were surprising, as previous data revealed that *lys-3* or *clec-1* knockout exerts a detrimental effect on the aggregation of the *C. elegans* endogenous, aggregation-prone lipid-binding protein 2 (LBP-2) (Gallotta et al., 2020). LBP-2 was observed to be a secreted protein with high abundance in the extracellular space that becomes increasingly insoluble in strong-detergent buffers with aging (David et al., 2010). Puncta formation of LBP-2 endogenously tagged with red fluorescent protein (RFP) increased with aging and revealed LBP-2 aggregation in the living animals. However, it was not further analysed whether LBP-2 aggregates consist of a proper β-sheet-rich structure typically observed for amyloidogenic proteins (i.e Aβ, Tau, Huntingtin etc.) associated with neurodegenerative disease. Hence, LBP-2 aggregation may not properly recapitulate pathogenic protein aggregation as it is observed in the Aβ_{1-42} *C. elegans* model used for this study. Consequently, the effects of the ECMs LYS-3 or CLEC-1 on the aggregation of either LBP-2 or Aβ_{1-42} can differ. My initial hypothesis was that *lys-3* or *clec-1* knockout would aggravate Aβ_{1-42} aggregation, which would be detrimental for the nematodes. Surprisingly, my data

showed the opposite. The raises the question: How can the ECMs LYS-3 and CLEC-1 increase $A\beta_{1-42}$ aggregation? A possible explanation could arise from the involvement of ECMs in $A\beta_{1-42}$ spreading and propagation. Spreading and propagation of amyloidogenic proteins between cells can occur as a consequence of disaggregation (Nachman et al., 2020; Tittelmeier et al., 2020; Saha et al., 2023). Molecular chaperones can effectively disaggregate or break down Tau or α-synuclein fibrils, producing oligomeric, spreading-competent protein species. These species can act as seeds in secondary nucleation events, thus exacerbating aggregation. Oligomeric protein species readily spread between neurons and other tissue, increasing aggregation across cells. Consequently, protein aggregation is not necessarily beneficial, especially in animal models like *C. elegans,* and can be a double-edged sword in neurodegenerative disease (Tittelmeier et al., 2020). Notably, I demonstrated that *lys-3* and *clec-1* knockout reduced $A\beta_{1-42}$ spreading, as evidenced by lower $A\beta_{1-42}$ levels in coelomocytes. This suggest that the presence of ECMs LYS-3 and CLEC-1 promotes $A\beta_{1-42}$ spreading, which in turn accelerates aggregation. The reduced amyloidogenic burden upon *lys-3* knockout led to an amelioration of lifespan and developmental defects. Interestingly, LYS-3 appears more effective in younger animals, as only the median lifespan changed, but not the maximum lifespan. This suggests a detrimental role of the LYS-3 ECM on $A\beta_{1-42}$ aggregation and proteotoxicity. Phenotypic analysis of *clec-1* knockout $A\beta_{1-42}$ nematodes did not yield meaningful insights as *clec-1* mutant animals already exhibit a strong pathogenic phenotype on their own. Therefore, while *clec-1* mutants are not suited for phenotypic analysis, CLEC-1 still proved to be detrimental for $A\beta_{1-42}$ aggregation.

Intracellular chaperones of the proteostasis machinery disaggregate and supress aggregation in an ATP-dependent manner (Scior et al., 2018; Nachman et al., 2020; Tittelmeier et al., 2020; Ayala Mariscal et al., 2022). While there is evidence of intracellular chaperones being secreted and present in the body fluids, it is unlikely that these are involved in fragmenting and refolding extracellular misfolded proteins. The extracellular space presents unique challenges: low and fluctuating pH, low ATP availability and low protein density making protein interactions challenging (Chaplot et al., 2020). Shear stress, oxidative stress and pathogen invasion further complicate the functionality of the proteostasis system in this environment (Wyatt et al., 2013). Given

these harsh conditions, extracellular chaperones are thought to act as “holdases” – preventing protein aggregation and precipitation of proteins without actively refolding or disaggregating them (Chaplot et al., 2020). By binding to exposed hydrophobic regions of misfolded proteins, extracellular chaperones keep proteins soluble, allowing them to be cleared from the extracellular space and internalised by receptive cells. This internalisation occurs through specific membrane-bound cell surface receptors. Once inside, these protein species can be refolded or degraded through the autophagy or the UPS system (Wyatt et al., 2013; Chaplot et al., 2020). I speculate that CLEC-1 and LYS-3, as extracellular modifiers, could have a holdase-like function. They might sequester small $A\beta_{1\text{-}42}$ species, which are then targeted for internalisation to neighbouring cells and neurons. In recipient neurons, these internalised oligomers could act as seeds, enhancing $A\beta_{1\text{-}42}$ aggregation instead of being degraded. To support this hypothesis, it needs to be clarified if and how LYS-3 and CLEC-1 can bind to $A\beta_{1\text{-}42}$, and whether other proteins are involved in this interaction.

The potential role of LYS-3 and CLEC-1 as ECMs in *C. elegans* is novel and previously undescribed. Gallotta and co-authors provided the first evidence of LYS-3 and CLEC-1 as modulators for extracellular protein aggregation. Generally, protein functions of LYS-3 and CLEC-1 are poorly understood and are scarcely characterised in existing literature. Of the two, only CLEC-1 has predicted human orthologues, such as several proteins that belong to the class of C-type lectins. CLEC-1 contains a C-type lectin fold that typically facilitates glycan-binding activity through its carbohydrate-recognition domain (CRD), which is conserved among different C-type lectin classes. In general, proteins containing C-type lectin folds have a wide range of functions and are thought to act as adhesion and signalling reporters in the immune system, as well as having endocytic reporter function. In their role as transmembrane proteins, they bind glycosylated, soluble ligands that are internalised through clathrin-mediated endocytosis and targeted to the endolysosomal pathway (Cummings et al., 2022). While some of the CLEC-1 orthologues have been implicated in AD pathology, a clear link to $A\beta$ remains elusive. However, the presence of the C-type lectin domain and its functionality as an endocytic receptor at the cell surface allows speculation as to whether CLEC-1 functions in binding and targeting $A\beta_{1\text{-}42}$ to the intracellular space. For LYS-3, it remains unclear whether specific human orthologues exist and how these

proteins might be related to AD pathology, Aβ aggregation and proteotoxicity. LYS-3 is one of ten lysozymes expressed in *C. elegans* and is involved in the stress response to copper ions. It is upregulated in response to stress in a KGB-1 dependent manner (Hattori et al., 2013). KGB-1 is *C. elegans* homologue of a c-Jun N-terminal kinase (JNK), a subgroup of mitogen-activated protein kinases (MAPKs) (Mizuno et al., 2004). Protein fold prediction of LYS-3 by Phyre2 suggests the presence of a hydrolysis and triose-phosphate isomerase (TIM) β/α-barrel fold, but this does not allow any conclusion to be drawn as to how LYS-3 specifically functions as an ECMs.

Despite the vague and speculative nature of LYS-3 and CLEC-1 functions in exisiting literature, I could show that knockout of *lys-3* or *clec-1* decreases $A\beta_{1-42}$ aggregation This effect could result from LYS-3 and/or CLEC-1 being involved in $A\beta_{1-42}$ spreading and propagation through a holdase chaperone function, or from other yet uncharacterised functions. My findings have advanced the understanding of extracellular proteostasis on amyloidogenic proteins within the context of neurodegenerative disease and showcased the utility of *C. elegans* for this research. However, further investigations are necessary to gain a more mechanistic view of ECM function and to clarify whether extracellular chaperones positively or negatively affect the progression and proteotoxicity of protein aggregation.

5 MATERIAL

5.1 Chemicals and solutions

Table 5.1: *List of chemicals used in this study.*

Name	Manufacturer
Acetic acid	VWR, Radnor, USA
Agar	Carl Roth, Karlsruhe, Germany
Agarose	Biozym, Oldendorf, Germany
Agarose universal	Bio&SELL, Nürnberg, Germany
Ammonium peroxodisulphate (APS)	SERVA Feinbiochemica, Heidelberg, Germany
Ampicillin	Sigma Aldrich, St. Louis, USA
Bacto Peptone	Carl Roth, Karlsruhe, Germany
Benzaldehyde	Carl Roth, Karlsruhe, Germany
Boric acid	Carl Roth, Karlsruhe, Germany
Bromphenol blue	Merck, Darmstadt, Germany
Calcium chloride	Sigma Aldrich, St. Louis, USA
Cholest	Sigma Aldrich, St. Louis, USA
Coomassie Brilliant Blue G-250	Serva Feinbiochemica, Heidelberg, Germany
Dimethyl sulfoxide (DMSO)	Carl Roth, Karlsruhe, Germany
Disodium phosphate	Merck, Darmstadt, Germany
Dithiothreitol	Carl Roth, Karlsruhe, Germany
Eryhtrosin B	Sigma Aldrich, St. Louis, USA
Ethanol	Chemsolute
Ethidium bromide	Carl Roth, Karlsruhe, Germany

Ethylenediaminetetraacetic acid (EDTA)	Carl Roth, Karlsruhe, Germany
Glucose	Carl Roth, Karlsruhe, Germany
Glycerol	Carl Roth, Karlsruhe, Germany
Glycine	Carl Roth, Karlsruhe, Germany
Gold powder 0.3 – 3 µm	chemPUR, Karlsruhe, Germany
Hydrochloric acid (37%)	VWR, Radnor, USA
Kanamycin	Carl Roth, Karlsruhe, Germany
Magnesium chloride	Carl Roth, Karlsruhe, Germany
Magnesium sulphate	Carl Roth, Karlsruhe, Germany
Methanol	VWR, Radnor, USA
Milk powder	Carl Roth, Karlsruhe, Germany
Mono- & dipotassium phosphate	Merck, Darmstadt, Germany
Mono- & disodium phosphate	Carl Roth, Karlsruhe, Germany
Nemadipine A	Abcam, Cambridge, UK
Nuclease-free water	Sigma Aldrich, St. Louis, USA
Polybead Microspheres 0.1 µm	Polyscience, Inc., Warrington, USA
Polyvinylpyrrolidone	Merck, Darmstadt, Germany
Potassium chloride	Merck, Darmstadt, Germany
Potassium hydroxide	Merck, Darmstadt, Germany
Rotiphorese Gel 30 (37.5:1)	Carl Roth, Karlsruhe, Germany
Sodium azide	Carl Roth, Karlsruhe, Germany
Sodium chloride	Carl Roth, Karlsruhe, Germany
Monosodium phosphate	Merck, Darmstadt, Germany
Sodium dodecyl sulphate (SDS)	Carl Roth, Karlsruhe, Germany

Sodium hydroxide	Carl Roth, Karlsruhe, Germany
Spermidine	Sigma Aldrich, St. Louis, USA
SYLGARD® 184 Silicone Elastomer	Dow Chemical Company, Midland, USA
SYLGARD® 184 Silicone Elastomer Curing Agent	Dow Chemical Company, Midland, USA
Tetramethylethylenediamine (TEMED)	Merck. Darmstadt, Germany
Triton X-100	Sigma Aldrich, St. Louis, USA
Tris(hydroxymethyl)aminomethane (Tris) hydrochlorid	Carl Roth, Karlsruhe, Germany
Tris	Merck, Darmstadt, Germany
Tryptone	AppliChem, Darmstadt, Germany
Tween 20	Serva Feinbiochemica, Heidelberg, Germany
Yeast extract	Carl Roth, Karlsruhe, Germany

5.2 Buffers

Table 5.2: *List of buffers used for this study.*

Name	Composition
Coomassie staining solution *Used for: SDS-PAGE*	2.5% (v/v) Coomassie brilliant blue G-250 40% (v/v) Methanol 10% (v/v) Acetic acid
Destaining solution *Used for: SDS-PAGE*	40% (v/v) Ethanol 10% (v/v) Acetic Acid
4x Laemmli loading buffer *Used for: SDS-PAGE, nematode lysis*	100 mM Tris-HCl (pH 6.8) 4% (w/v) SDS 30% (v/v) Glycerol

	0.2% (w/v) Bromphenol blue 100 mM DTT
1x M9 buffer *Used for: Washing of nematodes, Thrashing assay*	6 g/l Na_2HPO_4 3 g/l KH_2PO_4 5 g/l $NaCl_2$ + 1 ml 1 M $MgSO_4$ after autoclaving
PVP solution	100 mg/l PVP 99.5 (v/v) Ethanol
10x SDS-PAGE running buffer *Used for: SDS-PAGE*	25 mM Tris-HCl (pH 8.8) 192 mM Glycine 0.1 % (w/v) SDS
Separation gel buffer *Used for: SDS-PAGE*	1.5 M Tris-HCl (pH 8.8) 0.04% (w/v) SDS
Stacking gel buffer *Used for: SDS-PAGE*	0.5 M Tris-HCl (pH 6.8) 0.04% (w/v) SDS
5x TBE *Used for: Agarose gel electrophoresis*	445 mM Tris 445 mM Boric acid 10 mM EDTA
10x TBS *Used for: Western blot*	200 mM Tris 1.5 M NaCl
10x TBS-T *Used for: Western blot*	200 mM Tris 1.5 M NaCl 1% (v/v) Tween 20

1x Transfer buffer (semi-dry blotting) *Used for: Western blot*	1x Turbo Transfer buffer 20% (v/v) Ethanol

5.3 Growth media

Table 5.3: *List of growth media used for this study.*

Name	Composition
1x Lysogeny broth (LB) agar *Used for: Transformation, bacterial growth*	15 g/l Agar 10 g/l Tryptone 5 g/l Yeast extract 5 g/l NaCl + 100 mg/ml Ampicillin (optional) + 25 mg/ml Kanamycin (optional) after autoclaving before casting
1x LB medium *Used for: Transformation, bacterial growth*	10 g/l Tryptone 5 g/l Yeast extract 5 g/l NaCl + 100 mg/ml Ampicillin (optional) + 25 mg/ml Kanamycin (optional) after autoclaving
Nematode growth medium (NGM) agar *Used for: Nematode culture*	50 mM NaCl 2.5 g/l Bacto Peptone 17 g/l Agar + 1 mM $CaCl_2$ + 1mM $MgSo_4$ + 5 µg/ml Cholesterol + 25 mM KH_2PO_4 (pH 6.0) + 2 µM Nemadipine A (optional) after autoclaving before casting

Super Optimal broth with Catabolite repression (SOC) medium *Used for: Transformation*	20 g/l Tryptone 5 g/l Yeast extract 1 M NaCl 1 M KCl + 2 M $MgCl_2$ / $MgSO_4$ buffer + 2 M Glucose after autoclaving

5.4 Kits

***Table 5.4**: List of kits used for this study.*

Product	Company	Usage
GeneJET Plasmid Miniprep Kit	Thermo Fisher Scientific, Waltham, USA	Plasmid isolation
Gibson Assembly Cloning Kit	New England Biolabs, Ipswich, USA	Gibson cloning
NucleoBond Xtra Midi kit	Macherey-Nagel, Düren, Germany	Plasmid isolation
Phire Tissue Direct PCR Master Mix	Thermo Fisher Scientific, Waltham, USA	Nematode genotyping
Phusion High-Fidelity PCR Kit	New England Biolabs, Ipswich, USA	Polymerase chain reaction (PCR)
Pierce ECL Plus Western Blotting Substrate	Thermo Fisher Scientific, Waltham, USA	Western blot detection
QIAquick PCR Purification Kit	Qiagen, Hilden, Germany	PCR purification

Trans-Blot Turbo RTA Mini 0.2 µm Nitrocellulose Transfer Kit	Bio-Rad, Hercules, USA	Western blot transfer

5.5 Enzymes

5.5.1 Restriction enzymes

***Table 5.5:**. List of restriction enzymes used for this study.*

Enzyme	Manufacturer
NcoI (+ Tango buffer)	Thermo Fisher Scientific, Waltham, USA
ApaI (+ Tango buffer)	Thermo Fisher Scientific, Waltham, USA

5.5.2 Other enzymes

***Table 5.6:** List of other enzymes used for this study.*

Enzyme	Manufacturer
Phusion High-Fidelity DNA Polymerase + High-Fidelity buffer	New England Biolabs, Ipswich, USA

5.6 Ladders and loading dyes

***Table 5.7**: List of ladders and loading dyes used for this study.*

Product	Manufacturer
DNA loading dye (6x)	Thermo Fisher Scientific, Waltham, USA
GeneRuler 1 kb DNA ladder	Thermo Fisher Scientific, Waltham, USA
GeneRuler 50 bp DNA ladder	Thermo Fisher Scientific, Waltham, USA
PageRuler Plus Prestained Protein Ladder	Thermo Fisher Scientific, Waltham, USA

5.7 Antibodies

5.7.1 Primary antibodies

Table 5.8: *List of primary antibodies used for this study.*

Antibody	Origin	Dilution	Source
α-GAPDH monoclonal	Mouse	1:20000	Proteintech, Rosemont, USA
α-GFP (B34) monoclonal	Mouse	1:2000	Enzo Life Science. Farmingdale, USA

5.7.2 Secondary antibodies

Table 5.9: *List of secondary antibodies used in this study.*

Antibody	Origin	Dilution	Source
Goat IgG anti-Mouse IgG (H+L)-HRPO	Goat	1:10000	Dianova, Eching, Germany

5.8 Primer sequences

All primer sequences are given in 5' end → 3' end direction. Primer were ordered through Biomers, Ulm, Germany. Primer working concentration stocks were 10 mM, 500 nM were used for PCR and 5 mM were used for sequencing reactions.

Primers for cloning

***Table 5.10**: List of primers for cloning used in this study.*

Primer Name	Sequence
Mt_IRES-wrmSca_fwd	gcagggtttgtaaaccggttgctctccc
Mt_IRES-wrmSca_rev	gctcagcggagctagccttgtagagctc
Mt_Vektor w/o ScaBeta_fwd	gctcagccatcccggtcgtcgtcgtcgt
Tau Mt (Methionine)_fwd	gacgaccgggatggctgagccccgccag
Tau Mt (Methionine)_rev	aaccggtttacaaaccctgcttggccagg
Tau Mt w/o Serine_fwd	caaggctagctccgctgagccccgccaggag
Tau Mt w/o Serine_rev	tctcgagctacaaaccctgcttggccaggg
Tau Wt (Serine)_fwd	caaggctagctccgctgagccccgccag
Tau Wt (Serine)_rev	gtatctcgagtcacaaaccctgcttggccagg
Tau Wt w/o ATG_fwd	gacgaccgggatggctgagccccgccaggag
Tau Wt w/o ATG_rev	agcaaccggttcacaaaccctgcttggccag
Vektor w/o ScaBeta_rev	gctcagccatcccggtcgtcgtcgtcgt
Wt_IRES-mSca_fwd	gggtttgtgaaccggttgctctccctcac
Wt_IRES-mSca_rev	gctcagcggagctagccttgtagagctcgtc
Wt_Vektor w/o ScaBeta_fwd	gggtttgtgactcgagatacccagatcatatgaaacggc

5.8.1 Primers for sequencing

***Table 5.11**: List of sequencing primers used in this study.*

Primer Name	Sequence
pPD95-77 SeqPrimer_rev	gtgtcttgtagttcccgtcatc
rgef-1 SeqPrimer_fwd	tcagaccattaccaacgttctttc
Seq_wrmScarlet_rev	ccttgaaacgcatgaactc
wrmSca SeqPrimer_fwd	acaccgtcgtcgagcaatac
SeqPrimer_unc-13_n2813_for	gaaacaactgccgaatgcca
SeqPrimer_unc-13_n2813_rev	tggttgctcttgacttggga

5.8.2 Primers for genotyping

***Table 5.12**: List of primers for genotyping used in this study.*

Primer Name	Sequence
clec-1_tm1291_for	ccggtttcctaacttgaggt
clec-1_tm1291_rev	atttaagagcggtgacgcat
dod-21_ok1569_for	aagagccccatgtattgcac
dod-21_ok1569_rev	tcgtggttttccgagttttc
FX544_tm544_for	catcgaagaacaacacgcaa
FX544_tm544_rev	acataatggcctcggttcca
FX659_tm659_for	tttaaccatggcctcagttc
FX659_tm659_rev	ttcaaatcgagatcggcgga-
lys-3_tm2505_rev	gtctgcccacattcaactaa
lys-3_tm5205_for	cccacgttcagaggcgaatt
ptl-1_ok621_for	cctcctaccacccatctgaa
ptl-1_ok621_rev	caacatgctcagggaagtca
tag-196_ok822_for	ccttgggagacaccacaact
tag-196_ok822_rev	cctgcactccacacacattc
unc-13_n2813_for	tgaccactttggaaccccat
unc-13_n2813_rev	gcatcggagtttcagtattctgtt

5.9 Plasmids

Table 5.13: *List of plasmids used for this study.*

Name	Insert	Resistance	Origin
pN1 FLTau0N4RLM YFP	$Tau^{P301L, V337M}$-EYFP	Kan	Hipp Lab
pPD_nTau$^{P301L, V337M}$	*rgef-1p*:: $Tau^{P301L, V337M}$:: hsp-3^{IRES}::wrmScarlet-$Tau^{P301L, V337M}$	Amp	this work
pPD_nTau^{WT}	*rgef-1p*:: Tau^{WT}:: hsp-3^{IRES}::wrmScarlet-Tau^{WT}	Amp	this work
pRK5-EGFP-Tau	EGFP-Tau^{WT}	Amp	Ashe Lab
pPD_nAbeta$_{1-42}$	*rgef-1p*::SigPep-Abeta$_{1-42}$:: hsp-3^{IRES}::wrmScarlet-Abeta$_{1-42}$	Amp	Kirstein Lab

5.10 *C. elegans* strains

Table 5.14: *List of C. elegans strains used in this study.*

Strain name	Genotype	Source
FX01291	*clec-1(tm1291) V*	NBRP *C. elegans*
FX02505	*lys-3 (tm2505) V*	NBRP *C. elegans*
mAβ_{1-42} × nGCaMP6m	Is [*myo-3p*::SigPep-Aβ_{1-42}::hsp-3^{IRES}::wrmScarlet-Aβ_{1-42} +	Kirstein Lab (this work)

	rps-0p::hygR CeOpt; *rgef-1p*::GCaMP6m]	
mAβ_{1-42}	Is [*myo-3p*::SigPep-Aβ_{1-42}::hsp-3^{IRES}::wrmScarlet-Aβ_{1-42} + *rps-0p*::hygR CeOpt]	Kirstein Lab (Gallrein et al., 2021)
mmScarlet × nGCaMP6m	Is [*myo-3p*::SigPep-Aβ_{1-42}::hsp-3^{IRES}::wrmScarlet-Aβ_{1-42} + *rps-0p*::hygR CeOpt; *rgef-1p*::GCaMP6m]	Kirstein Lab (this work)
mmScarlet	Is [*myo-3p*::wrmScarlet_ext + *rps-0p*::hygR CeOpt]	Kirstein Lab (Gallrein et al., 2021)
MT8004	*unc-13(n2813) I*	CGC
N2 wild-type	*C. elegans* wild isolate	CGC
nAβ_{1-42} × FX01291	Is [*rgef-1p*::SigPep-Aβ_{1-42}::hsp-3^{IRES}::wrmScarlet-Aβ_{1-42} + *rps-0p*::hygR CeOpt]; *clec-1 (tm1291) V*	Kirstein Lab (this work)
nAβ_{1-42} × FX02505	Is [*rgef-1p*::SigPep-Aβ_{1-42}::hsp-3^{IRES}::wrmScarlet-Aβ_{1-42} + *rps-0p*::hygR CeOpt]; *lys-3 (tm2505) V*	Kirstein Lab (this work)
nAβ_{1-42} × nGCaMP6m	Is [*rgef-1p*::SigPep-Aβ_{1-42}::hsp-3^{IRES}::wrmScarlet-Aβ_{1-42} + *rps-0p*::hygR CeOpt; *rgef-1p*::GCaMP6m]	Kirstein Lab (this work)

nAβ$_{1-42}$ × RB1384	Is [*rgef-1p*::SigPep-Aβ$_{1-42}$::hsp-3^{IRES}::wrmScarlet-Aβ$_{1-42}$ + *rps-0p*::hygR CeOpt]; *dod-21* & C32H11.11 *(ok1569) IV*	Kirstein Lab (this work)
nAβ$_{1-42}$ × RB939	Is [*rgef-1p*::SigPep-Aβ$_{1-42}$::hsp-3^{IRES}::wrmScarlet-Aβ$_{1-42}$ + *rps-0p*::hygR CeOpt]; *tag-196 (ok822) V*	Kirstein Lab (this work)
nAβ$_{1-42}$ × ZIM1048	Is [*rgef-1p*::SigPep-Aβ$_{1-42}$::hsp-3^{IRES}::wrmScarlet-Aβ$_{1-42}$ + *rps-0p*::hygR CeOpt; mzmIs4 (*unc-31p::*NLSGCaMP5Kf + *unc-122p*::GFP); *lite-1 (ce314) X]*	Kirstein Lab (Gallrein et al., 2021)
nAβ$_{1-42}$ × ZIM1048 × FX01291	Is [*rgef-1p*::SigPep-Aβ$_{1-42}$::hsp-3^{IRES}::wrmScarlet-Aβ$_{1-42}$ + *rps-0p*::hygR CeOpt; mzmIs4 (*unc-31p::*NLSGCaMP5Kf + *unc-122p*::GFP); *lite-1 (ce314) X]; clec-1 (tm1291) V*	Kirstein Lab (this work)
nAβ$_{1-42}$ × ZIM1048 × FX02505	Is [*rgef-1p*::SigPep-Aβ$_{1-42}$::hsp-3^{IRES}::wrmScarlet-Aβ$_{1-42}$ + *rps-0p*::hygR CeOpt; mzmIs4 (*unc-31p::*NLSGCaMP5Kf + *unc-122p*::GFP); *lite-1 (ce314) X]; lys-3 (tm2505) V*	Kirstein Lab (this work)

nAβ_{1-42}	Is [*rgef-1p*::SigPep-Aβ_{1-42}::hsp-3^{IRES}::wrmScarlet-Aβ_{1-42} + *rps-0p*::hygR CeOpt]	Kirstein Lab (Gallrein et al., 2021)
nGCaMP6m	Is [*rgef-1p*::GCaMP6m]	Kirstein Lab
nGCaMP6m × MT8004	Is [*rgef-1p*::GCaMP6m]; *unc-13 (n2813) I*]	Kirstein Lab (this work)
nmScarlet	Is [*rgef-1p*::hsp3^{IRES}::mScarlet]	Kirstein Lab (Pigazzini et al., 2021)
nmScarlet × FX01291	Is [*rgef-1p*::hsp3^{IRES}::mScarlet]; *clec-1 (tm1291) V*	Kirstein Lab (this work)
nmScarlet × FX02505	Is [*rgef-1p*::hsp3^{IRES}::mScarlet]; *lys-3 (tm2505) V*	Kirstein Lab (this work)
nmScarlet × nGCaMP6m	Is [*rgef-1p*::hsp3^{IRES}::mScarlet; *rgef-1p*::GCaMP6m]	Kirstein Lab (this work)
nmScarlet × ZIM1048	Is [*rgef-1p*::hsp3^{IRES}::mScarlet; mzmIs4 (*unc-31p::*NLSGCaMP5Kf + *unc-122p*::GFP); *lite-1 (ce314) X]*	Kirstein Lab (this work)
nTau^{P301L,V337M}	Is [*rgef-1p*::TauP$^{301L, V337M::}$hsp-3^{IRES}::wrmScarlet-Tau$^{P301L, V337M}$ + *rps-0p*::hygR CeOpt]	Kirstein Lab (this work)
nTau^{P301L,V337M} × nGCaMP6m	Is [*rgef-1p*::TauP$^{301L, V337M::}$hsp-3^{IRES}::wrmScarlet-Tau$^{P301L, V337M}$ +	Kirstein Lab (this work)

	rps-0p::hygR CeOpt; *rgef-1p*::GCaMP6m≈	
nTau^{P301L,V337M} × RB809	Is [*rgef-1p*::Tau$P^{301L, V337M}$::hsp-3^{IRES}::wrmScarlet-Tau$^{P301L, V337M}$ + *rps-0p*::hygR CeOpt]; *ptl-1 (ok621) III*	Kirstein Lab (this work)
nTau^{P301L,V337M} × ZIM1048	Is [*rgef-1p*::Tau$P^{301L, V337M}$::hsp-3^{IRES}::wrmScarlet-Tau$^{P301L, V337M}$ + *rps-0p*::hygR CeOpt; mzmIs4 (*unc-31p::*NLSGCaMP5Kf + *unc-122p*::GFP); *lite-1 (ce314) X]*	Kirstein Lab (this work)
nTau^{WT}	Is [*rgef-1p*::Tau^{WT}::hsp-3^{IRES}::wrmScarlet-Tau^{WT} + *rps-0p*::hygR CeOpt]	Kirstein Lab (this work)
nTau^{WT} × nGCaMP6m	Is [*rgef-1p*::Tau^{WT}::hsp-3^{IRES}::wrmScarlet-Tau^{WT} + *rps-0p*::hygR CeOpt; *rgef-1p*::GCaMP6m]	Kirstein Lab (this work)
nTau^{WT} × RB809	Is [*rgef-1p*::Tau^{WT}::hsp-3^{IRES}::wrmScarlet-Tau^{WT} + *rps-0p*::hygR CeOpt]; *ptl-1 (ok621) III*	Kirstein Lab (this work)
nTau^{WT} × ZIM1048	Is [*rgef-1p*::Tau^{WT}::hsp-3^{IRES}::wrmScarlet-Tau^{WT} + *rps-0p*::hygR CeOpt; mzmIs4 (*unc-31p::*NLSGCaMP5Kf + *unc-122p*::GFP); *lite-*	Kirstein Lab (this work)

	1 (ce314) X]	
RB1384	*dod-21 &* C32H11.11 *(ok1569) IV*	CGC
RB809	*ptl-1 (ok621) III*	CGC
RB939	*tag-196 (ok822) V*	CGC
ZIM1048	Is [mzmIs4 (*unc-31p::*NLSGCaMP5Kf + *unc-122p*::GFP); *lite-1 (ce314) X]*	Zimmer Lab

5.11 Bacterial strains

Table 5.15: *List of bacterial strains used in this study.*

Bacterial strain	Application	Genotype
E. coli DH5α	Cloning	*dlacZDeltaM15, Delta(lacZYA-argF)U169, recA1, endA1, hsdR17(rK- mK+), supE44 thi-1, gyrA96, relA1*
E. coli OP50	*C elegans* food source	uracil auxotroph

5.12 Consumables

Table 5.16*: List of consumables used in this study.*

Name	Manufacturer
CyroPure tube 2 ml	Sarstedt, Nürnberg, Germany
Disposal bags	Sarstedt, Nürnberg, Germany
Falcon tubes (15 ml, 50 ml)	Sarstedt, Nürnberg, Germany

Glass Microscopy Coverslips (24 mm × 24 mm)	Epredia, Braunschweig, Germany
Glass Microscopy Slides (26 mm × 76 mm)	Epredia, Braunschweig, Germany
Laboratory bottles with cap	Schott, Mainz, Germany
Low binding tubes (1.5 ml)	Sarstedt, Nürnberg, Germany
Parafilm	Carl Roth, Karlsruhe, Germany
Pasteur pipettes	Brand, Wertheim, Germany
PCR tubes	Sarstedt, Nürnberg, Germany
Petri dishes (35 mm, 60 mm, 100 mm)	Thermo Fisher Scientific, Waltham, USA
Pipette tips (1000 µl, 200 µl, 10 µl)	Sarstedt, Nürnberg, Germany
Platinum wire (0.3 mm)	Carl Roth, Karlsruhe, Germany
PVDF membrane (0.45 µm)	Carl Roth, Karlsruhe, Germany
Reaction tubes (1.5 ml, 2 ml)	Sarstedt, Nürnberg, Germany
Serological pipettes (5 ml, 10 ml, 25 ml)	Sarstedt, Nürnberg, Germany
Sterile tube round bottom (14 ml)	Greiner Bio-one, Kremsmünster, Austria

5.13 Laboratory equipment

***Table 5.17**: List of laboratory equipment used in this study.*

Device	Name	Manufacturer
Centrifuge	Centrifuge 5415 D	Eppendorf, Hamburg, Germany
	Centrifuge 5810 R	Eppendorf, Hamburg, Germany
	Centrifuge MiniSpin	Eppendorf, Hamburg, Germany
Confocal Laser Scanning Microscope (CLSM)	LSM 880 with Airyscan	Zeiss, Oberkochen, Germany

Fluorescence lifetime imaging microscopy	Pulsed laser	PicoQuant, Berlin, Germany
GeneGun		Leibniz-Forschungsinstitut für Molekulare Pharmakologie (FMP) work shop facility
Heating Block	Heating-Thermo Shaker MHR 11	Ditabis, Pforzheim, Germany
	Thermomixer Compact	Eppendorf, Hamburg, Germany
Incubator	Labwit Ultimate ZWYC-290A	Labwit Scientific, Melbourne, Australia
Magnetic stirrer	Heidolph Magnetic stirrer MR2002	Heidolph, Schwabach, Germany
pH meter		Mettler Toledo, Ohio, USA
Photometer	NanoPhotometer N60	IMPLEN, Munich, Germany
Pipettor	Pipetboy	Integra Bioscience, Bibertal, Germany
Power supply	PowerPac Basic	Bio-Rad, Hercules, USA
	Delta Elektronika E0300-0.1 Power supply	Delta Elektronika, Zierikzee, The Netherlands
Scale	BP 221 S	Sartorius, Göttingen, Germany
	BL 1500	Sartorius, Göttingen, Germany
SDS-PAGE system	Mini-PROTEAN Tetra Cell	Bio-Rad, Hercules, USA
Shaker	GFL Shaker 3016	Lauda, Lauda-Königshofen, Germany
	WT 16	Biometra, Göttingen, Germany

Sonication water bath	Sonorex Super RK 31	BRANDELIN, Berlin, Germany
Stereo microscope	Nikon SMZ745	Nikon, Tokyo, Japan
Stereo fluorescence microscope	Leica M165 FC	Leica, Wetzlar, Germany
Thermocycler	C1000 Touch	Bio-Rad, Hercules, USA
Tube roller	ROLLER 6 digital	IKA Labortechnik, Staufen, Germany
UV crosslinker	Fluo-Link (TFL-20M, 312 nm)	Biometra, Göttingen, Germany
Vacuum pump		KNF Lab, New Jersey, USA
Vortex	Vortex VF2	Janke & Kunkel Labortechnik, Staufen im Breisgau, Germany
Western blot and agarose gel detection system	ChemoStar Touch ECL & Fluorescence Imager	Intas, Göttingen, Germany
Western blot system (semi-dry)	Trans-Blot Turbo Transfer System	Bio-Rad, Hercules, USA
Widefield fluorescence microscope		University of Cambridge, Cambridge, UK

5.14 Softwares and online tools

Table 5.18: *List of softwares and online tools used in this study.*

Software / tools	Company / Source
BioRender	Science Suite Inc., Toronto, Canada
BLASTn	National Library of Medicine, Bethesda, USA
ChemoStarTS	Instas, Göttingen, Germany
Fiji v2.3	Schindelin et al., 2012

FLIMFit v5.1.1	Warren et al., 2013
Microsoft Office 365 (Word, Excel, PowerPoint)	Microsoft Corporation, Washington, USA
NEBuilder Assembly Tool	New England Biolabs, Ipswich, USA
Oasis 2	Han et al., 2016
Primer-BLAST	National Library of Medicine, Bethesda, USA
Prism 9	GraphPad Software, Boston, USA
SnapGene	GSL Biotech LLC, Boston, USA
SymPho Time 64	PicoQuant, Berlin, Germany
T_m Calculator	Thermo Fisher Scientific, Waltham, USA
Widefield fluorescence microscope software	University of Cambridge, Cambridge, UK
WormBase	WormBase Consortium, 2000
WormLab	MBF Bioscience, Williston, USA
Zen 2.3 SP1	Zeiss, Oberkochen, Germany
Zen Blue	Zeiss, Oberkochen, Germany
Zen PicoQuant Application	Zeiss, Oberkochen, Germany

6 METHODS

6.1 Molecular biology methods

6.1.1 Polymerase chain reaction (PCR)

Polymerase chain reaction (PCR) was used to amplify specific DNA sequences. PCR primers were manually designed to bind specifically to the gene of interest (GOI). For genomic DNA templates, Primer-BLAST (NCBI) was used to find specific primers. Gibson Assembly primers were designed using the NEBuilder Assembly Tool (NEB). Primers for Gibson Assembly cloning were designed to be complementary to the two sequences to be ligated, therefore the designed primers are homologous at the 5' end to the 3' end of the respective upstream fragment. All primers were checked for specificity using Blastn (NCBI), and annealing temperatures were calculated using the T_m calculator tool (Thermo Fisher Scientific). PCR reactions were performed using Phusion High-Fidelity DNA polymerase in a reaction volume of 50 µl. Components were mixed on ice by adding nuclease-free water, 1x Phusion High-Fidelity reaction buffer, 200 µM dNTPs, 0.5 µM forward primers, 0.5 µM reverse primers, 3% DMSO, 10 ng plasmid DNA as template and 1 U Phusion DNA polymerase. A no-template control (NTC) was used by adding 1 µl of nuclease-free water instead of the DNA template. The reactions consisted of an initial denaturation at 98°C for 1 minutes, followed by 35 cycles of denaturation (98°C for 30 s), annealing (calculated annealing temperature of the primer pair for 30 s) and elongation (72°C for 1 minute per kilobase). A final extension at 72°C for 10 minutes was performed after the last cycle. Amplification of specific DNA sequences from nematode gDNA is described in the section on nematode genotyping.

6.1.2 Agarose gel electrophoresis

Agarose gel electrophoresis was used to verify the successful amplification and correct size of the DNA sequences. A 1% (w/v) agarose was dissolved in 1x TBE buffer by gentle boiling. 25 nM ethidium bromide was added to the cooled down agarose solution and poured into a horizontal chamber. After solidification, DNA samples and a DNA ladder (1 kb or 50 bp) were mixed with 1x loading dye and loaded onto the gel. Electrophoresis was performed at 70-80 V for 40-60 minutes.DNA fragments were visualised by UV light using ChemoStarTS (Intas).

6.1.3 Molecular cloning / Gibson assembly

All genes were expressed using the plasmid pPD95_77 as the backbone. DNA sequences for cloning were amplified using Phusion High-Fidelity DNA polymerase as described above and purified using a spin column (Qiagen). The construct for neuronal expression of Tau^{WT} with substoichiometric expression of mScarlet::Tau^{WT} and of $Tau^{P301L,V337M}$ mScarlet::$Tau^{P301L,V337M}$ with substoichiometric expression of mScarlet::$Tau^{P301L,V337M}$ was generated by ligation of 4 amplified fragments (3 inserts, 1 vector backbone) by Gibson Assembly (NEB). A total amount of 0.6 pmol of fragments was added to 1x Gibson Assembly Master Mix and topped up with nuclease-free water to a final volume of 20 µl. A 1:1:1:1 molar ratio of inserts:vector backbone was used, and care was taken to ensure that the total volume of PCR fragments in the assembly reaction did not exceed 20%. Ligation was carried out at 50°C for 60 minutes. Reactions were kept on ice or at -20°C for subsequent transformation.

Cloning of the Tau^{WT}-$hsp3^{IRES}$-mScarlet-Tau^{WT} plasmid.

The human *Tau^{WT}* gene was amplified from the pRK5-EGFP-Tau plasmid using the primers Tau Wt w/o ATG_fwd with homologous overlaps to the *rgef-1* promoter sequence of the plasmid backbone at the 5' end and Tau Wt w/o ATG_rev with homologous overlaps to the *hsp-3^{IRES}* sequence at the 3' end. The *hsp-3^{IRES}*-mScarlet sequence was amplified from the pPD_nAbeta$_{1-42}$ (Gallrein et al., 2021) using the primers Wt_IRES-mSca_fwd with homologous overlaps to the *Tau^{WT}* sequence at the 5' end and with Wt_IRES-mSca_rev with homologous overlaps to the *Tau^{WT}* sequence at the 3' end. The human *Tau^{WT}* gene for the expression of the Tau^{WT} substoichiometrically tagged to the mScarlet fluorophore was amplified from the pRK5-EGFP-Tau plasmid using the primers Tau Wt (Serine)_fwd with homologous overlaps to the *hsp-3^{IRES}-mScarlet* sequence at the 3' end and with Tau Wt (Serine)_rev with homologous overlaps to the plasmid backbone at the 3' end. The plasmid backbone containing the *rgef*-1 promoter sequence was amplified from the plasmid pPD_nAbeta$_{1-42}$ (Gallrein et al., 2021) using the primers Wt_Vektor w/o ScaBeta_fwd with homologous overlaps to the *Tau^{WT}* sequence at the 5' end and with Vektor w/o ScaBeta_rev with homologous overlaps to the *Tau^{WT}* sequence at the 3' end. Gibson Assembly was performed as described above to produce the final plasmid containing all four fragments (pPD_nTau^{WT}).

Cloning of the Tau^{P301L,V337M}-hsp3^{IRES}-mScarlet-Tau^{P301L,V337M} plasmid.

The human *Tau^{P301L,V337M}* gene was amplified from the pN1 FLTau0N4RLM YFP plasmid using the primers Tau Mt (Methionine)_fwd with homologous overlaps to the *rgef-1* promoter sequence of the plasmid backbone at the 5' end and Tau Mt (Methionine)_rev with homologous overlaps to the *hsp-3^{IRES}* sequence at the 3' end. The *hsp-3^{IRES}-mScarlet* sequence was amplified from the pPD_nAbeta$_{1-42}$ (Gallrein et al., 2021) using the primers Mt_IRES-wrmSca_fwd with homologous overlaps to the *Tau^{P301L,V337M}* sequence at the 5' end and with Mt_IRES-wrmSca_rev with homologous overlaps to the *Tau^{P301L,V337M}* sequence at the 3' end. The human *Tau^{P301L,V337M}* gene for the expression of the Tau^{P301L,V337M} substoichiometrically tagged to the mScarlet fluorophore was amplified from the pN1 FLTau0N4RLM YFP plasmid using the primers Tau Mt w/o Serine_fwd with homologous overlaps to the *hsp-3^{IRES}-mScarlet* sequence at the 3' end and with Tau Mt w/o Serine_rev with homologous overlaps to the plasmid backbone at the 3' end. The plasmid backbone containing the *rgef-1* promoter sequence was amplified from the plasmid pPD_nAbeta$_{1-42}$ (Gallrein et al., 2021) using the primers Mt_Vektor w/o ScaBeta_fwd with homologous overlaps to the *Tau^{P301L,V337M}* sequence at the 5' end and with Vektor w/o ScaBeta_rev with homologous overlaps to the *Tau^{P301L,V337M}* sequence at the 3' end. Gibson Assembly was performed as described above to produce the final plasmid containing all 4 fragments (pPD_nTau^{P301L,V337M}).

6.1.4 Bacterial transformation using heat shock

Chemically competent DH5α *E. coli* cells were thawed on ice and transformation was carried out by adding either 50-100 ng plasmid DNA or 2 µl Gibson Assembly reaction to 50 µl of thawed DH5α *E. coli* cells. The mixture was kept on ice for 30 minutes and then heat shocked at 42°C for 45 seconds using a heating block, followed by a further incubation step on ice for 2 minutes.500 µl of pre-warmed SOC medium without antibiotics was added to the mixture and bacteria were grown at 37°C for 1 hour using a heating block and shaking at 750 rpm. The bacteria were then pelleted by centrifugation, and the pellet was resuspended in 100 µl SOC medium. The bacteria were plated on LB agar plates containing appropriate antibiotics and grown overnight at 37°C.

6.1.5 Plasmid DNA preparation

Positive DH5α *E. coli* colonies were selected from the LB agar plates and incubated in LB medium with appropriate antibiotics. For a plasmid miniprep, 10-15 ml of LB medium was used, while for a plasmid midiprep, a volume of 50-75 ml was used. Bacteria were grown overnight at 37°C on a rotating shaker. The following day, the plasmids were extracted from the bacterial culture using the GeneJET Plasmid Miniprep Kit (Thermo Fisher Scientific) or NucleoBond Xtra Midi kit (Macherey-Nagel) according to the manufacturer's instructions for extraction of low copy plasmids. Plasmid DNA was eluted in nuclease-free water and stored at -20°C until further use. DNA concentration was measured using a NanoPhotometer N60 (IMPLEN). To ensure correct ligation and assembly of the plasmids, DNA sequences were checked by restriction enzyme digestion and confirmed by DNA sequencing (LGC Genomics).

6.2 Biochemical methods

6.2.1 Sodium dodecyl sulphate polyacrylamide gel electrophoresis (SDS-PAGE)

SDS-PAGE was used to separate proteins according to their molecular weight. SDS-PAGE mini gels (1.5 mm thick) were cast in a commercially available system (Bio-Rad) by assembling cleaned glass plates in the casting frame. First, a 10% separating gel was poured into the space between the glass plates and covered with isopropanol. After solidification, the isopropanol was removed, and the surface of the gel was cleaned with double-distilled water. A 4% stacking gel was poured onto the separating gel and a 10- or 15-well comb was added, depending on the number of samples.
Recipe for a 1.5 mm gel:

***Table 6.1**: SDS-PAGE recipe.*

Components	Separating gel (10%)	Stacking gel (4%)
Rotiphorese Gel (37.4:1)	4 ml	0.67 ml
Separation gel buffer	2.5 ml	--
Stacking gel buffer	--	1.25 ml
20% SDS	50 µl	25 µl
Double-distilled water	3.32 ml	3 ml

APS	74 µl	50 µl
TEMED	20 µl	7 µl

The stacking gel was allowed to solidify for 20 minutes and transferred to a vertical electrophoresis chamber (Min-Protean Tetra Bio-Rad) containing 1x SDS-PAGE running buffer. Samples for SDS-PAGE were boiled at 95°C for 10 minutes and then loaded onto the gel together with 5 µl of a pre-stained protein ladder. The gel was subjected to 60 V until the samples reached the separating gel, followed by 100-120 V for 60-90 minutes.

6.2.2 Western blot (WB)

SDS-PAGE was followed by Western blot (WB) to identify and quantify the abundance of proteins of interest (i.e., GCaMP6m). Proteins were transferred onto a PVDF membrane using a semi-dry blot approach (Trans Blot Turbo Transfer System Bio-Rad). The PVDF membrane was activated in methanol until the membrane was translucent and the 5x transfer buffer from the Trans Blot Turbo Transfer kit was diluted to 1x with double-distilled water and ethanol according to the manufacturer's instructions. The activated membrane and two transfer stacks were equilibrated in 1x transfer buffer and the blotting sandwich was assembled as follow: transfer stack, activated PVDF membrane, gel, transfer stack. The sandwich was gently rolled with a rolling pin to remove any residual air bubbles. Blotting was performed at 25 V for 30 minutes. The membrane was blocked with 3% (w/v) milk powder in TBS-T for 1 h at room temperature with shaking. The blocking solution was removed, and the primary antibody (dilution indicated in the Materials section) was added in 3% (w/v) milk powder in TBS-T for overnight incubation at 4°C. The membrane was washed three times with TBS-T for 10 minutes and the secondary antibody in 3% (w/v) milk powder in TBS-T was added for 60 minutes incubation at room temperature with shaking. The membrane was washed three times with TBS-T for 10 minutes and imaged by chemiluminescence using ECL reagent (Pierce) and the ChemoStarTS (Intas).

6.2.3 Western blot quantification using Fiji

Raw Western blot images were uploaded to Fiji software and converted to 3-3-2 LUT profile for better visualisation of the signals. To quantify the intensity of each protein

band, the area, integrated density, mean grey value and minimum and maximum grey value were selected in the 'Analyse' menu of 'set measurements'. A rectangle was drawn around a single protein band using the drawing tools and the intensity was quantified by clicking 'Measure'. The dimensions of the rectangle were kept the same for each protein band and the rectangle was dragged from one protein band to another until all protein bands were quantified. For background subtraction, five measurements were taken within an area of no signal. The data was copied to Excel and the integrated density of the background measurements was averaged. This value was subtracted from each integrated density of the protein bands. The intensity of the protein of interest was normalised to the intensity of GAPDH that served as loading control for the same sample. Data were presented as relative values to a control sample (i.e. nmScarlet or mmScarlet), in which case the GAPDH-normalised intensities were divided by the average of the control sample.

6.3 *C. elegans* methods

6.3.1 *C. elegans* maintenance

C. elegans were grown on solid nematode growth medium (NGM) plates seeded with *E. coli* OP50 as a food source. Nematodes were maintained on 60 mm dishes containing 8 ml NGM at 20°C in the dark. Every four days, five to ten nematodes (depending on the strain) were transferred to fresh plates to avoid starvation and contamination. All $A\beta_{1-42}$ strains were passaged using a fluorescence stereomicroscope by selecting animals with the brightest fluorescence to prevent adaptation of these strains. All experiments were carried out at 20°C.

6.3.2 Generation of males through heat shock

To produce male nematodes for genetic crossings, eight to ten L4 hermaphrodites were transferred to seeded NGM plates. The nematodes were incubated at 31°C for 5 to 6 hours before being returned to 20°C. After three to four days, the progeny of the heat-shocked nematodes were screened for males, which were then transferred to a fresh plate together with at least one L4 hermaphrodite of the same genotype. To maintain male populations, males and L4 hermaphrodites were mixed in a 3:1 ratio.

6.3.3 Genetic crossing

Genetic crosses were made to create a new nematode strain that combined two different genetic traits. Male nematodes of one genotype were produced as described above. For crossing, ten males were transferred to a fresh plate and one L4 hermaphrodite of the other genotype was added. To increase mating efficiency, crossing was performed using 35 mm plates. After three to four days of incubation at 20°C, the progeny (F1 generation) was examined.

If both parental strains expressed a fluorescent marker, the F1 generation would show double fluorescence, but with a lower fluorescence intensity compared to the parental strain, as they are only heterozygous for each trait. Five to ten L4 hermaphrodites of the F1 generation were isolated on 35 mm plates and allowed to self-fertilise at 20°C for three to four days. The progeny (F2 generation) were screened for homozygous animals with strong fluorescence intensity for both markers. Ten to twenty L4 hermaphrodites of the F2 generation were isolated on 35 mm and the progeny (F3 generation) were screened after incubation at 20°C for three to four days. If all animals of the F3 generation showed a strong fluorescence of both markers, the nematodes were homozygous and the strain was maintained as described above.

The crossing procedure was slightly different, when the genetic trait of one of the parental strains was not linked to a fluorescent marker and a PCR was performed to confirm the correct genotype. In this case, male nematodes of the strain without a fluorescent marker were produced. Ten male nematodes were transferred to a fresh 35 mm plate and one L4 hermaphrodite of the fluorescence-marked strain was added. From the F1 generation, one heterozygous L4 hermaphrodite was transferred to a new plate and ten males of the parental strain without a fluorescent marker were added. Within the resulting F2 generation, 50% of the animals were homozygous for the genetic trait without a fluorescent marker. Ten to twenty L4 hermaphrodites of the F2 generation were isolated on 35 mm plates and cultured at 20°C for three to four days. The progeny (F3 generation) was genotyped to select the strains that were homozygous for the genetic trait without a fluorescent marker. From these nematodes, only those animals with a strong fluorescence were selected to obtain double homozygous nematodes.

6.3.4 Nematode genotyping

Nematode genotyping was required for crosses with *C. elegans* strains that do not express a fluorescent marker but have a specific DNA deletion within a gene of interest (e.g., FX02505, FX01291, RB809 etc.). Specific primers were designed to amplify a region within the gene of interest that contains the deleted area. Genotyping PCR of nematodes with a homozygous deletion within a gene of interest produces a shorter DNA fragment than from N2 wild-type animals. To genotype nematodes and to distinguish between homozygous and heterozygous animals, 20 - 25 nematodes were picked into 20 µl of dilution buffer (Phire Tissue Direct PCR Master Mix, Thermo Fisher Scientific). 0.5 µl of DNA Release additive was added, and the sample was vortexed and centrifuged. For nematode lysis and genomic DNA release, the sample was incubated for 15 minutes at room temperature followed by 2 minutes at 98°C in a heating block. The sample was centrifuged at 13.000 rpm for 1 minute and the supernatant was used immediately or stored at -20°C until further use. PCR reactions were performed using Phire Tissue Direct PCR Master Mix in a 20 µl reaction volume. Components were mixed on ice by adding nuclease-free water, 1x Phire Tissue Direct PCR Master Mix containing dNTPs, Phire Hot Start II DNA polymerase and additives, 0.5 µM forward primers, 0.5 µM reverse primer and 1 µl of nematode genomic DNA. DNA was amplified using a 3-step cycling protocol consisting of 5 minutes initial denaturation at 98°C followed by 40 cycles of 5 seconds denaturation at 98°C, 5 seconds annealing at the temperature specific to the primer pair, 20 seconds per kilobase extension at 72°C and a final extension step of 1 minute at 72°C. 3-5 µl of PCR product was analysed by agarose gel electrophoresis to visualise the amplified PCR sequence.

6.3.5 Nematode lysis and protein extraction

Lysis of nematodes for extraction of total proteins was performed by boiling in Laemmli loading buffer. Nematodes were synchronised and 150-200 L4 hermaphrodites were picked. Nematodes were grown to the desired age (i.e., day 4, day 7, or day 10), transferred to fresh plates each day to separate them from the progeny, and picked on the day of harvest into a low-binding tube containing 1 ml of M9 buffer. Nematodes were pelleted by centrifugation at 2000 rpm for 1 minute. The supernatant was discarded and 1 ml of M9 buffer was added. The procedure was repeated at least three

to four times until the supernatant was free of residual bacteria. After the last wash, the supernatant was removed and 30 µl of 4x Laemmli buffer was added. The sample was briefly centrifuged and boiled in a heating block for 15 minutes at 99°C and 1000 rpm shaking. After boiling, the sample was centrifuged at 130000 rpm for 1 minute and stored at -20°C until further use. 10-15 µl of the sample was used for SDS-PAGE and Western blot.

6.3.6 Ballistic transformation - microparticle bombardment

Microparticle bombardment was used to generate transgenic *C. elegans* strains. Plasmid DNA was coated onto gold particles (0.3-3 µm) and bombarded onto young adult N2 wild-type nematodes using a gene gun. Synchronisation of N2 wild-type animals was performed by transferring 3×100 fertile hermaphrodites on a 100 mm plate. Nematodes were incubated overnight at 20°C, fertile nematodes were removed the next day and grown until the majority reached young adulthood.

1 mg of gold particles were resuspended in 100 µl of spermidine solution (50 mM) and sonicated in a water bath for 30 seconds at room temperature. The suspension was incubated for 10 minutes at room temperature, resuspending by flicking every minute. 10 µg of plasmid DNA was added and again incubated for 10 minutes at room temperature and resuspending by flicking every minute. After incubation, double-distilled water was added to a final volume of 360 µl and the mixture was incubated for a further 10 minutes at room temperature, resuspending by flicking every minute. Then 100 µl of $CaCl_2$ (1 M) was added dropwise, vortexed for 10 seconds and incubated for 10 minutes at room temperature, resuspending by flicking every minute. DNA coated gold particles were pelleted by centrifugation at 13000 rpm for 30 s. The supernatant was removed, and the pellet was washed three to four times with 500 µl ethanol (absolute). After the last wash, the ethanol was completely removed, and the pellet was resuspended in 300 µl PVP solution (0.1 mg/ml).

Intermittently, synchronised nematodes were washed from the plates with M9 buffer and harvested in a 15 ml falcon tube by centrifugation at 2000 rpm for 2 minutes. The supernatant was removed until the nematode pellet was covered with 1 ml of liquid and the nematodes were cooled on ice. Five 35 mm shooter plates (unseeded NGM plates)

were seeded with 12 µl of OP50 and allowed to dry. Seeded shooter plates were cooled on ice and 20 µl of the cooled nematodes were added onto the OP50 spot. Shooter plates containing nematodes were kept on ice.

30 µl of coated gold particles in PVP solution was loaded into the gene gun. A shooter plate containing nematodes was placed in the centre of the shooting chamber and the chamber was sealed airtight and evacuated to -0.4 bar. The shoot was released with helium gas at a pressure of 8 bar. After shooting, nematodes were recovered from the shooter plates with 600 µl of M9 buffer and transferred to two seeded 100 mm plates each. The nematodes were incubated overnight at 15°C and then incubated at 20°C. Plates were checked daily for positive transformants of the F1 and transgenic animals were isolated onto 35 mm plates. Progeny of positive transformants were screened for transmission of the extrachromosomal array to the next generation and transgenic strains were maintained by selecting only transgenic animals until subjected to UV integration.

6.3.7 UV Integration

UV integration was used to stably integrate extra-chromosomal DNA arrays into the genomic DNA of the nematodes. For this, 100-150 transgenic, L4 hermaphrodites were picked and washed from the plate with M9 buffer into a low-binding tube. Nematodes were washed five times with M9 buffer + 0.05% (v/v) Triton X-100 by centrifugation at 2000 rpm for 1 minute to remove residual bacteria. After the final wash, nematodes were pipetted onto an unseeded 35 mm NGM plate and allowed to crawl for approximately 20 minutes. The nematodes were exposed to 50 mJ/cm^2 UV light of 312 nm using a DNA crosslinker (Fluo-Link Biometra). The nematodes were then transferred in groups of five to seeded 60 mm NGM plates. Nematodes were incubated at 20°C for up to seven days and chunked to fresh 60 mm NGM plates. After allowing the larvae to crawl off the piece of agar for 20 to 30 minutes, approximately 300 transgenic L1 larvae were isolated onto 35 mm plates. The nematodes were incubated at 20°C for 1 week, and the progeny were scored. Integration was considered successful if at least one of the plates showed that 100% of the animals were transgenic.

6.3.8 Backcrossing

Because UV integration may cause mutations of the genome, transgenic integrated strains were backcrossed four to six times with N2 wild-type nematodes Briefly, ten N2 wild-type males were incubated with one L4 hermaphrodite of the transgenic, integrated strain (first backcross) for three to four days at 20°C. Ten heterozygous male animals were then selected from the F1 generation and transferred to a fresh plate together with one N2 wild-type L4 hermaphrodite (second backcross). After three to four days of incubation at 20°C, up to ten L4 hermaphrodites of the F2 generation were isolated onto seeded 35 mm plates and allowed to self-fertilise. After three to four days at 20°C, homozygous L4 hermaphrodites were picked from the F3 generation to obtain a twice-backcrossed homozygous strain. The procedure was repeated one or two more times to obtain four or six times backcrossed homozygous strains. The crosses were made using 35 mm seeded NGM plates.

6.3.9 Synchronisation of *C. elegans*

To obtain a population of *C. elegans* of approximately the same age, nematodes were synchronised by egg laying and L4 picking. 20 to 40 fertile nematodes were picked onto a 60 mm seeded NGM plate and incubated at 20°C for 5 to 6 hours (= day 1). The fertile nematodes were then removed from the plates and the plates with the laid eggs were incubated at 20°C for two days (= day 3). L4 hermaphrodites were picked from these plates onto fresh NGM plates and incubated at 20°C until the next day when the nematodes reached adulthood (= day 4). As nematodes carrying the $A\beta_{1\text{-}42}$ transgene are developmentally delayed, synchronisation was performed one day earlier compared to healthy nematodes (referred to as day 0, with the counting scheme as described above).

6.3.10 Lifespan assay

A lifespan assay reports on the organismal fitness of *C. elegans.* Nematodes were synchronised and 100 to 180 L4 hermaphrodites were transferred onto seeded NGM plates in groups of 10 to 20 (= day 3). Alive, dead, and censored nematodes were scored daily, and alive nematodes were transferred to fresh NGM plates every other day until the end of their fertile period. If no obvious movement of the nematodes was visible, a platinum wire was used to gently tap first the agar surrounding the nematode

or second the head, mid-body, and tail region of the nematode. If no reaction was observed, the nematode was considered to be dead and removed from the plate. Nematodes that disappeared from the plates or were damaged during transfer were censored and removed from the analysis.

The survival at each day (S_i) was calculated as:

$$S_i = \frac{A_i}{N_i} \quad \text{(equation 1.1)}$$

A_i = alive nematodes at day i
N_i = total number of nematodes as sum of alive and dead at day i

The cumulative survival ($S_{cumulative}$) was calculated as:

$$S_{cumulative} = S_1 \times S_2 \times \ldots \times S_i \quad \text{(equation 1.2)}$$

S_i = survival of nematodes at day i

Two to three independent biological replicates were performed for each strain, and the final survival curve for each strain is presented as the sum of all replicates. Statistical significance was tested with a Log-rank test using the online tool Oasis 2 (Han et al., 2016).

6.3.11 Fecundity assay

A fecundity assay was used to assess the reproductive fitness of the nematodes. Animals were synchronised and 25 to 40 L4 hermaphrodites were singled out onto 35 mm seeded NGM plates. The nematodes were kept at 20°C and each animal was transferred daily to a fresh plate until they stopped laying eggs (usually by day 9). The viable offspring of each nematode were counted after the parental animals were removed. To facilitate counting, plates were divided into four quadrants with a marker and placed on ice to immobilise the larvae.

6.3.12 Developmental assay

A developmental assay monitors the development of the nematodes from egg to fertile adults. Nematodes were synchronised for two hours, and 60 eggs were singled out into groups of ten onto seeded 35 mm plates. Nematodes were incubated overnight at 20°C and nematodes that had not hatched the next morning were excluded from the analysis. The developmental stage of each nematode was checked daily until adulthood was reached. An animal was considered adult when the first fertilised eggs were visible in the uterus.

6.3.13 Chemotaxis assay

A chemotaxis assay was used to test the chemotactic behaviour of the nematodes to volatile odours. To test chemotaxis of the nematodes at day 4, nematodes were synchronised and 600 L4 hermaphrodites per strain were picked onto seeded 60 mm plates. The animals were incubated overnight at 20°C and washed from the plates with M9 buffer + 0.05% (v/v) Triton X-100 into a low-binding tube. The nematodes were pelleted by centrifugation at 2000 rpm for 1 minute and the supernatant was removed. The nematodes were washed by centrifugation until the supernatant was clear and free of residual bacteria. After the final wash, the nematodes were kept in M9 buffer and starved for 90 minutes at 20°C in the dark. Meanwhile, unseeded NGM plates were marked with four quadrants and a circle in the centre. Two opposite quadrants were marked as tests and 2 µl of odour sample substances was added. The other two quadrants were marked as controls and 2 µl of control substance was added. Odorant sample substances were mixed with sodium azide (500 mM) in a 1:1 (v/v) ratio with either pure benzaldehyde (test repellent) or with diluted benzaldehyde (2% v/v in water) (test attractant). Water was used as a control substance in a mixture with sodium azide. After starvation, 10 µl of the pelleted nematodes were pipetted into the centre of the prepared plate and the liquid was gently absorbed with the tip of a folded tissue. The plates were sealed with parafilm and incubated at 20°C for 2 hours to allow the nematodes to crawl on the plates. The nematodes were then counted in each quadrant and the chemotaxis index (ci) was calculated:

$$ci = \frac{(Test_{Quadrant_1} + Test_{Quadrant_2}) - (Control_{Quadrant_1} + Control_{Quadrant_2})}{total\ number\ of\ nematodes} \quad \text{(equation 2)}$$

Experiments were conducted in 3-4 biological replicates per strain, with 3 plates of each test attractant and repellent per replicate.

6.3.14 Thrashing assay

To analyse the muscle activity of the nematodes, thrashing behaviour of the nematodes in liquid medium was analysed. Thrashing was analysed on day 4 and day 10 of the nematode life. Nematodes were synchronised and grown to day 4 or day 10. 3 ml of M9 medium was added to an empty 35 mm plate and 10 to 15 nematodes were transferred into the liquid. The nematodes were allowed to swim for 3 minutes before video recording began. Videos were recorded at 7.3x magnification at a frame rate of 30 frames per second using a stereomicroscope equipped with a camera and recording software (Leica M165 FC). Recordings were made for 20 s, producing a total of 600 frames, with the interval between frames set at 33.3 msec. The exposure time was 1 msec, and the contrast was set to 0.4. Each group of nematodes (10-15) was recorded in triplicate and the nematodes were separated from each other with an eyelash. Videos were exported as .avi files and were uploaded to the WormLab software (MBF Bioscience). Videos were adjusted with background smoothing set to 5 and Gaussian smoothing set to 5. The detection frequency was set to 10 frames without width fitting. The software was allowed to track the video from frame 1 to 600 with a maximum tracking hypothesis of 1. Nematodes were only included in the final analysis if the tracking lasted for at least 300 frames (minimum tracking duration). Thrashing frequency was analysed using the bend angle (midpoint) analysis option with an amplitude threshold of 20 degrees and a duration threshold of 10 s. The frequency values provided by the WormLab software were exported to Excel.

6.4 Microscopy

6.4.1 Nematode mounting for standard confocal imaging and fluorescence lifetime imaging microscopy (FLIM)

Confocal microscopy of *C. elegans* was performed on alive animals anaesthetised with 250 mM sodium azide or immobilised with a 2.5% (w/v) polystyrene bead solution (Polyscience, Inc.). For both options, a 3% agarose solution in double-distilled water was prepared and aliquoted into 1.5 ml tubes. Solid 3% agarose was stored at 4°C and was dissolved at 95°C in a heating block prior to imaging. 200 µl of the melted agarose

was pipetted onto a glass slide and a second glass slide was placed on top, which was carefully removed after the agarose pad had solidified. 10-20 µl of sodium azide (250 mM) or polystyrene beads were pipetted onto the agarose pad and 5-7 nematodes were picked into the droplet. An eyelash was used to remove residual bacteria and to separate nematodes from each other. For the bead option, a 2 µl droplet of polystyrene beads was applied on top of the nematodes before placing a coverslip on top. Before placing the coverslip on the nematodes in sodium azide, the nematodes were allowed to immobilise for 30-60 seconds without the coverslip.

6.4.2 Confocal fluorescence microscopy

Confocal images were acquired using a laser-scanning microscope LSM-880 (Zeiss). The objectives were either 'EC Plan-Neofluar 10x/0.3 M27' or 'Plan-Apochromat 40x/1.4 Oil DIC M27'. Excitation of GFP/GCaMP6m was achieved using an argon laser at 488 nm, while mScarlet was excited by a HeNe laser at 543 nm. The laser power was set to 2%, and the master gain was calibrated for each experiment, fluorophore, and magnification to prevent pixel saturation. The digital gain was set to 1.0, and the pinhole was adjusted between 2 and 16.57 AU. Transmitted-light images of the nematodes (T-PMT transmission) were superimposed with fluorescent images. The pixel dimensions of the images were 2048 × 2048 or 1024 × 1024, with a pixel depth of 16 bits. To ensure the reliability of the quantitative measurements, the parameters, particularly the gain, were kept consistent throughout the experimental procedure.

6.4.3 Fluorescence lifetime imaging microscopy

The fluorescence lifetime was measured by correlated single photon counting (TCSPC) using a confocal laser scanning microscope LSM-880 (Zeiss) that was coupled to a pulsed laser (PicoQuant). The FLIM setup comprised several components, including a PDL 828-S Sepia with a diode laser, a Timeharp260 TCSPC unit and two PMS-hybrid detection units. To assess the aggregation of mScarlet-tagged $A\beta_{1-42}$ or Tau, mScarlet was excited at 560 nm with a pulsed laser at 40 MHz and 60% laser intensity. Emission was measured from 575 - 625 nm. The nematodes were mounted onto an agarose pad and anaesthetised with sodium azide, as described above. A 'Plan-Apochromat 40x/1.4 Oil DIC M27' objective was employed to measure the fluorescence lifetime in the head neurons situated between the

metacorpus and the terminal bulb of the pharynx. The frame size was 512 × 512 pixels with a pixel size of 0.231 µm and a digital zoom of 1.8. Image recording was performed until 3000 counts were accumulated in the brightest pixel using the SymPho Time 64 software (PicoQuant). The measurement settings were maintained consistently across all strains and conditions. The internal response function (IRF) was recorded using Erythrosine B. Data analysis was performed using FlimFit software (version 5.1.1) (Warren et al., 2013) applying pixel-wise fitting. The IRF was uploaded and aligned. The integrated value was set to 30 with laser repetition rate set to 40 MHz. The monoexponential decay model was selected and the data were fitted between 1500 and 4000 picoseconds.

6.4.4 Polydimethylsiloxane (PDMS) microchannels fabrication for imaging nGCaMP6m intensity

The recording of nGCaMP6m intensities was performed on living animals that were trapped within polydimethylsiloxane (PDMS) microfluidic channels. To prepare the PDMS, Sylgard 184 curing agent and Sylgard 184 base elastomer (Dow) were combined in a 1:10 ratio (w/w) followed by vigorous mixing for 5 minutes. The mixture was then poured over the SU-8 mold and the PDMS was placed into a desiccator. The degassing of the PDMS was performed by multiple repeats of evacuating and re-evacuating of the desiccator for about 30 minutes, until no air bubbles were visible within the PDMS. The PDMS was allowed to solidify in an oven at 50°C overnight, before being cut and carefully peeled off the wafer. The wafer-sised PDMS was then separated into single devices using a razor blade. Inlets and outlets of 1.5 mm were applied using a biopsy punch (Ted Pella). Dust was removed from individual devices using tape before being cleaned using soap water (Decon 90, Decon Laboratories), 70% ethanol and ultrapure water. To remove any residual water or ethanol, PDMS devices were dried using compressed air and incubated on a hot plate at 120°C for 5 minutes. Bonding of PDMS devices to glass coverslips (No. 1.5) was performed using a plasma asher (Zepto, Diener Electronic). For that, the surfaces of the glass and the PDMS were exposed to the air plasma for 30 seconds before being brought into contact immediately under gentle pressure. The bond was then stabilised by baking the devices at 80°C for 5 minutes on a hotplate. To load the nematodes into the PDMS channels, a 1 ml low-binding pipette tip was placed at the inlet and a syringe with a

flexible tubing was added at the outlet. The syringe was filled with M9 medium, and the channels were flushed from the outlet until the pipette at the inlet was filled halfway. The nematodes were picked from the plates into the M9 reservoir within the pipette tip and the animals were allowed to sink by gravity. By pulling slightly on the syringe, the nematodes entered the device and were separated into the microchannels, where they were trapped along the side of the body.

6.4.5 Widefield fluorescence microscopy for imaging GCaMP6m intensity

GCaMP6m intensities of nematodes were recorded on days 4, 7, and 10 of life, with day 1 being the day of synchronisation. Nematodes were synchronised and grown to the desired age and loaded onto the fabricated PDMS microfluidic devices as described above in groups of up to six animals. For day 4-old nematodes, channels with a width of 40 µm were used while older animals (day 7 and day 10) were imaged in 60 µm wide channels. Images of individual nematodes were taken using a custom-built widefield microscope (IX83, Olympus) equipped with an sCMOS camera (Zyla 5.5, Andor) and a 10x objective (Plan N 10x / 0.25, Olympus). GCaMP6m was excited at 470 nm by a four-wavelength high-power light-emitting diode light source (LED4D067, Thorlabs). To record GCaMP6m of individual nematodes, two sets of image series of 10 images each were acquired with an exposure time of 170 milliseconds using the software Micro-Manager software (Edelstein et al., 2014). Additionally, one brightfield image series of each nematode was taken with an exposure time of 10 ms taken as a reference. Fluorescence intensities of individual nematodes were quantified using Fiji. Normalisation of the acquired GCaMP6m intensities to the GCaMP6m protein levels was performed to account for varying GCaMP6m expressions of different strains. Based on the GAPDH-normalised GCAMP6m protein levels, a normalisation factor was calculated by dividing the mean expression level of control nematodes (i.e., neuronal or muscular expressing mScarlet strains) by the value for Abeta/Tau-expressing nematodes for day 4, 7, and 10 respectively. Subsequently, the GCaMP6m intensity values were multiplied by the normalisation factor, resulting in GCaMP6m intensities normalised to protein levels.

nGCAMP6m intensities of nemadipine A- and DMSO-treated animals were recorded using a confocal laser-scanning microscope LSM-880 (Zeiss). Animals were

immobilised on a glass slide containing a 10% agarose pad using 0.1 µm polystyrene microbeads (Polyscience 00876-15). Analysis and normalisation were performed as described above.

6.4.6 Quantification of fluorescence intensity using Fiji

Intensities of fluorescent proteins or fluorescently labelled proteins were quantified from raw confocal images. For this, images were uploaded to Fiji (Schindelin et al., 2012) and opened as hyperstacks in composite colour mode. The region of interest (ROI), which was either the whole nematode or the head region, was selected using the rectangle drawing tool. Area, integrated density, mean grey and minimum and maximum grey value, were selected from the set measurement option. The quantification in the ROI was performed by clicking 'Measure'. Five background regions without fluorescence were selected and quantified, keeping the dimensions of the rectangle constant for each region. The data obtained were copied to Excel and the fluorescence intensity was calculated as corrected total cell fluorescence (CTCF):

$$CTCF = Integrated\ density\ (ROI) - (Area\ (ROI)\ x\ averaged\ intensity\ of\ background\ readings) \quad \text{(equation 3)}$$

6.5 Statistical analysis

Statistical analysis was performed with GraphPad Prism version 9. Normality was tested using the D'Agostino-Pearson normality test. Student's t-test with Welch's correction or one/two-way ANOVA with Bonferroni post hoc test were used as parametric tests. Non-parametric tests used were Mann-Whitney-U test or Kruskal-Wallis test with Dunn's post hoc test. Significance for lifespan analysis was tested using the Oasis2 online tool (Han et al., 2016). For all datasets p-values were chosen as: ns = $p > 0.5$; * = $p \leq 0.05$; ** = $p \leq 0.01$; *** = $p \leq 0.001$; **** = $p \leq 0.0001$.

7 REFERENCES

Altun, Z. F., & Hall, D. H. (2012). Introduction to *C. elegans* anatomy. In *WormAtlas*.

Alvarez, J., Alvarez-Illera, P., Santo-Domingo, J., Fonteriz, R. I., & Montero, M. (2022). Modeling Alzheimer's Disease in *Caenorhabditis elegans*. *Biomedicines*. https://doi.org/10.3390/biomedicines10020288.

Alzheimer, A. (1907). Über eine eigenartige Erkankung der Hirnrinde. *Clinical Anatomy*. https://doi.org/10.1002/ca.980080612.

Aman, Y., Schmauck-Medina, T., Hansen, M., Morimoto, R. I., Simon, A. K., Bjedov, I., Palikaras, K., Simonsen, A., Johansen, T., Tavernarakis, N., Rubinsztein, D. C., Partridge, L., Kroemer, G., Labbadia, J., & Fang, E. F. (2021). Autophagy in healthy aging and disease. *Nature Aging*. https://doi.org/10.1038/s43587-021-00098-4.

Amro, Z., Yool, A. J., & Collins-Praino, L. E. (2021). The potential role of glial cells in driving the prion-like transcellular propagation of tau in Tauopathies. *Brain, Behavior, and Immunity - Health*. https://doi.org/10.1016/j.bbih.2021.100242.

Anderson, J. L., Morran, L. T., & Phillips, P. C. (2010). Outcrossing and the maintenance of males within *C. elegans* populations. *Journal of Heredity*. https://doi.org/10.1093/jhered/esq003.

Andorfer, C., Acker, C. M., Kress, Y., Hof, P. R., Duff, K., & Davies, P. (2005). Cell-cycle reentry and cell death in transgenic mice expressing nonmutant human tau isoforms. *Journal of Neuroscience*. https://doi.org/10.1523/JNEUROSCI.4637-04.2005.

Andronesi, O. C., Von Bergen, M., Biernat, J., Seidel, K., Griesinger, C., Mandelkow, E., & Baldus, M. (2008). Characterization of Alzheimer's-like paired helical filaments from the core domain of tau protein using solid-state NMR spectroscopy. *Journal of the American Chemical Society*. https://doi.org/10.1021/ja7100517.

Aquino Nunez, W., Combs, B., Gamblin, T. C., & Ackley, B. D. (2022). Age-dependent accumulation of tau aggregation in *Caenorhabditis elegans*. *Frontiers in Aging*. https://doi.org/10.3389/fragi.2022.928574.

Ayala Mariscal, S. M., Pigazzini, M. L., Richter, Y., Özel, M., Grothaus, I. L., Protze, J., Ziege, K., Kulke, M., ElBediwi, M., Vermaas, J. V., Colombi Ciacchi, L., Köppen, S., Liu, F., & Kirstein, J. (2022). Identification of a HTT-specific binding motif in

DNAJB1 essential for suppression and disaggregation of HTT. *Nature Communications*. https://doi.org/10.1038/s41467-022-32370-5.

Ayala Mariscal, S. M., & Kirstein, J. (2021). J-domain proteins interaction with neurodegenerative disease-related proteins. *Experimental Cell Research*. https://doi.org/10.1016/j.yexcr.2021.112491.

Ayton, S., & Bush, A. I. (2021). β-amyloid: The known unknowns. *Ageing Research Reviews*. https://doi.org/10.1016/j.arr.2020.101212.

Becker, W. (2012). Fluorescence lifetime imaging - techniques and applications. *Journal of Microscopy*. https://doi.org/10.1111/j.1365-2818.2012.03618.x.

Ben-Zvi, A., Miller, E. A., & Morimoto, R. I. (2009). Collapse of proteostasis represents an early molecular event in *Caenorhabditis elegans* aging. *PNAS*. https://doi.org/10.1073/pnas.0902882106.

Bindels, D. S., Haarbosch, L., Van Weeren, L., Postma, M., Wiese, K. E., Mastop, M., Aumonier, S., Gotthard, G., Royant, A., Hink, M. A., & Gadella, T. W. J. (2016). MScarlet: A bright monomeric red fluorescent protein for cellular imaging. *Nature Methods*. https://doi.org/10.1038/nmeth.4074.

Braak, H, & Braak, E. (1991). Neuropathological stageing of Alzheimer-related changes. *Acta Neuropathologica*. https://doi.org/10.1007/BF00308809.

Braak, H., Alafuzoff, I., Arzberger, T., Kretzschmar, H., & Tredici, K. (2006). Staging of Alzheimer disease-associated neurofibrillary pathology using paraffin sections and immunocytochemistry. *Acta Neuropathologica*. https://doi.org/10.1007/s00401-006-0127-z.

Braun, J. E. A. (2023). Extracellular chaperone networks and the export of J-domain proteins. *Journal of Biological Chemistry*. https://doi.org/10.1016/j.jbc.2022.102840.

Brehme, M., Voisine, C., Rolland, T., Wachi, S., Soper, J. H., Zhu, Y., Orton, K., Villella, A., Garza, D., Vidal, M., Ge, H., & Morimoto, R. I. (2014). A chaperome subnetwork safeguards proteostasis in aging and neurodegenerative disease. *Cell Reports*. https://doi.org/10.1016/j.celrep.2014.09.042.

Brenner, S. (1973). The Genetics of Behaviour. *British Medical Bulletin*. https://doi.org/10.1093/oxfordjournals.bmb.a071019.

Brunello, C. A., Merezhko, M., Uronen, R. L., & Huttunen, H. J. (2020). Mechanisms of secretion and spreading of pathological tau protein. *Cellular and Molecular Life Sciences*. https://doi.org/10.1007/s00018-019-03349-1.

Buchholz, S., & Zempel, H. (2024). The six brain-specific TAU isoforms and their role in Alzheimer's disease and related neurodegenerative dementia syndromes. *Alzheimer's and Dementia*. https://doi.org/10.1002/alz.13784.

Busche, M. A., Chen, X., Henning, H. A., Reichwald, J., Staufenbiel, M., Sakmann, B., & Konnerth, A. (2012). Critical role of soluble amyloid-β for early hippocampal hyperactivity in a mouse model of Alzheimer's disease. *Proceedings of the National Academy of Sciences of the United States of America*. https://doi.org/10.1073/pnas.1206171109.

Busche, M. A., Eichhoff, G., Adelsberger, H., Abramowski, D., Wiederhold, Ka.-H., Haass, C., Staufenbiel, M., Konnerth, A., & Garaschuk, O. (2003). Clusters of Hyperactive Neurons Near Amyloid Plaques in a Mouse Model of Alzheimer's Disease. *Science*. https://doi.org/10.1126/science.1157052.

Busche, M. A., & Konnerth, A. (2016). Impairments of neural circuit function in Alzheimer's disease. *Philosophical Transactions of the Royal Society B: Biological Sciences*. https://doi.org/10.1098/rstb.2015.0429.

Calahorro, F., & Izquierdo, P. G. (2018). The presynaptic machinery at the synapse of *C. elegans*. In *Invertebrate Neuroscience* (Vol. 18, Issue 2). Springer Verlag. https://doi.org/10.1007/s10158-018-0207-5.

Chaplot, K., Jarvela, T. S., & Lindberg, I. (2020). Secreted Chaperones in Neurodegeneration. *Frontiers in Aging Neuroscience*. https://doi.org/10.3389/fnagi.2020.00268.

Chen, T. W., Wardill, T. J., Sun, Y., Pulver, S. R., Renninger, S. L., Baohan, A., Schreiter, E. R., Kerr, R. A., Orger, M. B., Jayaraman, V., Looger, L. L., Svoboda, K., & Kim, D. S. (2013). Ultrasensitive fluorescent proteins for imaging neuronal activity. *Nature*. https://doi.org/10.1038/nature12354.

Chew, Y. L., Fan, X., Götz, J., & Nicholas, H. R. (2013). PTL-1 regulates neuronal integrity and lifespan in *C. elegans. Journal of Cell Science*. https://doi.org/10.1242/jcs.jcs124404.

Cho, J. Y., Choi, T. W., Kim, S. H., Ahnn, J., & Lee, S. K. (2021). Morphological characterization of small, dumpy, and long phenotypes in *Caenorhabditis elegans*. *Molecules and Cells*. https://doi.org/10.14348/molcells.2021.2236.

Cleveland, D. W., Hwo, S.-Y., & Kirschner, M. W. (1977). Purification of Tau, a Microtubule-associated Protein that Induces Assembly of Microtubules from

Purified Tubulin. *Journal of Molecular Biology*. https://doi.org/10.1016/0022-2836(77)90213-3.

Cline, E. N., Bicca, M. A., Viola, K. L., & Klein, W. L. (2018). The Amyloid-β Oligomer Hypothesis: Beginning of the Third Decade. *Journal of Alzheimer's Disease*. https://doi.org/10.3233/JAD-179941.

Cohen, S. I. A., Linse, S., Luheshi, L. M., Hellstrand, E., White, D. A., Rajah, L., Otzen, D. E., Vendruscolo, M., Dobson, C. M., & Knowles, T. P. J. (2013). Proliferation of amyloid-β42 aggregates occurs through a secondary nucleation mechanism. *Proceedings of the National Academy of Sciences of the United States of America*. https://doi.org/10.1073/pnas.1218402110.

Cook, S. J., Jarrell, T. A., Brittin, C. A., Wang, Y., Bloniarz, A. E., Yakovlev, M. A., Nguyen, K. C. Q., Tang, L. T. H., Bayer, E. A., Duerr, J. S., Bülow, H. E., Hobert, O., Hall, D. H., & Emmons, S. W. (2019). Whole-animal connectomes of both *Caenorhabditis elegans* sexes. *Nature*. https://doi.org/10.1038/s41586-019-1352-7.

Corsi, A. K. (2015). A Transparent window into biology: A primer on *Caenorhabditis elegans*. *WormBook*. https://doi.org/10.1895/wormbook.1.177.1.

Crimins, J. L., Rocher, A. B., & Luebke, J. I. (2012). Electrophysiological changes precede morphological changes to frontal cortical pyramidal neurons in the rTg4510 mouse model of progressive tauopathy. *Acta Neuropathologica*. https://doi.org/10.1007/s00401-012-1038-9.

Crnich, E., Lullo, R., Tabaka, A., Havens, M. A., & Kissel, D. S. (2021). Interactions of copper and copper chelate compounds with the amyloid beta peptide: An investigation into electrochemistry, reactive oxygen species and peptide aggregation. *Journal of Inorganic Biochemistry*. https://doi.org/10.1016/j.jinorgbio.2021.111493.

Cummings, R. D., Chiffoleau, E., van Kooyk, Y., & McEver, R. P. (2022). C-Type Lectins. In *Essentials of Glycobiology*. Cold Spring Harbor Laboratory Press. https://doi.org/10.1101/glycobiology.4e.34.

Daigle, I., & Li, C. (1993). apl-1, a *Caenorhabditis elegans* gene encoding a protein related to the human beta-amyloid protein precursor. *PNAS*. https://doi.org/10.1073/pnas.90.24.12045.

David, D. C., Ollikainen, N., Trinidad, J. C., Cary, M. P., Burlingame, A. L., & Kenyon, C. (2010). Widespread protein aggregation as an inherent part of aging in *C. elegans*. *PLOS Biology*. https://doi.org/10.1371/journal.pbio.1000450.

De Felice, F. G., Velasco, P. T., Lambert, M. P., Viola, K., Fernandez, S. J., Ferreira, S. T., & Klein, W. L. (2007). Aβ oligomers induce neuronal oxidative stress through an N-methyl-D-aspartate receptor-dependent mechanism that is blocked by the Alzheimer drug memantine. *Journal of Biological Chemistry*. https://doi.org/10.1074/jbc.M607483200.

Dorman, J. B., Albinder, B., Shroyer, T., & Kenyon, C. (1995). The age-1 and daf-2 Genes Function in a Common Pathway to Control the Lifespan of *Caenorhabditis elegans*. *Genetics*. https://doi.org/10.1093/genetics/141.4.1399.

Dregni, A. J., Mandala, V. S., Wu, H., Elkins, M. R., Wang, H. K., Hung, I., DeGrado, W. F., & Hong, M. (2019). In vitro 0N4R tau fibrils contain a monomorphic β-sheet core enclosed by dynamically heterogeneous fuzzy coat segments. *Proceedings of the National Academy of Sciences of the United States of America*. https://doi.org/10.1073/pnas.1906839116.

Dumanchin, C., Camuzat, A., Campion, D., Verpillat, P., Hannequin, D., Dubois, B., Saugier-Veber, P., Martin, C., Penet, C., Charbonnier, F., Agid, Y., Frebourg, T., & Brice, A. (1998). Segregation of a missense mutation in the microtubule-associated protein tau gene with familial frontotemporal dementia and parkinsonism. *Human Molecular Genetics*. https://doi.org/10.1093/hmg/7.11.1825.

Edelstein, A. D., Tsuchida, M. A., Amodaj, N., Pinkard, H., Vale, R. D., & Stuurman, N. (2014). Advanced methods of microscope control using μManager software. *Journal of Biological Methods*. https://doi.org/10.14440/jbm.2014.36.

Ewald, C. Y., Raps, D. A., & Li, C. (2012). APL-1, the Alzheimer's Amyloid precursor protein in *Caenorhabditis elegans*, modulates multiple metabolic pathways throughout development. *Genetics*. https://doi.org/10.1534/genetics.112.138768.

Fani, G., Mannini, B., Vecchi, G., Cascella, R., Cecchi, C., Dobson, C. M., Vendruscolo, M., & Chiti, F. (2021). Aβ Oligomers Dysregulate Calcium Homeostasis by Mechanosensitive Activation of AMPA and NMDA Receptors. *ACS Chemical Neuroscience*. https://doi.org/10.1021/acschemneuro.0c00811.

Fares, H., & Greenwald, I. (2001). Genetic Analysis of Endocytosis in *Caenorhabditis elegans*: Coelomocyte Uptake Defective Mutants. *Genetics*. https://doi.org/10.1093/genetics/159.1.133.

Fatouros, C., Pir, G. J., Biernat, J., Koushika, S. P., Mandelkow, E., Mandelkow, E. M., Schmidt, E., & Baumeister, R. (2012). Inhibition of Tau aggregation in a novel *Caenorhabditis elegans* model of tauopathy mitigates proteotoxicity. *Human Molecular Genetics*. https://doi.org/10.1093/hmg/dds190.

Fedele, E. (2023). Anti-Amyloid Therapies for Alzheimer's Disease and the Amyloid Cascade Hypothesis. *International Journal of Molecular Sciences*. https://doi.org/10.3390/ijms241914499.

Fu, H., Rodriguez, G. A., Herman, M., Emrani, S., Nahmani, E., Barrett, G., Figueroa, H. Y., Goldberg, E., Hussaini, S. A., & Duff, K. E. (2017). Tau Pathology Induces Excitatory Neuron Loss, Grid Cell Dysfunction, and Spatial Memory Deficits Reminiscent of Early Alzheimer's Disease. *Neuron*. https://doi.org/10.1016/j.neuron.2016.12.023.

Gallotta, I., Sandhu, A., Peters, M., Haslbeck, M., Jung, R., Agilkaya, S., Blersch, J. L., Rödelsperger, C., Röseler, W., Huang, C., Sommer, R. J., & David, D. C. (2020). Extracellular proteostasis prevents aggregation during pathogenic attack. *Nature*. https://doi.org/10.1038/s41586-020-2461-z.

Gallrein, C., Ilburg, M., Michelberger, T., Kocak, A., Puchkov, D., Lio, F., Mariscal, S. M. A., Nayak, T., Schierle, G. S. K., & Kirstein, J. (2021). Novel amyloid-beta pathology *C. elegans* model reveals distinct neurons as seeds of pathogenicity. *Progress in Neurobiology*. https://doi.org/10.1016/j.pneurobio.2020.101907.

Gallrein, C., Williams, A. B., Meyer, D. H., Messling, J. E., Garcia, A., & Schumacher, B. (2023). baz-2 enhances systemic proteostasis in vivo by regulating acetylcholine metabolism. *Cell Reports*. https://doi.org/10.1016/j.celrep.2023.113577.

Gao, X., Carroni, M., Nussbaum-Krammer, C., Mogk, A., Nillegoda, N. B., Szlachcic, A., Guilbride, D. L., Saibil, H. R., Mayer, M. P., & Bukau, B. (2015). Human Hsp70 Disaggregase Reverses Parkinson's-Linked α-Synuclein Amyloid Fibrils. *Molecular Cell*. https://doi.org/10.1016/j.molcel.2015.07.012.

Geraghty, N. J., Satapathy, S., Kelly, M., Cheng, F., Lee, A., & Wilson, M. R. (2021). Expanding the family of extracellular chaperones: Identification of human plasma

proteins with chaperone activity. *Protein Science*. https://doi.org/10.1002/pro.4189.

Giorgio, J., Adams, J. N., Maass, A., Jagust, W. J., & Breakspear, M. (2024). Amyloid induced hyperexcitability in default mode network drives medial temporal hyperactivity and early tau accumulation. *Neuron*. https://doi.org/10.1016/j.neuron.2023.11.014.

Glass, D. J., & Arnold, S. E. (2012). Some evolutionary perspectives on Alzheimer's disease pathogenesis and pathology. *Alzheimer's and Dementia*. https://doi.org/10.1016/j.jalz.2011.05.2408.

Glenner, G. G., & Wong, C. W. (1984). Alzheimer's Disease: Initial report of the purification and characterization of a novel cerebrovascular amyloid protein. *Biochemical and Biophysical Research Communication*. https://doi.org/10.1016/s0006-291x(84)80190-4.

Goedert, M, Baur, C. P., Ahringer, J., Jakes, R., Hasegawa, M., Spillantini, M. G., Smith, M. J., & Hill, F. (1996). PTL-1, a microtubule-associated protein with tau-like repeats from the nematode *Caenorhabditis elegans*. *Journal of Cell Science*. https://doi.org/10.1242/jcs.109.11.2661.

Goedert, M. (2005). Tau gene mutations and their effects. *Movement Disorders*. https://doi.org/10.1002/mds.20539.

Gómez-Isla, T., Hollister, R., West, H., Mui, S., Growdon, J. H., Petersen, R. C., Parisi, J. E., & Hyman, B. T. (1997). Neuronal loss correlates with but exceeds neurofibrillary tangles in Alzheimer's disease. *Annals of Neurology*. https://doi.org/10.1002/ana.410410106.

Good, S., & van Oosten-Hawle, P. (2020). *Caenorhabditis elegans* as a model organism for protein homeostasis diseases. In *Protein Homeostasis Diseases: Mechanisms and Novel Therapies* (pp. 41–69). Elsevier. https://doi.org/10.1016/B978-0-12-819132-3.00003-8.

Gordon, P., Hingula, L., Krasny, M. L., Swienckowski, J. L., Pokrywka, N. J., & Raley-Susman, K. M. (2008). The invertebrate microtubule-associated protein PTL-1 functions in mechanosensation and development in *Caenorhabditis elegans*. *Development Genes and Evolution*. https://doi.org/10.1007/s00427-008-0250-z.

Hampel, H., Hardy, J., Blennow, K., Chen, C., Perry, G., Kim, S. H., Villemagne, V. L., Aisen, P., Vendruscolo, M., Iwatsubo, T., Masters, C. L., Cho, M., Lannfelt, L.,

Cummings, J. L., & Vergallo, A. (2021). The Amyloid-β Pathway in Alzheimer's Disease. *Molecular Psychiatry*. https://doi.org/10.1038/s41380-021-01249-0.

Han, S. K., Lee, D., Lee, H., Kim, D., Son, H. G., Yang, J.-S., Lee, S.-J. V, & Kim, S. (2016). OASIS 2: online application for survival analysis 2 with features for the analysis of maximal lifespan and healthspan in aging research. *Oncotarget*. https://doi.org/10.18632/oncotarget.11269.

Hard, J. A., & Higgins, G. A. (1992). Alzheimer's Disease: The Amyloid Cascade Hypothesis. *Science*. https://doi.org/10.1126/science.1566067.

Hartl, F. U., Bracher, A., & Hayer-Hartl, M. (2011). Molecular chaperones in protein folding and proteostasis. *Nature*. https://doi.org/10.1038/nature10317.

Hatch, R. J., Wei, Y., Xia, D., & Götz, J. (2017). Hyperphosphorylated tau causes reduced hippocampal CA1 excitability by relocating the axon initial segment. *Acta Neuropathologica*. https://doi.org/10.1007/s00401-017-1674-1.

Hattori, A., Mizuno, T., Akamatsu, M., Hisamoto, N., & Matsumoto, K. (2013). The *Caenorhabditis elegans* JNK Signalling Pathway Activates Expression of Stress Response Genes by Derepressing the Fos/HDAC Repressor Complex. *PLOS Genetics*. https://doi.org/10.1371/journal.pgen.1003315.

Hillier, L. D. W., Coulson, A., Murray, J. I., Bao, Z., Sulston, J. E., & Waterston, R. H. (2005). Genomics in *C. elegans*: So many genes, such a little worm. *Genome Research*. https://doi.org/10.1101/gr.3729105.

Hipp, M. S., & Hartl, F. U. (2024). Interplay of Proteostasis Capacity and Protein Aggregation: Implications for Cellular Function and Disease. *Journal of Molecular Biology*. https://doi.org/10.1016/j.jmb.2024.168615.

Hipp, M. S., Kasturi, P., & Hartl, F. U. (2019). The proteostasis network and its decline in ageing. *Nature Reviews Molecular Cell Biology*. https://doi.org/10.1038/s41580-019-0101-y.

Hulme, S. E., Shevkoplyas, S. S., Apfeld, J., Fontana, W., & Whitesides, G. M. (2007). A microfabricated array of clamps for immobilizing and imaging *C. elegans*. *Lab on a Chip*. https://doi.org/10.1039/b707861g.

Humphreys, D. T., Carver, J. A., Easterbrook-Smith, S. B., & Wilson, M. R. (1999). Clusterin has chaperone-like activity similar to that of small heat shock proteins. *Journal of Biological Chemistry*. https://doi.org/10.1074/jbc.274.11.6875.

Hutton, M., Lendon, C. L., Rizzu, P., Baker, M., Froelich, S., Houlden, H., Pickering-Brown, S., Chakraverty, S., Isaacs, A., Grover, A., Hackett, J., Adamson, J.,

Lincoln, S., Dickson, D., Davies, P., Petersen, R. C., Stevens, M., De Graaff, E., Wauters, E., … Heutink, P. (1998). Association of missense and 5-splice-site mutations in tau with the inherited dementia FTDP-17. *Nature*. https://doi.org/10.1212/wnl.56.suppl_4.s21.

Irwin, R., Faust, O., Petrovic, I., Wolf, S. G., Hofmann, H., & Rosenzweig, R. (2021). Hsp40s play complementary roles in the prevention of tau amyloid formation. *ELife*. https://doi.org/10.7554/ELIFE.69601.

Itakura, E., Chiba, M., Murata, T., & Matsuura, A. (2020). Heparan sulfate is a clearance receptor for aberrant extracellular proteins. *Journal of Cell Biology*. https://doi.org/10.1083/JCB.201911126.

Janowska, M. K., Baughman, H. E. R., Woods, C. N., & Klevit, R. E. (2019). Mechanisms of small heat shock proteins. *Cold Spring Harbor Perspectives in Biology*. https://doi.org/10.1101/cshperspect.a034025.

Ji, G., Feldman, M. E., Deng, K. Y., Greene, K. S., Wilson, J., Lee, J. C., Johnston, R. C., Rishniw, M., Tallini, Y., Zhang, J., Wier, W. G., Blaustein, M. P., Xin, H. B., Nakai, J., & Kotlikoff, M. I. (2004). Ca2+-sensing transgenic mice: Postsynaptic signalling in smooth muscle. *Journal of Biological Chemistry*. https://doi.org/10.1074/jbc.M401084200.

Johansson, A. S., Berglind-Dehlin, F., Karlsson, G., Edwards, K., Gellerfors, P., & Lannfelt, L. (2006). Physiochemical characterization of the Alzheimer's disease-related peptides Aβ1-42Arctic and Aβ1-42wt. *FEBS Journal*. https://doi.org/10.1111/j.1742-4658.2006.05263.x.

Jongsma, E., Goyala, A., Mateos, J. M., & Ewald, C. Y. (2023). Removal of extracellular human amyloid beta aggregates by extracellular proteases in *C. elegans* . *ELife*. https://doi.org/10.7554/ELIFE.83465.

Jucker, M., & Walker, L. C. (2013). Self-propagation of pathogenic protein aggregates in neurodegenerative diseases. *Nature*. https://doi.org/10.1038/nature12481.

Kaminski Schierle, G. S., Bertoncini, C. W., Chan, F. T. S., Van Der Goot, A. T., Schwedler, S., Skepper, J., Schlachter, S., Van Ham, T., Esposito, A., Kumita, J. R., Nollen, E. A. A., Dobson, C. M., & Kaminski, C. F. (2011). A FRET sensor for non-invasive imaging of amyloid formation in vivo. *ChemPhysChem*. https://doi.org/10.1002/cphc.201000996.

Kampinga, H. H., Hageman, J., Vos, M. J., Kubota, H., Tanguay, R. M., Bruford, E. A., Cheetham, M. E., Chen, B., & Hightower, L. E. (2009). Guidelines for the

nomenclature of the human heat shock proteins. *Cell Stress and Chaperones*. https://doi.org/10.1007/s12192-008-0068-7.

Klyucherev, T. O., Olszewski, P., Shalimova, A. A., Chubarev, V. N., Tarasov, V. V., Attwood, M. M., Syvänen, S., & Schiöth, H. B. (2022). Advances in the development of new biomarkers for Alzheimer's disease. *Translational Neurodegeneration*. https://doi.org/10.1186/s40035-022-00296-z.

Knopman, D. S., Amieva, H., Petersen, R. C., Chételat, G., Holtzman, D. M., Hyman, B. T., Nixon, R. A., & Jones, D. T. (2021). Alzheimer disease. *Nature Reviews Disease Primers*. https://doi.org/10.1038/s41572-021-00269-y.

Knowles, T. P. J., Vendruscolo, M., & Dobson, C. M. (2014). The amyloid state and its association with protein misfolding diseases. *Nature Reviews Molecular Cell Biology*. https://doi.org/10.1038/nrm3810.

Kosik, K. S., Joachim, C. L., & Selkoe, D. J. (1986). Microtubule-associated protein tau (T) is a major antigenic component of paired helical filaments in Alzheimer disease. *PNAS*. https://doi.org/10.1073/pnas.83.11.4044.

Kraemer, B. C., Burgess, J. K., Chen, J. H., Thomas, J. H., & Schellenberg, G. D. (2006). Molecular pathways that influence human tau-induced pathology in *Caenorhabditis elegans*. *Human Molecular Genetics*. https://doi.org/10.1093/hmg/ddl067.

Kraemer, B. C., & Schellenberg, G. D. (2007). SUT-1 enables tau-induced neurotoxicity in *C. elegans*. *Human Molecular Genetics*. https://doi.org/10.1093/hmg/ddm143.

Kraemer, B. C., Zhang, B., Leverenz, J. B., Thomas, J. H., Trojanowski, J. Q., & Schellenberg, G. D. (2003). Neurodegeneration and defective neurotransmission in a *Caenorhabditis elegans* model of tauopathy. *Proceedings of the National Academy of Sciences of the United States of America*. https://doi.org/10.1073/pnas.1533448100.

Kulenkampff, K., Wolf Perez, A. M., Sormanni, P., Habchi, J., & Vendruscolo, M. (2021). Quantifying misfolded protein oligomers as drug targets and biomarkers in Alzheimer and Parkinson diseases. *Nature Reviews Chemistry*. https://doi.org/10.1038/s41570-021-00254-9.

Kwok, T. C. Y., Ricker, N., Fraser, R., Chan, A. W., Burns, A., Stanley, E. F., McCourt, P., Cutler, S. R., & Roy, P. J. (2006). A small-molecule screen in *C. elegans* yields a new calcium channel antagonist. *Nature*. https://doi.org/10.1038/nature04657.

Labbadia, J., & Morimoto, R. I. (2014). Proteostasis and longevity: When does aging really begin? In *F1000Prime Reports* (Vol. 6). https://doi.org/10.12703/P6-7.

Labbadia, J., & Morimoto, R. I. (2014). Proteostasis and longevity: When does aging really begin? *F1000 Prime Reports*. https://doi.org/10.12703/P6-7.

Labbadia, J., & Morimoto, R. I. (2015). The biology of proteostasis in aging and disease. *Annual Review of Biochemistry*. https://doi.org/10.1146/annurev-biochem-060614-033955.

Lai, C.-H., Chou, C.-Y., Ch'ang, L.-Y., Liu, C.-S., & Lin, W.-C. (2000). Identification of Novel Human Genes Evolutionarily Conserved in *Caenorhabditis elegans* by Comparative Proteomics. *Genome Research*. https://doi.org/10.1101/gr.10.5.703.

Laine, R. F., Sinnige, T., Ma, K. Y., Haack, A. J., Poudel, C., Gaida, P., Curry, N., Perni, M., Nollen, E. A. A., Dobson, C. M., Vendruscolo, M., Kaminski Schierle, G. S., & Kaminski, C. F. (2019). Fast Fluorescence Lifetime Imaging Reveals the Aggregation Processes of α-Synuclein and Polyglutamine in Aging *Caenorhabditis elegans*. *ACS Chemical Biology*. https://doi.org/10.1021/acschembio.9b00354.

Lane, C. A., Hardy, J., & Schott, J. M. (2018). Alzheimer's disease. *European Journal of Neurology*. https://doi.org/10.1111/ene.13439.

Langer, F., Eisele, Y. S., Fritschi, S. K., Staufenbiel, M., Walker, L. C., & Jucker, M. (2011). Soluble aβ seeds are potent inducers of cerebral β-amyloid deposition. *Journal of Neuroscience*. https://doi.org/10.1523/JNEUROSCI.3088-11.2011.

Larsch, J., Ventimiglia, D., Bargmann, C. I., & Albrecht, D. R. (2013). High-throughput imaging of neuronal activity in *Caenorhabditis elegans*. *Proceedings of the National Academy of Sciences of the United States of America*. https://doi.org/10.1073/pnas.1318325110.

Lerdkrai, C., Asavapanumas, N., Brawek, B., Kovalchuk, Y., Mojtahedi, N., Del Moral, M. O., & Garaschuk, O. (2018). Intracellular Ca2+ stores control in vivo neuronal hyperactivity in a mouse model of Alzheimer's disease. *Proceedings of the National Academy of Sciences of the United States of America*. https://doi.org/10.1073/pnas.1714409115.

Levine, E., & Lee, K. S. (2020). Microfluidic approaches for *Caenorhabditis elegans* research. *Animal Cells and Systems*. https://doi.org/10.1080/19768354.2020.1837951.

Link, C. D. (1995). Expression of human beta-amyloid peptide in transgenic *Caenorhabditis elegans*. *PNAS*. https://www.pnas.org

Long, S., Benoist, C., & Weidner, W. (2023). *World Alzheimer Report 2023 Reducing dementia risk: never too early, never too late*. https://doi.org/https://www.alzint.org/resource/world-alzheimer-report-2023/.

Lu, J. X., Qiang, W., Yau, W. M., Schwieters, C. D., Meredith, S. C., & Tycko, R. (2013). Molecular structure of β-amyloid fibrils in alzheimer's disease brain tissue. *Cell*. https://doi.org/10.1016/j.cell.2013.08.035.

Lyon, M. S., & Milligan, C. (2019). Extracellular heat shock proteins in neurodegenerative diseases: New perspectives. *Neuroscience Letters*. https://doi.org/10.1016/j.neulet.2019.134462.

Mack, H. I. D., Heimbucher, T., & Murphy, C. T. (2018). The nematode *Caenorhabditis elegans* as a model for aging research. In *Drug Discovery Today: Disease Models* (Vol. 27, pp. 3–13). Elsevier Ltd. https://doi.org/10.1016/j.ddmod.2018.11.001.

Mahaman, Y. A. R., Embaye, K. S., Huang, F., Li, L., Zhu, F., Wang, J. Z., Liu, R., Feng, J., & Wang, X. (2022). Biomarkers used in Alzheimer's disease diagnosis, treatment, and prevention. *Ageing Research Reviews*. https://doi.org/10.1016/j.arr.2021.101544.

Malinverni, D., Zamuner, S., Rebeaud, M. E., Barducci, A., Nillegoda, N. B., & Rios, P. D. L. (2023). Data-driven large-scale genomic analysis reveals an intricate phylogenetic and functional landscape in J-domain proteins. *Proceedings of the National Academy of Sciences of the United States of America*. https://doi.org/10.1073/pnas.2218217120.

Mammeri, N. El, Duan, P., Dregni, A. J., & Hong, M. (2023). Amyloid fibril structures of tau: Conformational plasticity of the second microtubule-binding repeat. *Science Advances*. https://doi.org/10.1126/sciadv.adh4731.

Mannini, B., Cascella, R., Zampagni, M., Van Waarde-Verhagen, M., Meehan, S., Roodveldt, C., Campioni, S., Boninsegna, M., Penco, A., Relini, A., Kampinga, H. H., Dobson, C. M., Wilson, M. R., Cecchi, C., & Chiti, F. (2012). Molecular mechanisms used by chaperones to reduce the toxicity of aberrant protein oligomers. *Proceedings of the National Academy of Sciences of the United States of America*. https://doi.org/10.1073/pnas.1117799109.

McColl, G., Roberts, B. R., Gunn, A. P., Perez, K. A., Tew, D. J., Masters, C. L., Barnham, K. J., Cherny, R. A., & Bush, A. I. (2009). The *Caenorhabditis elegans*

Aβ1-42 model of Alzheimer disease predominantly Expresses Aβ 3-42. *Journal of Biological Chemistry*. https://doi.org/10.1074/jbc.C109.028514.

McCormick, A. V., Wheeler, J. M., Guthrie, C. R., Liachko, N. F., & Kraemer, B. C. (2013). Dopamine D2 receptor antagonism suppresses tau aggregation and neurotoxicity. *Biological Psychiatry*. https://doi.org/10.1016/j.biopsych.2012.08.027.

Meng, X., Song, Q., Liu, Z., Liu, X., Wang, Y., & Liu, J. (2024). Neurotoxic β-amyloid oligomers cause mitochondrial dysfunction—the trigger for PANoptosis in neurons. *Frontiers in Aging Neuroscience*. https://doi.org/10.3389/fnagi.2024.1400544.

Meraz-Ríos, M. A., Lira-De León, K. I., Campos-Peña, V., De Anda-Hernández, M. A., & Mena-López, R. (2010). Tau oligomers and aggregation in Alzheimer's disease. *Journal of Neurochemistry*. https://doi.org/10.1111/j.1471-4159.2009.06511.x.

Mesgarzadeh, J. S., Buxbaum, J. N., & Luke Wiseman, R. (2022). Stress-responsive regulation of extracellular proteostasis. *Journal of Cell Biology*. https://doi.org/10.1083/jcb.202112104.

Michel, C. H., Kumar, S., Pinotsi, D., Tunnacliffe, A., George-Hyslop, P. S., Mandelkow, E., Mandelkow, E. M., Kaminski, C. F., & Schierle, G. S. K. (2014). Extracellular monomeric tau protein is sufficient to initiate the spread of tau protein pathology. *Journal of Biological Chemistry*. https://doi.org/10.1074/jbc.M113.515445.

Midkiff, D., & San-Miguel, A. (2019). Microfluidic technologies for high throughput screening through sorting and on-chip culture of *C. elegans*. *Molecules*. https://doi.org/10.3390/molecules24234292.

Miles, J., Townend, S., Milonaitytė, D., Smith, W., Hodge, F., Westhead, D. R., & Oosten-Hawle, P. van. (2023). Transcellular chaperone signalling is an intercellular stress-response distinct from the HSF-1–mediated heat shock response. *PLOS Biology*. https://doi.org/10.1371/journal.pbio.3001605.

Miyasaka, T., Ding, Z., Gengyo-Ando, K., Oue, M., Yamaguchi, H., Mitani, S., & Ihara, Y. (2005). Progressive neurodegeneration in *C. elegans* model of tauopathy. *Neurobiology of Disease*. https://doi.org/10.1016/j.nbd.2005.03.017.

Mizuno, T., Hisamoto, N., Terada, T., Kondo, T., Adachi, M., Nishida, E., Kim, D. H., Ausubel, F. M., & Matsumoto, K. (2004). The *Caenorhabditis elegans* MAPK

phosphatase VHP-1 mediates a novel JNK-like signalling pathway in stress response. *EMBO Journal*. https://doi.org/10.1038/sj.emboj.7600226.

Mondal, S., Hegarty, E., Martin, C., Gökçe, S. K., Ghorashian, N., & Ben-Yakar, A. (2016). Large-scale microfluidics providing high-resolution and high-throughput screening of *Caenorhabditis elegans* poly-glutamine aggregation model. *Nature Communications*. https://doi.org/10.1038/ncomms13023.

Montresor, S., Pigazzini, M. L., Baskaran, S., Sleiman, M., Adhikari, G., Basilicata, L., Secker, L., Jacob, N., Ehlert, Y., Kelkar, A., Kalsi, G. K., Kulkarni, N., Spellerberg, P., & Kirstein, J. (2024). HSP110 is a modulator of amyloid beta (Aβ) aggregation and proteotoxicity. *Journal of Neurochemistry*. https://doi.org/10.1111/jnc.16214.

Morelli, F., Romeo, M., Barzago, M. M., Bolis, M., Mattioni, D., Rossi, G., Tagliavini, F., Bastone, A., Salmona, M., & Diomede, L. (2018). V363I and V363A mutated tau affect aggregation and neuronal dysfunction differently in *C. elegans*. *Neurobiology of Disease*. https://doi.org/10.1016/j.nbd.2018.06.018.

Morley, J. E., Farr, S. A., Banks, W. A., Johnson, S. N., Yamada, K. A., & Xu, L. (2009). A Physiological Role for Amyloid-beta Protein: Enhancement of Learning and Memory. *Journal of Alzheimer's Disease*. https://doi.org/10.3233/JAD-2009-1230.

Morsch, R. B., Simon, W., & Coleman, P. D. (1999). Neurons may live for decades with neurofibrillary tangles. *Jounrnal of Neuropathology and Experimental Neurology*. https://doi.org/10.1097/00005072-199902000-00008.

Mucke, L., Masliah, E., Yu, G.-Q., Mallory, M., Rockenstein, E. M., Tatsuno, G., Hu, K., Kholodenko, D., Johnson-Wood, K., & Mcconlogue, L. (2000). High-Level Neuronal Expression of A 1-42 in Wild-Type Human Amyloid Protein Precursor Transgenic Mice: Synaptotoxicity without Plaque Formation. *The Journal of Neuroscience*. https://doi.org/10.1523/JNEUROSCI.20-11-04050.2000.

Müller, U. C., Deller, T., & Korte, M. (2017). Not just amyloid: Physiological functions of the amyloid precursor protein family. *Nature Reviews Neuroscience*. https://doi.org/10.1038/nrn.2017.29.

Nachman, E., Wentink, A. S., Madiona, K., Bousset, L., Katsinelos, T., Allinson, K., Kampinga, H., McEwan, W. A., Jahn, T. R., Melki, R., Mogk, A., Bukau, B., & Nussbaum-Krammer, C. (2020). Disassembly of Tau fibrils by the human Hsp70 disaggregation machinery generates small seeding-competent species. *Journal of Biological Chemistry*. https://doi.org/10.1074/jbc.RA120.013478.

Nakai, J., Ohkura, M., & Imoto, K. (2001). A high signal-to-noise Ca2+ probe composed of a single green fluorescent protein. *Nature*. https://doi.org/10.1038/84397.

Narayan, P., Orte, A., Clarke, R. W., Bolognesi, B., Hook, S., Ganzinger, K. A., Meehan, S., Wilson, M. R., Dobson, C. M., & Klenerman, D. (2012). The extracellular chaperone clusterin sequesters oligomeric forms of the amyloid-β 1-40 peptide. *Nature Structural and Molecular Biology*. https://doi.org/10.1038/nsmb.2191.

Natale, C., Barzago, M. M., & Diomede, L. (2020). *Caenorhabditis elegans* Models to Investigate the Mechanisms Underlying Tau Toxicity in Tauopathies. *Brain Sciences*. https://doi.org/10.3390/brainsci10110838.

Nichols, E., Steinmetz, J. D., Vollset, S. E., Fukutaki, K., Chalek, J., Abd-Allah, F., Abdoli, A., Abualhasan, A., Abu-Gharbieh, E., Akram, T. T., Al Hamad, H., Alahdab, F., Alanezi, F. M., Alipour, V., Almustanyir, S., Amu, H., Ansari, I., Arabloo, J., Ashraf, T., … Vos, T. (2022). Estimation of the global prevalence of dementia in 2019 and forecasted prevalence in 2050: an analysis for the Global Burden of Disease Study 2019. *The Lancet Public Health*. https://doi.org/10.1016/S2468-2667(21)00249-8.

Nikolaidis, N., & Nei, M. (2004). Concerted and Nonconcerted Evolution of the Hsp70 Gene Superfamily in Two Sibling Species of Nematodes. *Molecular Biology and Evolution*. https://doi.org/10.1093/molbev/msh041.

Norambuena, A., Wallrabe, H., Cao, R., Wang, D. B., Silva, A., Svindrych, Z., Periasamy, A., Hu, S., Tanzi, R. E., Kim, D. Y., & Bloom, G. S. (2018). A novel lysosome-to-mitochondria signalling pathway disrupted by amyloid-β oligomers. *The EMBO Journal*. https://doi.org/10.15252/embj.2018100241.

Nussbaum-Krammer, C. I., Neto, M. F., Brielmann, R. M., Pedersen, J. S., & Morimoto, R. I. (2015). Investigating the spreading and toxicity of prion-like proteins using the metazoan model organism *C. elegans*. *Journal of Visualized Experiments*, *95*. https://doi.org/10.3791/52321.

Ochiishi, T., Doi, M., Yamasaki, K., Hirose, K., Kitamura, A., Urabe, T., Hattori, N., Kinjo, M., Ebihara, T., & Shimura, H. (2016). Development of new fusion proteins for visualizing amyloid-β oligomers in vivo. *Scientific Reports*. https://doi.org/10.1038/srep22712.

Palop, J. J., Chin, J., Roberson, E. D., Wang, J., Thwin, M. T., Bien-Ly, N., Yoo, J., Ho, K. O., Yu, G. Q., Kreitzer, A., Finkbeiner, S., Noebels, J. L., & Mucke, L. (2007).

Aberrant Excitatory Neuronal Activity and Compensatory Remodeling of Inhibitory Hippocampal Circuits in Mouse Models of Alzheimer's Disease. *Neuron*. https://doi.org/10.1016/j.neuron.2007.07.025.

Palop, J. J., & Mucke, L. (2016). Network abnormalities and interneuron dysfunction in Alzheimer disease. *Nature Reviews Neuroscience*. https://doi.org/10.1038/nrn.2016.141.

Parra Bravo, C., Naguib, S. A., & Gan, L. (2024). Cellular and pathological functions of tau. *Nature Reviews Molecular Cell Biology*. https://doi.org/10.1038/s41580-024-00753-9.

Peter, E., & Candido, M. (2002). The Small Heat Shock Proteins of the Nematodes *Caenorhabditis elegans*: Structure, Regulation and Biology. *Progress in Molecular and Subcellular Biology*. https://doi.org/10.1007/978-3-642-56348-5_4.

Pigazzini, M. L., Lawrenz, M., Margineanu, A., Kaminski Schierle, G. S., & Kirstein, J. (2021). An Expanded Polyproline Domain Maintains Mutant Huntingtin Soluble in vivo and During Aging. *Frontiers in Molecular Neuroscience*. https://doi.org/10.3389/fnmol.2021.721749.

Pir, G. J., Choudhary, B., & Mandelkow, E. (2017). *Caenorhabditis elegans* models of tauopathy. *FASEB Journal*. https://doi.org/10.1096/fj.201701007.

Pir, G. J., Choudhary, B., Mandelkow, E., & Mandelkow, E. M. (2016). Tau mutant A152T, a risk factor for FTD/PSP, induces neuronal dysfunction and reduced lifespan independently of aggregation in a *C. elegans* Tauopathy model. *Molecular Neurodegeneration*. https://doi.org/10.1186/s13024-016-0096-1.

Pizzarelli, R., Pediconi, N., & Di Angelantonio, S. (2020). Molecular Imaging of Tau Protein: New Insights and Future Directions. *Frontiers in Molecular Neuroscience*. https://doi.org/10.3389/fnmol.2020.586169.

Polanco, J. C., Li, C., Bodea, L. G., Martinez-Marmol, R., Meunier, F. A., & Götz, J. (2018). Amyloid-β and tau complexity - Towards improved biomarkers and targeted therapies. In *Nature Reviews Neurology* (Vol. 14, Issue 1, pp. 22–40). Nature Publishing Group. https://doi.org/10.1038/nrneurol.2017.162.

Poorkaj, P., Bird, T. D., Wijsman, E., Nemens, E., Garruto, R. M., Anderson, L., Andreadis, A., Wiederholt, W. C., Raskind, M., & Schellenberg, G. D. (1998). Tau is a candidate gene for chromosome 17 frontotemporal dementia. *Annals of Neurology*. https://doi.org/10.1002/ana.410430617.

Portelius, E., Bogdanovic, N., Gustavsson, M. K., Volkmann, I., Brinkmalm, G., Zetterberg, H., Winblad, B., & Blennow, K. (2010). Mass spectrometric characterization of brain amyloid beta isoform signatures in familial and sporadic Alzheimer's disease. *Acta Neuropathologica*. https://doi.org/10.1007/s00401-010-0690-1.

Pras, A., Houben, B., Aprile, F. A., Seinstra, R., Gallardo, R., Janssen, L., Hogewerf, W., Gallrein, C., De Vleeschouwer, M., Mata-Cabana, A., Koopman, M., Stroo, E., de Vries, M., Louise Edwards, S., Kirstein, J., Vendruscolo, M., Falsone, S. F., Rousseau, F., Schymkowitz, J., & Nollen, E. A. A. (2021). The cellular modifier MOAG-4/SERF drives amyloid formation through charge complementation. *The EMBO Journal*. https://doi.org/10.15252/embj.2020107568.

Puzzo, D., Privitera, L., Leznik, E., Fà, M., Staniszewski, A., Palmeri, A., & Arancio, O. (2008). Picomolar amyloid-β positively modulates synaptic plasticity and memory in hippocampus. *Journal of Neuroscience*. https://doi.org/10.1523/JNEUROSCI.2692-08.2008.

Rampelt, H., Kirstein-Miles, J., Nillegoda, N. B., Chi, K., Scholz, S. R., Morimoto, R. I., & Bukau, B. (2012). Metazoan Hsp70 machines use Hsp110 to power protein disaggregation. *EMBO Journal*. https://doi.org/10.1038/emboj.2012.264.

Richmond, J. E., Davis, W. S., & Jorgensen, E. M. (1999). UNC-13 is required for synapticvesicle fusion in *C. elegans*. *Nature*. https://doi.org/10.1016/j.cub.2005.10.049.

Rosenzweig, R., Nillegoda, N. B., Mayer, M. P., & Bukau, B. (2019). The Hsp70 chaperone network. *Nature Reviews Molecular Cell Biology*. https://doi.org/10.1038/s41580-019-0133-3.

Saha, I., Yuste-Checa, P., Da Silva Padilha, M., Guo, Q., Körner, R., Holthusen, H., Trinkaus, V. A., Dudanova, I., Fernández-Busnadiego, R., Baumeister, W., Sanders, D. W., Gautam, S., Diamond, M. I., Hartl, F. U., & Hipp, M. S. (2023). The AAA+ chaperone VCP disaggregates Tau fibrils and generates aggregate seeds in a cellular system. *Nature Communications*. https://doi.org/10.1038/s41467-023-36058-2.

Salminen, A., Ojala, J., Kauppinen, A., Kaarniranta, K., & Suuronen, T. (2009). Inflammation in Alzheimer's disease: Amyloid-β oligomers trigger innate immunity defence via pattern recognition receptors. *Progress in Neurobiology*. https://doi.org/10.1016/j.pneurobio.2009.01.001.

San-Miguel, A., & Lu, H. (2013). Microfluidics as a tool for *C. elegans* research. *WormBook*. https://doi.org/10.1895/wormbook.1.162.1.

SantaCruz, K., Lewis, J., Spires, T., Paulson, J., Kotilinek, L., Ingelsson, M., Guimaraes, A., DeTure, M., Ramsden, M., McGowan, E., Forster, C., Yue, M., Orne, J., Janus, C., Mariash, A., Kuskowski, M., Hyman, B., Hutton, M., & Ashe, K. H. (2005). Tau Suppression in a Neurodegenerative Mouse Model Improves Memory Function. *Science*. https://doi.org/10.1126/science.1110289.

Satapathy, S., & Wilson, M. R. (2022). Identifying new molecular players in extracellular proteostasis. *Biochemical Society Transactions*. https://doi.org/10.1042/BST20210369.

Schiavi, A., Cirotti, C., Gerber, L. S., Di Lauro, G., Maglioni, S., Shibao, P. Y. T., Montresor, S., Kirstein, J., Petzsch, P., Köhrer, K., Schins, R. P. F., Wahle, T., Barilà, D., & Ventura, N. (2023). Abl depletion via autophagy mediates the beneficial effects of quercetin against Alzheimer pathology across species. *Cell Death Discovery*. https://doi.org/10.1038/s41420-023-01592-x.

Schindelin, J., Arganda-Carreras, I., Frise, E., Kaynig, V., Longair, M., Pietzsch, T., Preibisch, S., Rueden, C., Saalfeld, S., Schmid, B., Tinevez, J. Y., White, D. J., Hartenstein, V., Eliceiri, K., Tomancak, P., & Cardona, A. (2012). Fiji: An open-source platform for biological-image analysis. *Nature Methods*. https://doi.org/10.1038/nmeth.2019.

Schrödel, T., Prevedel, R., Aumayr, K., Zimmer, M., & Vaziri, A. (2013). Brain-wide 3D imaging of neuronal activity in *Caenorhabditis elegans* with sculpted light. *Nature Methods*. https://doi.org/10.1038/nmeth.2637.

Sciacca, M. F. M., La Rosa, C., & Milardi, D. (2021). Amyloid-Mediated Mechanisms of Membrane Disruption. *Biophysica*. https://doi.org/10.3390/biophysica1020011.

Scior, A., Buntru, A., Arnsburg, K., Ast, A., Iburg, M., Juenemann, K., Pigazzini, M. L., Mlody, B., Puchkov, D., Priller, J., Wanker, E. E., Prigione, A., & Kirstein, J. (2018). Complete suppression of Htt fibrilization and disaggregation of Htt fibrils by a trimeric chaperone complex. *The EMBO Journal*. https://doi.org/10.15252/embj.201797212.

Sexton, C., Snyder, H., Beher, D., Boxer, A. L., Brannelly, P., Brion, J. P., Buée, L., Cacace, A. M., Chételat, G., Citron, M., DeVos, S. L., Diaz, K., Feldman, H. H., Frost, B., Goate, A. M., Gold, M., Hyman, B., Johnson, K., Karch, C. M., … Carrillo,

M. C. (2022). Current directions in tau research: Highlights from Tau 2020. *Alzheimer's and Dementia*. https://doi.org/10.1002/alz.12452.

Sharma, A., Shah, O. P., Sharma, L., Gulati, M., Behl, T., Khalid, A., Mohan, S., Najmi, A., & Zoghebi, K. (2024). Molecular Chaperones as Therapeutic Target: Hallmark of Neurodegenerative Disorders. *Molecular Neurobiology*. https://doi.org/10.1007/s12035-023-03846-2.

Šišková, Z., Justus, D., Kaneko, H., Friedrichs, D., Henneberg, N., Beutel, T., Pitsch, J., Schoch, S., Becker, A., vonderKammer, H., & Remy, S. (2014). Dendritic structural degeneration is functionally linked to cellular hyperexcitability in a mouse model of alzheimer's disease. *Neuron*. https://doi.org/10.1016/j.neuron.2014.10.024.

Soucek, T., Cumming, R., Dargusch, R., Maher, P., & Schubert, D. (2003). The Regulation of Glucose Metabolism by HIF-1 Mediates a Neuroprotective Response to Amyloid Beta Peptide. *Neuron*. https://doi.org/10.1016/s0896-6273(03)00367-2.

Sperling, R., Mormino, E., & Johnson, K. (2014). The evolution of preclinical Alzheimer's disease: Implications for prevention trials. In *Neuron* (Vol. 84, Issue 3, pp. 608–622). Cell Press. https://doi.org/10.1016/j.neuron.2014.10.038.

Stargardt, A., Swaab, D. F., & Bossers, K. (2015). The storm before the quiet: Neuronal hyperactivity and Aβ in the presymptomatic stages of Alzheimer's disease. *Neurobiology of Aging*. https://doi.org/10.1016/j.neurobiolaging.2014.08.014.

Stöhr, J., Watts, J. C., Mensinger, Z. L., Oehler, A., Grillo, S. K., DeArmond, S. J., Prusiner, S. B., & Giles, K. (2012). Purified and synthetic Alzheimer's amyloid beta (Aβ) prions. *Proceedings of the National Academy of Sciences of the United States of America*. https://doi.org/10.1073/pnas.1206555109.

St-Onge, F., Chapleau, M., Breitner, J. C. S., Villeneuve, S., & Binette, A. P. (2024). Tau accumulation and its spatial progression across the Alzheimer's disease spectrum. *Brain Communications*. https://doi.org/10.1093/braincomms/fcae031.

Sultan, A., Nesslany, F., Violet, M., Bégard, S., Loyens, A., Talahari, S., Mansuroglu, Z., Marzin, D., Sergeant, N., Humez, S., Colin, M., Bonnefoy, E., Buée, L., & Galas, M. C. (2011). Nuclear Tau, a key player in neuronal DNA protection. *Journal of Biological Chemistry*. https://doi.org/10.1074/jbc.M110.199976.

Tai, H. C., & Schuman, E. M. (2008). Ubiquitin, the proteasome and protein degradation in neuronal function and dysfunction. *Nature Reviews Neuroscience*. https://doi.org/10.1038/nrn2499.

Tallini, Y. N., Ohkura, M., Choi, B.-R., Ji, G., Imoto, K., Doran, R., Lee, J., Plan, P., Wilson, J., Xin, H.-B., Sanbe, A., Gulick, J., Mathai, J., Robbins, J., Salama, G., Nakai, J., & Kotlikoff, M. I. (2006). Imaging cellular signals in the heart in vivo: Cardiac expression of the high-signal Ca2+ indicator GCaMP2. *PNAS*. https://doi.org/10.1073/pnas.0509378103.

Tanemura, K., Murayama, M., Akagi, T., Hashikawa, T., Tominaga, T., Ichikawa, M., Yamaguchi, H., & Takashima, A. (2001). Neurodegeneration with Tau Accumulation in a Transgenic Mouse Expressing V337M Human Tau. *The Journal of Neuroscience*. https://doi.org/10.1523/JNEUROSCI.22-01-00133.2002.

Tanley, S., & Rusiner, B. P. (2001). Shattuck Lecture — Neurodegenerative disease and prions. *The New England Journal of Medicine*. https://doi.org/10.1056/NEJM200105173442006.

Targa Dias Anastacio, H., Matosin, N., & Ooi, L. (2022). Neuronal hyperexcitability in Alzheimer's disease: what are the drivers behind this aberrant phenotype? *Translational Psychiatry*. https://doi.org/10.1038/s41398-022-02024-7.

The *C. elegans* Sequence Consortium. (1998). Genome Sequence of the Nematode *C. elegans*: A Platform for Investigating Biology the *C. elegans* Sequencing Consortium. *Science*. www.sciencemag.org

Thomas, K. R., Bangen, K. J., Weigand, A. J., Edmonds, E. C., Wong, C. G., Cooper, S., Delano-Wood, L., & Bondi, M. W. (2020). Objective subtle cognitive difficulties predict future amyloid accumulation and neurodegeneration. *Neurology*. https://doi.org/10.1212/WNL.0000000000008838.

Tittelmeier, J., Druffel-Augustin, S., Alik, A., Melki, R., & Nussbaum-Krammer, C. (2022). Dissecting aggregation and seeding dynamics of α-Syn polymorphs using the phasor approach to FLIM. *Communications Biology*. https://doi.org/10.1038/s42003-022-04289-6.

Tittelmeier, J., Nachman, E., & Nussbaum-Krammer, C. (2020). Molecular Chaperones: A Double-Edged Sword in Neurodegenerative Diseases. *Frontiers in Aging Neuroscience*. https://doi.org/10.3389/fnagi.2020.581374.

Tittelmeier, J., Sandhof, C. A., Ries, H. M., Druffel-Augustin, S., Mogk, A., Bukau, B., & Nussbaum-Krammer, C. (2020). The HSP110/HSP70 disaggregation system

generates spreading-competent toxic α-synuclein species. *The EMBO Journal*. https://doi.org/10.15252/embj.2019103954.

Tracy, T. E., Madero-Pérez, J., Swaney, D. L., Chang, T. S., Moritz, M., Konrad, C., Ward, M. E., Stevenson, E., Hüttenhain, R., Kauwe, G., Mercedes, M., Sweetland-Martin, L., Chen, X., Mok, S. A., Wong, M. Y., Telpoukhovskaia, M., Min, S. W., Wang, C., Sohn, P. D., … Gan, L. (2022). Tau interactome maps synaptic and mitochondrial processes associated with neurodegeneration. *Cell*. https://doi.org/10.1016/j.cell.2021.12.041.

Vabulas, R. M., Raychaudhuri, S., Hayer-Hartl, M., & Hartl, F. U. (2010). Protein folding in the cytoplasm and the heat shock response. *Cold Spring Harbor Perspectives in Biology*. https://doi.org/10.1101/cshperspect.a004390.

van Oosten-Hawle, P. (2023). Exploiting inter-tissue stress signalling mechanisms to preserve organismal proteostasis during aging. *Frontiers in Physiology*. https://doi.org/10.3389/fphys.2023.1228490.

van Oosten-Hawle, P., Porter, R. S., & Morimoto, R. I. (2013). Regulation of organismal proteostasis by transcellular chaperone signalling. *Cell*. https://doi.org/10.1016/j.cell.2013.05.015.

Vanhooren, V., & Libert, C. (2013). The mouse as a model organism in aging research: Usefulness, pitfalls and possibilities. *Ageing Research Reviews*. https://doi.org/10.1016/j.arr.2012.03.010.

Vega, I. E., Cui, L., Propst, J. A., Hutton, M. L., Lee, G., & Yen, S. H. (2005). Increase in tau tyrosine phosphorylation correlates with the formation of tau aggregates. *Molecular Brain Research*. https://doi.org/10.1016/j.molbrainres.2005.04.015.

Viles, J. H. (2023). Imaging Amyloid-β Membrane Interactions: Ion-Channel Pores and Lipid-Bilayer Permeability in Alzheimer's Disease. *Angewandte Chemie - International Edition*. https://doi.org/10.1002/anie.202215785.

Violet, M., Delattre, L., Tardivel, M., Sultan, A., Chauderlier, A., Caillierez, R., Talahari, S., Nesslany, F., Lefebvre, B., Bonnefoy, E., Buée, L., & Galas, M. C. (2014). A major role for Tau in neuronal DNA and RNA protection in vivo under physiological and hyperthermic conditions. *Frontiers in Cellular Neuroscience*. https://doi.org/10.3389/fncel.2014.00084.

Vogel, J. W., Iturria-Medina, Y., Strandberg, O. T., Smith, R., Levitis, E., Evans, A. C., Hansson, O., Weiner, M., Aisen, P., Petersen, R., Jack, C. R., Jagust, W., Trojanowki, J. Q., Toga, A. W., Beckett, L., Green, R. C., Saykin, A. J., Morris, J.,

Shaw, L. M., … Wollmer, P. (2020). Spread of pathological tau proteins through communicating neurons in human Alzheimer's disease. *Nature Communications*. https://doi.org/10.1038/s41467-020-15701-2.

Von Bergen, M., Friedhoff, P., Biernat, J., Heberle, J., Mandelkow, E.-M., & Mandelkow, E. (1999). Assembly of protein into Alzheimer paired helical filaments depends on a local sequence motif (306VQIVYK311) forming structure. *PNAS*. https://doi.org/10.1073/pnas.97.10.5129.

Walsh, D. M., Lomakin, A., Benedek, G. B., Condron, M. M., & Teplow, D. B. (1997). Amyloid β-protein fibrillogenesis: Detection of a protofibrillar intermediate. *Journal of Biological Chemistry*. https://doi.org/10.1074/jbc.272.35.22364.

Wang, Y., & Mandelkow, E. (2016). Tau in physiology and pathology. *Nature Reviews Neuroscience*. https://doi.org/10.1038/nrn.2015.1.

Warren, S. C., Margineanu, A., Alibhai, D., Kelly, D. J., Talbot, C., Alexandrov, Y., Munro, I., Katan, M., Dunsby, C., & French, P. M. W. (2013). Rapid Global Fitting of Large Fluorescence Lifetime Imaging Microscopy Datasets. *PLOS ONE*. https://doi.org/10.1371/journal.pone.0070687.

Wegmann, S., Biernat, J., & Mandelkow, E. (2021). A current view on Tau protein phosphorylation in Alzheimer's disease. *Current Opinion in Neurobiology*. https://doi.org/10.1016/j.conb.2021.03.003.

White, J. A., Manelli, A. M., Holmberg, K. H., Van Eldik, L. J., & LaDu, M. J. (2005). Differential effects of oligomeric and fibrillar amyloid-β1-42 on astrocyte-mediated inflammation. *Neurobiology of Disease*. https://doi.org/10.1016/j.nbd.2004.12.013.

Whitehouse, P. J., Price, D. L., Clark, A. W., Coyle, J. T., & DeLong, M. R. (1981). Alzheimer disease: Evidence for selective loss of cholinergic neurons in the nucleus basalis. *Annals of Neurology*. https://doi.org/10.1002/ana.410100203.

Wilcox, K. C., Lacor, P. N., Pitt, J., & Klein, W. L. (2011). Aβ oligomer-induced synapse degeneration in Alzheimer's disease. *Cellular and Molecular Neurobiology*. https://doi.org/10.1007/s10571-011-9691-4.

Wilson, M. R., Satapathy, S., & Vendruscolo, M. (2023). Extracellular protein homeostasis in neurodegenerative diseases. *Nature Reviews Neurology*. https://doi.org/10.1038/s41582-023-00786-2.

Wyatt, A. R., Yerbury, J. J., Ecroyd, H., & Wilson, M. R. (2013). Extracellular chaperones and proteostasis. *Annual Review of Biochemistry*. https://doi.org/10.1146/annurev-biochem-072711-163904.

Yakubu, U. M., & Morano, K. A. (2018). Roles of the nucleotide exchange factor and chaperone Hsp110 in cellular proteostasis and diseases of protein misfolding. *Biological Chemistry*. https://doi.org/10.1515/hsz-2018-0209.

Yang, Y., Arseni, D., Zhang, W., Huang, M., Lövestam, S., Schweighauser, M., Kotecha, A., Murzin, A. G., Peak-Chew, S. Y., Macdonald, J., Lavenir, I., Garringer, H. J., Gelpi, E., Newell, K. L., Kovacs, G. G., Vidal, R., Ghetti, B., Ryskeldi-Falcon, B., W Scheres, S. H., & Goedert, M. (2022). Cryo-EM structures of amyloid-beta 42 filaments from human brains. *Science*. https://doi.org/10.1126/science.abm7285.

Yepes, M. (2021). The plasminogen activating system in the pathogenesis of Alzheimer's disease. *Neural Regeneration Research*. https://doi.org/10.4103/1673-5374.308076.

Yerbury, J. J., Poon, S., Meehan, S., Thompson, B., Kumita, J. R., Dobson, C. M., & Wilson, M. R. (2007). The extracellular chaperone clusterin influences amyloid formation and toxicity by interacting with prefibrillar structures. *The FASEB Journal*. https://doi.org/10.1096/fj.06-7986com.

Yogev, S., Cooper, R., Fetter, R., Horowitz, M., & Shen, K. (2016). Microtubule Organization Determines Axonal Transport Dynamics. *Neuron*. https://doi.org/10.1016/j.neuron.2016.09.036.

Yu, L., Edalji, R., Harlan, J. E., Holzman, T. F., Lopez, A. P., Labkovsky, B., Hillen, H., Barghorn, S., Ebert, U., Richardson, P. L., Miesbauer, L., Solomon, L., Bartley, D., Walter, K., Johnson, R. W., Hajduk, P. J., & Olejniczak, E. T. (2009). Structural characterization of a soluble amyloid β-peptide oligomer. *Biochemistry*. https://doi.org/10.1021/bi802046n.

Yuste-Checa, P., Bracher, A., & Hartl, F. U. (2022). The chaperone Clusterin in neurodegeneration − friend or foe? *BioEssays*. https://doi.org/10.1002/bies.202100287.

Zeng, Y., Yang, J., Zhang, B., Gao, M., Su, Z., & Huang, Y. (2021). The structure and phase of tau: from monomer to amyloid filament. *Cellular and Molecular Life Sciences*. https://doi.org/10.1007/s00018-020-03681-x.

Zhang, J., Zhang, Y., Wang, J., Xia, Y., Zhang, J., & Chen, L. (2024). Recent advances in Alzheimer's disease: Mechanisms, clinical trials and new drug development strategies. *Signal Transduction and Targeted Therapy*. https://doi.org/10.1038/s41392-024-01911-3.

Zhang, Y., Chen, H., Li, R., Sterling, K., & Song, W. (2023). Amyloid β-based therapy for Alzheimer's disease: challenges, successes and future. *Signal Transduction and Targeted Therapy*. https://doi.org/10.1038/s41392-023-01484-7.

Zullo, J. M., Drake, D., Aron, L., O'Hern, P., Dhamne, S. C., Davidsohn, N., Mao, C. A., Klein, W. H., Rotenberg, A., Bennett, D. A., Church, G. M., Colaiácovo, M. P., & Yankner, B. A. (2019). Regulation of lifespan by neural excitation and REST. *Nature*. https://doi.org/10.1038/s41586-019-1647-8.

8 SUPPLEMENT

Quantification of mScarlet-Aβ$_{1-42}$ fluorescence intensities.

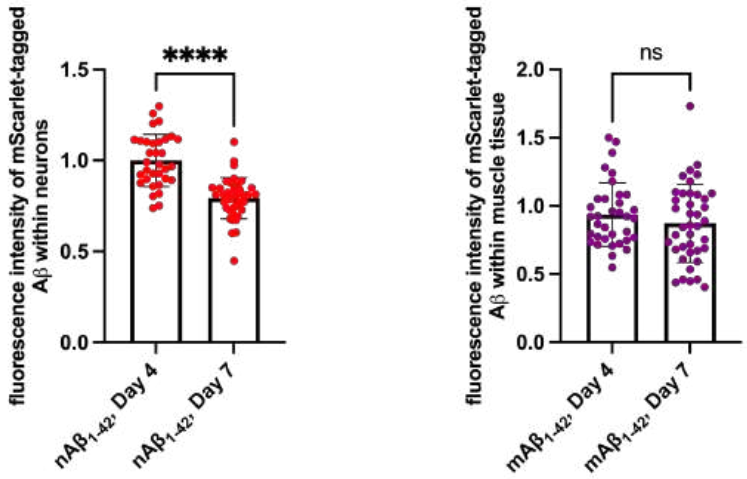

Figure 8.1: *Quantification of fluorescence intensity levels of mScarlet-tagged Aβ$_{1-42}$.*

Quantification of mScarlet-Aβ$_{1-42}$ fluorescence intensity of young adult (day 4-old) and adult (day 7-old) nematodes of the nAβ$_{1-42}$ (left graph) and mAβ$_{1-42}$ (right graph) strain. Confocal fluorescent images of three cohorts of a total of 33-40 nematodes were recorded, fluorescence intensities were quantified by Fiji and normalised to day 4. Data are displayed as mean fluorescence intensity ± SD. Student's t-test with Welch's correction was performed to assess significance (**** = $p < 0.0001$; ns = $p > 0.05$).

Non-normalised fluorescence intensities of neuronal GCaMP6m.

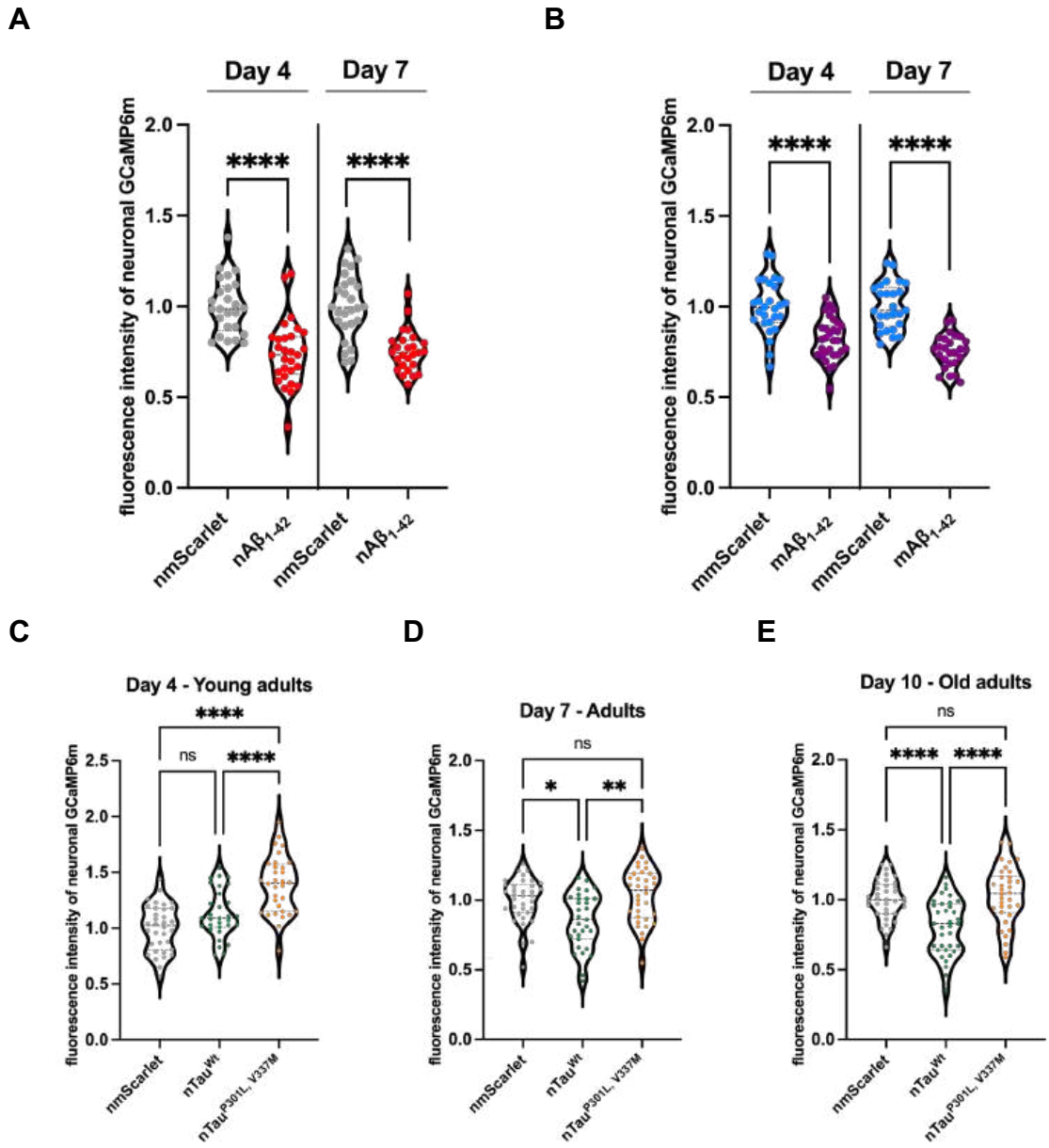

Figure 8.2: *Fluorescence intensity of neuronal GCaMP6m before normalisation to GCaMP6m protein levels.*

A Violin dot plot of the average GCaMP6m fluorescence intensity of young adult animals (day 4-old) and adult animals (day 7-old) of nmScarlet and nAβ_{1-42} before normalisation to GCaMP6m protein levels. GCaMP6m intensities were measured in alive animals using microfluidic devices with a widefield fluorescence microscope and intensities were quantified using Fiji. Every dot represents the neuronal GCaMP6m fluorescence intensity of a single animal of nmScarlet (grey) and nAβ_{1-42} (red). n = 3 and N = 25-29 animals. Significance was assessed between nmScarlet day 4 and nAβ_{1-42} day 4 and nmScarlet day 7 and nAβ_{1-42} day 7 respectively by unpaired Student's t-test with Welch's correction (**** = $p \leq 0.0001$).

B Violin dot plot of the average GCaMP6m fluorescence intensity of young adult animals (day 4-old) and adult animals (day 7-old) of mmScarlet and mAβ_{1-42} before normalisation to GCaMP6m protein levels. GCaMP6m intensities were measured in alive animals using microfluidic devices with a widefield fluorescence microscope and intensities were quantified using Fiji. Every dot represents the neuronal GCaMP6m fluorescence intensity of a single animal of mmScarlet (turquoise) and mAβ_{1-42} (purple). n = 3-4 and N = 26-30 animals. Significance was assessed between mmScarlet day 4 and mAβ_{1-42} day 4 and mmScarlet day 7 and mAβ_{1-42} day 7 respectively by unpaired Student's t-test with Welch's correction (**** = $p \leq 0.0001$).

C Violin dot plot of the average GCaMP6m fluorescence intensity of young adult animals (day 4-old) of the control strain nmScarlet, nTau^{WT} and nTau^{P301L,V337M} before normalisation to GCaMP6m protein levels. GCaMP6m intensities were measured in alive animals using microfluidic devices with a widefield fluorescence microscope and intensities were quantified using Fiji. Every dot represents the neuronal GCaMP6m fluorescence intensity of a single animal of nmScarlet (grey) and nTau^{WT} (green) and nTau^{P301L,V337M} (orange). n = 5 and N = 31-34 animals. Significance was assessed by one-way ANOVA + Bonferroni post hoc test (ns = $p > 0.05$; **** = $p \leq 0.0001$.

D Violin dot plot of the average GCaMP6m fluorescence intensity of adult animals (day 7-old) of the control strain nmScarlet, nTau^{WT} and nTau^{P301L,V337M} before normalisation to GCaMP6m protein levels. GCaMP6m intensities were measured in alive animals using microfluidic devices with a widefield fluorescence microscope and intensities were quantified using Fiji. Every dot represents the neuronal GCaMP6m fluorescence intensity of a single animal of nmScarlet (grey) and nTau^{WT} (green) and nTau^{P301L,V337M} (orange). n = 4-5 and N = 31-35 animals. Significance was assessed by Kruskal-Wallis test with Dunn's post hoc test (ns = $p > 0.05$; * = $p \leq 0.05$; **= $p \leq 0.01$).

E Violin dot plot of the average GCaMP6m fluorescence intensity of old adult animals (day 10-old) of the control strain nmScarlet, nTau^{WT} and nTau^{P301L,V337M} before normalisation to GCaMP6m protein levels. GCaMP6m intensities were measured in alive animals using microfluidic devices with a widefield fluorescence microscope and intensities were quantified using Fiji. Every dot represents the neuronal GCaMP6m fluorescence intensity of a single animal of nmScarlet (grey) and nTau^{WT} (green) and nTau^{P301L,V337M} (orange). n = 4-5 and N = 34-37 animals. Significance was assessed by one-way ANOVA + Bonferroni post hoc test (ns = $p > 0.05$; **** = $p \leq 0.0001$)

Quantification of GCaMP6m protein levels in Aβ$_{1-42}$-expressing strains.

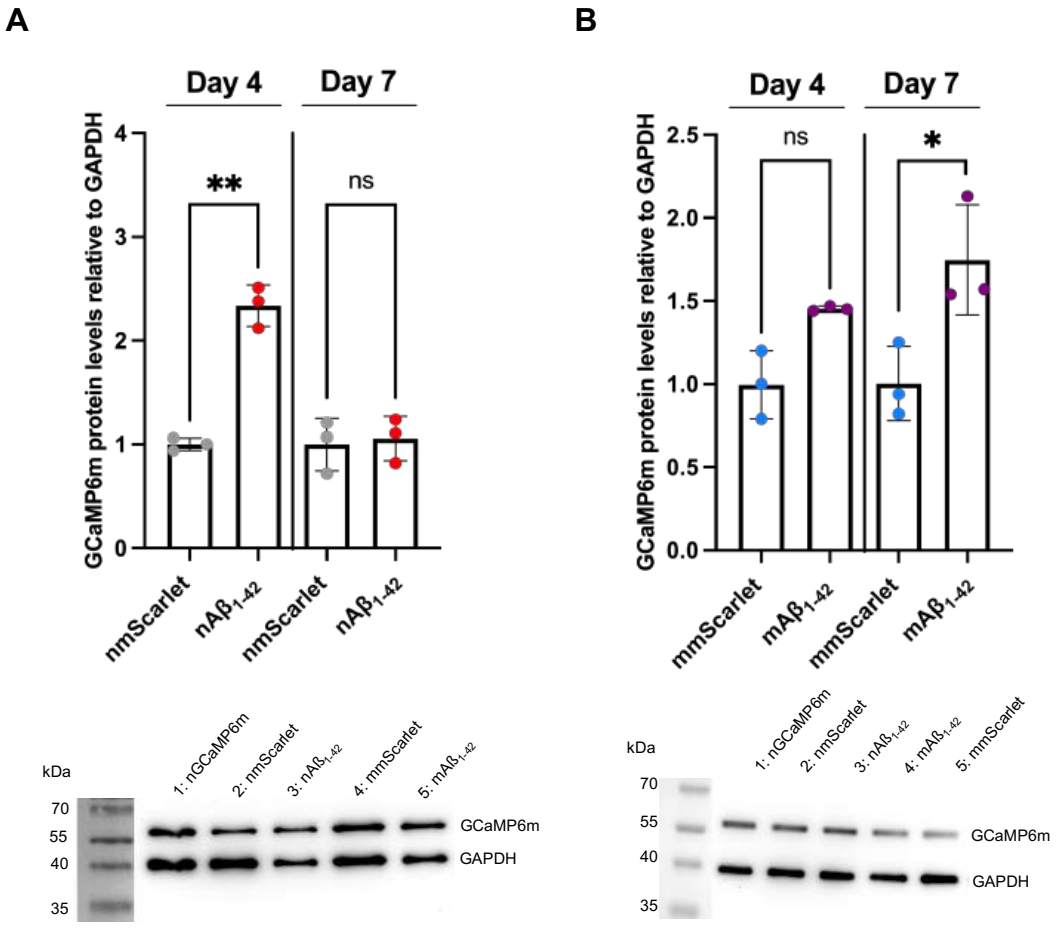

Figure 8.3: *Quantification of GCaMP6m protein levels in neuronal and muscle Aβ$_{1-42}$ and respective mScarlet control strains.*

A Quantification of GCaMP6m protein levels by Western blots of total protein lysates of young adult (day 4-old) and adult animals (day 7-old) of nmScarlet (grey) and nAβ$_{1-42}$ (red) animals. Scatter dot plot shows quantification of GCaMP6m protein levels relative to GAPDH from three independent cohorts. Significance was assessed between nmScarlet day 4 and nAβ$_{1-42}$ day 4 and nmScarlet day 7 and nAβ$_{1-42}$ day 7, respectively, by unpaired Student's t-test with Welch's correction (ns = $p > 0.05$; **= $p \leq 0.01$). Image below is a representative Western blot using mouse anti-GFP(B34) antibodies to detect GCaMP6m.

B Quantification of GCaMP6m protein levels by Western blot of total protein lysates of young adult (day 4-old) and adult animals (day 7-old) of mmScarlet (turquoise) and mAβ$_{1-42}$ (purple) animals. Scatter dot plot shows quantification of GCaMP6m protein levels relative to GAPDH from 3 independent cohorts. Significance was assessed between mmScarlet day 4 and mAβ$_{1-42}$ day 4 and mmScarlet day 7 and mAβ$_{1-42}$ day 7, respectively, by unpaired Student's t-test with Welch's correction (ns = $p > 0.05$; * = $p < 0.05$). Image below is a representative Western blot using mouse anti-GFP(B34) antibodies to detect GCaMP6m.

Quantification of GCaMP6m protein levels in Tau-expressing strains.

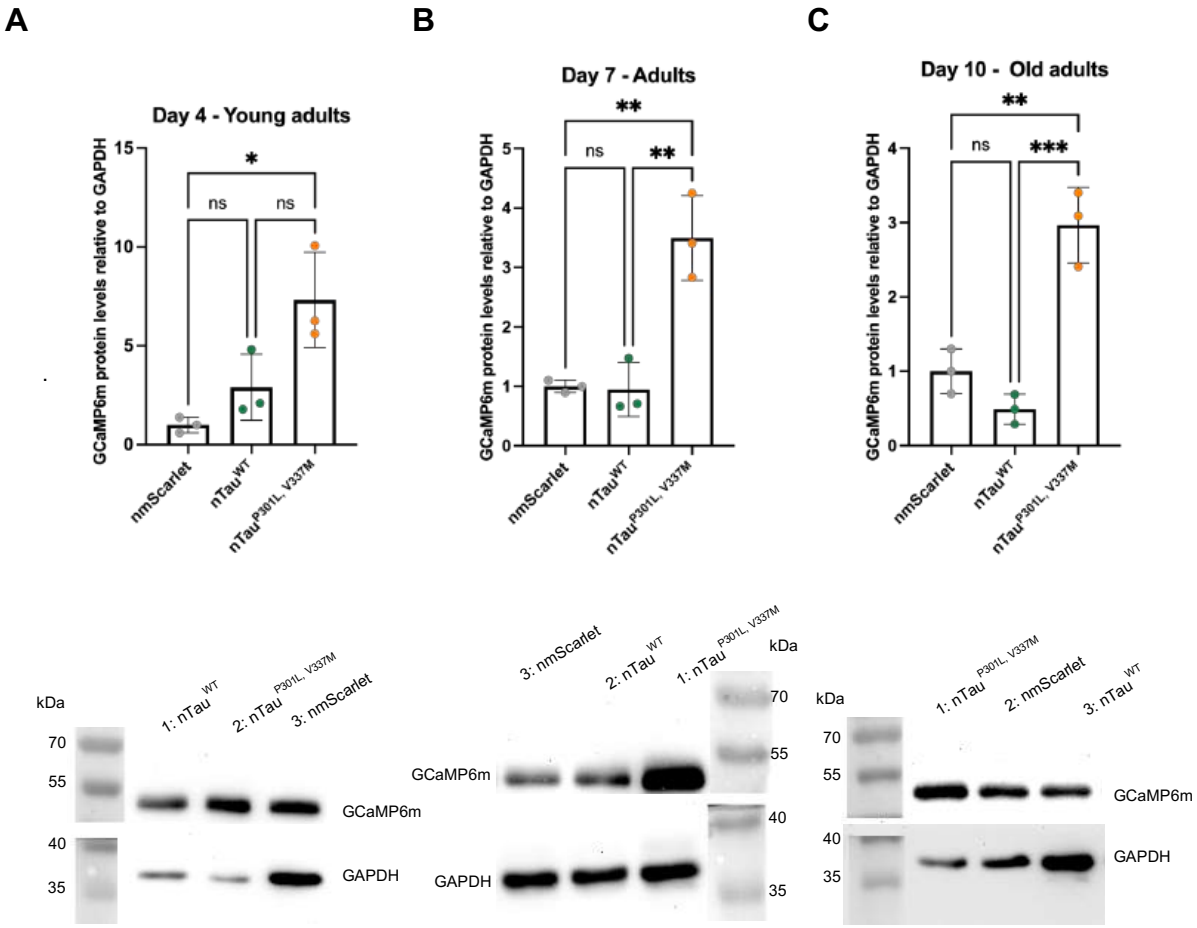

Figure 8.4: *Quantification of GCaMP6m protein levels in C. elegans strains expressing Tau and nmScarlet.*

A Quantification of GCaMP6m protein levels by Western blot of total protein lysates of young adult (day 4-old) of nmScarlet (grey), nTau^{WT} (green) and nTau^{P301L,V337M} (orange) animals. Scatter dot plot shows quantification of GCaMP6m protein levels relative to GAPDH of three independent cohorts. Significance was assessed by one-way ANOVA + Bonferroni post hoc test (ns = $p > 0.05$; * = $p < 0.05$). Image below is a representative Western blot using mouse anti-GFP(B34) antibodies to detect GCaMP6m.

B Quantification of GCaMP6m protein levels by Western blot of total protein lysates of adult (day 7-old) of nmScarlet (grey), nTau^{WT} (green) and nTau^{P301L,V337M} (orange) animals. Scatter dot plot shows quantification of GCaMP6m protein levels relative to GAPDH from three independent cohorts. Significance was assessed by one-way ANOVA + Bonferroni post hoc test (ns = $p > 0.05$; ** = $p \leq 0.01$). Image below is a representative Western blot using mouse anti-GFP(B34) antibodies to detect GCaMP6m.

C Quantification of GCaMP6m protein levels by Western blot of total protein lysates of old adult (day 10-old) of nmScarlet (grey), $nTau^{WT}$ (green) and $nTau^{P301L,V337M}$ (orange) animals. Scatter dot plot shows quantification of GCaMP6m protein levels relative to GAPDH from three independent cohorts. Significance was assessed by one-way ANOVA + Bonferroni post hoc test (ns = $p > 0.05$; ** = $p \leq 0.01$; *** = $p \leq 0.001$). Image below is a representative Western blot using mouse anti-GFP(B34) antibodies to detect GCaMP6m.

Extracellular modifiers TAG-196 and DOD-21 do not affect Aβ$_{1-42}$ aggregation.

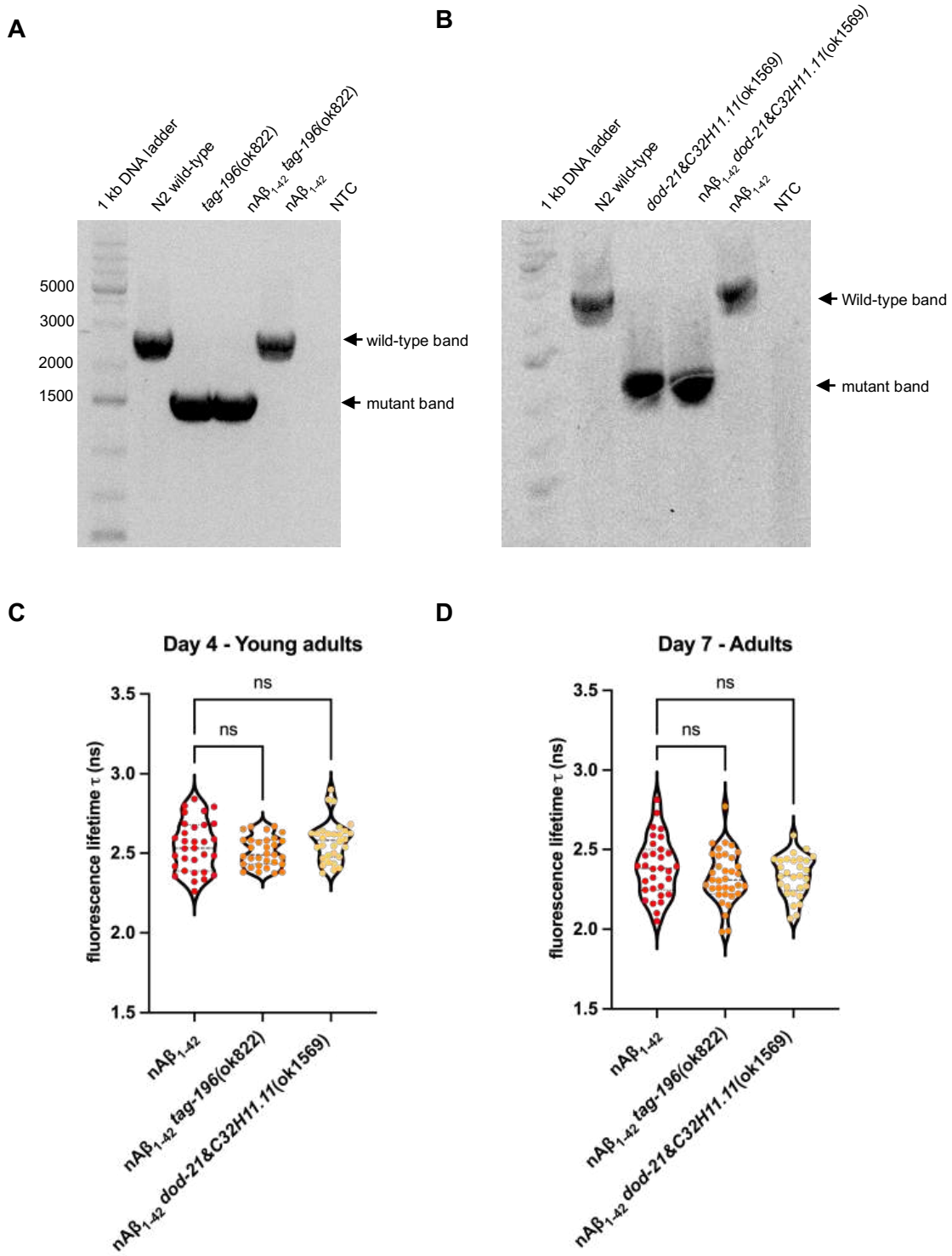

Figure 8.5: *Knockout of the extracellular modifiers TAG-196 and DOD-21 does not affect Aβ$_{1-42}$* aggregation.

A Agarose gel electrophoresis of genotyping the *tag-196* gene locus in nematodes of N2 wild-type, tag-196(ok822), nAβ_{1-42} *tag-196*(ok822) and nAβ_{1-42}. Nematodes without the *tag-196* deletion (i.e., N2 wild-type and nAβ_{1-42}) exhibit a band of 2729 bp while nematodes with the *tag-196* deletion exhibit a band of 1579 bp (*tag-196*(ok822) and nAβ_{1-42} *tag-196*(ok822)). A no-template control (NTC) was employed to check for contamination or non-specific amplification

B Agarose gel electrophoresis of genotyping the *dod-21&C32H11.1* gene locus in nematodes of N2 wild-type, *dod-21&C32H11.1*(ok1569), nAβ_{1-42} *dod-21&C32H11.1*(ok1569) and nAβ_{1-42}. Nematodes without the *dod-21&C32H11.1* deletion (i.e., N2 wild-type and nAβ_{1-42}) exhibit a band of 3041 bp while nematodes with *dod-21&C32H11.1* deletion exhibit a band of 1240 bp (*dod-21&C32H11.1*(ok1569) and nAβ_{1-42} *dod-21&C32H11.1*(ok1569)). A no-template control (NTC) was employed to check for contamination or non-specific amplification.

C Violin dot plot of the average fluorescent lifetime (τ) of young adult animals (day 4-old) of nAβ_{1-42}, nAβ_{1-42} *tag-196*(ok822) and nAβ_{1-42} *dod-21&C32H11.1*(ok1569). Data displays average fluorescent lifetimes ± SD of nAβ_{1-42} (red), nAβ_{1-42} *tag-196*(ok822) (orange), nAβ_{1-42} *dod-21&C32H11.1*(ok1569) (yellow). Every dot represents the average fluorescent lifetime for the head neurons of one single nematode. Three independent cohorts of in total 30-31 animals were analysed. Significance was tested by one-way ANOVA + Bonferroni post hoc test (ns = $p > 0.05$)

D Violin dot plot of the average fluorescent lifetime (τ) of adult animals (day 7-old) of nAβ_{1-42}, nAβ_{1-42} *tag-196*(ok822) and nAβ_{1-42} *dod-21&C32H11.1*(ok1569). Data displays average fluorescent lifetimes ± SD of nAβ_{1-42} (red), nAβ_{1-42} *tag-196*(ok822) (orange), nAβ_{1-42} *dod-21&C32H11.1*(ok1569) (yellow). Every dot represents the average fluorescent lifetime for the head neurons of one single nematode. Three independent cohorts of in total 30-31 animals were analysed. Significance was tested by one-way ANOVA + Bonferroni post hoc test (ns = $p > 0.05$).

LIST OF FIGURES

LIST OF TABLES

LIST OF ABBREVIATIONS

°C	Degree Celsius
Aβ	Amyloid beta
A152E	Alanine to glutamic acid mutation at residue 152 of Tau
A152T	Alanine to tyrosine mutation at residue 152 of Tau
AD	Alzheimer's disease
ALS	Amyotrophic lateral sclerosis
APL-1	Amyloid precursor like protein 1
APP	Amyloid precursor protein
APS	Ammoniumperoxodisulfat
au	Arbitrary units
bp	Base pairs
C. elegans	*Caenorhabditis elegans*
CGC	*Caenorhabditis* genetic center
CJD	Creutzfeldt-Jakob disease
CLEC-1	C-type lectin domain-containing protein 1
CLSM	Confocal laser scanning microscope
cryo-EM	Cryo-electron microscopy
CSF	Cerebrospinal fluid
CTD	C-terminal domain
DMSO	Dimethyl sulfoxide
DNA	Deoxyribonucleic acid
dNTP	Deoxynucleotide triphosphate
Dpy	Dumpy
DTT	Dithiothreitol
E. coli	*Escherichia coli*
EC	Extracellular chaperone
ECL	Enhanced chemiluminescence
ECM	Extracellular modifier
EDTA	Ethylenediaminetetraacetic acid
Ex	Extra-chromosomal array
FLIM	Fluorescence lifetime imaging microscopy

For	forward
FTD	Frontotemporal dementia
FTLD	Frontotemporal lobar degeneration
FUS	RNA-binding protein fused in sarcoma
g (µg, mg)	Gram (microgram, milligram)
GAPDH	Glycerinaldehyd 3-phosphat dehydrogenase
GECI	Genetically encoded calcium indicator
GFP	Green fluorescent protein
h	Hour
HD	Huntington's disease
HSE	Heat-shock element
HSF-1	Heat-shock factor 1
HSP	Heat-shock protein
Hz	Hertz
IL2	Inner labial sensilla 2 (set of six ciliated neurons)
IRES	Internal ribosome entry site
IRF	Instrument response function
Is	Integrated strain
JDP	J-domain protein
kb	kilobase
kDa	kilodalton
KO	Knockout
l, (µl, ml)	Liter (microliter, millilitre)
L1 – L4	Nematode larval stages 1 to 4
LB	Luria broth
LBP-2	Lipid-binding protein 2
LSM	Laser scanning microscope
LYS-3	Lysozyme-like protein 3
m	muscular
M (pM, nM, µM, mM)	Molar (picomolar, nanomolar, micromolar, millimolar)
MAP	Microtubule-associated protein
MAPT	Microtubule-associated protein tau
MCI	Mild cognitive impairment

mRNA	Messenger RNA
MTBD	Microtubule-binding domain
myo-3	Myosin heavy chains structural gene 3
n	neuronal
NCBI	National Center for Biotechnology Information
NFT	Neurofibrillary tangles
NGM	Nematode growth medium
ns	Nanoseconds or non significant
NTD	N-terminal domain
P301L	Proline to leucin mutation at residue 301 of Tau
P301S	Proline to serine mutation at residue 301 of Tau
PCR	Polymerase chain reachtion
PD	Parkinson's disease
PDMS	Polydimethylsiloxane
PGPF	Protease-generated protein fragments
PHF	Paired helical filament
PN	Proteostasis network
PRD	Proline-rich domain
PS1/2	Presenilin 1 or 2
PSP	Progressive supranuclear palsy
PTL-1	Protein with tau-like repeats
PTM	Post-translational modification
PVDF	Polyvinylidene fluoride
PXXP	Proline-X-X-proline
R406W	Arginine to tryptophan mutation at residue 406 of Tau
rab-3	Ras-related protein gene 3
Rev	reverse
rgef-1	Rap Guanine nucleotide Exchange factor homolog gene 1
RNA	Ribonucleic acid
RNAi	RNA-interference
ROI	Region of interest
rpm	Revolutions per minute
RT	Room temperature (around 20°C)

s / sec	Second
SD	Standard deviation
SDS	Sodium dodecyl sulphate
SDS-PAGE	SDS-polyacrylamide gel electrophoresis
SH3	SRC homology 3
sHSP	Small heat-shock protein
Snb-1	Synaptobrevin gene 1
SOD1	Superoxide dismutase 1
ssNMR	Solid-state nuclear magnetic resonance
Tau	Tau protein
τ	Fluorescence lifetime
TBE	Tris-borate-EDTA
TBS-(T)	Tris-buffered saline (with Tween 20)
TDP-43	Transactive response DNA binding protein 43 kDa
TEMED	Tetramethylethylenediamine
T_m	Melting temperature
Tris	Tris(hydroxymethyl)aminomethane
UNC-13	Uncoordinated phenotype related protein 13
UPS	Ubiquitin-proteasome System
UTR	Untranslated region
UTR	Untranslated region
UV	Ultraviolet
V	Volt
v/v	Volume per volume
V337M	Valine to methionine mutation at residue 337 of Tau
V363A	Valine to alanine mutation at residue 363 of Tau
V363I	Valine to isoleucine mutation at residue 363 of Tau
w/v	Weight per volume
WB	Western blot
WT	Wild-type

DECLARATION

Universität Bremen | Fachbereich 02 | Postfach 33 04 40, 28334 Bremen

Universität Bremen
Fachbereich 2
Prüfungsamt Chemie
z. Hd. Frau Frauke Ernst
Leobener Straße

28359 Bremen
Deutschland

Prüfungsamt
Chemie

Frauke Ernst
Geschäftsstelle
Fachbereich 02
Leobener Str. / NW2
D-28359 Bremen

Verwaltungspavillon 06
Tel. 0421 218-62802
Fax 0421 218-9862802
frauke.ernst@uni-bremen.de
www.fb2.uni-bremen.de

Versicherung an Eides Statt

Name, Vorname	Hirsch, Franziska
Matrikel-Nr.	-
Straße	
Ort, PLZ	

Ich, Franziska Hirsch

versichere an Eides Statt durch meine Unterschrift, dass ich die vorstehende Arbeit selbständig und ohne fremde Hilfe angefertigt und alle Stellen, die ich wörtlich dem Sinne nach aus Veröffentlichungen entnommen habe, als solche kenntlich gemacht habe, mich auch keiner anderen als der angegebenen Literatur oder sonstiger Hilfsmittel bedient habe.
Ich versichere an Eides Statt, dass ich die vorgenannten Angaben nach bestem Wissen und Gewissen gemacht habe und dass die Angaben der Wahrheit entsprechen und ich nichts verschwiegen habe.
Die Strafbarkeit einer falschen eidesstattlichen Versicherung ist mir bekannt, namentlich die Strafandrohung gemäß § 156 StGB bis zu drei Jahren Freiheitsstrafe oder Geldstrafe bei vorsätzlicher Begehung der Tat bzw. gemäß § 161 Abs. 1 StGB bis zu einem Jahr Freiheitsstrafe oder Geldstrafe bei fahrlässiger Begehung.

Ort, Datum / Unterschrift

ACKNOWLEDGEMENT

I would like to express my deepest gratitude and appreciation to Prof. Dr. Janine Kirstein. I am profoundly thankful and appreciate her guidance, mentorship and trust throughout the past few years.

I would also like to thank Prof. Dr. Olivia Masseck for kindly aggreeing to be the second reviewer of my PhD thesis.

I am deeply grateful to Prof. Gabriele Kaminski Schierle and Dr. Nino Läubli for offering me the opportunity to visit and work in their lab, where I learned about microfluidics and microscopy techniques.

A special thanks goes to all former and present members of the Kirstein group from Bremen and Jena. I am truly grateful for the supportive, collaborative and kind environment that we shared. In particular, I owe a special thanks to Dr. Annette Peter for her guidance in microscopy work as well as to Regina Nahrstedt, Yvonne Woitzat and Verena Fischer for always lending your helping hand in- and outside the lab. Special thanks are extended to Dr. Christian Gallrein for his valuable contributions to the GCaMP6m-Tau-Aβ manuscript. Many thanks to Dr. Priscila Shibao and Sudarson Baskaran for your helpful suggestions and advice whenever I needed it. I am grateful to Sabrina Montresor for our close collaboration, friendship and our many engaging discussions about worms. I would also like to thank Mira Sleiman for always being by my side, your words and advices were always a source of encouragement and motivation.

A very special thanks goes to my family and my closest friends, who feel like family. Your constant support and encouragement have been my anchor throughout this journey. What would life be without you? I am so grateful to have you by my side!

Lastly, I would like to thank my life partner and best friend, Bendix. For almost eight years, you have been my rock, accompanying me through every high and low. You are my home, and *wherever life takes us, I will always go with you.*